McMaster University
DigitalCommons@McMaster

Open Access Dissertations and Theses | Open Dissertations and Theses

Study of Luminescent Silicon-Rich Silicon Nitride and Cerium and Terbium Doped Silicon Oxide Thin Films

Patrick R. J. Wilson

Follow this and additional works at: http://digitalcommons.mcmaster.ca/opendissertations

Part of the Semiconductor and Optical Materials Commons

This Thesis is brought to you for free and open access by the Open Dissertations and Theses at DigitalCommons@McMaster. It has been accepted for inclusion in Open Access Dissertations and Theses by an authorized administrator of DigitalCommons@McMaster. For more information, please contact scom@mcmaster.ca.

Study of Luminescent Silicon-Rich Silicon Nitride and Cerium and Terbium Doped Silicon Oxide Thin Films

Study of Luminescent Silicon-Rich Silicon Nitride and Cerium and Terbium Doped Silicon Oxide Thin Films

By

Patrick Robert James Wilson, B.Eng.

A Thesis

Submitted to the School of Graduate Studies

in Partial Fulfillment of the Requirements

for the Degree

Doctor of Philosophy

McMaster University

© Copyright by Patrick Robert James Wilson, June 2013

DOCTOR OF PHILOSOPHY (2013) McMaster University
(Department of Engineering Physics) Hamilton, Ontario

TITLE: Study of Luminescent Silicon-Rich Silicon Nitride and Cerium and Terbium Doped Silicon Oxide Thin Films

AUTHOR: Patrick Robert James Wilson, B.Eng. (McMaster University)

SUPERVISOR: Professor Peter Mascher

NUMBER OF PAGES: xix, 187

Abstract

Silicon nanostructures formed in silicon-rich silicon nitride (SRSN) and cerium and terbium doped silicon oxide thin films grown using different types of plasma-enhanced chemical vapour deposition have been studied through photoluminescence (PL) and synchrotron-based X-ray absorption spectroscopies to determine the effects of deposition and processing parameters on the luminescent and structural properties of these materials. The SRSN films exhibited bright PL attributed to quantum confinement effects in the silicon nanoclusters (Si-ncs) as well as radiative defects in the silicon nitride host matrix. The peak emission energy could be tuned from the near-infrared across the entire visible spectrum by controlling the film composition and the post-deposition annealing temperature and time to change the size of the Si-ncs. Preliminary experiments on cerium doped SRSN samples indicated that although the cerium ions coordinate in the optically active trivalent oxidation state, they were not effectively sensitized by Si-ncs in the films tested, most likely due to the nanoclusters having bandgap energies that were unsuitable for this purpose. In cerium and terbium co-doped silicon oxide films, cerium disilicate ($Ce_2Si_2O_7$) nanocrystallites were formed by annealing at temperatures of 900°C and higher. The A-$Ce_2Si_2O_7$, G-$Ce_2Si_2O_7$, and $Ce_6[Si_4O_{13}][SiO_4]_2$ phases of cerium disilicate were observed to form under different deposition and annealing conditions. All three phases exhibited extremely bright violet-blue PL and were found to efficiently sensitize green emission from co-dopant Tb^{3+} ions in the films. The Tb^{3+} luminescence predominantly corresponded to the $^5D_4 \rightarrow {}^7F_{3-6}$ emission lines, although weak $^5D_3 \rightarrow {}^7F_{2-6}$ emission lines were also observed in films containing relatively high concentrations of terbium indicating that the sensitization of Tb^{3+} ions occurred through the $^5D_3$, $^5L_{10}$, or $^5D_2$ energy levels.

Acknowledgements

For any journey, it is often the people you share it with that define the experience and are the cornerstone to success. The research conducted for this thesis was supported by the combined efforts of many remarkable individuals across several disciplines and institutions. Without their vital contributions, it would not have been possible to complete this work.

First and foremost, I would like to thank my mother Anna, father Robert, and brother Timothy for their boundless support, encouragement, and inspiration throughout my academic career. There are no words to describe how important their patience, love, and support has been in all areas of my life. I would also like to thank my family, friends, and teachers, especially Ruth Smith and Michael Foltz, for their invaluable contributions over many years to my personal and intellectual growth and development.

Special thanks goes to my supervisor, Peter Mascher, for the many opportunities and valuable direction he has provided over the course of my graduate studies. A true gentleman and role model, I could not have wished for a better mentor or more devoted supervisor. I would also like to thank the past and present members of Peter Mascher's research group who contributed greatly to this research, particularly Tyler Roschuk, Zahra Khatami, Kayne Dunn, Ryszard Dabkowski, Sneha Bernard, and Austin Brown, all of whom dedicated extensive time towards conducting arduous

synchrotron experiments Saskatoon, Saskatchewan, at times braving temperatures below -50°C. I am also immensely grateful for the tremendous guidance and support I received from Tyler in the initial years of my graduate studies as well as the extensive training, assistance, and advice provided by research associates Jacek Wojcik and Evgueni Chelomentsev in the growth and characterization of the thin films studied. Jacek deserves special recognition for going above and beyond the call of duty in committing his time and effort towards ensuring the successful completion of my experiments.

I would like to thank my supervisory committee members Andrew Knights and Adrian Kitai from the Department of Engineering Physics, research engineers Doris Stevanovic and Zhilin Peng from the Centre for Emerging Device Technologies (CEDT), Jim Garrett from the Brockhouse Institute for Materials Research (BIMR), Jim Britten and Victoria Jarvis from the McMaster Analytical X-Ray Diffraction Facility (MAX), as well as Carmen Andrej, Andreas Korinek, and Karleen Dudeck from the Canadian Centre for Electron Microscopy (CCEM) at McMaster University for their valuable insights and assistance in performing various aspects of the sample preparation and analysis over the course of this research.

Finally, I would like to thank Tom Regier, Lucia Zuin, Yongfeng Hu, Robert Blythe, David Chevrier, and Chris Ryan for their help in conducting X-ray absorption spectroscopy (XAS) experiments at the Canadian Light Source (CLS) synchrotron facility, T. K. Sham from the Department of Chemisty at Western University for valuable advice and discussions related to XAS analysis of silicon nanostructures, and Jack Hendriks and William Lennard from the Tandetron Laboratory at Western University for their help with Rutherford backscattering spectrometry (RBS) experiments.

This work has been supported by the Centre for Photonics, a division of Ontario Centres of Excellence (OCE) Inc., by the Canadian Institute for Photonics Innovations

(CIPI), and by the Natural Sciences and Engineering Research Council of Canada (NSERC). Part of this work was performed at the CLS facility, which is supported by NSERC, Canadian Institutes of Health Research (CIHR), National Research Council Canada (NRC), and other government agencies.

This work is dedicated to my parents, Anna and Robert, and my brother Timothy.

Table of Contents

Front Matter i

Abstract . . . iii

Acknowledgements . . . iv

List of Figures . . . x

List of Tables . . . xv

List of Acronyms . . . xvi

1 Introduction **1**

1.1 Light Emission from Silicon-Based Materials . . . 2

1.2 Thesis Objectives and Methods . . . 5

1.3 Contributions to the Field . . . 9

1.4 Outline of the Thesis . . . 12

2 Luminescence from Silicon-Based Materials **14**

2.1 Quantum Confinement in Silicon Nanostructures . . . 17

2.2 Rare Earth Doped Nanostructures . . . 27

2.3 Cerium Disilicate . . . 38

3 Sample Fabrication **42**

3.1 Deposition of Silicon Nitride Thin Films . . . 42

3.2 Deposition of Cerium and Terbium Doped Silicon Oxide Thin Films . 44
3.3 Post-Deposition Annealing 46

4 Methods of Sample Characterization 49
4.1 Rutherford Backscattering Spectrometry 49
4.2 Ellipsometry 52
4.3 Transmission Electron Microscopy 54
4.4 Photoluminescence Spectroscopy 55
4.5 X-Ray Absorption Spectroscopy 57
4.6 X-Ray Diffraction 68

5 Study of Silicon-Rich Silicon Nitride Thin Films 69
5.1 Sample Composition 70
5.2 Isochronal Annealing Comparison of Deposition Systems 71
5.3 Isothermal Annealing at 600℃ 84
5.4 Isothermal Annealing at 800℃ 89
5.5 Cerium Doped Silicon-Rich Silicon Nitride 92

6 Study of Cerium and Terbium Doped Silicon Oxide Thin Films 96
6.1 Growth and Characterization of As-Deposited Films 98
6.2 Isochronal Annealing of Cerium Doped Silicon Oxide 113
6.3 Isochronal Annealing of Cerium and Terbium Co-Doped Silicon Oxide 134
6.4 Isothermal Annealing of Cerium and Terbium Co-Doped Silicon Oxide 145

7 Conclusions 156

8 Future Work 163

References 167

List of Figures

2.1 Band structures for gallium arsenide and silicon crystals 15

2.2 Radiative recombination through direct, indirect, and quasi-direct transitions in semiconductors 18

2.3 Comparison between experimental and theoretical PL energies in porous silicon as a function of crystallite size 20

2.4 Electronic states in Si nanocrystals as a function of cluster size and surface passivation 21

2.5 Ratio of surface to volume atoms as a function of silicon nanocrystal size based on Xie's simplified model 23

2.6 Possible radiative transitions in SiN_x films 24

2.7 Diagram of 4f energy levels for visibly emitting trivalent rare earth ions in their grounds states 29

2.8 Ion-ion interaction processes that can occur between rare earth ions . 32

2.9 Carrier-mediated excitation transfer process in a terbium doped semiconductor 35

2.10 Sensitization of terbium ions by silicon nanoclusters through a Förster-Dexter coupling process 36

2.11 Visualization of the crystal structures of A-$Ce_2Si_2O_7$, G-$Ce_2Si_2O_7$, and $Ce_6[Si_4O_{13}][SiO_4]_2$ cerium disilicate phases 40

3.1 Photograph of two quartz tube furnaces used in the annealing studies 47
3.2 Photograph of the Qualiflow Jipelec Jetfirst 100 rapid thermal processor used in the annealing studies 48

4.1 Fitted RBS spectrum for an as-deposited cerium and terbium co-doped silicon oxide film (CeORSO-02) 51
4.2 Photograph of the J. A. Woollam M-2000U UV-Vis VASE instrument 53
4.3 Top-down view of the SGM and VLS PGM beamlines branching out from the CLS storage ring 58
4.4 The CLS storage ring with the SGM beamline protruding 59
4.5 Energy resolved fluorescence spectrum for a film containing 8.9 at.% Ce annealed at 1200℃ with the integrated O K_α and Ce M_α PFY-XANES spectra plotted underneath 63
4.6 Comparison of O IPFY-, TEY-, and TFY-XANES spectra for a film containing 8.9 at.% Ce annealed at various temperatures 65
4.7 Comparison of O IPFY- and TFY-XANES spectra for three films containing different concentrations of Ce annealed at temperatures above 1100℃ 67

5.1 PL spectra for as-deposited SRSN films grown by PECVD, ECR PECVD, and ICP CVD 72
5.2 PL spectra for SRSN films annealed for 60 minutes 74
5.3 STEM image of amorphous Si-ncs formed in an ICP CVD grown SRSN film with high excess silicon content following 1100℃ annealing . . . 75
5.4 TEY-XANES spectra for as-deposited PECVD, ECR PECVD, and ICP CVD films at the Si K-edge 77
5.5 TFY-XANES spectra for as-deposited PECVD and ICP CVD films at the Si $L_{3,2}$-edge 78

5.6 TEY-XANES spectra at the Si K-edge for annealed low and high excess silicon content films deposited by ICP CVD 81
5.7 TFY-XANES spectra at the Si $L_{3,2}$-edge for annealed low and high excess silicon content films deposited by ICP CVD 82
5.8 TFY-XANES spectra at the Si $L_{3,2}$-edge for a high excess silicon content PECVD film 83
5.9 PL spectra for films with Si_{ex}=3% annealed at 600°C 85
5.10 Peak PL energy and total power density for films with Si_{ex}=3% annealed at 600 and 800°C 86
5.11 TEY-XANES spectra at the Si K-edge for a film with Si_{ex}=2% annealed for different times at 600°C 88
5.12 TFY-XANES spectra at the Si $L_{3,2}$-edge for a film with Si_{ex}=3% annealed for different times at 600°C 89
5.13 PL spectra for Si_{ex}=3% films annealed at 800°C 90
5.14 TEY-XANES spectra at the Si K-edge for a film with Si_{ex}=2% annealed for different times at 800°C 92
5.15 PL spectra for a cerium doped SRSN film with Si_{ex}=1% and 0.6 at.% cerium 94
5.16 TEY- and TFY-XANES spectra at the Ce $M_{5,4}$-edge for a cerium doped SRSN film with Si_{ex}=1% and 0.6 at.% cerium 95

6.1 Cerium incorporation in silicon oxide films grown using the GIV ECR PECVD system with different cell temperatures 105
6.2 Silicon and oxygen atomic fractions as a function of rare earth incorporation 106
6.3 Refractive index as a function of rare earth incorporation 107
6.4 Mass density as a function of rare earth incorporation 107

6.5 PL spectra for different compositions of as-deposited cerium doped silicon oxide films 109
6.6 Ce $M_{5,4}$-edge IPFY-XANES spectrum for as-deposited CeORSO-01 . 111
6.7 HRTEM image of as-deposited CeORSO-03 exhibiting a non-uniform microstructure with a marbled appearance 112
6.8 PL spectra for CeSiO2-01 annealed at different temperatures 114
6.9 Ce $M_{5,4}$-edge TEY- and TFY-XANES spectra for CeSiO2-01 annealed at different temperatures 115
6.10 PL spectra for CeSiOx-07 annealed at different temperatures 116
6.11 Ce $M_{5,4}$-edge TEY-, TFY-, and PLY-XANES spectra for CeSiOx-07 annealed at 600 and 1200℃ 117
6.12 PL spectra for CeSiOx-03 annealed at different temperatures 119
6.13 PL spectra for CeSiOx-05 annealed at different temperatures 120
6.14 PL spectra for CeSiOx-01 annealed at different temperatures 121
6.15 Photograph of the PL from CeORSO-03 after 1100℃ annealing . . . 122
6.16 PL total power densities for several cerium doped silicon oxide films annealed at different temperatures 123
6.17 Cross-sectional HRTEM images of cerium disilicate nanocrystallites formed in CeORSO-01 annealed at 1000℃ 125
6.18 Cross-sectional HAADF STEM and HRTEM images of cerium disilicate nanocrystallites formed in CeORSO-03 annealed at 1100℃ 127
6.19 XRD spectra for CeORSO-02 and CeORSO-03 annealed at 1200℃ . . 129
6.20 XRD spectra for CeORSO-25b annealed at 900–1200℃ 131
6.21 XRD spectra for CeSiOx-08 annealed at 900–1200℃ 133
6.22 Comparison of peak PL intensities of cerium and terbium ions for CeSiO2-01 annealed at different temperatures 136

6.23 Comparison of XANES and XEOL spectra for 600 and 1000℃ annealed CeSiO2-01 at the O K, Ce $M_{5,4}$, and Si K absorption edges 138
6.24 Comparison of peak PL intensities of cerium and terbium ions for CeSiOx-05 annealed at different temperatures 140
6.25 Comparison of the PL spectra and peak intensities of cerium and terbium ions for CeORSO-25b annealed at different temperatures . . 141
6.26 Comparison of XANES and XEOL spectra for 1200℃ annealed CeSiOx-08 and CeORSO-25b at the O K and Ce $M_{5,4}$ absorption edges . . . 144
6.27 Comparison of the PL spectra and peak intensities of cerium and terbium ions for CeSiOx-08 annealed for different times at 1200℃ . . 146
6.28 XRD spectra for CeSiOx-08 annealed at 1200℃ for 7.5–240 minutes . 147
6.29 Comparison of the PL spectra and peak intensities of cerium and terbium ions for CeORSO-25b annealed for different times at 1200℃ . 149
6.30 Comparison of the low temperature PL spectra, total power density, and peak intensities of cerium and terbium ions at different sample temperatures for CeORSO-03 annealed at 1200℃ for 60 minutes . . . 150
6.31 Comparison of PL spectra for films containing different ratios of cerium and terbium co-dopants annealed at 1200℃ for 60 minutes 153
6.32 CIE 1931 chromaticity diagram depicting the emission colour for films containing different ratios of cerium and terbium co-dopants annealed at 1200℃ for 60 minutes 154
6.33 Photographic comparison of PL from cerium and terbium co-doped silicon oxide and silicon-rich silicon nitride films 155

List of Tables

3.1 System specific details for SRSN thin film depositions 43

6.1 MAC ECR PECVD system parameters and film properties 99

6.2 MAC ECR PECVD system parameters and film properties (cont'd) . 100

6.3 GIV ECR PECVD system parameters and film properties 101

List of Acronyms

AD as-deposited

BIMR Brockhouse Institute for Materials Research

CCD charge-coupled device

CCEM Canadian Centre for Electron Microscopy

CEDT Centre for Emerging Device Technologies

CIE International Commission on Illumination

CIHR Canadian Institutes of Health Research

CIPI Canadian Institute for Photonics Innovations

CLS Canadian Light Source

CMOS complimentary metal-oxide semiconductor

ECR PECVD electron cyclotron resonance plasma-enhanced chemical vapour deposition

EFTEM energy filtered transmission electron microscopy

EMA effective medium approximation

FTIR Fourier transform infrared spectroscopy

GADDS General Area Detector Diffraction System

GIV refer to GIV ECR PECVD

GIV ECR PECVD Group IV ECR PECVD, the newer ECR PECVD system

HAADF high-angle annular dark-field

HRTEM high resolution transmission electron microscopy

ICP CVD inductively coupled plasma chemical vapour deposition

IPFY inverse partial fluorescence yield

LED light emitting diode

MAC refer to MAC ECR PECVD

MAC ECR PECVD McMaster ECR PECVD, the older ECR PECVD systems

MAX McMaster Analytical X-Ray Diffraction Facility

MCP microchannel plate

MW microwave

NSERC Natural Sciences and Engineering Research Council of Canada

NRC National Research Council Canada

N/R not recorded

OCE Ontario Centres of Excellence

ORSO oxygen-rich silicon oxide

PECVD plasma-enhanced chemical vapour deposition

PFY partial fluorescence yield

PL	photoluminescence
PLE	photoluminescence excitation
PLY	photoluminescence yield
PV-TCHZ	modified Thompson-Cox-Hastings pseudo-Voight
RBS	Rutherford backscattering spectrometry
RF	radio frequency
RTP	rapid thermal processor
SGM	high resolution spherical grating monochromator
Si-nc	silicon nanocluster
SRSO	silicon-rich silicon oxide
SRSN	silicon-rich silicon nitride
STEM	scanning transmission electron microscopy
SWE	single wavelength ellipsometry
TEM	transmission electron microscopy
TEY	total electron yield
TFY	total fluorescence yield
VASE	variable wavelength spectroscopic ellipsometry
VLS PGM	variable line spacing plane grating monochromator
VLSI	very large scale integration
XANES	X-ray absorption near edge structure

XAS X-ray absorption spectroscopy

XEDS X-ray energy dispersive spectroscopy

XEOL X-ray excited optical luminescence

XPS X-ray photoelectron spectroscopy

XRD X-ray diffraction

YAG:Ce cerium doped $[Y_{1\text{-}x}Gd_x]_3[Al_{1\text{-}y}Ga_y]_5O_{12}$

Chapter 1

Introduction

For more than forty years, the microelectronics industry has sought to improve device performance in line with the empirical trend observed by Intel co-founder Gordon E. Moore in 1965 [1, 2] that has become known as Moore's Law. Moore initially noted that integrated circuit manufacturers were doubling the performance of integrated circuits every year, a rate that was later revised [3] to doubling every two years. Until recently, this rate of technological development has been achieved by increasing the component density on integrated circuits through reductions in their size and separation [4]. However, the performance of conventional microelectronic devices based on complimentary metal-oxide semiconductor (CMOS) technology with metal interconnects has reached fundamental limitations imposed by resistive-capacitance delays that cannot be resolved through further downscaling [4–7]. To temporarily extend the lifetime of the existing silicon architecture, the microelectronics industry has adapted the platform by switching from aluminum to copper interconnects, introducing lattice strain into the silicon channel of CMOS transistors to enhance the transport characteristics, and replacing the silicon dioxide gate dielectric in transistors with high dielectric constant materials [4]. However, a more radical technological shift will be required to allow for continued performance improvements in the near future.

As a long term solution, the concept of computers and other electronic devices constructed using integrated photonic circuits continues to show promise as a replacement architecture to circumvent the impending performance barrier [8, 9]. For such a solution to be cost effective and perhaps viable for large scale implementation, it would be ideal for the circuit components to be entirely silicon-based devices which adhere to CMOS fabrication standards. Silicon has the advantage of being a very cheap and plentiful material that has been a staple of the microelectronics industry and silicon-based devices could be produced utilizing the existing fabrication facilities. Due in large part to the telecommunications boom at the end of the 20th century, two of the three fundamental circuit components – waveguides and photodetectors – have already been developed with suitable performance capabilities [8]. Considering the recent advances in high-speed silicon modulator technology [10], the only principal component missing is an efficient, monolithic silicon-based light source. The advantages associated with a silicon-based light source are transferrable to other large scale applications including solid state lighting, which further augments the significant potential such a technology holds.

1.1 Light Emission from Silicon-Based Materials

Unfortunately, obtaining light emission from bulk silicon is not as straightforward as other semiconductors such as gallium arsenide or indium phosphide due to its indirect band structure, which severely restricts the efficiency of radiative recombination at room temperature. However, it has been found that the radiative efficiency can be greatly enhanced by reducing the dimensions of silicon to the nanometer scale through the use of quantum confinement effects [9]. Under these conditions, the limiting factors afflicting bulk silicon luminescence, specifically the requirement for phonon-mediation to conserve momentum in the radiative recombination process, become

relaxed allowing for radiative transitions to occur more readily and thereby providing a means of obtaining brightly luminescent silicon at room temperature. Utilizing quantum confinement effects has the additional benefit of allowing control of the energy (*i.e.*, colour) of emitted photons since the bandgap energy in a quantum confinement system scales with the inverse square of the dimensions of the structure [11], allowing for visible luminescence despite bulk silicon having a near-infrared bandgap energy of 1.11 eV at room temperature [12].

While obtaining light emission from silicon has been experimentally realized through a variety of quantum confinement structures including porous silicon, silicon nanowires, and silicon quantum dots [9, 13, 14], many aspects of these complex materials systems remain poorly understood and difficulties have arisen in creating electrically-pumped lasers and light emitting devices suitable for practical devices. Among the silicon quantum confinement systems, efficient light emission has been achieved from silicon nanoclusters (Si-ncs) formed in a dielectric host matrix. While the properties of this luminescence have been observed to depend on the size of the Si-ncs, effects related to the Si-nc/dielectric interface as well as from the specific physical properties of the dielectric matrix have been challenging to reconcile. This situation is further compounded by fabrication-specific issues, where the use of different deposition systems or source gases for the fabrication of silicon nanocluster containing thin films can alter the observed optical behaviour of the materials [15, 16]. Accordingly, these materials continue to be heavily researched with a strong focus on gaining a better understanding of their complicated behaviour and improving their efficiencies.

Early studies of silicon nanoclusters were heavily focused on the silicon-rich silicon oxide (SRSO) material system [17–22] stemming from L. T. Canham's initial work on porous silicon [13]. However, forming Si-ncs in a silicon nitride host matrix offers several key advantages over silicon oxide. Silicon-rich silicon nitride (SRSN) is a promising

material system since silicon nitride is a structurally stable dielectric commonly used in microelectronic fabrication processes. SRSN has more favourable electrical properties than SRSO, such as a lower tunneling barrier for carrier injection into Si-ncs, making these films better suited for electroluminescent device applications [23]. Additionally, unlike Si-ncs coordinated with oxygen atoms which are restricted to emission at red and near-infrared wavelengths regardless of their dimensions [24], nitride-passivated Si-ncs do not exhibit the same limitation and have been demonstrated to emit at energies across the entire visible spectrum [23, 25, 26]. Luminescent SRSN films also benefit from lower thermal budget requirements compared with SRSO, where temperatures must typically exceed 1000°C to obtain strong luminescence [27]. In fact, even before annealing, SRSN films grown by plasma-enhanced chemical vapour deposition (PECVD) can exhibit bright luminescence. However, the formation of Si-ncs in SRSN films has been found to occur in a more complex fashion, with formation of both amorphous and crystalline clusters being reported and a strong dependence on both deposition and processing conditions [23, 28–30]. For this reason, part of the research presented in this thesis focuses on the effects of a broad range of deposition and processing conditions on the luminescence and structure of PECVD grown silicon-rich silicon nitride thin films.

In many cases, rather than obtaining emission from silicon nanoclusters directly, it is favourable to grow or implant silicon-rich silicon dielectric films with luminescent rare earth dopants. Rare earth dopants are of particular interest in the development of many light emitting materials due to their high radiative recombination efficiency and consistent colour rendition at characteristic visible and near-infrared wavelengths which is not strongly influenced by their host environment. This is particularly important in telecommunications and display applications where colour sensitivity is very important. These properties make rare earth luminescence preferable to the less

consistent and more difficult to control silicon nanocluster emission. However, direct excitation of rare earth ions is difficult due to their small absorption cross-sections. As a result, for practical applications, the rare earth ions are typically sensitized by nearby nanostructures or defects which can be excited more readily and efficiently transfer energy to them.

In silicon oxide, efficient blue luminescence has been observed when doped with cerium ions while terbium doping has been found to produce strong green emission. It has also been found that in SiO_2 films co-doped with cerium and terbium, Ce^{3+} ions may sensitize the Tb^{3+} ions resulting in enhanced green emission [31–34]. For certain compositions of cerium doped silicon oxide films, cerium disilicate ($Ce_2Si_2O_7$) nanocrystallites have been observed to form after high temperature annealing [35–38] which exhibit very strong photoluminescence at blue wavelengths. If combined with an appropriate red emitter, such as trivalent europium or praseodymium ions [36,39], these rare earth doped silicon oxide materials present interesting candidates for solid state lighting and display device applications in which chromaticities are typically controlled by varying the relative emission intensity from blue, green, and red components.

1.2 Thesis Objectives and Methods

The objective of the research conducted for this thesis project was to facilitate the development of a visible silicon-based light source which could be used in integrated photonics and solid state lighting applications through the fabrication and characterization of the luminescent and structural properties of silicon nanostructures formed in rare earth doped and undoped silicon-based dielectric thin films grown using plasma-enhanced chemical vapour deposition. The influences of a broad range of fabrication and processing parameters on the material properties were studied experimentally in an effort to gain a better understanding of the silicon-rich silicon nitride and cerium

and terbium co-doped silicon oxide materials systems. The advances in materials science and engineering yielded through this research may provide crucial information that can be applied towards developing efficient and economical devices using these materials.

Silicon nanoclusters formed in silicon-rich silicon nitride thin films deposited using plasma-enhanced chemical vapour deposition were initially investigated as an alternative to the more established silicon-rich silicon oxide materials system since oxide-passivated silicon nanostructures had already been heavily studied and nitride-passivation offered several key advantages over this system. In particular, nitride-passivated silicon nanoclusters were expected to be capable of light emission across the full range of the visible spectrum, whereas silicon nanoclusters formed in silicon oxide were limited to emission at red and near-infrared wavelengths. Further, silicon-rich silicon nitride was more promising from a device perspective due to relatively favourable electrical properties as will be discussed in more detail in Section 2.1.

The approach used in studying the SRSN materials system involved growing various compositions of films using three plasma-enhanced chemical vapour deposition systems featuring different methods of plasma generation and source gases to investigate the impact of the deposition parameters on the nucleation, growth, and luminescent properties of silicon nanoclusters within the silicon nitride host matrix. To study the thermal evolution of the films, annealing experiments were conducted on samples with different excess silicon concentrations and grown using the different deposition systems. Isochronal annealing was performed for 60 minutes over a broad range of temperatures and isothermal annealing was performed at 600 and 800°C for a large array of times ranging from seconds to hours. Additionally, the properties of films annealed under a flowing N_2 ambient gas were compared with those of identically prepared samples where forming gas (*i.e.*, 5% H_2 in N_2) was substituted as the annealing ambient.

A preliminary study of several cerium doped SRSN samples was also conducted to investigate the suitability of the SRSN material system for stimulating visible luminescence from rare earth ions.

Accurate measurements of the film compositions were vital to properly analyzing and comparing the trends in the luminescent and structural properties of the SRSN samples, particularly in comparing trends between samples grown using different deposition systems. To obtain this information, Rutherford backscattering spectrometry (RBS) analysis was performed on as-deposited pieces of each film. The luminescent properties of the different samples were characterized via room temperature ultraviolet-excited photoluminescence (PL) spectroscopy experiments, a standard technique employed in the study of silicon nanostructures. However, it was necessary to use a less conventional approach to study the structural properties of these films, particularly to analyze the structure of the silicon nanoclusters. Fourier transform infrared spectroscopy (FTIR) could not be used to obtain this information since this technique does not yield information on Si–Si bonding and X-ray photoelectron spectroscopy (XPS) is highly surface sensitive due to the short mean free path of electrons through solid matter [40], so this technique could not be relied upon to provide structural information representative of the bulk of the film. Also, since the silicon nanoclusters and silicon nitride host matrix were amorphous, X-ray diffraction (XRD) analysis could not provide any details of the film structure. Instead, the structural properties of the silicon nanoclusters and silicon nitride host matrix were probed using synchrotron-based X-ray absorption near edge structure (XANES) analysis at the Si $L_{3,2}$- and K-edges. X-ray excited optical luminescence (XEOL) experiments were also attempted on these films, but unfortunately the luminescence was found to rapidly quench under soft X-ray excitation, probably due to the removal of hydrogen passivation from the silicon nanoclusters.

A second materials system, cerium and terbium co-doped silicon oxide films, was also studied in-depth due to the intriguing luminescent properties of cerium disilicate nanocrystallites that could be formed in certain compositions of these films and the discovery early on in this work that terbium emission was strongly enhanced in cerium disilicate containing films. In this case, films were grown using electron cyclotron resonance plasma-enhanced chemical vapour deposition (ECR PECVD) with the rare earth dopants incorporated *in-situ*. Films were grown with varying concentrations of rare earth doping including different ratios of terbium to cerium ions in order to investigate how the composition affected the coordination of the rare earth ions, formation of cerium disilicate nanostructures and other potential phases, and the sensitization of terbium luminescence. The thermal evolution of the films was studied through isochronal annealing for 60 minutes over a broad range of temperatures and isothermal annealing at 1200℃ for times ranging from minutes to hours, both under flowing N_2 ambient gas.

As with the SRSN films, the compositions of cerium and terbium co-doped silicon oxide films were determined using RBS analysis and luminescent properties were primarily characterized using room temperature ultraviolet-excited PL spectroscopy. Optical properties including the refractive indices of these films were determined through variable wavelength spectroscopic ellipsometry (VASE) analysis. The formation, growth, and crystalline structure of cerium disilicate nanocrystallites were measured through high resolution transmission electron microscopy (HRTEM), scanning transmission electron microscopy (STEM), and XRD analysis. XANES and XEOL analysis at the Si $L_{3,2}$-, O and Si K-, and rare earth $M_{5,4}$-edges also provided valuable tools for analyzing the complex structural and luminescent properties of these films due to the chemical sensitivity and site specificity inherent to inner shell energy levels. In addition to the structural properties of the host matrix material, XANES

analysis was used to probe the details of rare earth incorporation at the surface and in the bulk of the film including the oxidation states of the ions. Unlike alternative structural analysis techniques such as XRD, the local bonding coordination of rare earth ions could be determined when incorporated in amorphous as well as crystalline structures. XEOL measurements, performed by scanning the change in optical luminescence as a function of excitation energy, supplemented the ultraviolet-excited photoluminescence spectroscopy data by identifying the sites responsible for exciting luminescence from cerium and terbium ions as well as possible energy transfer mechanisms responsible for the sensitization of terbium in co-doped films. Finally, the range of colour tuneability in these films was examined by calculating the chromaticity of photoluminescence for films containing different concentrations of cerium and terbium.

1.3 Contributions to the Field

The research discussed in this thesis was conducted with the overarching goal of contributing to the development of a silicon-based light source, particularly for visible light emitting applications. In pursuit of this goal, studies were performed to advance the knowledge of materials which could potentially be employed in such a device through the characterization of their optical and structural properties. In this work, two classes of materials grown by PECVD were investigated: silicon-rich silicon nitride and cerium and terbium co-doped silicon oxide thin films.

All of the materials studied in this work were produced by our research group using the fabrication facilities in the Department of Engineering Physics and the Centre for Emerging Device Technologies (CEDT) at McMaster University. This required significant time and effort towards calibrating and maintaining the equipment as well as optimizing the process parameters and procedures involved in fabrication. Whether reported in literature or remaining internal to our research group, such as in cases

where process parameters are system specific, the details of film growth and processing established through this work provide foundational knowledge that promotes future work on related materials by other academic researchers and industry collaborators. Similarly, many of the analytical procedures and tools, particularly computer code written to handle and analyze data from the XANES and XEOL experiments, were developed from the ground up requiring substantial time and effort but will benefit future group members and collaborators performing similar experiments on other materials.

The studies of the silicon-rich silicon nitride materials system compared the luminescent and structural properties of different compositions of films as a function of annealing conditions including time, temperature, and ambient gas. This work also included a comparison of films grown using radio frequency PECVD, ECR PECVD, and inductively coupled plasma chemical vapour deposition (ICP CVD). The film structure was primarily analyzed through XANES experiments at the Si $L_{3,2}$- and K-edges, which provided a means of measuring the formation and growth of silicon nanoclusters in addition to changes in the silicon nitride host matrix over a broad range of film compositions and annealing conditions. The structural information provided a basis for correlating changes in the film structure with trends in the luminescent properties. Based on this work, our research group was the first to report on XANES results for SRSN at the Si $L_{3,2}$-edge in any capacity and the first to report on the effects of annealing conditions on the Si $L_{3,2}$- and K-edge XANES in these materials. This research was also the first to provide an extensive analysis of the influence of annealing time on the luminescence and structural properties of silicon-rich silicon nitrides. The results of these studies have been published in one journal article [41], three conference proceedings articles [42–44], and four research reports [45–48] as well as presented at numerous national and international conferences including an invited

oral presentation in the *Nanocrystal Embedded Dielectrics for Electronic and Photonic Devices* Symposium of the 219th Meeting of the Electrochemical Society (2011).

The studies of cerium and terbium doped silicon oxide thin films compared the luminescent and structural properties for different compositions of films as well as the influence of annealing time and temperature. This work analyzed the influence of film composition and annealing conditions on the formation, growth, luminescence, and structure of cerium disilicate nanocrystallites in cerium doped silicon oxide films through PL, XRD, XANES, and XEOL experiments. This research constitutes the first extensive study of cerium disilicates formed in a deposited layer and is one of only a few studies of these materials altogether. The influence of terbium co-doping of cerium doped silicon oxide films was also studied in-depth using the same experimental techniques to investigate film properties, including the sensitization of Tb^{3+} ions by cerium disilicate, as a function of composition, annealing time, and annealing temperature. To date, only one other research group has reported on cerium and terbium co-doped silicon oxide materials and the research presented in this thesis is the first to consider the sensitization of Tb^{3+} ions by cerium disilicate. This work also represents the first reported use of the inverse partial fluorescence yield technique for overcoming saturation artifacts in XANES measurements of rare earth doped materials. Results related to this work have been published in one conference proceedings article [49] and have been presented at several international conferences including an invited oral presentation in the *Group IV Semiconductor Nanostructures and Applications* Symposium of the 2012 Materials Research Society Fall Meeting. Three U.S. provisional patent applications have also been filed corresponding to the sensitization of rare earth ions by cerium disilicate [50, 51] and the formation of rare earth silicate layers through deposition [52]. Several journal articles related to the studies of the optical and structural properties of cerium and terbium co-doped silicon

oxide thin films as well as the application of the inverse partial fluorescence yield technique in XANES analysis are currently being prepared for submission.

Finally, in addition to the research conducted which directly relates to this thesis, I have contributed to research projects in which the lead researcher was another group member or external collaborator. The results of these projects have been presented at numerous conferences and reported in journal articles and conference proceedings. The publications discuss the luminescent and structural properties of cerium doped and undoped silicon-rich silicon oxynitride thin films [53, 54], silicon-rich silicon oxide and silicon-rich silicon nitride gradient films [55], cerium doped and terbium doped silicon oxide thin films [38, 56, 57], and silicon carbonitride thin films [58–60]. Notably, the publication in *Physica Status Solidi (B)* [38] was selected as an editor's choice article and was featured on the journal cover.

1.4 Outline of the Thesis

This thesis consists of eight chapters with an emphasis on the fabrication and experimental characterization of two silicon-based materials systems capable of visible light emission: silicon-rich silicon nitride and cerium and terbium co-doped silicon oxide. This introductory chapter has provided an overview of the need for silicon-based light source, a brief background on the material systems studied, the motivation and methods behind the research conducted, and the contributions that have been made to the field of study over the course of this thesis project. The remainder of this section is dedicated to outlining the contents of the successive chapters.

Chapter 2 provides background information on topics relevant to the experiments conducted in the thesis research. A brief introduction to recent developments in silicon-based luminescent materials leads into a discussion on quantum confinement in silicon nanostructures including a survey of the results reported in literature pertaining to

the silicon-rich silicon nitride materials system. The discussion then turns to the topic of rare earth doped nanostructures and their application to silicon-based materials. In the final section of this chapter, experimental results corresponding to the intriguing but as of yet understudied cerium disilicate structure are reviewed.

A description of the equipment and procedures employed in fabricating and processing the samples used in experimental analysis is provided in Chapter 3. Here, the deposition systems and parameters used to grow silicon-rich silicon nitride and cerium and terbium co-doped silicon oxide thin films are discussed along with the details of post-deposition processing used in the isochronal and isothermal annealing studies carried out on both material systems.

Chapter 4 outlines the experimental details pertaining to the characterization techniques utilized in studying the luminescent and structural properties of the films. In this chapter, the equipment, methods, and parameters used for Rutherford backscattering spectrometry, ellipsometry, photoluminescence spectroscopy, X-ray absorption spectroscopy, and X-ray diffraction analysis are discussed along with complications that were encountered and insight for future researchers regarding how such issues may be addressed.

In Chapters 5 and 6, the experimental results for the silicon-rich silicon nitride and cerium and terbium co-doped silicon oxide materials are discussed, respectively. For both materials systems, the luminescent and structural properties of various compositions of films are examined and compared for samples in as-deposited (AD) form as well as those annealed under isochronal or isothermal conditions. This is followed by a summary of the conclusions drawn from this work in Chapter 7. Finally, a brief discussion on the future outlook and suggested follow-up work for each material is provided in Chapter 8.

Chapter 2

Luminescence from Silicon-Based Materials

Silicon has been the dominant material in microelectronics for over 50 years, owing to its wide availability as a resource, straightforward and versatile processing, stable and well-passivating native oxide, and universally adequate electrical and optical properties, all of which have contributed to its continued use as a platform for a wide range of microelectronic and photonic devices. However, for all of its favourable properties, bulk silicon is a very poor luminescent material. While sufficient performance has been attained in other key components of silicon photonics including waveguides, modulators, and detectors [8, 10], the continued lack of an efficient silicon-based light source remains a major obstacle, preventing silicon-based optoelectronic devices from becoming a viable technology.

In its diamond lattice form, the poor radiative efficiency of silicon is a consequence of its indirect band structure, which is shown in Figure 2.1 alongside that of gallium arsenide, a direct bandgap semiconductor. Here it can be seen that in silicon, the minimum of the conduction band is offset from the maximum of the valence band, which is located at the Brillouin zone centre (*i.e.*, the Γ point), along the Δ direction

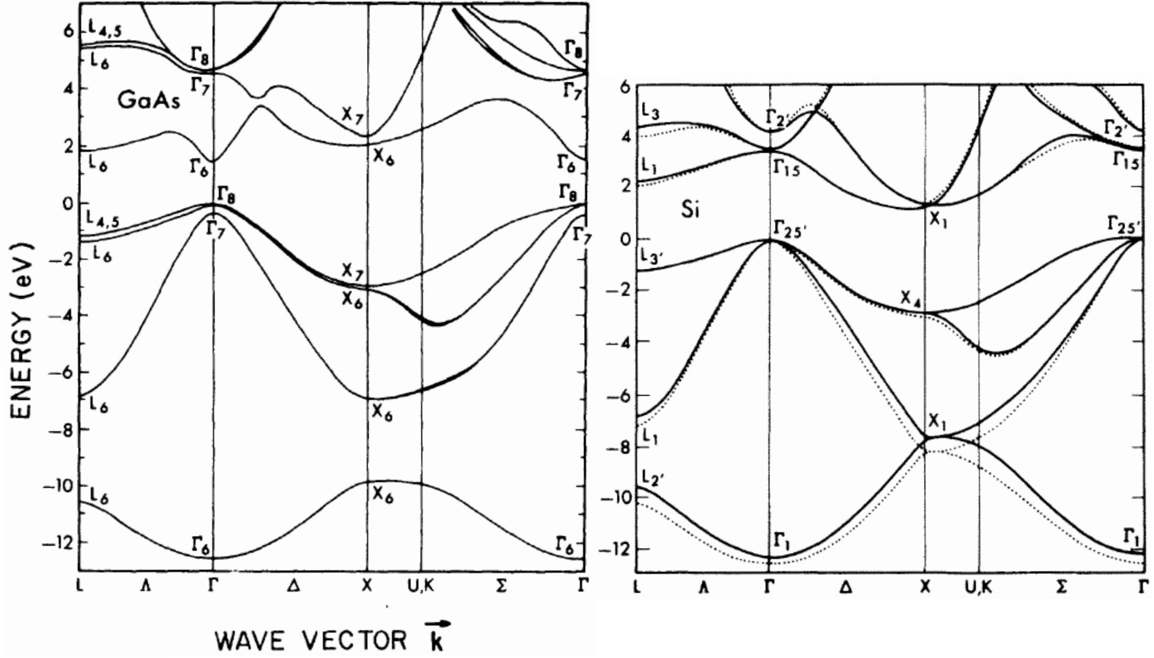

Figure 2.1: Band structures for (left) gallium arsenide and (right) silicon crystals. GaAs is a direct bandgap semiconductor as indicted by the minimum of the conduction band and maximum of the valence band occurring at the Γ point. The conduction band minimum in the indirect bandgap semiconductor Si is offset in k-space along the Δ direction. Reproduced with permission from [61] (© 1976 by the American Physical Society).

(*i.e.*, between Γ and X) close to the X point [61]. As a result, there is a difference in the wave vectors of the initial and final states of electron transitions between the conduction band minimum and valence band maximum. Therefore, radiative recombination in silicon requires phonon mediation (*i.e.*, phonon absorption or emission) involving a phonon with a wave vector of equal magnitude and opposite direction to that of the initial state in order to conserve momentum [14]. Consequently, the radiative lifetime in Si, which is on the order of milliseconds, is very long compared to that in a direct bandgap semiconductor like GaAs, which has a radiative lifetime on the order of nanoseconds [9].

At room temperature, non-radiative processes such as Auger and Shockley-Read-Hall recombination dominate such three-body transitions due to their relatively short lifetimes. Auger recombination rates are dependent on the doping level and

the lifetimes of these transitions, which can be theoretically calculated [62], range from 1 ns and 0.5 ms. By contrast, the Shockley-Read-Hall recombination rate is dependent on the concentration of deep trap states and typically has a lifetime on the order of nanoseconds [9]. The radiative and non-radiative lifetimes, denoted as τ_r and τ_{nr}, respectively, determine the radiative efficiency of a semiconducting material η as defined in Equations (2.1) and (2.2) [9]. From these equations, it is evident that the radiative lifetime must be significantly shorter than the non-radiative lifetime to obtain efficient luminescence from the material. At low temperatures where the non-radiative recombination rates are significantly reduced, the radiative recombination process becomes dominant and efficient luminescence has been observed under such conditions [63–67]. Unfortunately, cooling to such extremes is impractical for most device applications and so it is necessary to devise methods of overcoming the limitations imposed by the indirect band structure.

$$\eta = \frac{\tau_{nr}}{\tau_r + \tau_{nr}} \tag{2.1}$$

$$\tau_{nr} = \sum_i \frac{1}{\tau_{nr_i}} \tag{2.2}$$

One of the primary methods that have been developed to overcome bulk silicon's inherent inability to provide efficient luminescence is to reduce the dimensions of the material to the nanoscale in order to induce quantum confinement effects. To this end, various nanostructures have been employed including quantum wells, wires, and dots representing quantum confinement in 1, 2, and 3 dimensions, respectively [9, 13, 14, 68, 69]. An alternative approach has been to avoid the issue by using silicon-based structures to sensitize rare earth dopants which have much more favourable luminescent properties. Whichever the approach, an ideal solution would be compatible with the economics of silicon manufacturing as well as the processing standards associated

with CMOS very large scale integration (VLSI) chip fabrication [8, 70]. Silicon-based devices that stray too far outside these boundaries lose a significant portion of their cost advantage over devices based on hybrid design schemes or competing materials systems, such as direct bandgap III-V semiconductors, since they would no longer be manufacturable in a conventional microelectronics fabrication facility. Furthermore, it would be difficult to incorporate a non-CMOS compatible device as a component in a larger silicon-based optoelectronic architecture, although such designs could still be useful for niche applications if the fabrication costs were sufficiently low.

2.1 Quantum Confinement in Silicon Nanostructures

Beginning with the discovery of efficient visible luminescence from porous silicon at room temperature by L. T. Canham [13], considerable research related to quantum confinement based light emission from various silicon nanostructures has been conducted in the past 20 years. When the dimensions of silicon are reduced beyond the exciton Bohr radius, which is approximately 4.3 nm in crystalline silicon, the radiative recombination efficiency and emission energy in the structure increases as a result of strong quantum confinement effects. According to the Heisenberg Uncertainty Principle, there is a limit to the precision with which the position and momentum of a particle can be known as specified in Equation (2.3), where $\hbar$ is the reduced Planck constant and σ_x and σ_p are the standard deviations of position and momentum in the x direction, respectively.

$$\sigma_x \cdot \sigma_p \geq \frac{\hbar}{2} \tag{2.3}$$

Reducing the dimensions of the silicon effectively increases the precision with which the position of the electrons and holes in the structure are known, causing a corresponding increase in the uncertainty of the momenta of the charge carriers. When

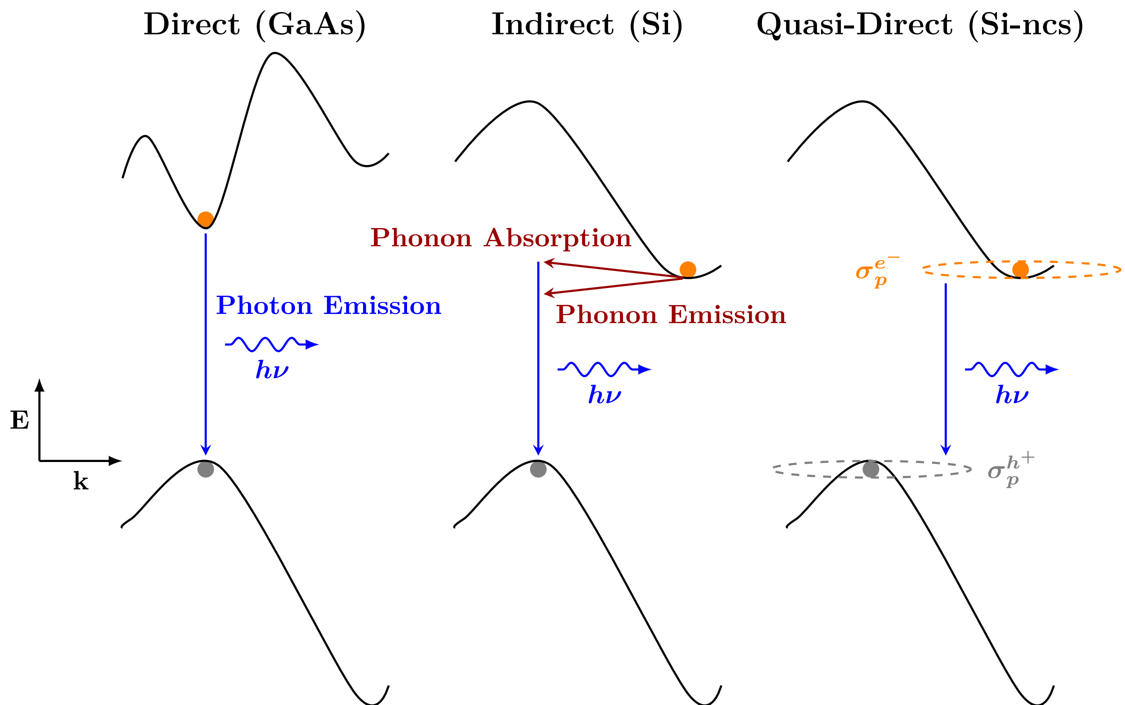

Figure 2.2: Radiative recombination through direct, indirect, and quasi-direct transitions in semiconductors. The orange dots represent electrons at the conduction band minima and the grey dots represent holes at the valence band maxima.

the silicon dimensions are reduced sufficiently, the uncertainty in the charge carrier momentum exceeds the difference in the initial and final wave vectors. Having relaxed the requirement for conservation of momentum, so-called "quasi-direct" transitions can take place, as shown in Figure 2.2, in which radiative recombination is allowed to occur without phonon mediation which significantly increases the light emission efficiency of the material. Another consequence of reducing the dimensions of silicon to the nanoscale is that it creates a "particle in a box" type of system in which the wavefunctions of the charge carriers can only correspond to states which have specific discrete energies which are determined by the dimensions of the structure. The allowed energy levels (E) for a particle in a three-dimensional box having infinite potential barriers are defined by Equation (2.4):

$$E_{n_x,n_y,n_z} = \frac{\hbar^2 \mathbf{k}^2_{n_x,n_y,n_z}}{2m} = \frac{\hbar^2}{2m}\left(\frac{\pi^2 n_x^2}{L_x^2} + \frac{\pi^2 n_y^2}{L_y^2} + \frac{\pi^2 n_z^2}{L_z^2}\right) \tag{2.4}$$

where n_x, n_y, and n_z are positive integers, m is the mass of the particle, $\mathbf{k}$ represents a three-dimensional wave vector, and L_x, L_y, and L_z are the x, y, and z dimensions of the box. For a real silicon quantum confinement system, the silicon nanostructures are typically embedded in a wide-gap dielectric such as SiO_2 (~9 eV) or Si_3N_4 (~4.6 eV) creating a large enough barrier height for the infinite potential barrier approximation to work, although the wavefunctions would not be completely contained in the potential well.

According to the model devised by L. Brus [11], the energy of the first excited electronic state in a spherical semiconducting nanocluster (E^*) can be approximated by Equation (2.5), which includes terms for the bandgap energy of the bulk material (E_g), energy shifting due to quantum confinement effects on the electrons and holes,

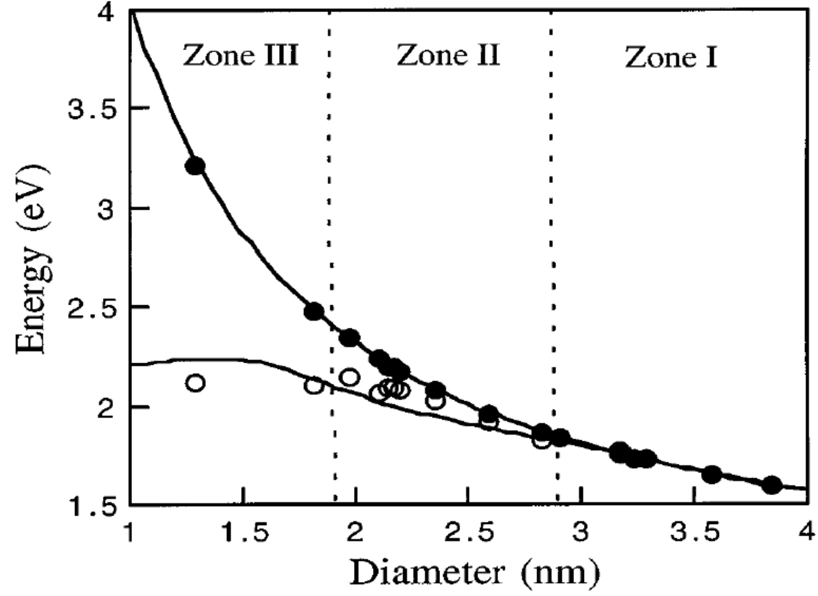

Figure 2.3: Comparison between experimental and theoretical PL energies in porous silicon as a function of crystallite size. The upper line is the free exciton band gap and the lower line is the lowest transition energy in the presence of a Si=O bond. The • and ◦ symbols represent the peak PL energies obtained from samples with different porosities kept under Ar atmosphere and exposed to air, respectively. In zone I the PL peak energies are identical, whether the samples have been exposed to oxygen or not. Reproduced with permission from [24] (© 1999 by the American Physical Society).

and Coulomb interactions between the charged particles.

$$E^* \cong E_g + \frac{\hbar^2\pi^2}{2R^2}\left(\frac{1}{m_e} + \frac{1}{m_h}\right) - \frac{1.8q^2}{\epsilon R} \tag{2.5}$$

Here, R represents the radius of the nanocluster, m_e is the effective mass of the electrons, m_h is the effective mass of the holes, q is the charge of an electron, and ϵ is the permittivity of the semiconductor.

While the observation of bright photoluminescence in porous silicon by Canham sparked larger research efforts into luminescent silicon nanostructures, experimental evidence of quantum confinement effects in hydrogen passivated silicon nanocrystals was actually reported by Takagi et al. [71] three months earlier. The results from these experiments demonstrated that the peak emission energy followed a $1/R^2$ relationship in small nanocrystals with radii ranging from 6 to 10 nm. However, as further research

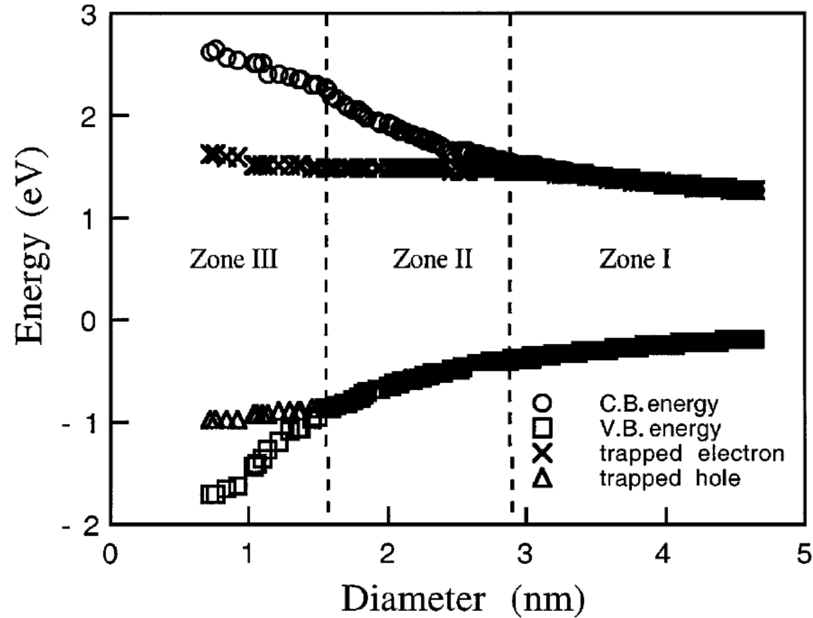

Figure 2.4: Electronic states in Si nanocrystals as a function of cluster size and surface passivation. The trapped electron state is a p-state localized on the Si atom of the Si=O bond and the trapped hole state is a p-state localized on the oxygen atom. Reproduced with permission from [24] (© 1999 by the American Physical Society).

was carried out in the porous silicon and silicon nanocrystal materials systems, it was found that the luminescence energy was lower than expected from a quantum confinement model and visible emission was limited to the green to red even for very small nanostructures despite their optical absorption following the expected trend. The ambiguous results were reconciled by Wolkin et al. [24] who calculated that the deviation from the expected emission energy in hydrogen- or oxide-passivated silicon nanocrystals could be explained by considering the effect of charge trapping at the nanostructure surface. In this work, it was found that silicon nanocrystals, such as those formed in silicon-rich silicon oxide, with diameters of 3 nm and larger will emit light with an energy corresponding to free excitonic recombination as described by Equation (2.5). However, at smaller diameters, electrons become localized on the Si atoms in Si=O bonds at the nanocrystal surface thereby reducing the emission energy below that of free excitonic recombination. At nanocrystal diameters below

2 nm, the holes also become localized on the Si atoms in Si=O bonds preventing the emission energy increasing with further reductions in size. The effects of the silicon nanocrystal size and passivation on the emission energy are shown in Figure 2.3 and the influence of these factors on the electronic states in silicon nanocrystals is illustrated in Figure 2.4.

The charge trapping effectively limits the light emission of porous silicon and silicon nanocrystals embedded in silicon oxide to energies below 2 eV, which limits the usefulness of these materials in visible lighting applications. In addition to influencing the emission energy of silicon nanocrystals, surface states can also contribute to quenching of luminescence altogether. Since the bonding structure at the interface between a silicon nanocrystal and its surrounding environment tends to be rather complex, quenching defects such as dangling bonds can be prominent and sample preparation plays an important role in the luminescence properties of the material. For example, hydrogen passivation through annealing in forming gas (5% H_2 in N_2) has been demonstrated to significantly reduce defect-related quenching in silicon nanocrystals [27]. It should not be too surprising thus, that the interface between a silicon nanocrystal and host matrix in which it is situated plays an important role in its optical properties since a large percentage of the nanocrystals' atoms are located at the surface. While the exact percentage is dependent on the specific shape and bonding structure of the nanocrystal, a reasonable estimate can be obtained from Xie's simplified model for calculating the ratio of surface to volume atoms (α) in a spherical nanoparticle specified in Equation (2.6) [72].

$$\alpha = \frac{3d}{R} \tag{2.6}$$

In this equation, d is the diameter of the atoms in the nanoparticle and R is the radius of the nanoparticle. This relationship is plotted in Figure 2.5 for a silicon

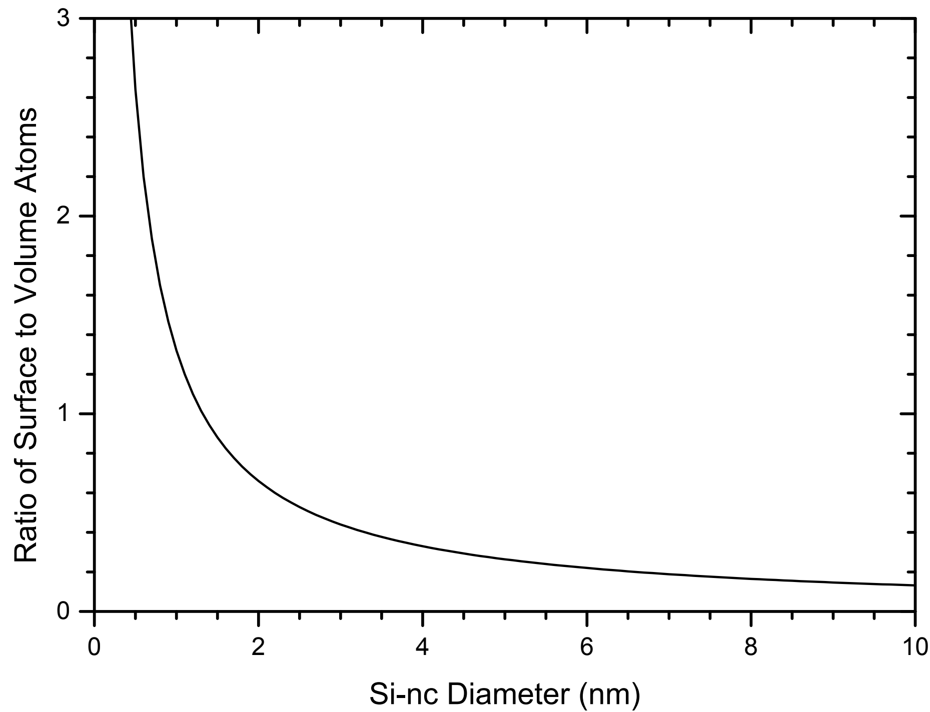

Figure 2.5: Ratio of surface to volume atoms as a function of silicon nanocrystal size based on Xie's simplified model [72].

atomic diameter of 2.2 Å for nanocrystals up to 10 nm in diameter. Based on this approximation, the majority of atoms in silicon nanocrystals with diameters less than 1.4 nm are located at the surface of the structure and even in larger nanocrystals with diameters up to 4.0 nm, more than one quarter of the atoms reside at the surface. Furthermore, Xie's model is based on spherical nanostructures, which would have the lowest surface to volume ratio of any shape, and so this prediction is likely a conservative estimate before even considering aspects like surface roughness or irregularities that would increase the ratio further. Considering the large fraction of atoms that are located at the silicon nanocrystal interface and the large influence that Si=O bonding has been found to have on their emission energy, it is obvious that the surface chemistry of the silicon nanocrystals plays a large role in determining their optical characteristics. Unfortunately, it is very difficult to characterize the

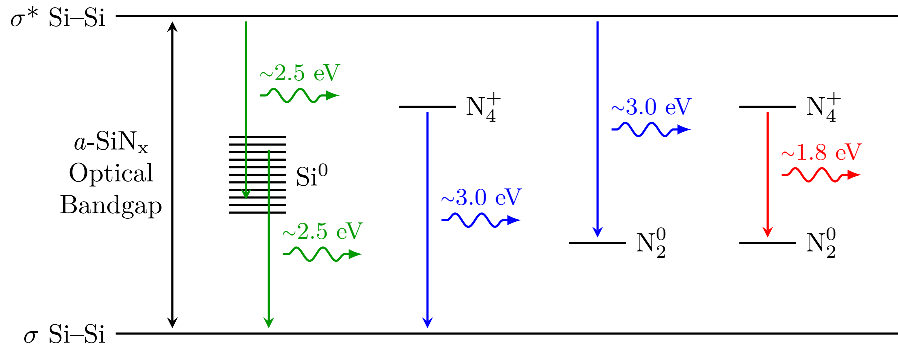

Figure 2.6: Possible radiative transitions in SiN_x films. After [74].

nanocrystal interface directly.

Attempts have been made to avoid the charge trapping issue by forming silicon nanocrystals in alternative host matrix materials, the most prominent of which has been silicon nitride. The silicon-rich silicon nitride system has proven to be considerably different from silicon-rich silicon oxide both in terms of the optical properties and the details of nanocluster formation as thoroughly discussed in T. Roschuk's doctoral thesis [73]. Without the Si=O bond, the peak luminescence is tuneable across the entire visible spectrum and into the near-infrared. However, the emission spectra from nitride-passivated silicon nanoclusters can be complicated by interactions with inter-bandgap defect levels related to the Si^0 dangling bond, N_4^+, and N_2^0 defect states in the silicon nitride host matrix which exhibit luminescence at energies of approximately 2.5, 3.0, and 1.8 eV [74], respectively, as depicted in Figure 2.6. This can make it difficult to determine whether spectral features are strictly related to quantum confinement effects in the silicon nanocluster, a radiative defect in silicon nitride, or a combination of both factors.

The complications in characterizing the luminescence of this materials system are further compounded by the nature of silicon nanocluster formation and growth in silicon-rich silicon nitride films, which has been found to be highly sensitive to the sample fabrication and processing conditions [41]. Compared to forming silicon

nanocrystals in silicon-rich silicon oxide films, there is a much narrower parameter window within which luminescent silicon nanoclusters will form in silicon-rich silicon nitride films. Furthermore, the sensitivity to fabrication and processing conditions has led to a wide variation in the results reported by different research groups, even for aspects as fundamental as whether the silicon nanoclusters are amorphous or crystalline. G. Y. Sung *et al.* reported that both amorphous and crystalline nanoclusters had been observed in their as-deposited films and proposed that complexities of the narrow growth window and discrepancies in silicon nanocluster structure were linked to the growth rate of the silicon-rich silicon nitride film [23]. In their studies, this research group was able to fit their photoluminescence data to the Brus model to establish relationships between peak emission energy and the nanocluster size for films containing crystalline [75] and amorphous [26] nanoclusters as defined in Equations (2.7) and (2.8), respectively. Based on these equations, the amorphous nanoclusters have higher energies than the same sized nanocrystals for diameters of approximately 5 nm and larger, which agrees with the higher bandgap energy associated with bulk amorphous silicon relative to crystalline silicon. In smaller nanostructures, the nanocrystal energy becomes larger than in equally sized amorphous nanoclusters, which could be explained by the crystalline structure providing a more defined phase separation for quantum confinement effects at such small scales.

$$E_c = 1.16 + \frac{11.8}{d^2} \tag{2.7}$$

$$E_a = 1.56 + \frac{2.40}{d^2} \tag{2.8}$$

However, in our own materials, despite attempting many variations of deposition parameters resulting in films grown at very different rates, we have yet to find evidence of crystalline structure in nitride-passivated silicon nanoclusters and there remains

no consensus on this topic in literature. Part of the issue may relate to the ease with which oxygen can contaminate the silicon nitride matrix during deposition or annealing, especially at high temperatures, which could unknowingly influence the films by producing an oxynitride layer. Unfortunately, most results that have been reported do not include proper compositional analysis of the films and so it could easily be overlooked if the oxygen contamination is low enough. With this possibility in mind, we have gone to extensive lengths to minimize the possibility of this occurring in our samples and yet there have still been instances where samples have been noticeably contaminated during annealing.

In attempting to address the complex photoluminescence behaviour observed in silicon-rich silicon nitride materials, additional models have been proposed besides quantum confinement to explain data trends. One of the more comprehensive studies suggested that photoluminescence in as-deposited and low temperature annealed samples is best accounted for by a band-tail state model while the behaviour at higher annealing temperatures fits better within a quantum confinement model [76]. Other groups have suggested that luminescence in silicon-rich silicon nitride films may originate from a complex band structure related to spatial chemical fluctuations (not solely limited to silicon nanoclusters) which give rise to potential wells with varying depths [77]. Unfortunately, discrepancies in the structural and photoluminescence properties of silicon-rich silicon nitride materials measured by different groups coupled with the wide variations in fabrication methods and processing conditions that have been used in these studies has made it difficult to evaluate the different models on a general level.

Despite these inconsistencies, silicon-rich silicon nitride remains a promising materials system for device applications. For electrical devices, silicon nitride is a better host matrix than silicon oxide due to its lower tunneling barrier for carrier injection into the

nanoclusters, which allows for better electroluminescence performance [23]. Further, the electric field strength required for injection of electrons and holes from silicon into silicon nitride is ~2–4 MV/cm, well below the strength at which breakdown occurs (~9 MV/cm), as compared to 6 MV/cm and 10 MV/cm for injection of electrons and holes into silicon oxide, respectively, which are close to the breakdown strength for silicon oxide [77]. Several groups have reported electroluminescence in both amorphous and annealed silicon-rich silicon nitride films [23,78–80]. Devices based on as-deposited films would be especially interesting from a fabrication perspective since it would alleviate the requirement of high temperature annealing allowing for increased flexibility for incorporating such a component in a larger design. Several groups have also reported photoluminescence [80–83] and electroluminescence [84] in rare earth doped silicon-rich silicon nitride films. While the efficiencies of the electroluminescent devices still leave much to be desired, the ability to excite rare earth luminescence is important since the high level of colour rendering associated with emission from rare earth ions is required for many applications. This may be especially important for optical amplifier or laser applications since, to date, optical gain in silicon-rich silicon nitride has not been reported and one study has suggested that, unlike silicon-rich silicon oxides [21, 85–87], it may not be possible to obtain gain in an undoped silicon-rich silicon nitride system [88].

2.2 Rare Earth Doped Nanostructures

Rare earth elements, also referred to as lanthanides, are located in the sixth row of the periodic table between lanthanum and ytterbium (atomic numbers 57 to 70). These elements share the unique characteristic of having partially filled 4f atomic orbitals that are shielded from the influence of external fields by the $5s^2$ and $5p^6$ shells. As a result of the electronic shielding, the 4f energy levels are only weakly sensitive to

the chemical environment in which they are incorporated and the energy levels are primarily influenced by spin-orbit interactions rather than the applied crystal field. While relatively minor, crystal field splitting causes a broadening of the energy levels in accordance with the Stark effect with the most significant broadening occurring in low symmetry hosts such as glasses. Since the crystal field splitting is small, the Stark levels tend to overlap at room temperature leading to inhomogeneous broadening of the emission band [89].

In crystalline or amorphous hosts, rare earth elements are typically incorporated as ions in their 2+, 3+, or 4+ oxidation states. Rare earth ions coordinated in the 3+ state have been found to exhibit intense luminescence with narrow linewidth in many host materials. This luminescence originates from intra-4f transitions since electron-phonon coupling is weak and the ions effectively behave in a manner similar to free ions due to the electronic shielding [89]. As a group, the rare earth ions luminesce at wavelengths ranging from ultraviolet to near-infrared wavelengths. The weak interaction with the surrounding chemical environment also means that the 4f energy levels and therefore, the wavelengths of the luminescent transitions are characteristic of the ion for a given oxidation state and do not change much in different hosts. Combined, these properties make rare earth ions ideal for a broad range of applications, especially where colour rendition is critical. For some rare earth ions such as europium, the 2+ oxidation state may also be optically active, although these systems have been far less studied. Energy level diagrams for a number of trivalent rare earth ions that emit in the visible spectrum are shown in Figure 2.7 along with their characteristic luminescent transitions.

In an isolated system, the intra-4f transitions are parity forbidden. However, when incorporated in a host material such that the bonding at the rare earth site is non-centrosymmetric, interactions with the crystal field result in mixing of opposite

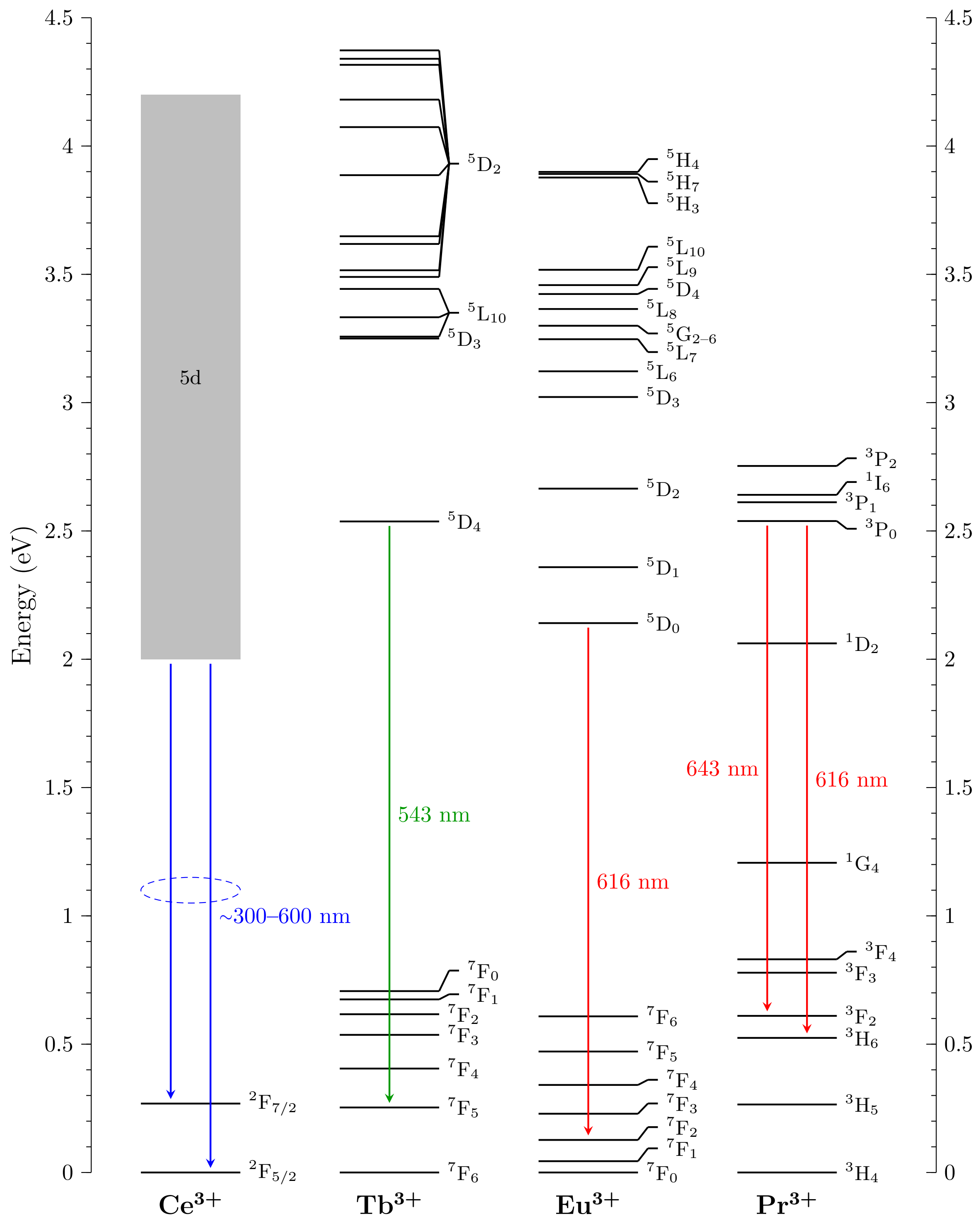

Figure 2.7: Diagram of 4f energy levels for visibly emitting trivalent rare earth ions in their ground states. Tb^{3+} ions are green emitters while Eu^{3+} and Pr^{3+} ions exhibit red luminescence. Ce^{3+} luminescence originates from 5d to 4f transitions resulting in a relatively broad emission peak that shifts over a wide range of energies depending on the surrounding chemical environment. After [39].

parity wavefunctions and the transitions become weakly dipole allowed. Since the crystal field induced mixing of wavefunctions is weaker in the lower energy states, typically only the transitions between these low energy levels are metastable [89]. The long lifetimes, typically on the order of milliseconds for metastable transitions and 1–100 microseconds for transitions between higher energy levels [89], and narrow linewidths associated with rare earth luminescence are a consequence of the intra-4f transitions being partially forbidden. Ce^{3+} ions present a special case where the radiative transition most commonly studied occurs from a 5d to a 4f energy level. This transition is not parity forbidden, and so it has a broader linewidth and shorter lifetime associated with it. Since the 5d orbital is not electronically shielded but rather directly involved in the cerium bonding, the energy of Ce^{3+} luminescence is dependent on its host environment. The probability of a specific intra-4f transition occurring in a rare earth ion is difficult to determine experimentally. Instead, these probabilities are conventionally approximated using the Judd-Ofelt theory [90, 91], which has proven to be quite accurate despite making several assumptions to simplify the calculations. A review of the historical background, principles, and practices associated with Judd-Ofelt theory goes beyond the scope of this work, but can be readily found in review papers and textbooks [92–95].

In practice, a major limitation to total light output is imposed on rare earth doped materials by the solubility of the ions within the host material. When the rare earth concentration exceeds a critical concentration that is host dependent, the rare earth ions will precipitate through the clustering of rare earth ions or the formation of compounds or alloys with elements from the host matrix (*e.g.*, rare earth oxides or silicates). In many cases, these precipitates are undesirable and result in a quenching of luminescence in the material since the rare earth ions either become coordinated in optically inactive states or the close proximity of the rare earth ions to one another

causes an increase in ion-ion interactions. The solubility limit, which can range from fractions of an atomic percent up to several atomic percent depending on the rare earth element and host material [89], can place technological constraints on device architecture. A common example is the erbium doped fibre amplifier, which requires meters of doped silica fibre to achieve sufficient gain.

As alluded to above, ion-ion interactions can play a significant role in the luminescence from rare earth doped materials, especially at high doping concentrations. The three predominant ion-ion interaction processes, co-operative upconversion, cross-relaxation, and energy migration, are depicted in Figure 2.8. In co-operative upconversion, two rare earth ions in metastable excited states with electrons at the upper luminescence level interact such that one electron decays to the ground state by transferring its energy to the other ion, causing it to be upconverted to a higher excitation level. The upconverted electron then either decays through a rapid, non-radiative process, which is the most common scenario in oxide glasses, or returns to the metastable state where it undergoes radiative recombination. Co-operative upconversion represents a quenching mechanism that is dependent on the rare earth concentration in the host material as well as the excitation intensity [89, 96].

Cross relaxation is the reverse of the co-operative upconversion process. Here, a highly excited rare earth ion transitions to the metastable state through an energy transfer to a second rare earth ion, promoting it from the ground state to the metastable state. Again, the probability of this interaction occurring is dependent on the rare earth concentration and the percentage of highly excited ions in the system, which may be dictated by the excitation power and energy transfer pathways employed [89, 96].

Finally, energy migration is the process in which a rare earth ion excited to the metastable state transitions to the ground state via transferring energy to a ground state rare earth ion, thereby promoting it to the metastable state. While this ion-ion

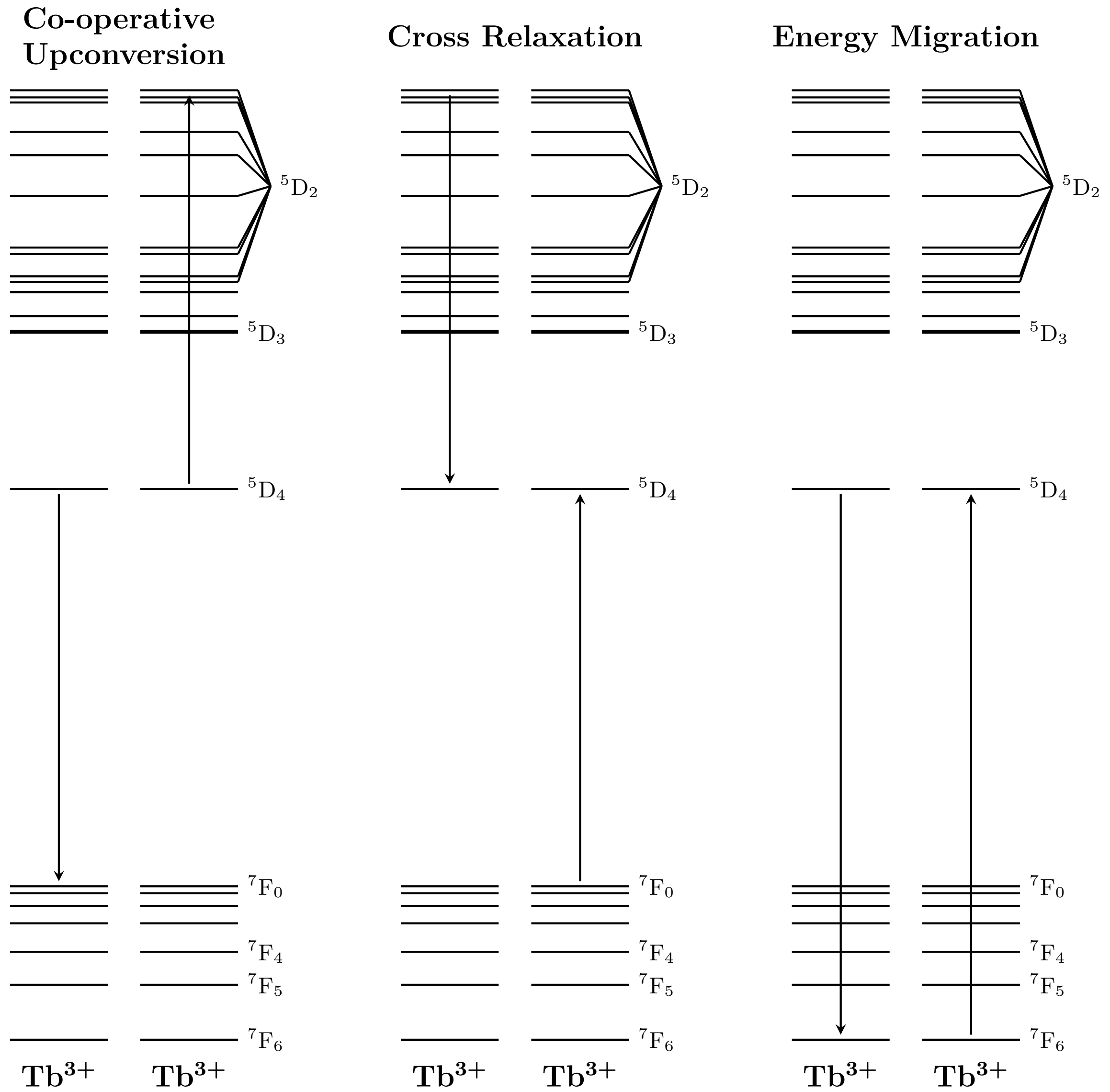

Figure 2.8: Three ion-ion interaction processes that can occur between rare earth ions: co-operature upconversion, cross relaxation, and energy migration. After [89, 96].

interaction may seem to have no net impact, there is an increase in the probability of non-radiative decay occurring with each energy migration event and so this interaction is also considered to be a quenching mechanism that is strongly dependent on the rare earth concentration [89, 96].

Akin to co-operative upconversion, excited state absorption is a loss mechanism that involves a rare earth ion in the metastable state being excited to a higher energy level from which it may decay back to the metastable state through radiative or non-radiative processes. However, as opposed to co-operative upconversion, excited state absorption results from the absorption of a photon rather than energy transferred from another excited rare earth ion. The probability of this process occurring is dependent on the lifetime of the excited state. In optical amplification devices, excited state absorption is problematic since the absorbed photon is lost as heat or radiative emission at an unintended wavelength, both of which suppress gain in the system. Further, if the energy spacing from the metastable state transition to a higher lying energy level is close to the energy used to optically pump the ground state ions, the metastable state will be depopulated through this process [89, 96].

Multiphonon relaxation can also limit the luminescence in rare earth ions via the rapid de-excitation of the upper energy level involved in the luminescent transition. This quenching mechanism becomes important when the energy gap between the upper and lower levels can be spanned by a small number of phonons. The impact of multiphonon relaxation is determined by the relative values of the phonon cut-off energy in the system and the energy of the luminescent transition. Conventionally, phonon cut-off energies exceeding 25% of the energy gap can be expected to completely quench the rare earth luminescence while quenching for cut-off energies below 10% is considered negligible. In between these values, the influence of multiphonon relaxation leads to a temperature dependence in the luminescence lifetime [89, 96].

An important consequence of the partially forbidden intra-4f transitions is that the absorption cross-sections of rare earth ions are very small, which makes it very difficult to excite them directly via resonant optical excitation or electroluminescence through hot electron collisions. Indirect methods have generally found to provide a more effective alternative. In semiconductors, carrier-mediated excitation transfer can be achieved if the rare earth ion is incorporated as an isoelectronic substitutional dopant [89] as depicted in Figure 2.9. In such materials, trap centres with large carrier cross-sections can be used to form bound excitons between the trapped carriers and free carriers via Coulombic interactions. The energy of the bound exciton can then be transferred to a rare earth ion through inelastic scattering or excitonic recombination, causing an electron to be promoted from the ground state to an excited energy level in the 4f shell. In most cases, the energy transferred to the rare earth ion will lead to excitation to an energy level that is higher than the upper level for luminescence and a phonon-mediated relaxation is required to populate the desired level. In insulating materials, indirect excitation can occur through a process referred to as dipole-dipole Förster-Dexter coupling [97, 98], which is illustrated in Figure 2.10. This process involves the excitation of a sensitizer, which then transfers energy to a nearby rare earth ion through a non-radiative Coulombic interaction. The strength of the coupling is dictated by the proximity of the rare earth ion to the sensitizer and typically this distance should be on the order of several nanometers.

Recently, various nanostructures including silicon nanoclusters have been studied as a means of providing indirect excitation of rare earth ions. One method has been to incorporate the rare earth ions within nanostructures that have a continuous morphology, such as porous silicon, to induce carrier-mediated excitation. This approach is advantageous since it allows for the excitation of rare earth ions with higher emission energies than the bulk bandgap energy of the host material. For

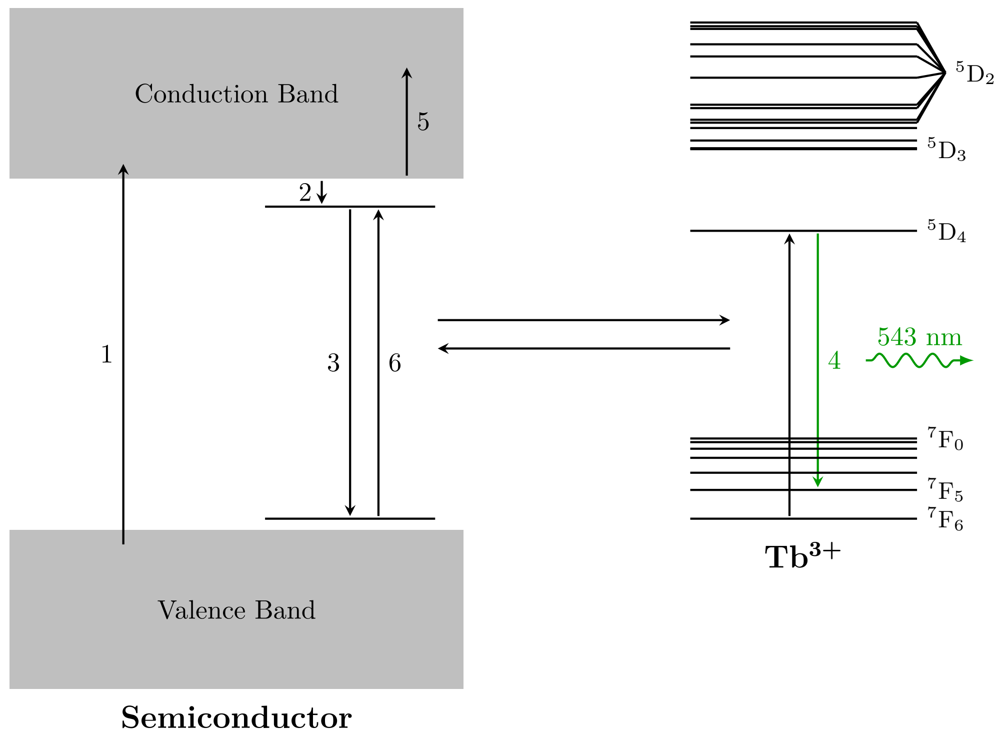

Figure 2.9: Carrier-mediated excitation transfer process in a terbium doped semiconductor: (1) electron-hole pair generation via electrical injection, (2) carrier trapping at Tb^{3+}-related trap centre in the semiconductor bandgap, (3) carrier recombination excites the Tb^{3+} ion from its ground state to the $^5D_4$ level, (4) radiative recombination of Tb^{3+} resulting in emission of a photon, (5) excitation of free carriers resulting from non-radiative Auger recombination of excited Tb^{3+} ion, (6) de-excitation of Tb^{3+} ion through backtransfer process generates a bound exciton at the trap centre (reverse of 3). After [89].

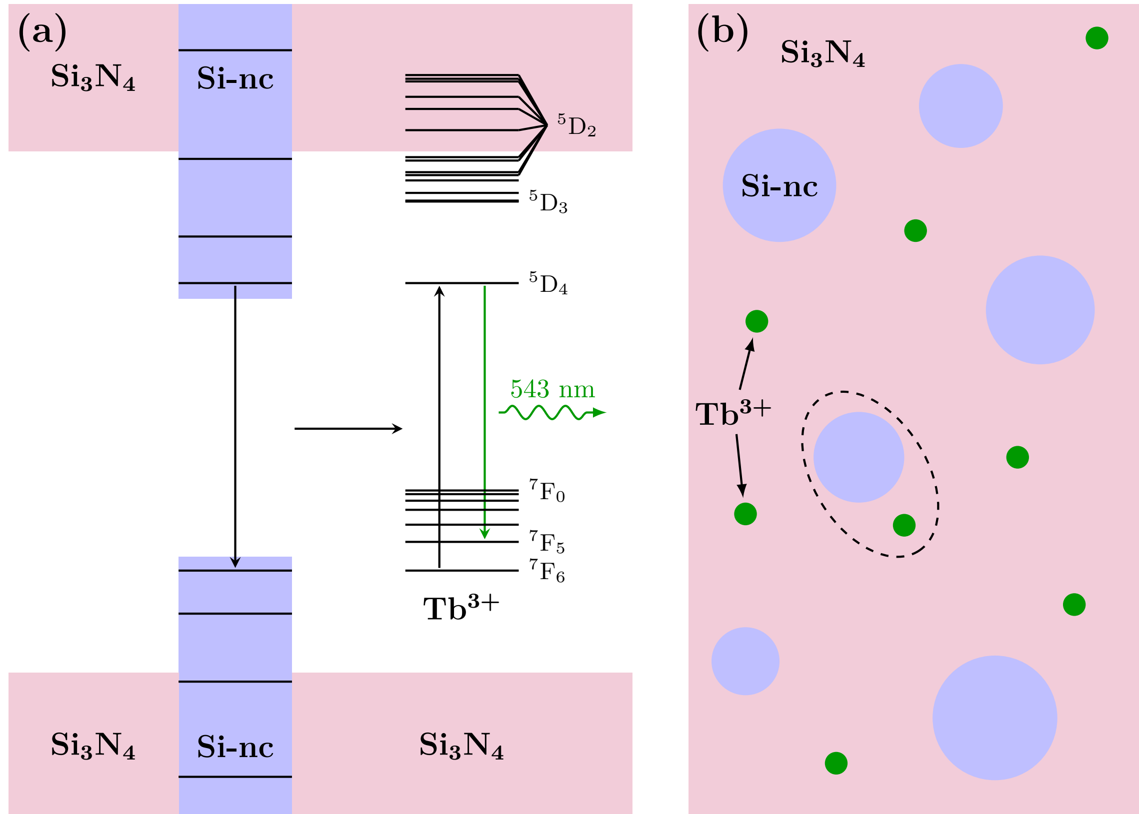

Figure 2.10: Sensitization of terbium ions by silicon nanoclusters through a Förster-Dexter coupling process. (a) Energy is transferred from an excited state Si-nc (donor) to a ground state Tb^{3+} ion (acceptor) in the surrounding Si_3N_4 host matrix, exciting an electron into the $^5D_4$ level. Radiative recombination occurs in the excited Tb^{3+} ion resulting in the emission of a photon. (b) The strength of the Förster-Dexter coupling process is strongly dependent on the separation distance between the Si-nc and Tb^{3+} ion. Typically, rare earth ions must be within several nanometers of a Si-nc with appropriate bandgap energy to be sensitized in this manner as depicted for the Si-nc and Tb^{3+} ion enclosed by the dashed line. After [99].

example, this method could allow for visible emission from rare earth doped porous silicon. The use of a nanostructure host is also beneficial since the radiative efficiency can be improved through the reduction of Auger recombination. Another approach has been to incorporate the rare earth ions in a host matrix material and using nanostructure sensitizers to excite the ions indirectly through a Förster-Dexter coupling process [97, 98], leading to emission through the rare earth ion's metastable state. By controlling the size of the nanostructures, their bandgap energy can be tuned through quantum confinement effects to match the optimal excitation energy for the rare earth ion being sensitized. In this type of system, luminescence from the nanostructure is in competition with the energy transfer to the rare earth ion. Also, electrical excitation can be difficult, especially if nanocrystals are used for the sensitizing structure since they would be embedded in an insulating medium, requiring either hot carrier excitation or carrier injection through quantum tunneling. However, using nanostructure sensitization is advantageous since loss mechanisms including Auger recombination and de-excitation back-transfer processes are suppressed as are the temperature dependent quenching effects.

Of course, the sensitization of the rare earth ions can also occur through interactions with radiative defect levels or the use of co-dopant ions. In a silicon oxide host, different defects may be present depending on the layer composition and it is important to consider their contribution in studying rare earth doping of these materials. For silicon-rich silicon oxides, radiative oxide defects include divalent silicon, neutral oxygen vacancies, and E_{δ}' centres which emit at energies of 4.35, 2.64–2.76, and 2.25–2.38 eV, respectively [100]. Radiative defects including weak oxygen bonds, peroxy radicals, non-bridging oxygen hole centres may be present in silicon oxides with stoichiometric or oxygen-rich compositions having emission energies of 2.99, 2.25, and 2.00 eV, respectively [100]. Similarly, it may be favourable to use a co-dopant rare

earth ion which is more readily excited to transfer energy to the emitting element as has been successfully utilized to enhance erbium emission through the use of ytterbium co-doping in silica [101].

Another method of obtaining visible luminescence that has been widely employed to create white light sources is to optically excite a phosphor coating with a light emitting diode (LED), which converts a portion of the LED luminescence to a lower wavelength through a downshifting or downconversion process. One such device that has received considerable attention as a white light source has been cerium doped $[Y_{1\text{-}x}Gd_x]_3[Al_{1\text{-}y}Ga_y]_5O_{12}$ (YAG:Ce) phosphor coatings applied to InGaN light emitting diodes [102]. In this system, the InGaN LED, which has a peak emission wavelength that can be shifted from 370 nm for pure GaN to approximately 470 nm with increased indium content, contributes a blue component to luminescence spectrum while also optically exciting the YAG:Ce, a broadband yellow phosphor [102, 103]. Utilizing this design, the colour temperature of the device can be tuned between 3000 and 8000 K by varying the levels of Gd and Ga in YAG:Ce, which causes the peak emission wavelength of the phosphor to shift from 510–580 nm. In theory, a similar method could be applied to obtain visible or white luminescence from rare earth doped silicon-based materials and, in fact, a number of silicon-based oxynitride and nitride phosphors have already been investigated for use in white light emitting diodes [104]. However, it is first necessary to develop an efficient silicon-based electroluminescent device that emits at blue or ultraviolet wavelengths for such a design to take full advantage of the silicon platform and become more practical or economical than competing technologies.

2.3 Cerium Disilicate

Cerium disilicates are a class of cerium containing silicon oxide crystals that share the stoichiometry of $Ce_2Si_2O_7$. Several polymorphs of this material have been ex-

perimentally observed [35, 37, 105–110], each from a different crystallographic space group. A-$Ce_2Si_2O_7$ has a tetragonal unit cell with a $P4_1$ space group, the G-$Ce_2Si_2O_7$ polymorph is monoclinic with P21/n symmetry, and $Ce_6[Si_4O_{13}][SiO_4]_2$ has an orthorhombic unit cell with $Pca2_1$ symmetry. However, it should be noted that this latter phase, as described in the study in which it was observed, was essentially hypothetical due to the experimental limitations and based on the cerium borosilicate ($Ce_3[BSiO_6][SiO_4]$) structure [110]. The unit cell structures of the different phases are shown in Figure 2.11. Typically these structures, along with other cerium silicates, have been formed by annealing cerium oxide layers deposited on silica or silicon substrates at high temperatures. In the $Ce_2Si_2O_7$ structures, the cerium ions are coordinated in the luminescent trivalent state. While these crystals were reported as having strong violet-blue luminescence at wavelengths in the 350–450 nm range [108, 109], they remain an understudied material system. In addition to the cerium disilicate structures, cerium silicate compounds with stoichiometries of Ce_2SiO_5 [105], $Ce_{9.33}[SiO_4]_6O_2$ [111], and $CeSiO_4$ [112] have been reported. However, the latter phase is not particularly interesting in the context of luminescent materials since the cerium ions in this structure are in the optically inactive 4+ oxidation state.

As part of her M.A.Sc. thesis project [36], former research group member J. Li recently found that nanocrystals of cerium disilicate could be formed in cerium doped oxygen-rich silicon oxide films after high temperature annealing at 1200℃. These nanocrystals exhibited bright blue photoluminescence with higher intensity than was observed in the same film at lower annealing temperatures. The structure of the nanocrystals was confirmed to be $Ce_2Si_2O_7$ structure through HRTEM analysis of the lattice spacing [37].

I decided to follow up on these results during my thesis project research since the cerium disilicate material seemed promising to me given the intense emission that

A-$Ce_2Si_2O_7$

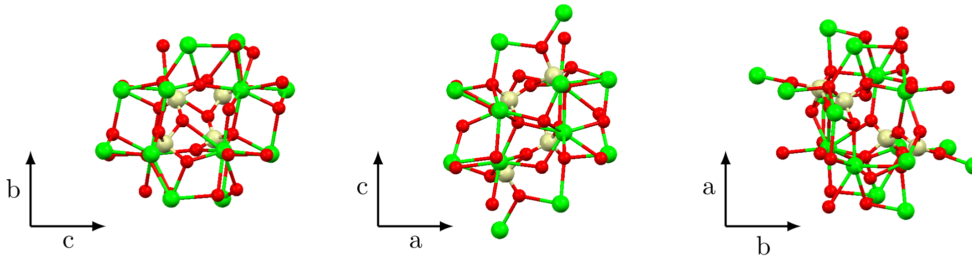

G-$Ce_2Si_2O_7$

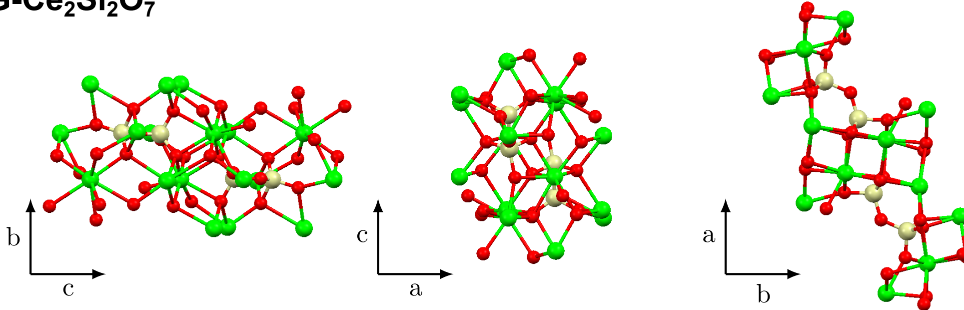

$Ce_6[Si_4O_{13}][SiO_4]_2$

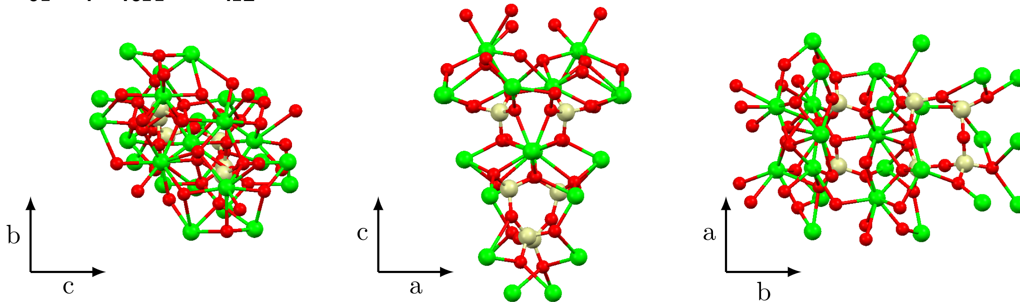

Figure 2.11: Visualization of the crystal structures of the A-$Ce_2Si_2O_7$, G-$Ce_2Si_2O_7$, and $Ce_6[Si_4O_{13}][SiO_4]_2$ cerium disilicate phases [107, 110] viewed along the a, b, and c crystallographic axes. The green, white, and red spheres represent cerium, silicon, and oxygen atoms, respectively.

was observed, especially considering that Jing's samples contained quite a low volume fraction of the structure within the layer which I anticipated that I could increase substantially. Additionally, the cerium disilicate structure seemed like an excellent method of incorporating a large concentration of cerium ions without suffering from the negative effects of clustering since all of the cerium ions in the structure are optically active and their coordination and spacing are kept constant due to the set lattice positions. Based on the stoichiometry of cerium disilicate, a cerium concentration of up to 18.2 at.% could be obtained in a film with 100% volume fraction of this structure, which far exceeds the typical doping levels that can be obtained in most rare earth materials before reaching the solubility limit. Due to the complex formation of the structure, it was not clear what volume fraction of cerium disilicate could be obtained in this manner. However, even a conservative volume fraction of 25% would yield a very favourable cerium concentration of 4.55 at.% with every ion coordinated in an optically active state. The results of this work are discussed in Chapter 6.

Chapter 3

Sample Fabrication

3.1 Deposition of Silicon Nitride Thin Films

Amorphous silicon nitride films with stoichiometric Si_3N_4 and silicon-rich compositions were grown on silicon substrates using plasma-enhanced chemical vapour deposition. The silicon nitride films were produced using three types of PECVD systems which utilized different methods of plasma generation and process gases in order to study the formation and luminescence of silicon nanoclusters within these layers. Films were produced on the different deposition systems for comparative purposes since the results for the silicon-rich silicon nitride materials system reported in literature by different research groups varied significantly and the specific details of growth (*e.g.*, growth rate) seemed to factor heavily even within a given deposition system. It was expected that the luminescent properties of the films grown using each system may be influenced by their respective atomic densities, density of nucleation sites, diffusion of excess silicon, bonding structure at the nanocluster interface, and interaction with defects in the host matrix.

The most rudimentary system, a Technics 900 Series Micro PECVD system, utilized a standard radio frequency (RF) generated capacitive plasma to dissociate the process

Table 3.1: System specific details for SRSN thin film depositions

CVD System	**Silicon Source Gas**	**Nitrogen Source Gas**	**RF/MW Power**	**Film Thickness**	**Deposition Rate**
PECVD	5% SiH_4/Ar	NH_3	50 W	2200–2600 Å	110–130 Å/min
ICP CVD	30% SiH_4/Ar	N_2	300 W	2400–3000 Å	26–30 Å/min
ECR PECVD	30% SiH_4/Ar	10% N_2/Ar	500 W	800–1200 Å	53–60 Å/min

gases while the other two systems had more sophisticated designs which utilized inductively coupled plasma and electron cyclotron resonance based plasma generation techniques. The ICP CVD and ECR PECVD systems produce higher quality films than the PECVD due to higher uniformity of deposition, a reduction in plasma damage from highly energetic ions and neutral radicals, and lower chamber pressures resulting in higher purity films. Of the three systems, only the ECR PECVD system was capable of incorporating rare earth dopants *in-situ*, and so all work that pertained to films doped in this manner was performed on this system. A detailed overview of the ICP CVD and ECR PECVD systems can be found in C. Zhang's [113] and D. Blakie's M.A.Sc. theses [100], respectively.

For comparing the three PECVD systems, silicon nitride thin films were deposited on n-type (100) silicon substrates. The sample compositions were controlled through the variation of the deposition gas flow rates, adjusting the nitrogen source rate while keeping the silicon source rate constant. Unless otherwise stated, all depositions were performed with a substrate heater temperature of 300°C. The system-specific data for the silicon and nitrogen source gas compositions, the RF power used for PECVD and ICP CVD, the microwave (MW) power used for ECR PECVD, the film thicknesses grown, and the deposition rates obtained are all listed in Table 3.1. The films studied in the isothermal annealing experiments were deposited by the ECR PECVD system using similar parameters as employed in the system comparison, except that the films in this case were grown to be approximately 3000 Å thick and were deposited

using a substrate heater temperature of 350°C (unless otherwise stated). The higher temperature was used since this was generally found to produce SRSN films with increased PL intensity for this particular system. The lateral uniformity of the films deposited using the ICP CVD and ECR PECVD systems was optimized through applying a 25 rotation per minute stage rotation during film growth. The PECVD system had a stationary stage, so a similar rotation could not be applied.

Cerium doped SRSN films were grown using the ECR PECVD system using a substrate heater temperature of 350°C and the same parameters that were used to deposit undoped SRSN films on this system, which are listed in Table 3.1. The cerium doping was performed *in-situ* by heating a remote cerium cell containing tetrakis[2,2,6,6-tetramethyl-3,5-heptanedionato]cerium[IV] ($Ce[tmhd]_4$), a volatile metal organic precursor, to a temperature of 200°C and transporting the sublimated cerium ions into the CVD reaction chamber using Ar carrier gas flowing at a rate of 5 sccm. The concentration of cerium incorporated into the films was controlled through the cerium cell temperature, which influenced the vapour pressure of sublimated cerium ions produced in the cell and therefore the concentration of cerium ions introduced to the reaction chamber in an exponential relationship. The rare earth lines and dispersion ring through which the sublimated cerium was transported into the chamber were heated to temperatures of 210°C to ensure that the cerium vapour did not re-solidify through cooling during transport.

3.2 Deposition of Cerium and Terbium Doped Silicon Oxide Thin Films

Cerium and terbium co-doped silicon oxide thin films were grown on silicon substrates using ECR PECVD. For certain depositions, the films were also simultaneously deposited on transparent 1” thick high quality quartz substrates for the purposes

of variable angle spectroscopic ellipsometry including the measurement of transmission spectra. The depositions were performed on two different systems: the MAC ECR PECVD, which was the same system used to grow samples for the silicon nitride studies, and the GIV ECR PECVD, which was a new system capable of aluminum doping. Details of the design and capabilities of the GIV system can be found in R. Dabkowski's M.A.Sc. thesis [114]. In the MAC system, the depositions were performed at a stage heater temperature of 300 or 350°C using 30% SiH_4 in Ar and 10% O_2 in Ar for the silicon and oxygen process gases, a microwave power of 500 W, and continuous stage rotation at approximately 25 rotations per minute. The cerium and terbium doping was performed *in-situ* by heating the metal organic precursors $Ce[tmhd]_4$ and tris[2,2,6,6-teramethyl-3,5-heptanedionato]terbium[III] ($Tb[tmhd]_3$), respectively, in separate remote cells and transporting the sublimated rare earth ions into the reaction chamber using an Ar carrier gas flowing at 5 or 10 sccm. For both systems, the rare earth lines and dispersion ring or towers were heated to temperatures exceeding the temperatures of the rare earth cells to avoid re-solidification due to cooling of the rare earth precursor during transport. Only the MAC system was equipped with terbium at the time of this study, although the rare earth manifolds for both systems were designed to have interchangeable rare earth precursors. In fact, up to the time of this writing, the GIV system has never had a terbium precursor installed. This is significant because the GIV system was used to produce reference samples without terbium co-doping since there were experimental difficulties with obtaining these samples from the MAC system as will be discussed in Section 6.1. The specific details of the deposition parameters and resulting film compositions and optical properties are provided in Section 6.1 (Tables 6.1 to 6.3).

3.3 Post-Deposition Annealing

The characteristics of Si-ncs formed in SRSN films are strongly dependent on both deposition and processing parameters, as evidenced by the variations in their measured luminescent properties and electronic structure, which will be discussed in Chapter 5. In order to investigate these properties, post-deposition, the SRSN samples were subjected to thermal annealing in a quartz tube furnace for 60 minutes under either flowing N_2 gas or forming gas (5% H_2 in N_2) ambient. The nitrogen provided an inert environment for annealing while the forming gas was used in an attempt to improve the luminescence intensity from silicon nanoclusters through the passivation of dangling bonds at their surface via hydrogen bonding. To minimize oxygen contamination during the annealing, the quartz tube furnace was designed with the tube extending well outside the furnace as shown in Figure 3.1, enabling sample to be loaded into the tube and purged with the ambient gas at room temperature before being transferred into the furnace for annealing. The samples were transferred in and out of the furnace using a quartz boat on the end of a long rod, which extended through a sealed section of the end-cap of the tube, which could be tightened to hold the boat in position and prevent oxygen back-diffusion during purging or annealing. The gas flowing through the quartz tube was exhausted through a tube connected to an oil bubbler, which was used as another measure to prevent oxygen back-diffusion through the outlet. As part of a standard procedure that was developed to prevent oxygen contamination and ensure consistent results, the samples were loaded into a room temperature region of the quartz tube which was then purged for approximately 15 minutes prior to insertion into the furnace. Upon extraction, the samples were left in a room temperature region of the sealed tube to cool for approximately 5–10 minutes.

The furnace temperatures were measured using a platinum k-type thermocouple. To obtain consistency across different samples, films of different compositions were

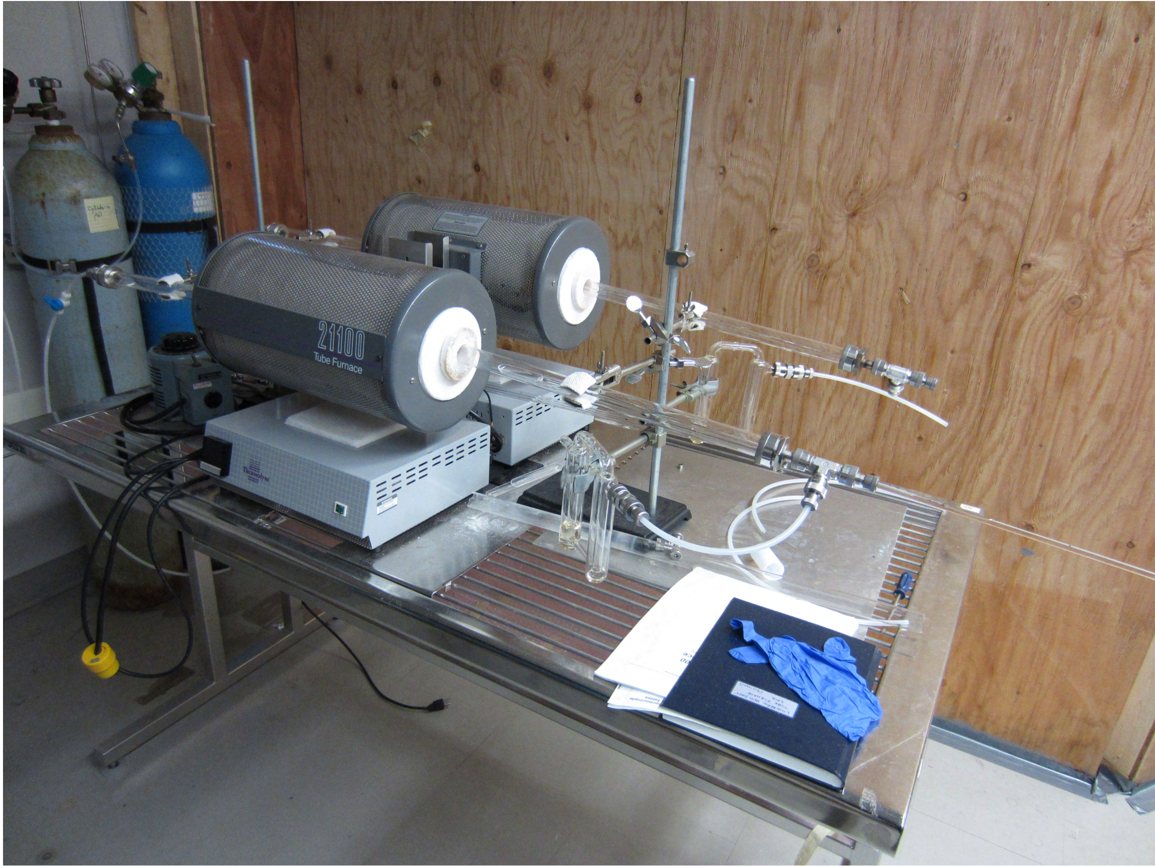

Figure 3.1: Photograph of two of the quartz tube furnaces used in the annealing studies of silicon-rich silicon nitride and cerium and terbium co-doped silicon oxide films.

annealed at the same time wherever possible and a thermocouple was used to verify that the different samples were positioned within a region of the furnace that was evenly heated. For consistency between annealing runs (*e.g.*, at different temperatures), samples from a given film were placed into the same positions in the boat, which was then inserted to a marked position in the furnace, and the ambient gas was set to flow at a fixed rate across all annealing runs.

Due to the short times involved in the isothermal annealing study of the SRSN films, it was performed using the Qualiflow Jipelec Jetfirst 100 rapid thermal processor (RTP) pictured in Figure 3.2 rather than a quartz tube furnace. The use of a RTP provided more control over the heating cycle and better temporal accuracy. The isothermal

Figure 3.2: Photograph of the Qualiflow Jipelec Jetfirst 100 rapid thermal processor used in the isothermal annealing studies of silicon-rich silicon nitride films.

study was performed using temperatures of 600 and 800°C with a ramp rate of 25°C/s under flowing N_2 gas for times ranging from 2–7200 seconds.

The post-deposition annealing of the cerium and terbium co-doped silicon oxide films was performed using similar methods to those described for the SRSN films. An isochronal annealing study was performed using a quartz tube furnace under flowing N_2 ambient gas at temperatures between 600–1200°C for 60 minutes. An isothermal annealing study was also conducted at 1200°C in a quartz tube furnace under flowing N_2 for times ranging from 5–540 minutes. For both sets of experiments, only N_2 gas was used since the nanostructures formed in these films were not found to be prone to defect-related quenching, rendering hydrogen passivation unnecessary.

Chapter 4

Methods of Sample Characterization

4.1 Rutherford Backscattering Spectrometry

The compositions of deposited films were determined using Rutherford backscattering spectrometry conducted in the Tandetron Accelerator Laboratory at Western University. For these measurements, the samples were probed in a Cornell geometry using 2–5 µC doses of 1.8 MeV $^{4}He^{+}$ ions with the samples tilted at an angle θ of 5°. The incident angle was chosen to reduce channeling in the substrate and a random rotation of ϕ was used during all measurements to further minimize any channeling effects, which were found to complicate the fitting procedure without providing a significant improvement to the signal-to-background levels. For most silicon nitride samples, a 5 µC dose was used to obtain a good signal-to-noise ratio while a 4 µC dose was found to be sufficient for rare earth doped silicon oxide films due to the stronger backscattering from higher Z elements.

The compositional information for each sample was obtained from a reference piece of as-deposited film deposited on a silicon substrate that was cleaved from the

region that was nearest to the centre of the deposition system's sample holder during growth. This central position was chosen to maintain consistency in comparing films by avoiding the effects of non-uniformity which could potentially occur at positions closer to the edge of the sample holder. In practice, the inhomogeneity in silicon dioxide films was found to be approximately 10% over the surface of a 2" wafer on the MAC ECR PECVD system and approximately 1% over the surface of a 3" wafer on the GIV ECR PECVD system during the commissioning of each system. Of course, since the uniformity of a given deposition depends on the growth parameters and system conditions, some deviation from these calibration values could be expected. With this in mind, samples to be used for a specific set of experiments (*e.g.*, an annealing study) were always cleaved from the same region of a film to minimize the impact of non-uniformity and, wherever possible, the samples were taken from near to the centre of the deposition stage.

While the use of carbon substrates is necessary for accurate analysis of carbon-containing films due to the low signal-to-background levels of the carbon peak on top of a silicon substrate signal [60, 115], the nitrogen and oxygen signals were found to be strong enough in all of the films studied that a low Z substrate was not required. Without this limitation, the RBS measurements were made using films grown on silicon substrates, for convenience and because it was simple to model.

The measured RBS spectra were fit using SIMNRA simulation software [116] to obtain the atomic concentrations (excluding hydrogen) as a function of depth in the films [117, 118]. The simulations were performed using calculation parameters accounting for elemental isotopes, multiple scattering, straggling, and dual large angle scattering based on the Ziegler/Biersack stopping powers, Chu and Yang energy-loss straggling model, and Andersen function accounting for the influence of partial electronic screening of nuclear charges on the Rutherford cross-section. The experimental

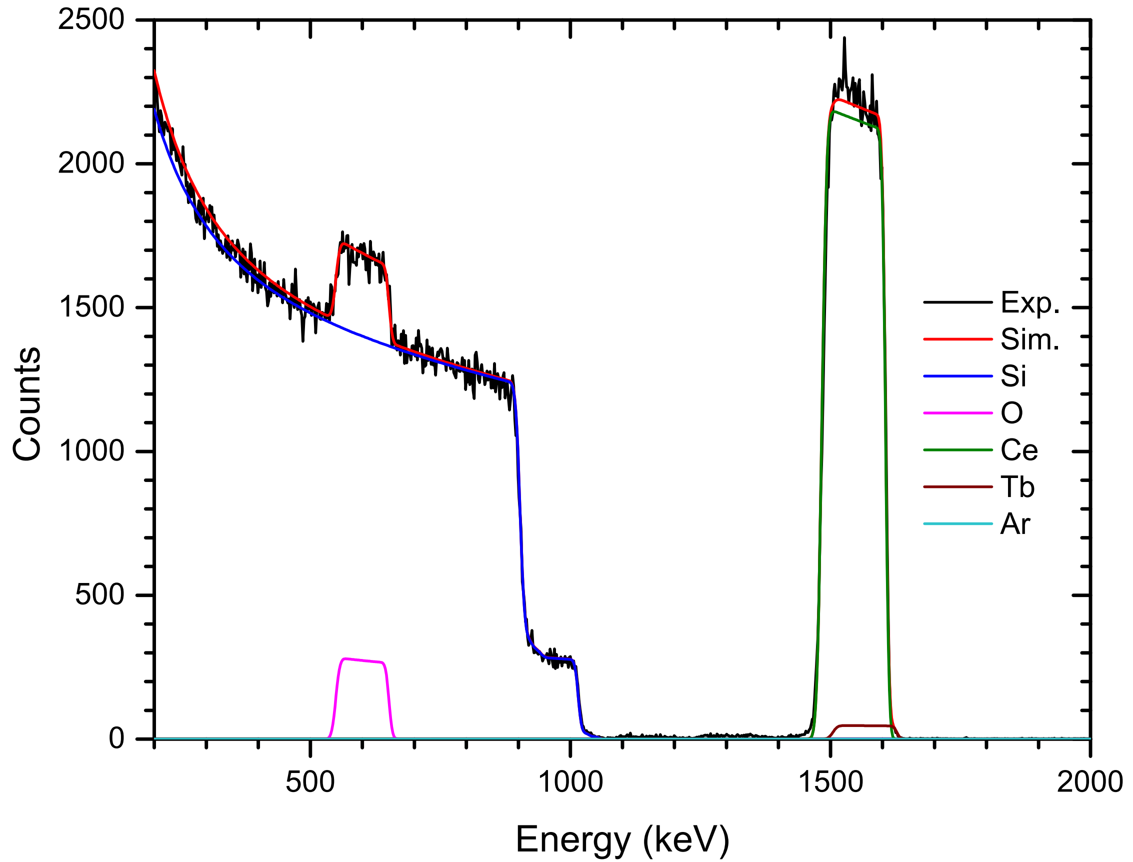

Figure 4.1: Fitted RBS spectrum for an as-deposited cerium and terbium co-doped silicon oxide film (CeORSO-02). The contributions of the constituent elements are included in addition to the experimental data (Exp.) and simulated fit (Sim.).

parameters were calibrated against reference samples consisting of silicon implanted with a known dose of bismuth or antimony that were measured as a part of each experimental run. An example fit of the as-deposited cerium and terbium co-doped silicon oxide film, CeORSO-02 (refer to Table 6.1 for sample information), is shown in Figure 4.1. The individual spectra corresponding to each element have been included in this plot as well as the experimental and simulated spectra to indicate the origin of the various spectral features. Here, the silicon feature has a high energy shoulder related to the silicon content in the film beginning at approximately 900 keV as well as a strong, broad component at lower energies corresponding to backscattering from the silicon substrate.

4.2 Ellipsometry

Ellipsometry provided a useful tool for determining the optical properties of both silicon nitride and rare earth doped silicon oxide films. In most cases, single wavelength ellipsometry (SWE) using a HeNe laser at 632.8 nm provided a quick and convenient measure of the thickness and approximate composition of films grown since the refractive index was found to scale with the excess silicon content in silicon-rich silicon nitride films and rare earth incorporation in silicon oxide films. Typically, the ellipsometry measurements were performed on the as-deposited films since an unprocessed sample provided the most consistent point of comparison between different films and the nanostructures formed in annealed films would require more advanced analysis. The ellipsometry measurements were best applied to films deposited on single-side polished silicon or properly prepared quartz substrates. Films deposited on double-side polished silicon provided less reliable results due to depolarization effects caused by backside reflections from the smooth surface on the bottom of the substrate, which could not be accounted for in the SWE analysis. For quartz substrates, which would otherwise be prone to depolarization effects unless the backside of the substrate was roughened, the issue was avoided by simply applying scotch tape to the backside surface to achieve a similar roughening effect without having to physically alter the substrate. The scotch tape method works for quartz since it has very similar optical constants and this approach is commonly employed in ellipsometry measurements due to its convenience. Unfortunately, there is not a readily available material that can be used to obtain a similar effect for double-side polished silicon.

More advanced analysis using variable angle spectroscopic ellipsometry on a J. A. Woollam M-2000U UV-Vis ellipsometer with near-infrared extension, pictured in Figure 4.2, was employed for several cerium and terbium co-doped silicon oxide films to study their absorption properties and to compare the optical properties of as-

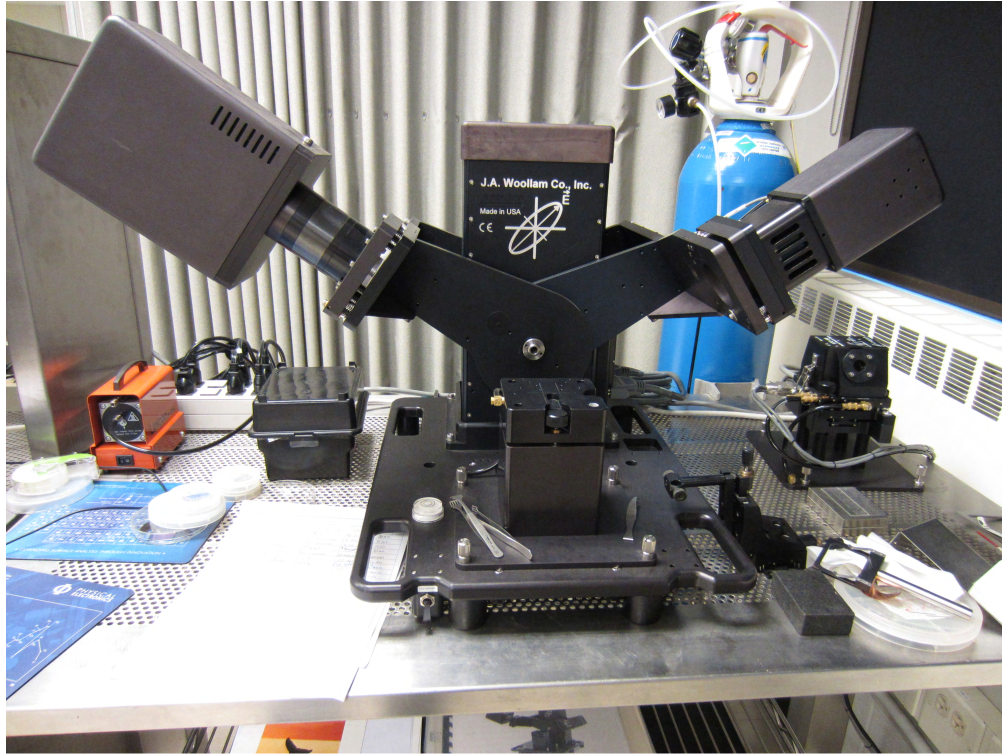

Figure 4.2: Photograph of the J. A. Woollam M-2000U UV-Vis VASE instrument.

deposited films to those of high temperature annealed films in which cerium disilicate nanocrystallites had formed. The modeling was performed using the J. A. Woollam's CompleteEASE™ software package [119]. For this analysis, a transparent region was modeled using a Cauchy model for wavelengths above 500 nm, which was then used to parameterize an effective medium approximation (EMA) model for the layer consisting of three weighted constituent materials. One constituent was based on a thermal SiO_2 model, a second was based on the Tauc-Lorentz general-oscillator model, and the third constituent was a void model to account for any open space volumes in the layer. The EMA model was then extended to the entire wavelength range measured to incorporate the absorbing regions into the analysis and calculate the percentage of the layer effectively composed of the two constituents. For films deposited on silicon, a standard silicon model was used while a model with uniaxial

anisotropy was applied for the substrate layer of films deposited on quartz to account for differences in ordinary and extraordinary directions of the crystal.

4.3 Transmission Electron Microscopy

Details of the film structure were investigated via cross-sectional high resolution transmission electron microscopy and scanning transmission electron microscopy using the JEOL 2010F and FEI Titan 80-300 Cryo *in-situ* microscope at the Canadian Centre for Electron Microscopy (CCEM) at McMaster University. The samples were prepared using the conventional technique of gluing together a stack of cleaved silicon bars with two sample bars in the middle oriented such that their film surfaces were facing. The stack was then thinned to approximately 100 µm via a polishing process, cut into discs which were then supported by gluing a molybdenum ring to the back, dimpled using a polishing wheel such that the centre of the disc was 10–20 µm thick, and finally ion milled at a shallow angle of 3–4° using an energy of 3–4 keV.

Due to the amorphous structure of the silicon nanoclusters formed in SRSN films, imaging of these nanostructures was difficult and required carefully prepared samples with very thin cross-sections. While it was not possible to see the silicon nanoclusters using HRTEM, they could be measured using STEM, where some contrast could be observed due to density differences between the Si-ncs and silicon nitride host matrix, or energy filtered transmission electron microscopy (EFTEM) using a narrow energy window centred on the low energy plasmon for silicon at 16.5 eV. Both microscopes were also used to obtain compositional information for the different features observed in the transmission electron microscopy (TEM) images through the use of X-ray energy dispersive spectroscopy (XEDS) including a compositional map of the cerium ions within the cerium and terbium co-doped silicon oxide films.

4.4 Photoluminescence Spectroscopy

The visible emission properties of the films were analysed through room temperature ultraviolet-excited photoluminescence spectroscopy experiments using a 325 nm HeCd laser excitation source. The laser beam was directed onto a sample holder at an angle of 52° using free space optics and the PL was collected through a lens which coupled the light into a fiber optic cable that was connected to a visible charge-coupled device (CCD) spectrometer. Two different spectometers were used in this work: an Ocean Optics S2000 and an Ocean Optics USB2000+. Both devices were spectrally calibrated using the same Ocean Optics LS-1-CAL calibrated tungsten halogen light source. The S2000 was used for all of the measurements of silicon-rich silicon nitride films while the USB2000+ was employed when measuring the cerium and terbium doped silicon oxide films due to its extended range in the near-ultraviolet wavelengths. However, the extended range was found to come at the expense of slightly lower resolution in the visible spectrum compared to the S2000, which could distinguish some finer details of Tb^{3+} emission peaks that were not exhibited in the spectra of the same samples measured with the USB2000+. The collection lens was mounted on an XYZ stage and its position was calibrated prior to data collection to maximize the signal intensity. In cases where the intensities of the measured spectra were compared for data collected on different days, a reference sample was used to renormalize the intensities of the spectra for consistency between data sets.

Aside from the calibration of the collection optics, the stability of the laser output power over years of operation can influence the measured PL spectra. When the system was originally commissioned in 2005, the laser was characterized as having an output power of 17 mW with an intensity of 640 mW/cm^2 [120]. However, over time the emission power has degraded to approximately 2.6 mW as of August 2012. For samples measured within a matter of days or even months, the change would

likely be negligible but it is important to consider such a change when comparing PL spectra measured over extended periods of times. Besides decreasing the intensity of PL from samples due to a reduction in incident photons, which can be accounted for using the same method as when considering the collection optics calibration, it is important to consider that excitation channels may become saturated at higher intensities resulting in altered spectral distributions compared to lower intensity excitation. It was particularly important to consider the possible ramifications for samples in which an optical centre with a relatively short radiative lifetime may sensitize an optical centre with longer radiative lifetime (*e.g.*, cerium and terbium co-doped silicon oxide films) since the latter channel would saturate under high enough incident photon flux while emission from the shorter radiative lifetime centre would continue to increase. For the purposes of this study, the decay of the laser output power was not observed to significantly influence the experimental findings for any of the materials studied, perhaps because samples for a given study were measured within a short enough period of time to avoid this potential issue. It has only been brought up as a cautionary message to researchers performing similar analysis in the future since it would be easy to overlook and could distort the trends observed in PL spectra if not accounted for or avoided.

For further information regarding the photoluminescence apparatus, please refer to the journal article by O. H. Y. Zalloum *et al.* which details the design and calibration of this setup [120]. Once measured, the PL spectra were imported into a spreadsheet for plotting in order to identify trends in the spectral features. Additionally, the total power densities of the films were calculated and, for cerium and terbium co-doped silicon oxide samples, the peak intensities of the Ce^{3+} and Tb^{3+} spectral components were determined to track the individual trends in emission from each element. The room temperature photoluminescence spectra were also used as a basis

for calculating the chromaticity of select films based on the International Commission on Illumination (CIE) 1931 standard [121]. The spectra were imported into a modified version of the ColorPy Python script [122], which integrated the product of the spectral intensity and the red, green, and blue colour matching functions to determine the x, y, and z chromaticity coordinates for the samples that indicated their positions on a CIE 1931 colour space chromaticity diagram. The script was also used to generate images depicting the simulated colour of emission based on a conversion from the calculated chromaticity values to RGB colour model components.

In addition to the room temperature photoluminescence spectra, select cerium and terbium co-doped silicon oxide samples were also measured in a cold temperature chamber using the same laser and spectrometer to observe changes in the PL properties. Here, the chamber in which the sample was mounted was cooled using a CTI-Cryogenics 8200 compressor controlled via a RMC Cryosystems Series 4000 cryogenic thermometer/controller with the temperature monitored using thermocouples located inside the chamber.

4.5 X-Ray Absorption Spectroscopy

Details of the electronic structure of the films were measured through X-ray absorption near edge structure analysis conducted on the high resolution spherical grating monochromator (SGM) 11ID-1 [123] and variable line spacing plane grating monochromator (VLS PGM) 11ID-2 [124] beamlines at the Canadian Light Source (CLS) synchrotron facility. Pictures of these beamlines and the CLS storage ring are shown in Figures 4.3 and 4.4, respectively. The VLS PGM beamline was used to probe the Si $L_{3,2}$ and Ce N_4 absorption edges while experiments on the SGM beamline were used to probe the N, O, and Si K-edges as well as the Ce and Tb $M_{5,4}$-edges. In these experiments, the total electron yield (TEY) and total fluorescence yield (TFY) signals

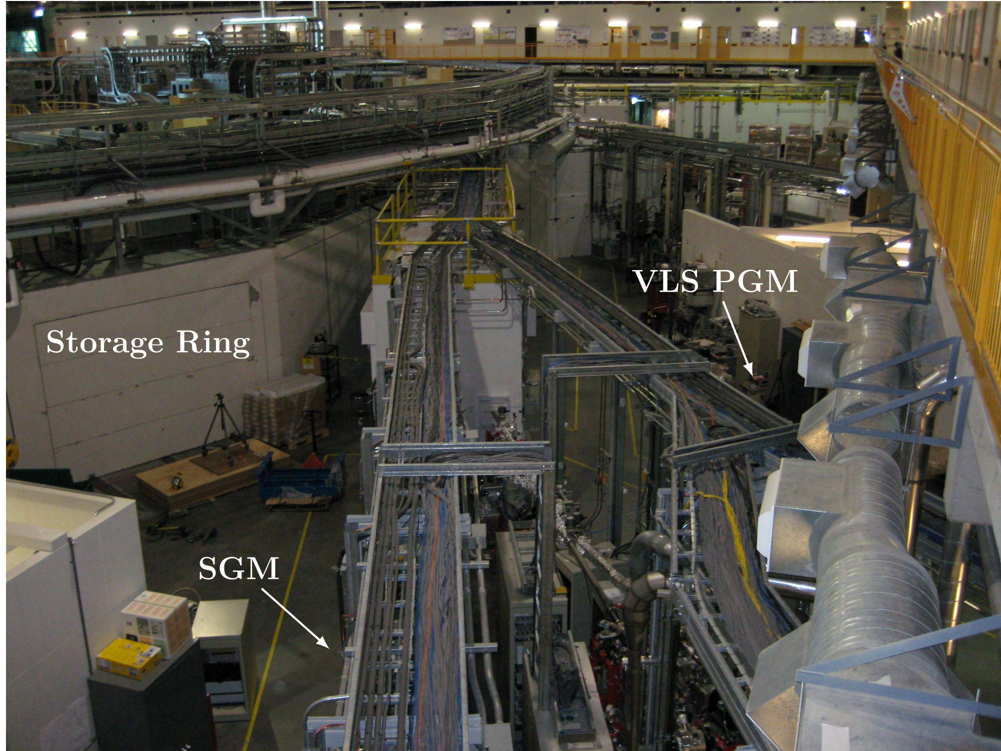

Figure 4.3: Top-down view of the SGM (left) and VLS PGM (right) beamlines branching out from the CLS storage ring.

were measured simultaneously as the incident X-ray energy was scanned across an absorption edge. The TEY spectra were acquired based on measurements of the drain current from the sample while the TFY spectra were measured with a microchannel plate (MCP) detector, which was oriented at a glancing angle with respect to the sample surface in order to minimize saturation effects.

With the exception of measurements at the Si K-edge, the TEY provided information from the near-surface region due to the short mean free path of secondary electrons generated at soft X-ray energies [40] while bulk information was obtained through TFY measurements. However, at the Si K-edge, the information depth of the TEY was approximately 700 Å [125] in the materials studied which was sufficient for bulk analysis while the TFY signal was saturated by fluorescence from the silicon substrates due to the long mean free path of fluorescence photons at these high energies.

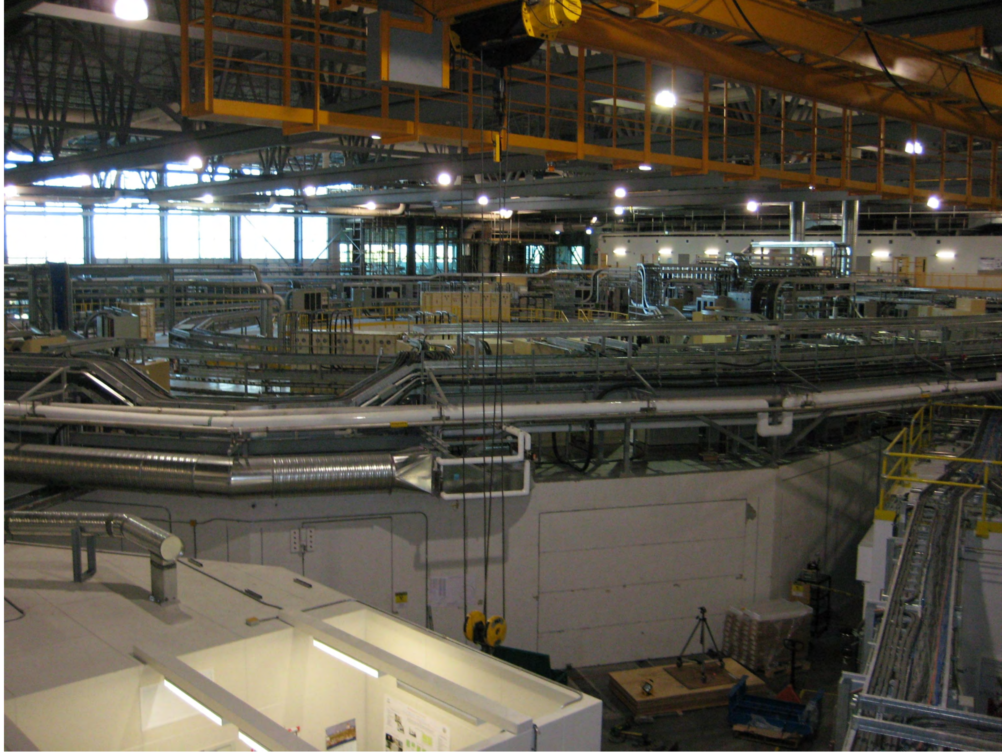

Figure 4.4: The CLS storage ring with the SGM beamline protruding at the bottom right.

Contributions from the substrate in the TFY were avoided at the Si $L_{3,2}$-edge by measuring films exceeding 2000 Å thickness, which was significantly larger than the estimated maximum sampling depth for fluorescence photons at these relatively low energies [125].

All of the measured XANES spectra were normalized to the incident X-ray intensity, I_0, which was obtained from the drain current of an in-line Au mesh. Background subtraction was performed on each spectrum by fitting a line to the pre-edge region and subtracting the extrapolated line from the entire spectrum. In general, the spectra were then renormalized by dividing the background subtracted signal by the post-edge level, thereby setting the absorption step height to unity. However, when comparing certain spectra, it was occasionally found to be advantageous to renormalize to the height of a specific spectral feature, such as in the case of the Si $L_{3,2}$-edge spectra,

where the post-edge region did not reach a plateau due to strong background features.

Unfortunately, obtaining accurate bulk sensitive X-ray absorption spectra at certain energies can be inhibited by strong saturation or self-absorption effects in the total fluorescence yield signal, which distort the spectral features in a manner that is non-trivial to account for in data analysis [126]. In fluorescence yield XANES, both of these phenomena are of practical importance because they deviate from the fundamental assumption that the absorption cross-section is proportional to the number of core-holes generated in the material as measured by the number of fluorescence photons emitted upon core-hole relaxation [127, 128]. While this principle holds true in most circumstances, spectral artifacts corresponding to self-absorption manifest themselves when the penetration depth of the incident X-ray beam abruptly changes near an absorption edge causing a decrease in fluorescence photon generation by non-resonant excited elements in the material which counteracts the increase in fluorescence of the resonant excited element, effectively suppressing the peak in the measured fluorescence yield spectrum and introducing a non-linearity with respect to the absorption coefficient [126, 129–131]. The distortions are most severe for measurements at absorption edges pertaining to highly concentrated elements and heavy elements located in a matrix of lighter atoms, such as in the case of rare earth ions incorporated in silicon-based dielectrics. At the same time, spectral artifacts due to saturation can arise when the incident X-ray penetration depth is comparable to the fluorescence photon mean free path resulting in distortion of the fluorescence signal as it becomes nearly independent of the absorption coefficient [126]. Saturation can occur if the incident X-ray beam is at a shallow angle with respect to the sample surface or at energies near the absorption edge of a highly concentrated element or heavy element within a light matrix. The problem must be avoided or corrected if one wishes to undertake quantitative or even proper qualitative analysis. Unfortunately,

this cannot be done using standard alternative measurements such as electron yield or transmission spectra since they are inherently unsuitable for bulk sensitive analysis at soft X-ray energies due to the limited escape depth of electrons and the short penetration depth of the incident X-ray beam, respectively. Both techniques are also subject to their own set of artifacts. In collecting electron yield spectra, charging can occur in insulated materials and saturation effects arise when the X-ray penetration and electron escape depths are similar [132–135] while transmission spectra can be distorted by X-ray leakage in samples which are too thick or inhomogeneous, among other effects [131, 136, 137].

In an effort to account for the distortions caused by self-absorption in fluorescence yield XANES, a couple of correction procedures have been developed [138, 139]. The computer program FLUO is the most well established to date and corrects measured data using tabulated absorption cross-sections and approximations in order to recover the actual absorption coefficient. While this tool can provide a good approximation of the absorption coefficient, the approach used for recovery is still limited to approximately 10% accuracy. In its current state, the software is only capable of correcting data measured at K and L absorption edges and so it is not suitable for XANES studies at the rare earth $M_{5,4}$-edges [139], which provide valuable structural information on the incorporation of dopant ions within the host matrix because it probes the partially filled 4f levels associated with luminescence. Of particular interest is the ability to use this information to identify the oxidation state of the rare earth ions, which indicates whether or not they may be optically active and the wavelength of emission. Unfortunately, in the study of rare earth doped silicon oxide films, the rare earth $M_{5,4}$-edges are also the most prone to self-absorption and saturation artifacts in the TFY spectra since the incident X-ray penetration depth is relatively low in this energy range and the rare earth ions are heavy elements incorporated in a light

host matrix. Furthermore, due to the short mean free path of electrons generated by X-ray absorption at the rare earth $M_{5,4}$-edges [40], TEY-XANES analysis of rare earth doped silicon oxide films is limited to surface sensitivity and may not provide data that is representative of the bulk of the film. As a strong insulator, silicon oxide films are also prone to charging effects which can distort and suppress the TEY-XANES signal.

It was recently found, however, that the self-absorption problem could be addressed for uniform samples of thickness greater than the X-ray attenuation length by measuring the partial fluorescence yield (PFY) spectrum of an element in the film undergoing non-resonant X-ray emission and inverting it [140]. This approach effectively measures the change in attenuation length of the incident X-ray beam, which is linearly correlated with the absorption coefficient of the material. Fortunately, in addition to overcoming self-absorption effects, it also provides a means of avoiding saturation artifacts since the resonant X-ray emission is entirely ignored.

This technique, referred to as the inverse partial fluorescence yield (IPFY), was applied to overcome self-absorption and saturation effects in XANES measurements of cerium doped silicon oxide thin films while retaining the bulk sensitivity necessary to properly analyze the cerium incorporation in the layers. In this analysis, the O K_α PFY spectra were measured at the Ce $M_{5,4}$-edge using a silicon drift detector, oriented approximately 20° below the incident X-ray beam's plane of polarization, with a resolution of approximately 100 eV. The O K_α PFY spectra were inverted to obtain the IPFY-XANES spectra, which were then processed using the methods of I_0 normalization, background subtraction, and renormalization outlined above.

The origin of the TFY distortion caused by the self-absorption and saturation phenomena can be observed in the energy resolved fluorescence map and partial fluorescence yield spectra of oxygen and cerium shown in Figure 4.5 for a 1200℃

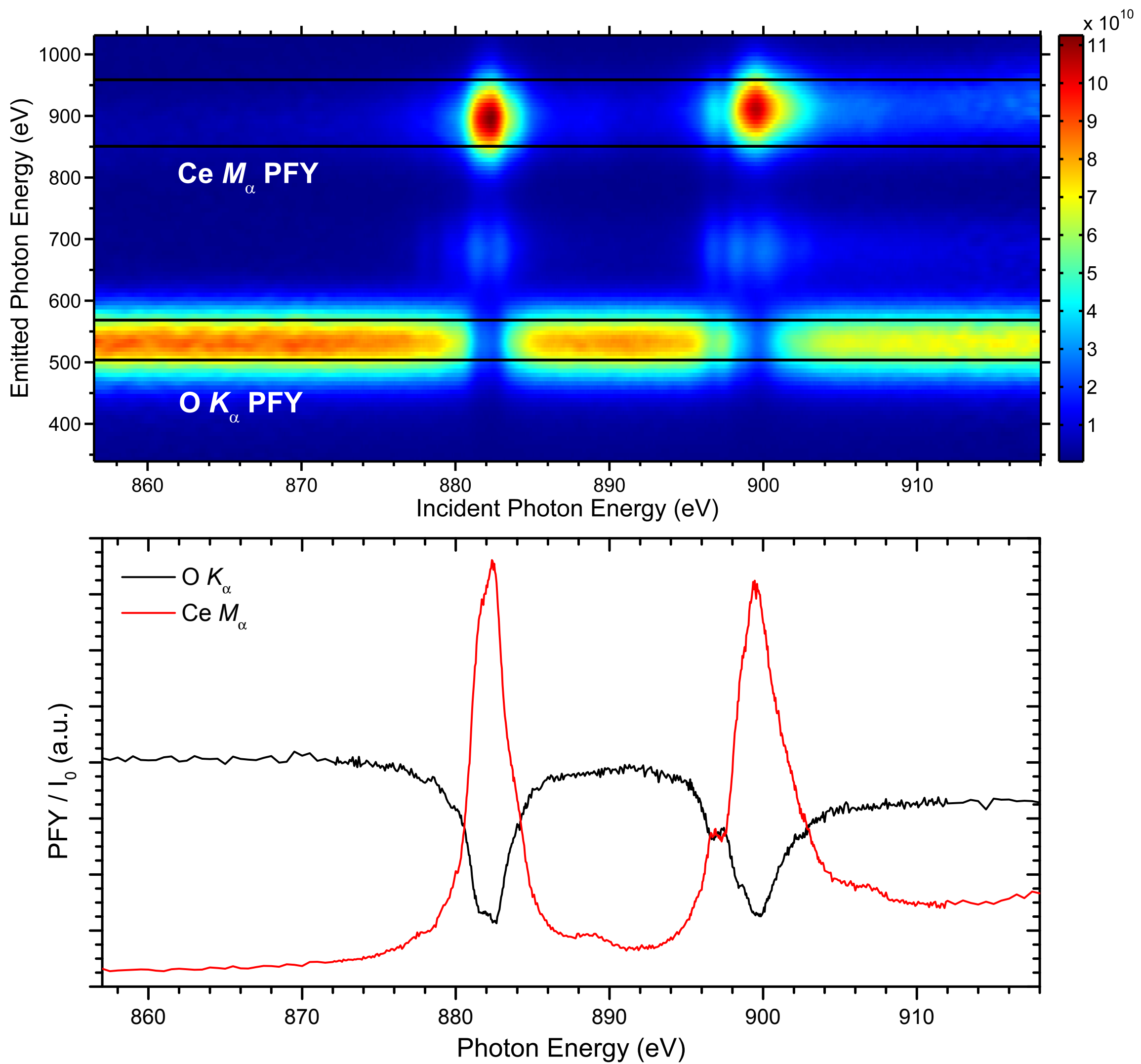

Figure 4.5: Energy resolved fluorescence spectrum for a film containing 8.9 at.% Ce annealed at 1200℃ with the integrated O K_α and Ce M_α PFY-XANES spectra plotted underneath. The regions of integration used to obtain the two PFY-XANES spectra are identified by pairs of black horizontal lines.

annealed cerium and terbium co-doped silicon oxide sample. The PFY spectra were obtained by integrating over the X-ray emission energy regions denoted on the map and based on this data, the Ce M_α PFY exhibits a distorted profile arising from saturation effects while the O K_α PFY, which is representative of the non-resonant X-ray emission and would normally be expected to remain flat over this energy range, is heavily influenced by self-absorption effects, fluctuating strongly due to the strong reduction in X-ray attenuation length with increased Ce absorption near the absorption edges. Combined, these phenomena cause the peaks in the TFY signal to become suppressed and distorted in shape. However, the inverse partial fluorescence yield spectra shown in Figure 4.6 can be obtained by inverting the O PFY, providing a measure of the change in X-ray attenuation length and thus the absorption coefficient. Figure 4.6a compares the renormalized O IPFY- and TEY-XANES spectra of the film containing 8.9 at.% Ce, annealed at different temperatures. Aside from the differences in Ce coordination at the surface versus the bulk of the film, the peak widths and Ce M_4 to M_5 peak ratios closely match at the lower temperatures before the onset of charging effects caused the relative intensity of the M_4 peak to decrease in the more insulating films annealed at 1100 and 1200℃.

In Figure 4.6b, a similar comparison is made between the renormalized O IPFY- and TFY-XANES spectra for the same set of films, which illustrates the degree to which the self-absorption and saturation artifacts can influence the XANES spectra in these materials. Even in the as-deposited film, the shape of the peaks is considerably altered and the degree of distortion, particularly with respect to the broadening, shape, and ratio of peaks, increases with annealing temperature as the film compresses. Unfortunately, the signal-to-noise ratio of the IPFY was poor relative to the TEY and TFY spectra due to limitations of the silicon drift detector which required the number of counts to remain below a threshold value to maintain linearity. The spectral noise

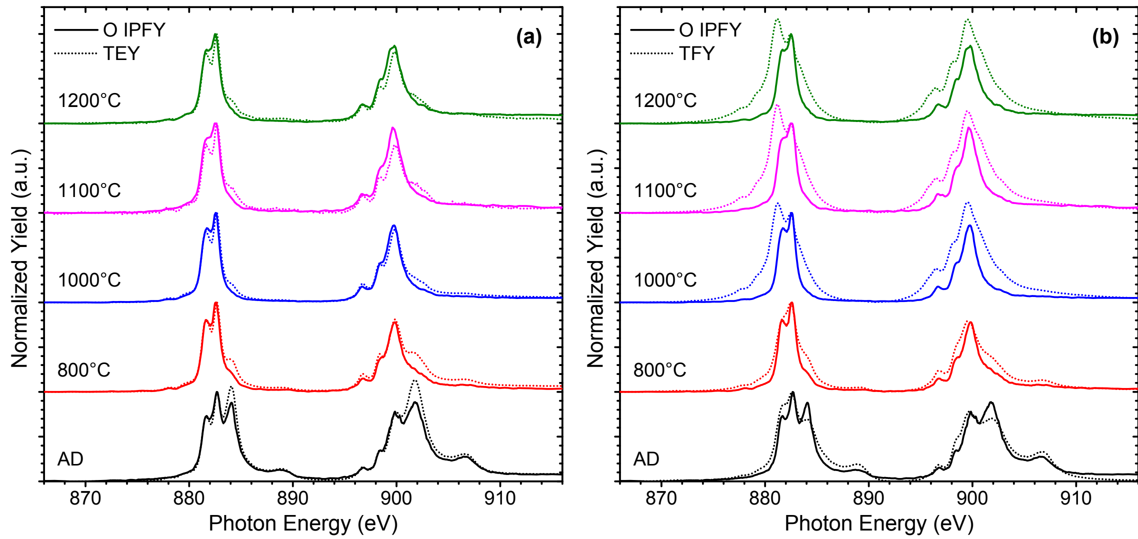

Figure 4.6: Comparison of O IPFY-XANES spectra for a film containing 8.9 at.% Ce annealed at various temperatures with the corresponding (a) TEY-XANES and (b) TFY-XANES spectra.

can make it difficult to resolve finer spectral features. However if this posed a large problem, the signal could be improved through averaging at the expense of increased measurement time or a more sophisticated type of energy resolved fluorescence detector could be employed. For our goal of discerning the oxidation states of the cerium ions this did not pose a problem and it was found that applying a Savitzky-Golay smoothing filter during data processing provided sufficient averaging of the spectra while maintaining spectral features [141, 142]. Combined, the comparison of the TEY-, TFY-, and O IPFY-XANES spectra supports the necessity for and effectiveness of this technique for addressing self-absorption and saturation related artifacts in cerium doped silicon oxide films with high doping concentrations.

For most materials and applications, rare earth doping concentrations are kept to lower levels to avoid agglomeration and ion-ion interactions, both of which are detrimental to the radiative efficiency [89], or due to practical barriers preventing such high levels of incorporation. At lower concentrations, the self-absorption and saturation effects would be less significant due to weaker absorption at the rare earth

absorption edge resulting in less fluctuation in X-ray attenuation length as well as reduced absorption near the film surface and when low enough, an IPFY correction would no longer be necessary. To determine an approximate cerium concentration in silicon oxide at which self-absorption and saturation becomes an issue, several compositions of cerium doped silicon oxide films were measured after annealing at temperatures above 1100℃ with the results plotted in Figure 4.7. Despite the O PFY showing minor changes in X-ray attenuation length, no noticeable artifacts were present in the Ce $M_{5,4}$-edge TFY-XANES spectrum of samples with as high as 0.4 at.% Ce. On the other hand, samples containing 2.6 and 5.3 at.% Ce exhibited strong self-absorption and saturation artifacts, although bulk sensitive information could be obtained using the O IPFY-XANES spectrum as an alternative.

The precise onset concentration depends on the experimental geometry as well as the thickness and density of the layer [129, 140]. However, based on this result, it is reasonable to suggest that bulk sensitive XANES experiments at the Ce $M_{5,4}$-edge conducted on cerium doped silicon oxide films with Ce concentrations in excess of 0.5 at.% may be prone to self-absorption and saturation effects. Conveniently, this was also approximately the lower limit at which the silicon drift detector could measure the fluctuations in O PFY signal without requiring extensive averaging to improve signal-to-noise ratio for analysis. A similar guideline could likely be extended to other cerium doped materials and even materials doped with other rare earth ions, although the onset concentration and degree of distortion will additionally depend on the absorption and fluorescence properties of the constituent elements.

To complement the XANES spectra and provide site specific information on the luminescent properties of the films, X-ray excited optical luminescence spectra were simultaneously collected using an Ocean Optics USB2000+ spectrometer which essentially measured the photoluminescence spectrum at each incident X-ray energy.

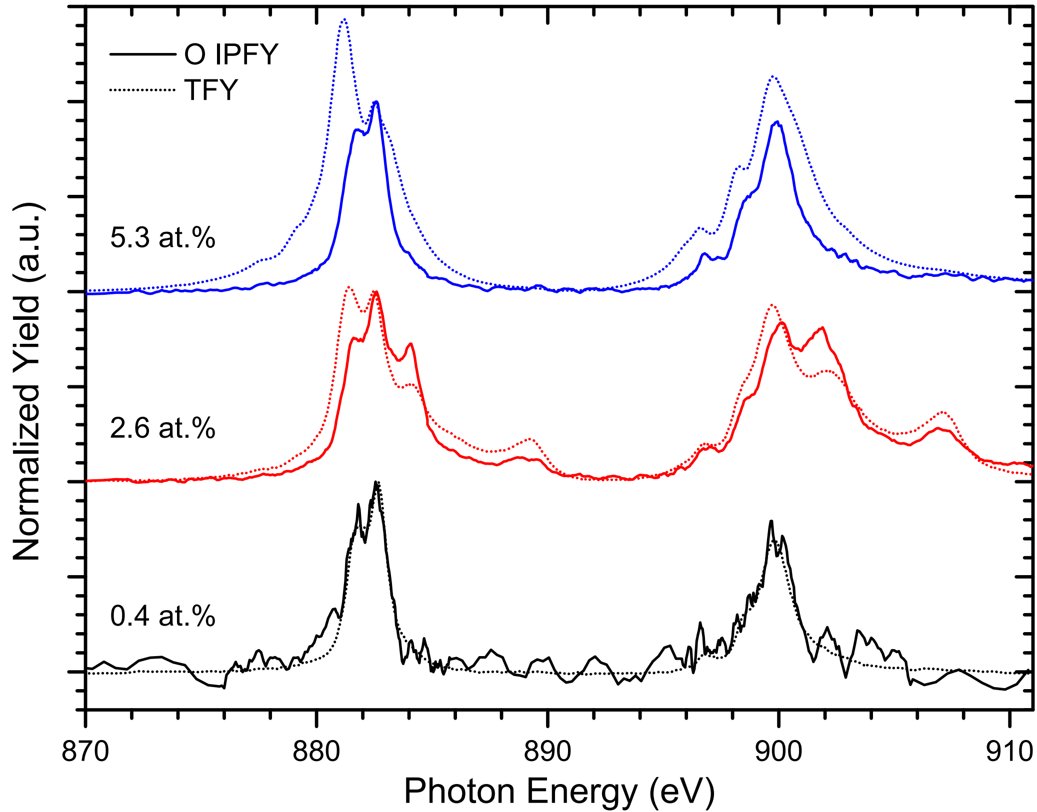

Figure 4.7: Comparison of O IPFY- and TFY-XANES spectra for three films containing different concentrations of Ce annealed at temperatures above 1100°C. Significant distortion of spectral features by self-absorption and saturation artifacts in TFY-XANES spectra was observed for films with Ce concentrations of 2.6 at.% and higher. No such artifacts were evident in films containing 0.4 at.% Ce or less.

The integrated photoluminescence intensity was calculated at each incident energy to obtain the photoluminescence yield (PLY) signal, which could be used to correlate changes in photoluminescence with features in the XANES spectra and help identify sites responsible for excitation of optical emission or sensitization channels in the films. For cerium and terbium co-doped silicon oxide films, in addition to the PLY of the entire spectra, smaller wavelength regions within the XEOL spectra corresponding to Ce^{3+} and Tb^{3+} emission were integrated to track the changes in photoluminescence from each component. As with the XANES spectra, the XEOL and PLY data was normalized to I_0 in order to account for changes in PL intensity due to variations in the

photon flux of the incident beam. The background subtraction and renormalization procedure was also performed in an identical manner to the XANES spectra.

4.6 X-Ray Diffraction

The structural properties of crystalline nanostructures formed within the cerium and terbium co-doped silicon oxide films were characterized through X-ray diffraction analysis at the McMaster Analytical X-Ray Diffraction Facility. Measurements were made using a powder diffractometer consisting of a Bruker Smart6000 CCD area detector, Bruker 3-circle D8 goniometer, Göebel cross-coupled parallel focusing mirrors, and Rigaku rotating copper anode source. The use of a rotating anode source and area detector provided the high intensity beam and measurement sensitivity necessary for obtaining strong diffraction signals from silicon nanostructures embedded in thin silicon-based dielectric films in short measurement times. Films deposited on (100) silicon substrates were measured at a 10° omega angle with a randomly rotating chi angle to minimize the effects of preferred orientation. To obtain the best signal-to-noise ratio, frames were selected to avoid diffraction peaks related to the silicon substrate, enabling longer scan times without saturating the detector. The measured frames from the area detector were loaded into the Bruker General Area Detector Diffraction System (GADDS) software package [143]. Using this software, a median smoothing filter was applied before integrating over chi angles normalized by solid angle with a step size of 0.01° to obtain intensity vs. 2θ plots curves for each frame of a sample. The curves from each frame were then merged to create a full intensity vs. 2θ plot data set which could be fit. The fitting and Reitveld refinement of structural features was performed using the Bruker Topas software package [144] using a 5th order Chebychev polynomial for the background and peak profiles based on the modified Thompson-Cox-Hastings pseudo-Voight (PV-TCHZ) function.

Chapter 5

Study of Silicon-Rich Silicon Nitride Thin Films

The characterization of the silicon-rich silicon nitride materials system came as a natural progression of prior research into luminescent silicon oxide materials by group members D. Comedi, T. Roschuk, D. Blakie, and J. Li [27, 36, 73, 100]. The silicon nitride host matrix was seen as a promising candidate material since it provided a structurally stable dielectric already used in many microelectronic fabrication processes and it offered several advantages over silicon oxide including more favourable electrical properties, relatively low temperature requirements for forming luminescent silicon nanoclusters, and the possibility for silicon nanocluster luminescence over the entire visible spectrum rather than being restricted to emission energies below 2 eV [23,24,73].

In this work, the structural and luminescent properties of Si-ncs formed in SRSN films deposited with varied compositions using three different plasma-enhanced chemical vapour deposition-based systems are compared and discussed: PECVD, ICP CVD, and ECR PECVD. Results from these studies have been previously reported in two conference proceedings and a journal article [41, 43, 44].

Most studies to date have employed isochronal annealing steps after deposition to

induce diffusion of excess silicon to nucleation sites. Conventionally, this has been done using a quartz tube furnace with an ambient gas of N_2 or 5% H_2 in N_2 (*i.e.*, forming gas) over 60 minutes. For consistency, this approach has been taken to provide a good comparison amongst the three deposition systems studied. However, whilst this provides for good comparison amongst the results of various studies, to date there has not been an in-depth isothermal study wherein the annealing is performed over a large time scale ranging from seconds to hours. To address this gap in reported data, in this study, SRSN thin films have been annealed for times ranging from two seconds to two hours using rapid thermal annealing to provide a basis for investigating the growth process and thermal evolution of these films as well as determining the flexibility of the processing conditions over which such a film could be incorporated into a larger device design. As an extension of this research, several films were also doped with cerium in an effort to evaluate the potential use of nitride passivated silicon nanoclusters as sensitizers for visibly emitting rare earth ions.

5.1 Sample Composition

The films produced by each of the three deposition systems for the isochronal annealing experiments covered a broad range of compositions from stoichiometric Si_3N_4 to 14 at.% excess silicon content (Si_{ex}) relative to stoichiometry. Here, the excess silicon content for substoichiometric silicon nitride films with composition SiN_x has been defined in terms of the atomic fractions of silicon ($Si_{at.\%}$) and nitrogen ($N_{at.\%}$) as specified in Equation (5.1).

$$\mathrm{Si_{ex}} \equiv \frac{Si_{at.\%}}{Si_{at.\%} + N_{at.\%}} - \frac{3}{7} = (1+x)^{-1} - \frac{3}{7} \tag{5.1}$$

Film compositions were determined by fitting experimental RBS data from the as-deposited films with simulated spectra using the SIMNRA software package [116]

and all quoted percentages in this study refer to atomic percentages derived from these measurements. Owing to the inherently poor sensitivity of RBS in measuring lower atomic number elements such as nitrogen, the values obtained from the fits have been rounded to the nearest percent, and values measured below 0.5% have been labelled as <1% to account for the uncertainty in the data. The films used in the isothermal annealing experiments were measured to be moderately silicon-rich, having excess silicon contents of 2–3%. Of these films, the one used to study the Si *K*-edge XANES was deposited at a slightly lower substrate temperature of 300℃, which could have a minor effect on the film's properties. However, for the purposes of this study, the compositions of these films were similar enough to draw qualitative comparisons between the trends observed in the PL and XANES spectra obtained from the different samples.

5.2 Isochronal Annealing Comparison of Deposition Systems

The luminescent properties of the various films were analysed through their room temperature ultraviolet-excited PL spectra. Figure 5.1 compares the PL spectra from the AD samples from the three systems. Note that the ECR PECVD film with 2% excess silicon content depicted in this figure was grown using a slightly higher substrate heater temperature of 350℃, which may have resulted in higher emission intensity than a film with similar composition deposited at 300℃. Despite the differences in deposition conditions between the systems, similar trends can be observed. Each system produces AD films exhibiting bright PL with emission energies that can be controlled through the full range of the visible and into the near-infrared portion of the electromagnetic spectrum by increasing the excess silicon content in the film. This correlates well with expected quantum confinement effects as Si-ncs increase in size. However, for each system, the emission occurs across a broad range of energies and

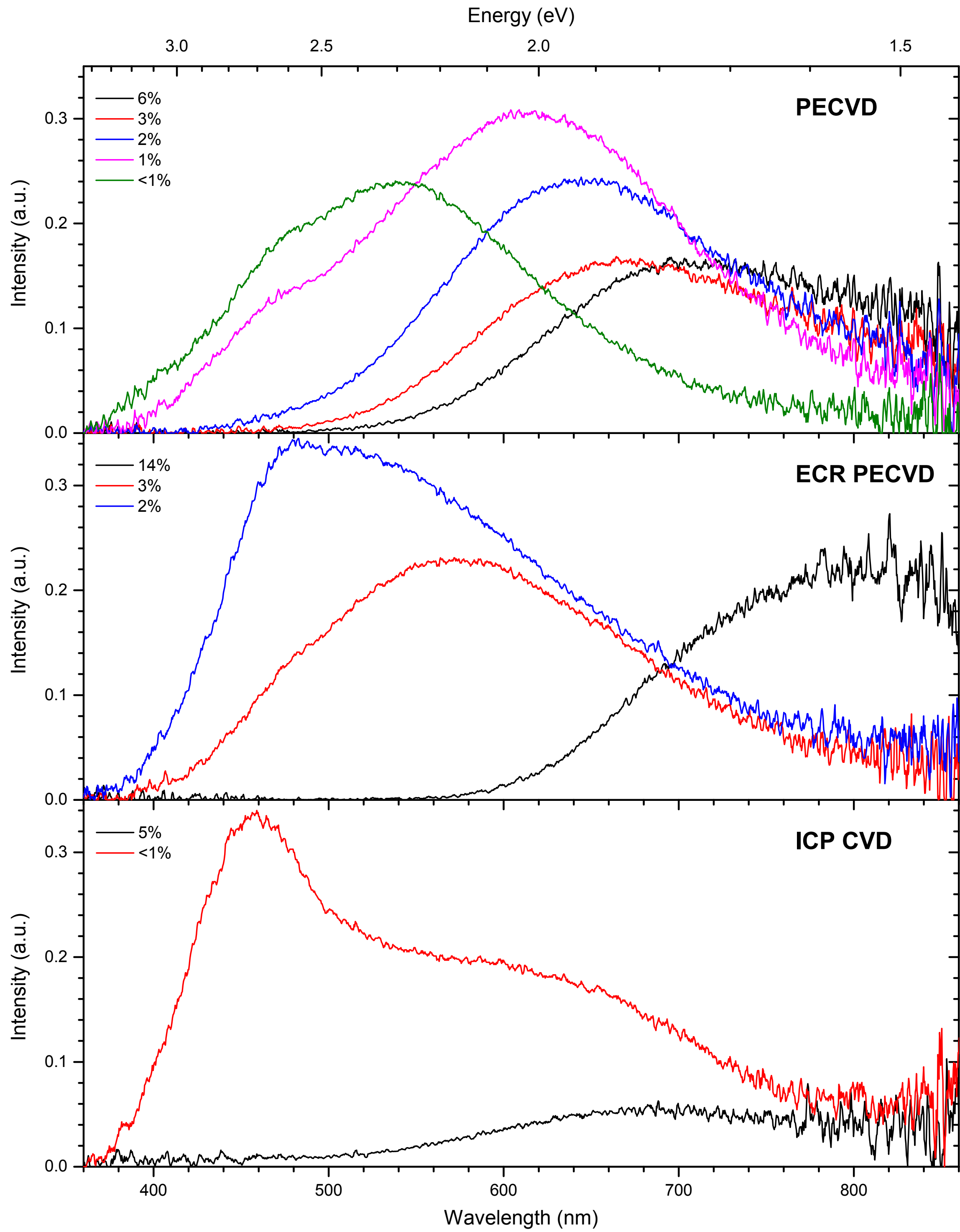

Figure 5.1: PL spectra for as-deposited SRSN films grown by PECVD, ECR PECVD, and ICP CVD with their respective excess silicon contents specified in the legend. As excess silicon content increases, emission shifts to lower energies. After [41].

appears to originate from a combination of quantum confinement effects and defect levels, which have peaks at approximately constant energies independent of the film composition. These defect-related peaks are most prominent in films with low excess silicon content, in which smaller Si-ncs form. As the dimensions of the Si-ncs are reduced, the defect levels become excited and emission through these levels becomes more dominant. The fact that significant PL intensity is observed in the AD films indicates that Si-ncs are formed within SRSN films without the assistance of annealing. This is different from what occurs in silicon-rich silicon oxide films where cluster formation and resulting luminescence occur only after high temperature annealing [27]. The PL intensity of the SRSN films in this study has been qualitatively described as 'bright', which is a rather arbitrary term. Since quantitative measurements of emission intensity have yet to be performed, the term 'bright' is qualified here as PL that is easily visible under typical room lighting conditions.

The effects of annealing a PECVD film with moderately high excess silicon content and an ICP CVD film with low excess silicon content using different ambient gases are compared in Figure 5.2. In general, the emission spectra for samples with higher excess silicon content tend to red-shift slightly as the annealing temperature is increased, whereas lower excess silicon content samples exhibit a slight blue-shift. In samples containing intermediate levels of excess silicon content, the PL peaks have also been observed to blue-shift relative to the AD spectra at low temperatures and red-shift as the annealing temperature is further increased. There appear to be at least two competing mechanisms in the Si-nc growth dynamics related to the growth of existing Si-ncs due to diffusion of silicon atoms in the film and the formation and subsequent growth of new Si-ncs at nucleation sites. The red-shifting resulting from Si-nc growth is much smaller than that observed in SRSO films, but this can be explained by the more diffusion-inhibiting structure of the silicon nitride matrix relative to the silicon

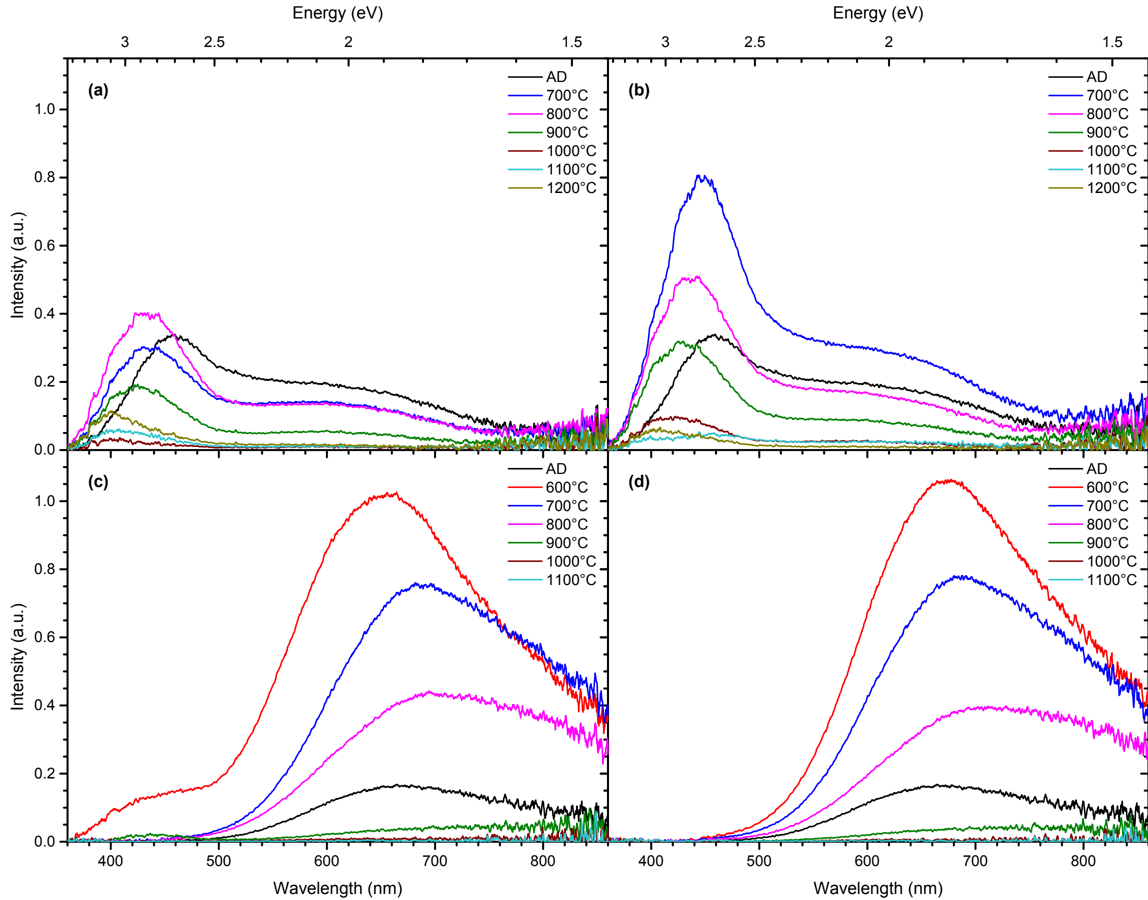

Figure 5.2: PL spectra for SRSN films annealed for 60 minutes in a quartz tube furnace. Shown are an ICP CVD film (Si_{ex}<1%) annealed in (a) N_2, (b) 5% H_2 in N_2 and a PECVD film (Si_{ex}=3%) annealed in (c) N_2, (d) 5% H_2 in N_2. After [41].

oxide matrix [145]. It is also possible that energy may be transferred between smaller and larger Si-ncs, which affects the observed PL spectra. In all of the samples, the most intense emission consistently occurred when annealing was performed at 800℃ or below, with peak intensities being observed at lower temperatures for higher silicon content samples. The reason for the decay in PL intensity at higher temperatures is unknown at this time since (a) Si-ncs are still present in EFTEM and STEM images, as evidenced by the STEM image of a film annealed at 1100℃ in Figure 5.3, as well as in X-ray absorption spectra of these films and (b) the Si-ncs have not grown beyond the quantum confinement regime because of the inhibitive nature of the nitride matrix.

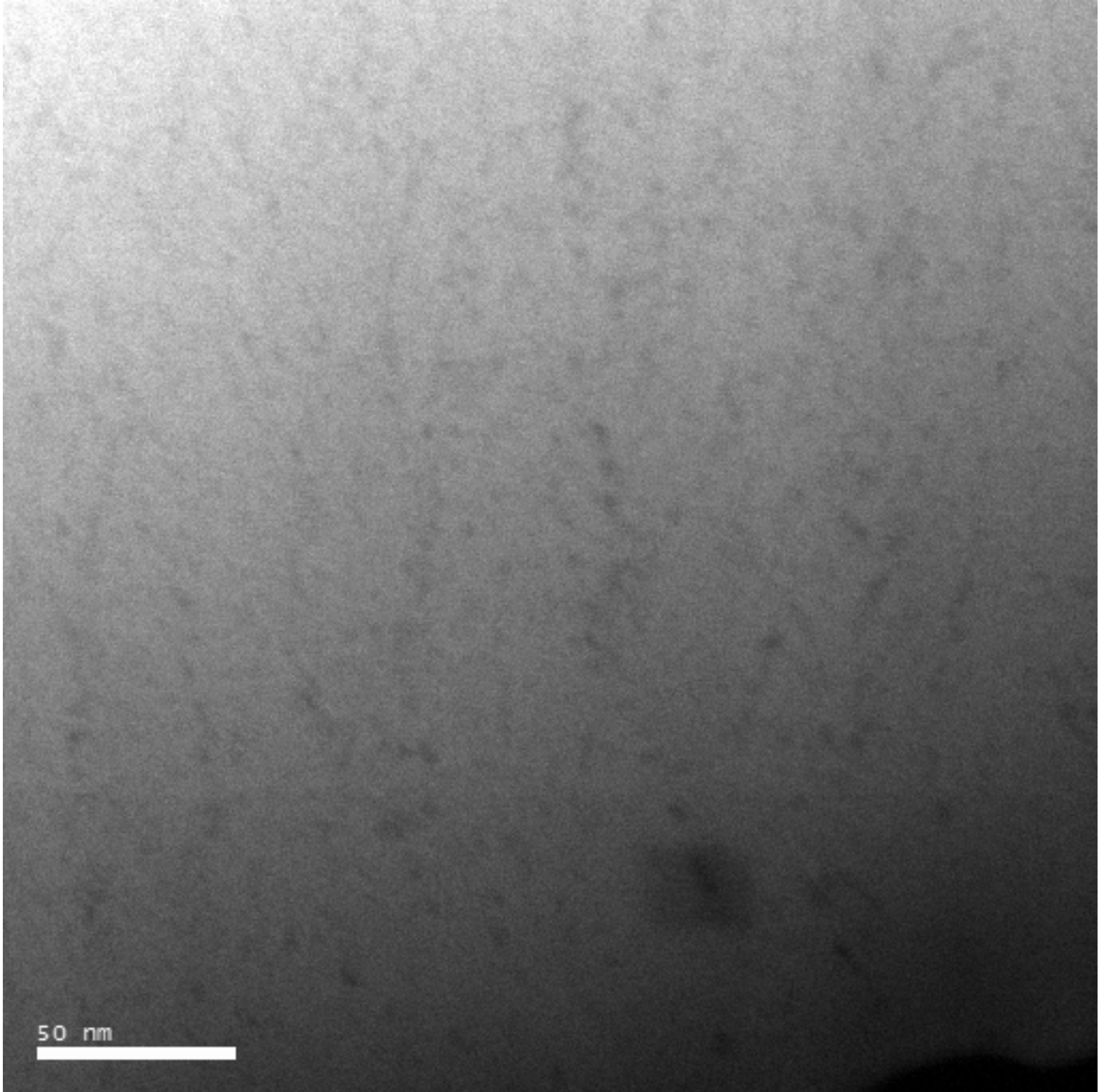

Figure 5.3: STEM image of amorphous Si-ncs formed in an ICP CVD grown SRSN film with high excess silicon content following 1100°C annealing. This image was captured by group member T. Roschuk during his Ph.D. thesis research [73].

As the decay in luminescence does not appear to relate to structural changes in the Si-nc, this suggests that it results from changes in the host nitride matrix or at the Si-nc surface. Such effects could arise from the strain induced in the Si-ncs by the nitride matrix or a re-ordering of the nitride matrix structure at the Si-nc interface such that non-radiative recombination pathways become available. However, further investigation is required to accurately attribute the source of this phenomenon.

Hydrogen passivation of dangling bonds at the Si-nc interface is also observed to play a significant role in improving the PL efficiency. The use of 5% H_2 in N_2 rather than pure N_2 as an ambient gas in the annealing process significantly improves the emission intensity in the ICP CVD- and ECR PECVD-deposited films. This enhancement is not observed in the PECVD-deposited films, which may be because this system uses NH_3 as a nitrogen source. Higher concentrations of hydrogen may remain in the film after dissociating from the NH_3 gas molecules during the CVD reaction process. Having increased levels of hydrogen in the AD PECVD films could be very beneficial when considering incorporating these types of luminescent films into a larger scale design process, such as for electroluminescent and integrated circuit device processing, provided it does not reduce the quality of the film through increased porosity or the effects of out-gassing. Low temperature rapid thermal annealing is preferable in such cases due to the shorter timescale and reduced thermal budget, providing better compatibility with other materials, structures, or processes. Lower temperatures with shorter anneals become particularly important for avoiding the diffusion of metals from contacts, and potentially reducing the number of design steps required compared to the typically longer quartz tube furnace annealing. The effects of the annealing time on the growth, structure and luminescence of SRSN films are addressed in Section 5.3 ‘Isothermal anneals at 600℃’ and Section 5.4 ‘Isothermal anneals at 800℃’ later in this chapter.

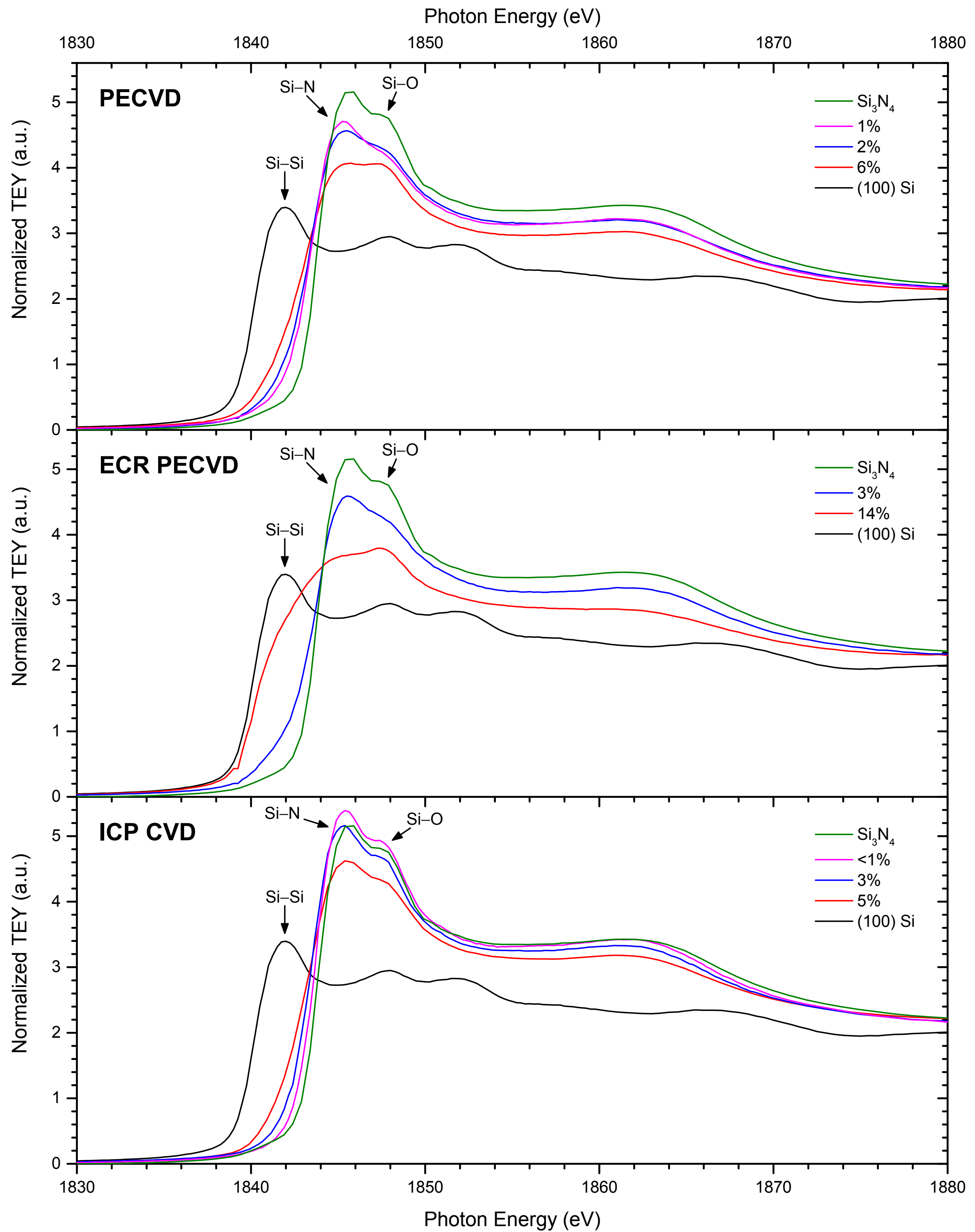

Figure 5.4: TEY-XANES spectra for as-deposited PECVD, ECR PECVD, and ICP CVD films at the Si K-edge. The peaks corresponding to Si–Si, Si–N, and Si–O resonances are labelled. After [41].

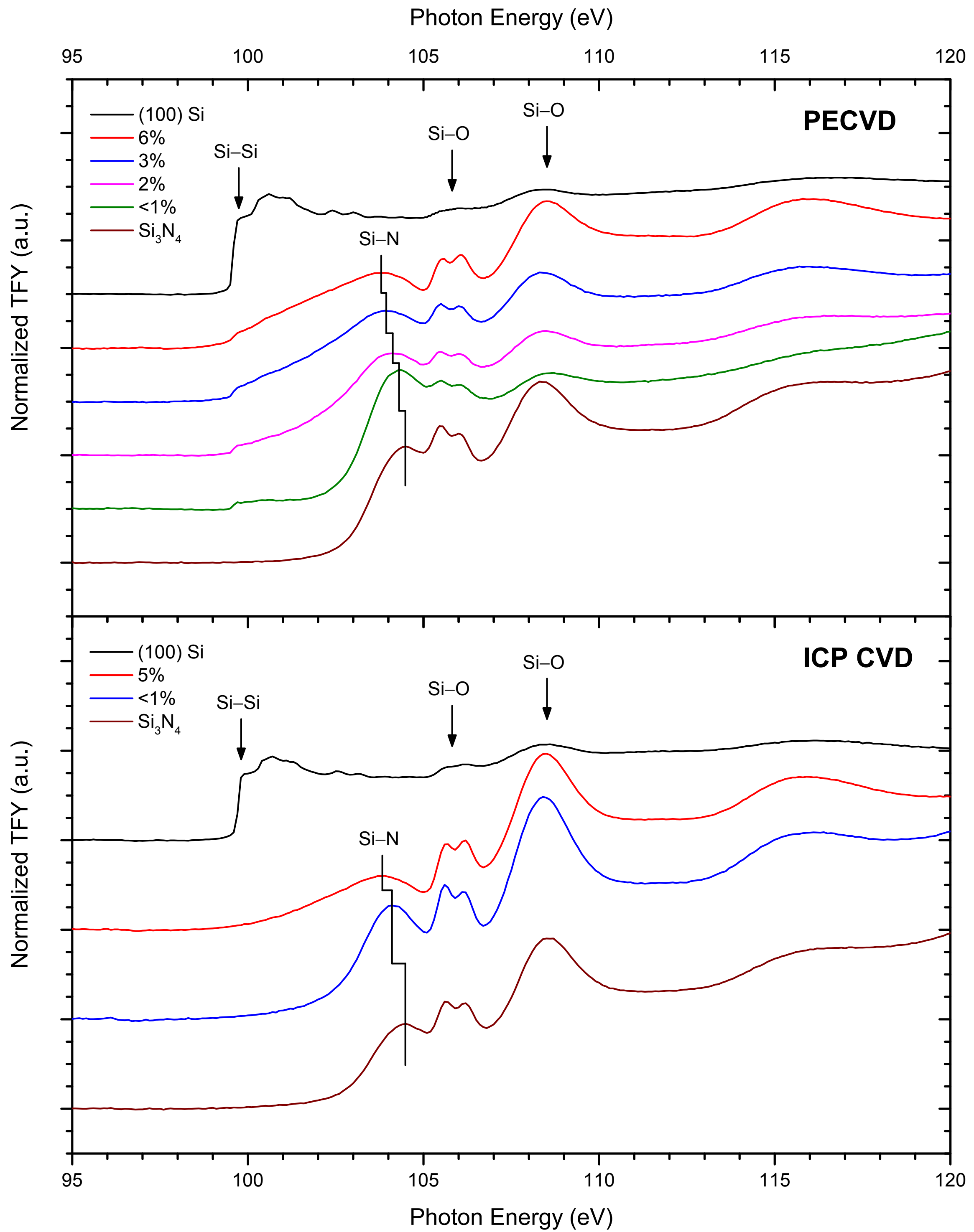

Figure 5.5: TFY-XANES spectra for as-deposited PECVD and ICP CVD films at the Si $L_{3,2}$-edge. For clarity, the spectra have been offset in the order they are listed in the legend. The Si–N resonance peak shifts to lower energies in films with higher excess silicon content. After [41].

The electronic structure was probed through X-ray absorption near edge structure experiments at the silicon K- and $L_{3,2}$-edges, where differences in structure within the films can be identified by shifts in their spectral features [146–150]. Results of the XANES measurements performed at the silicon K-edge for AD films from each system are shown in Figure 5.4, which reveal common trends in the Si-nc structure. The spectra of the ICP CVD films were measured from 2-µm-thick films, much larger than the information depth at either absorption edge [125], to ensure that the substrate would not contribute to the TEY or TFY. However, through further experiments, it has since been found that film thicknesses greater than 1500 Å are sufficient to avoid substrate effects in the TEY data at the Si K-edge, or either the TEY or TFY data at the Si $L_{3,2}$-edge. A low-doped, n-type (100) silicon wafer was used as a crystalline silicon reference for all of the XANES experiments, and the Si_3N_4 reference sample was an AD ICP CVD film with stoichiometric composition. As the silicon content is increased in the films, the absorption edge shifts to lower energies because of the increase of the Si–Si resonance peak at 1842 eV and reduction of the peak related to Si–N bonding located at 1845.5 eV. The weak Si–O peak at 1848 eV in the crystalline silicon reference spectrum arises from the native oxide layer formed at the silicon surface while any Si–O signal exhibited by the SRSN films originates from oxygen contamination at the surface of the film and should not be taken as an indication of Si–O bonding within the bulk of these films. Figure 5.5 compares the silicon $L_{3,2}$-edge spectra for PECVD and ICP CVD AD films. Both sets of films follow similar trends, with the Si–N resonance peak ranging from 103.8 to 104.5 eV as it shifts to lower energies and broadens at higher excess silicon concentrations. However, the PECVD films have a well-defined Si–Si absorption edge at 99.7 eV, which is absent in the ICP CVD-deposited films. The prominence of the absorption edge in PECVD films could be attributed to a difference in the Si-nc structure or the generation of a

greater number of nucleation sites for Si-nc formation resulting from the dissociation of hydrogen from the NH_3 process gas. Unfortunately, the ECR PECVD films were too thin to avoid a large background signal from the silicon substrate at these energies, and so they have not been included in any of the Si $L_{3,2}$-edge comparisons.

Figures 5.6 and 5.7 show the changes in the Si K- and $L_{3,2}$-edge XANES spectra for two ICP CVD grown films, one with low excess silicon content ($Si_{ex}<1\%$) and the other with high excess silicon content ($Si_{ex}=5\%$), as the annealing temperature is increased. At temperatures of 900°C and above, films with low excess silicon concentration develop a shoulder at the Si–Si bonding energy of 1842 eV, suggesting a change in the Si-nc structure and increased phase separation in these films. The position of the Si–N resonance peak shifts to higher energies, from 1845.5 to 1846 eV, and increases in magnitude as the annealing temperature is increased. At the silicon $L_{3,2}$-edge, the Si–Si absorption edge at 99.7 eV is suppressed, and details of the Si clustering are not observed while the nitride matrix undergoes a clear change in structure up to 1100°C when the nitride matrix appears to break down. In films with high excess silicon content, the Si–Si shoulder in the silicon K-edge spectra appears at temperatures as low as 600°C. This indicates that the phase separation and Si-nc formation are not solely dependent on the nitride host matrix and are instead strongly influenced by the composition of the deposited film. Changes to the Si–N peaks in the silicon K- and $L_{3,2}$-edge spectra once again reflect structural changes in the nitride matrix. At the silicon $L_{3,2}$-edge, the details of Si–Si bonding are also suppressed in these films until 1100°C where the nitride matrix breaks down.

Analysis at the silicon $L_{3,2}$-edge is hindered by substantial distortion of the TFY signal due to either saturation effects, which intensify as the film density increases with higher annealing temperatures, or augmentation of X-ray scattering resulting from voids formed within the film [151]. Preliminary results from positron annihilation

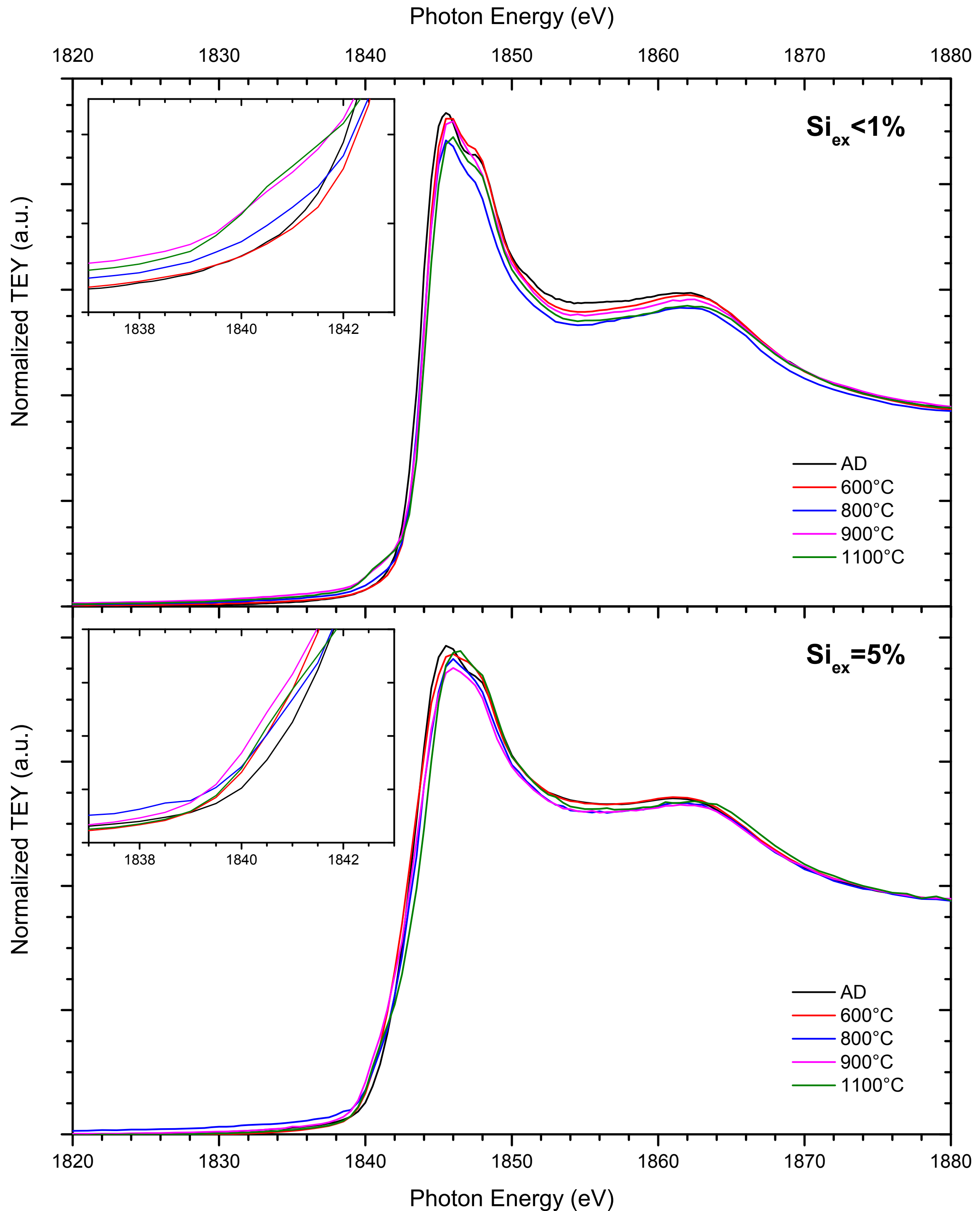

Figure 5.6: TEY-XANES spectra at the Si K-edge for low (Si_{ex}<1%) and high (Si_{ex}=5%) excess silicon content films deposited by the ICP CVD system and annealed in a quartz tube furnace under 5% H_2 in N_2 ambient gas. The insets included with each plot show a magnified view of the Si–Si absorption edge. A Si–Si resonance shoulder becomes visible at temperatures as low as 900°C in the low Si content film and 600°C in the high Si content film. After [41].

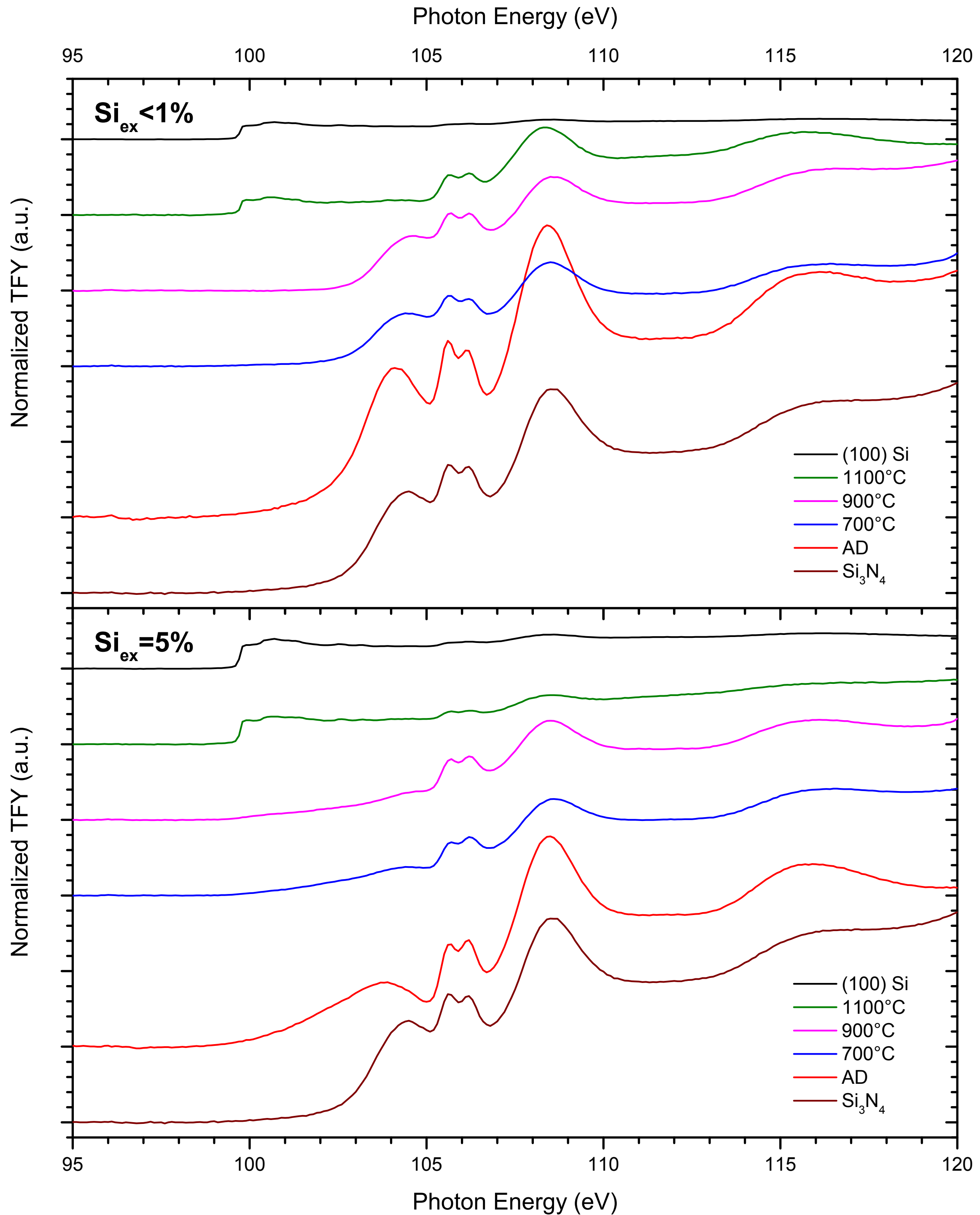

Figure 5.7: TFY-XANES spectra at the Si $L_{3,2}$-edge for low (Si_{ex}<1%) and high (Si_{ex}=5%) excess silicon content films deposited by the ICP CVD system and annealed in a quartz tube furnace under flowing 5% H_2 in N_2 gas. For clarity, the spectra are offset in the order they are listed in the legend and the (100) Si spectra are normalized to the Si–Si absorption edge step in the 1100°C spectra for better comparison. After [41].

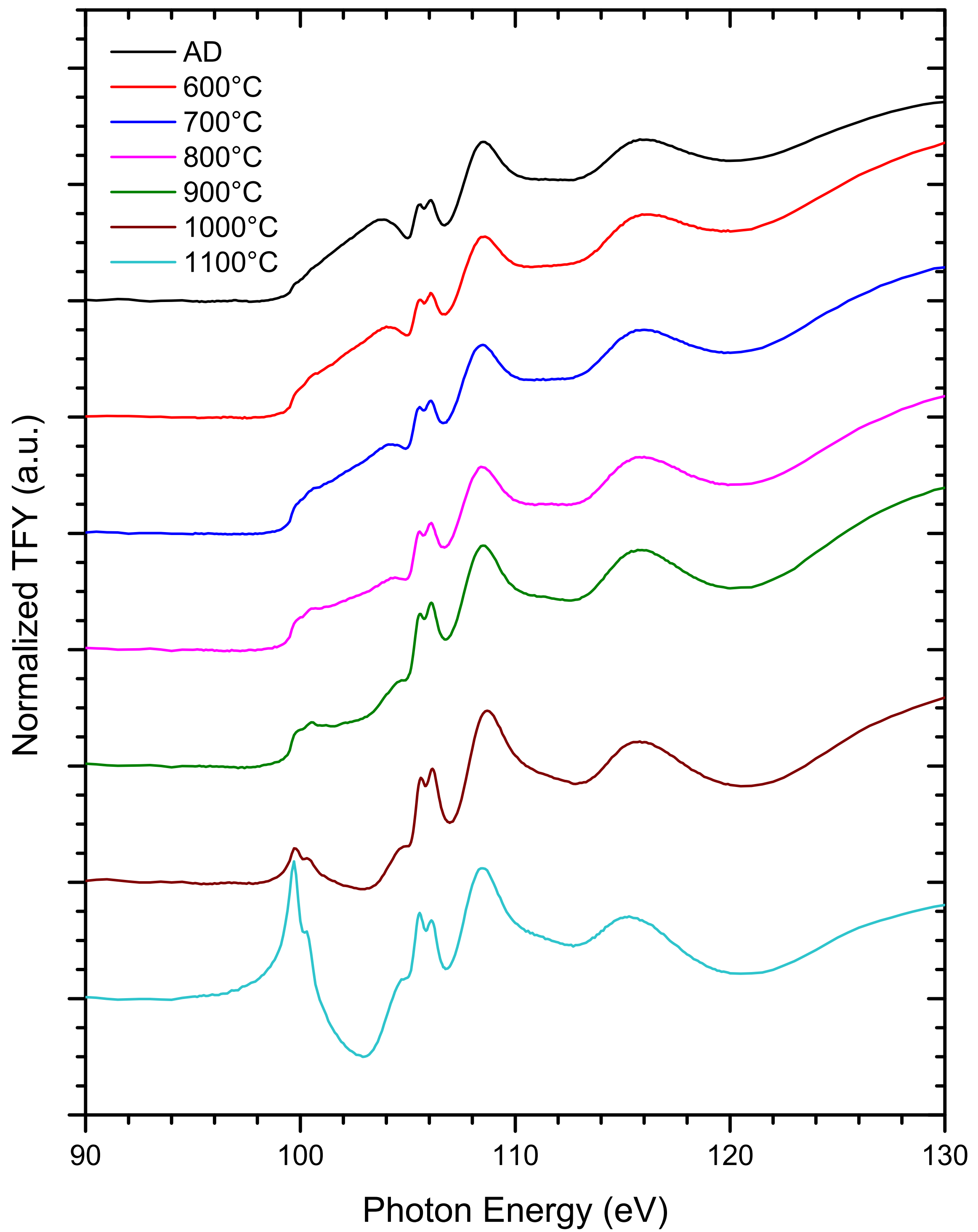

Figure 5.8: TFY-XANES spectra at the Si $L_{3,2}$-edge for a high excess silicon content PECVD film (Si_{ex}=6%) annealed in a quartz tube furnace under N_2 ambient gas. For clarity, the spectra are offset in the order they are listed in the legend. After [41].

spectroscopy experiments suggest that void formation is at least partially responsible for the distortion observed, but it remains to be established as a full investigation of this effect is still underway. The distortion is most prominent in high excess silicon content films deposited by the PECVD system, although it is observed to some degree in all of the SRSN films measured at the Si $L_{3,2}$-edge. An example of this effect is shown in Figure 5.8. As the annealing temperature is increased, a dip grows in the TFY at energies between the Si–Si absorption edge and the higher energy side of the Si–N resonance peak. A full account of this effect is a non-trivial challenge yet to be corrected for this data, but is certainly necessary to gain accurate and specific information on the changes in the silicon nitride host matrix.

5.3 Isothermal Annealing at 600°C

As described previously, in the case of isochronal annealing for 60 minutes in a quartz tube furnace, the PL of SRSN films with moderate-to-high excess silicon content tends to shift towards lower energies as the annealing temperature increases. Such a shift is in agreement with theory for quantum confinement effects corresponding to the growth of Si-ncs where the bandgap energy is proportional to the inverse square of the nanocluster diameter. Figure 5.9 shows the PL spectra for a film with 3% excess Si content annealed at 600°C for time intervals ranging from a mere 2 s to 2 h. In this figure, the annealed PL spectra were renormalized to have the same peak height to aid in comparing changes in emission energies while the AD spectra was renormalized to maintain its relative intensity compared to the 2 s anneal. Each spectrum consisted of a main peak that shifted to lower energies as the annealing time increased, and a higher energy shoulder that was most prominent in the AD film, which diminished as the annealing time increased. There was an abrupt red-shift in peak emission energy from 2.58 eV in the AD film to 2.13 eV after only 2 s of annealing along with

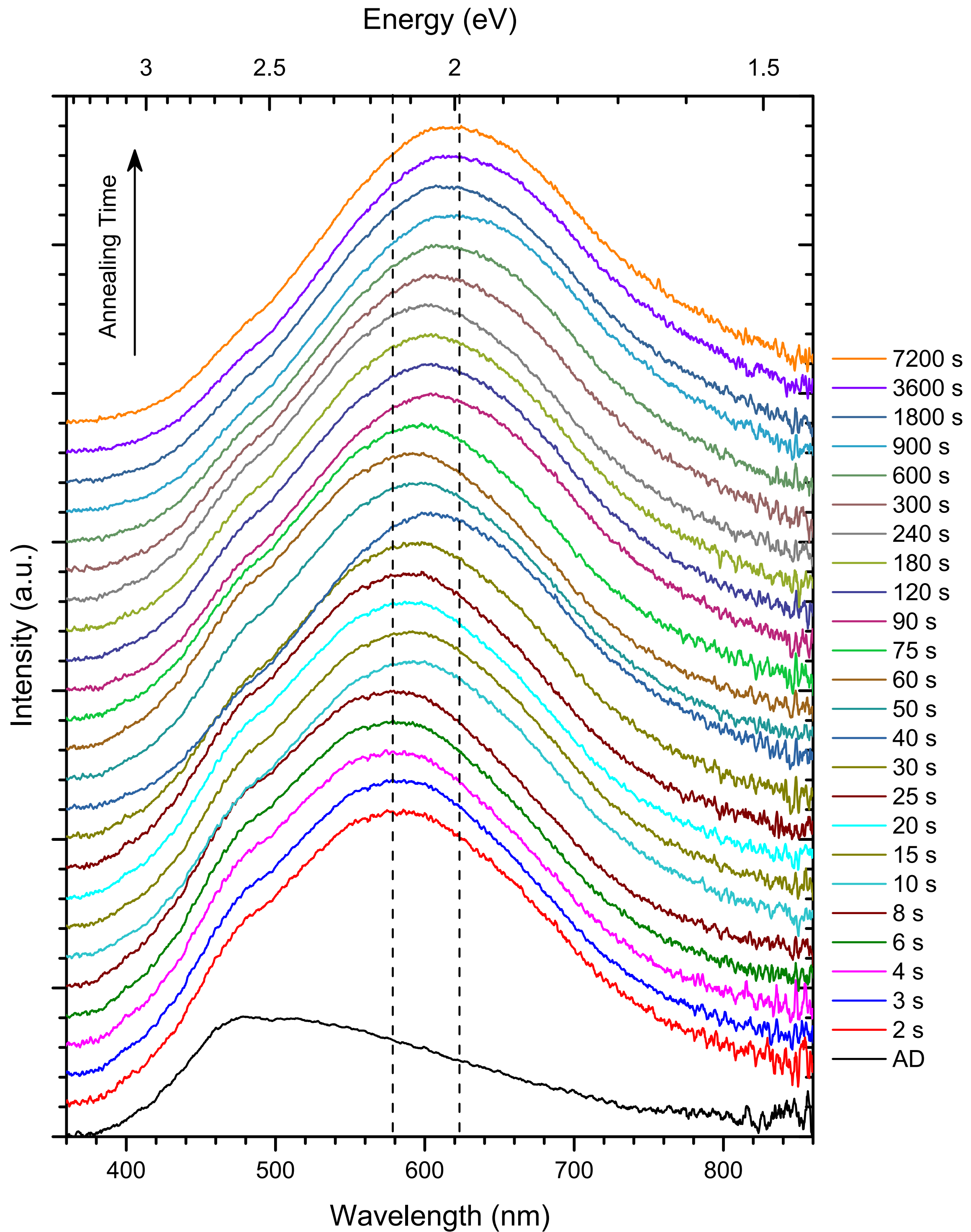

Figure 5.9: PL spectra for films with Si_{ex}=3% annealed at 600°C. The annealed spectra are renormalized to have equal peak heights and offset in order of annealing time as listed in the legend to clearly show the shifting in peak PL energy that occurred with annealing. Dashed lines mark the lowest and highest energies observed for the shifting peak. After [41].

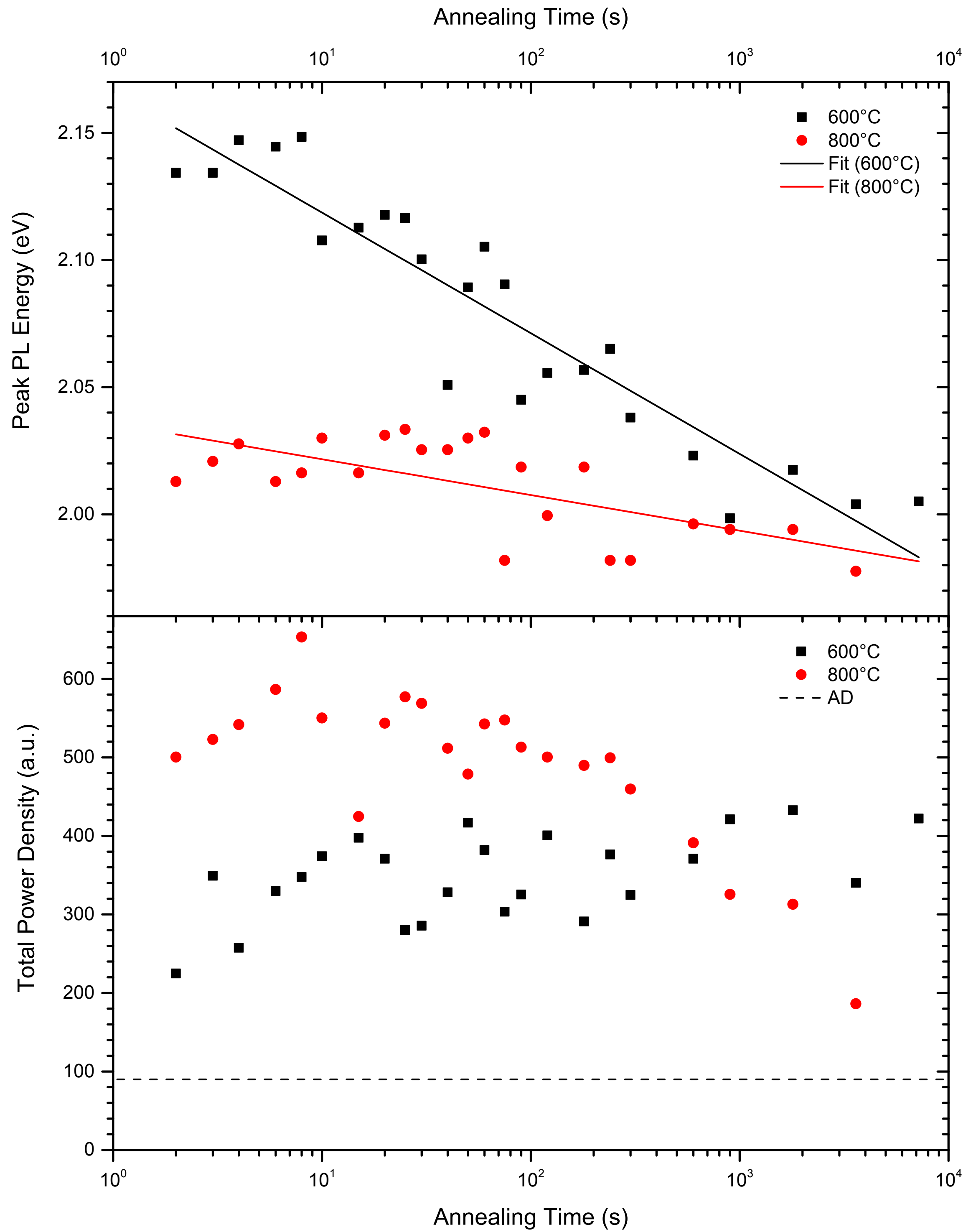

Figure 5.10: Peak PL energy and total power density for films with Si_{ex}=3% annealed at 600 and 800°C. After [41].

a large increase in intensity. As the annealing time was increased further, the PL peak continued to shift towards lower energies, but these changes were relatively small compared to the initial shift. This indicates that Si-ncs form and begin to grow very rapidly through a transient diffusion of excess silicon.

The peak emission energies of the annealed spectra are shown on a semi-log plot in Figure 5.10a. The peak PL energy was determined by applying a Savitzky-Golay smoothing filter [142] to remove the effects of noise without distorting the shape of the spectra and locating the energy at which the peak PL intensity occurred. There is a clear and steady shift from approximately 2.15 eV for the very short anneals towards 2.00 eV for annealing times approaching 2 h in length. The trend is characterized in the diagram by a logarithmic fit of the data points. The high energy shoulder in the PL spectra can be attributed to one of the silicon nitride inter-bandgap defect levels [74], which was annealed out as the length of annealing time increased. Figure 5.10b shows a semi-log plot of the total power density of the annealed films as a function of annealing time with a dashed line representing the total power density of the AD film. Annealing caused a sharp increase in the PL intensity even at the shortest annealing times. Following this sudden increase, the total power density for the 600℃ anneals continued to improve as the annealing time increased up to 2 h, albeit at a much slower rate.

XANES measurements provided insight on the structural ordering of the Si-ncs and the silicon nitride host matrix. Several spectra measured at the Si K- and $L_{3,2}$-edges are shown in Figures 5.11 and 5.12, respectively. At the Si K-edge, a gradual increase in Si–Si bonding was observed in a 3% excess Si content film with increasing annealing time corresponding to larger Si-ncs and increased phase separation. Also, there was a large increase in the Si–Si bonding resonance over the AD spectrum even at very short annealing times. Large restructuring of the silicon nitride host matrix was also

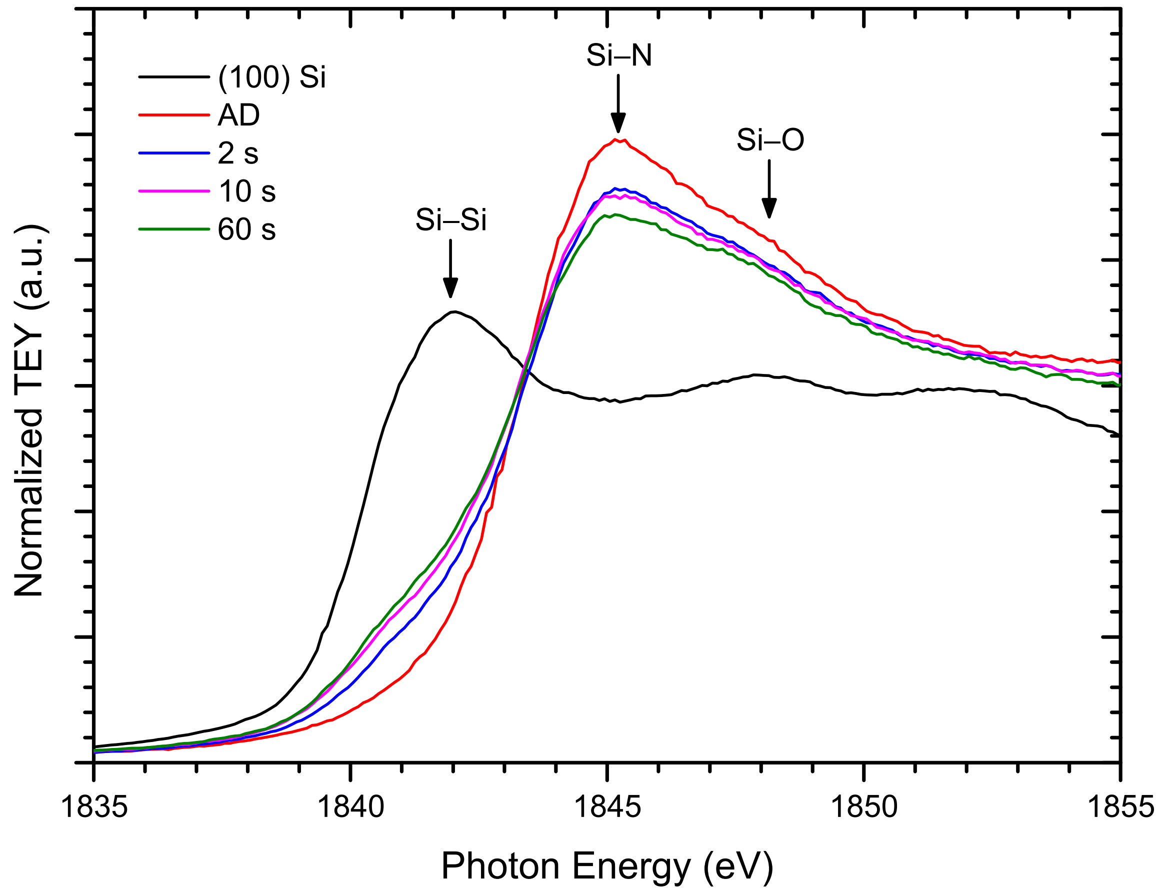

Figure 5.11: TEY-XANES spectra at the Si K-edge for a film with Si_{ex}=2% annealed for different times at 600℃. After [41].

observed on the same time scale as evidenced by the significant changes in the Si–N bonding resonance over the course of annealing. Similar changes were obtained at the Si $L_{3,2}$-edge for a film with 2% excess Si content, where the Si–Si absorption edge becomes very large after the 60 s anneal and significant changes in both the peak energy and the magnitude of the Si–N resonance are observed over the timescale studied. Combined with the large changes observed in the PL spectra for annealing times on the order of seconds, these results suggest that Si-ncs form much more rapidly than has been conventionally believed and it is likely the result of a fast transient diffusion mechanism for excess silicon in a silicon nitride film.

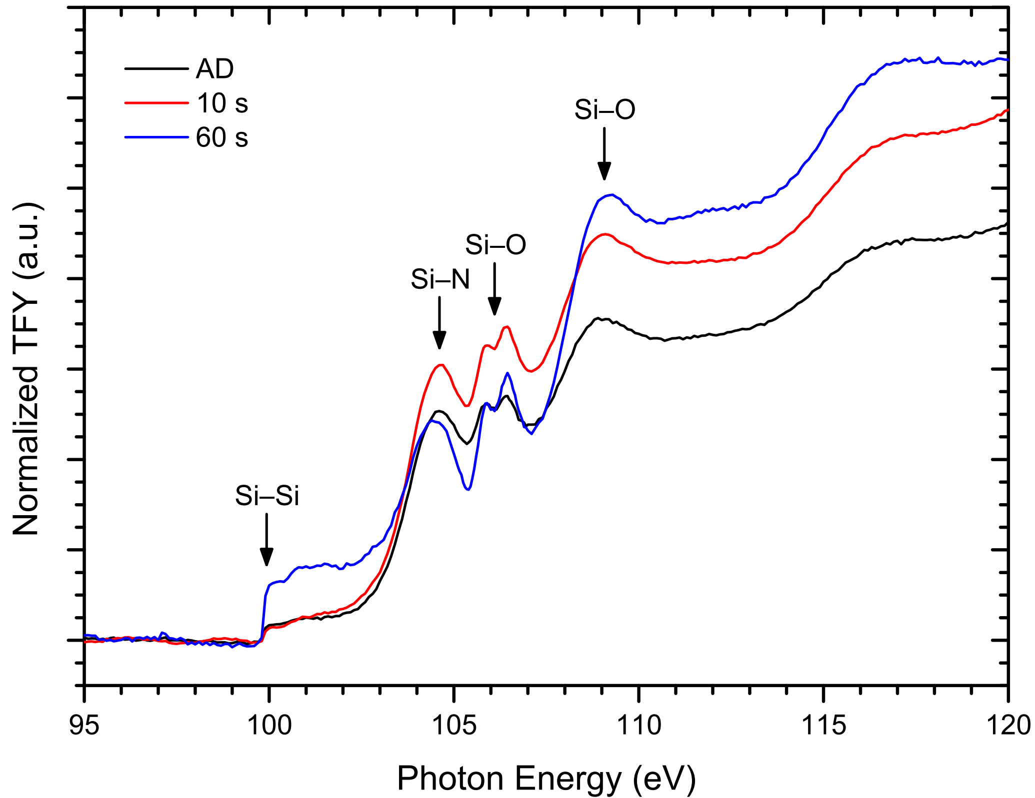

Figure 5.12: TFY-XANES spectra at the Si $L_{3,2}$-edge for a film with Si_{ex}=3% annealed for different times at 600°C. After [41].

5.4 Isothermal Annealing at 800°C

The PL spectra for the film with 3% excess silicon content annealed at 800°C exhibited the same features as those of the 600°C annealed films as can be seen in Figure 5.13. As in Figure 5.9, the annealed spectra have been renormalized so that they have the same peak intensity while the AD spectrum has been renormalized so that it maintained its relative intensity with the 2 s anneal. In this case, the AD peak appears smaller than in Figure 5.9 due to the relatively large PL intensity of the 2-s-annealed film at 800°C compared with its 600°C counterpart. At 800°C, there was still a main peak that red-shifted with longer annealing times and a high energy shoulder that was less pronounced than at the lower temperature and nearly disappeared at the longer annealing times. The peak PL energy is plotted in Figure 5.10a, which illustrates

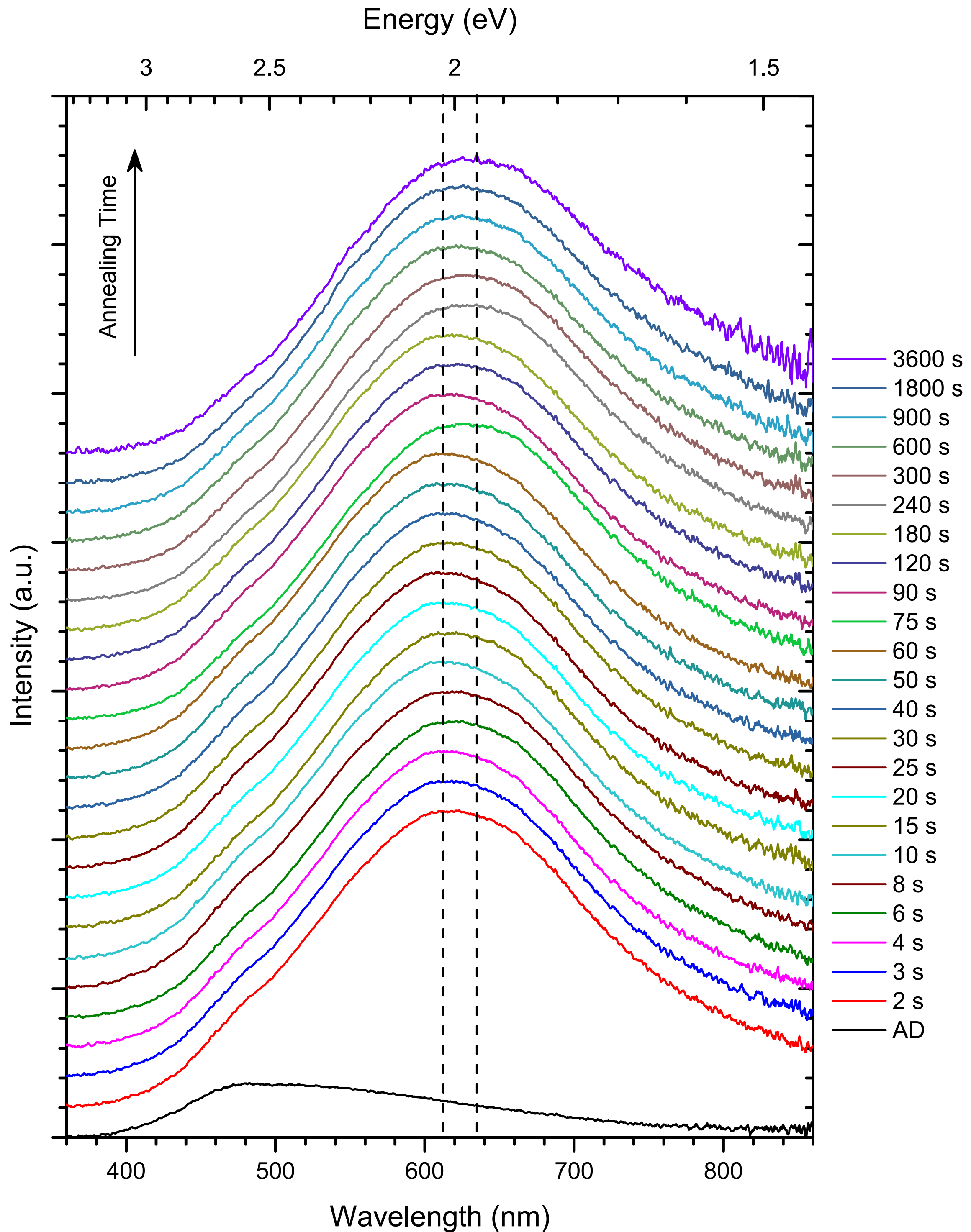

Figure 5.13: PL spectra for Si_{ex}=3% films annealed at 800°C. The annealed spectra are renormalized to have equal peak heights and offset in order of annealing time as listed in the legend to clearly show the shifting in peak PL energy that occurred with annealing. Dashed lines mark the lowest and highest energies observed for the shifting peak. After [41].

that the initial abrupt energy shift upon annealing is much larger than for the 600℃ anneals and even exceeds the shift observed for all but the longest anneals measured at this temperature. However, for longer anneals, the peak PL energy shifted at a much slower rate than at 600℃. This was likely due to the reduction of excess silicon in the film within close proximity of a Si-nc that has not already been incorporated into the structure and the larger number of additional Si atoms required for continuing to increase the diameter of a Si-nc as it grows. The total power density profile shown in Figure 5.10b shows some interesting differences to those observed after the 600℃ anneal. At 800℃, there was a very large increase in the emission intensity after just 2 s of annealing, which also far exceeded the total power densities measured for any of the 600℃ anneals. While an overall increase in total power density was observed at 600℃ over the range of annealing times studied, an intensity peak was observed between 6 and 30 s at the higher temperature, followed by a steady decline, eventually dropping below the 600℃ value at the 900 s mark. This decline may indicate Ostwald ripening or structural changes in the silicon nitride host matrix.

The occurrence of Ostwald ripening and silicon nitride structural reordering are further evidenced by the Si K-edge XANES spectra for the 2% excess Si content film shown in Figure 5.14. These spectra exhibit a large increase in the Si–Si resonance after just 2 s of annealing but no noticeable change as the annealing time is extended, suggesting that further increases in Si-nc size are due to larger nanoclusters growing at the expense of smaller ones. At the same time, large changes were observed in the Si–N resonance, which include a significant increase between the 10 and 60 s anneals.

It is probable that the decay in PL intensity observed for longer anneals at 800℃ will occur after annealing for a minimum time at higher temperatures as well. If this assumption is true and the onset of decay occurs at earlier times as the temperature is increased, then this phenomenon may be linked to the decrease in PL intensity observed

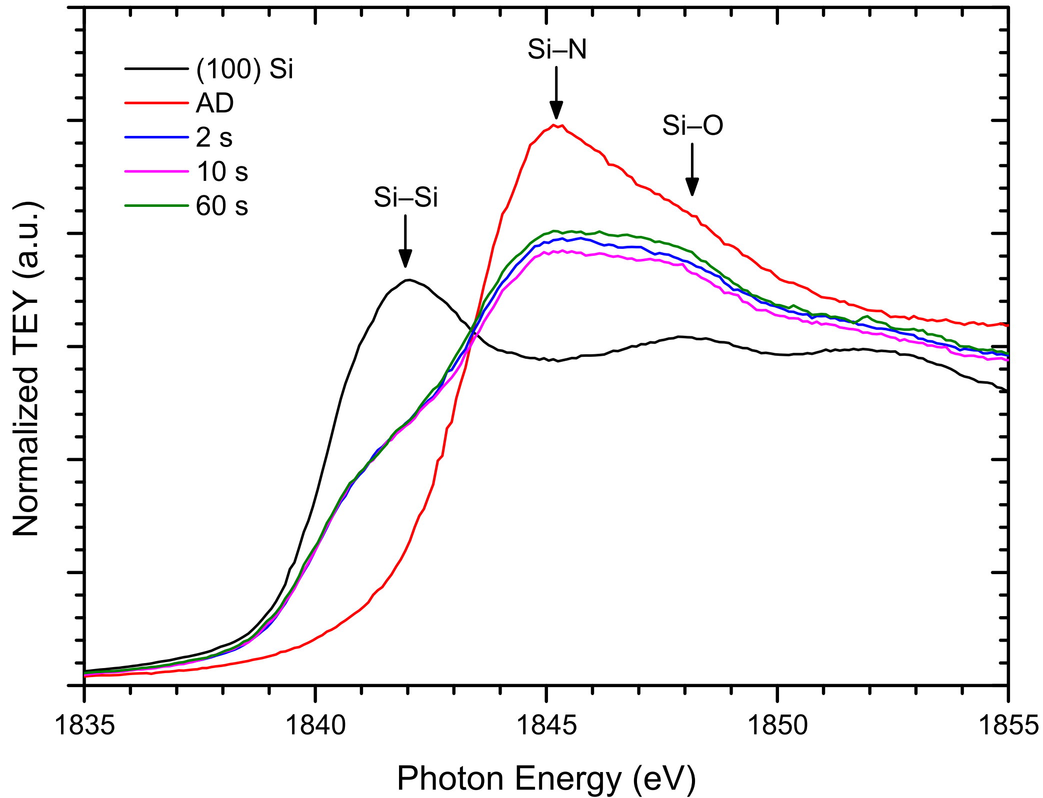

Figure 5.14: TEY-XANES spectra at the Si K-edge for a film with Si_{ex}=2% annealed for different times at 800°C. After [41].

in SRSN films annealed for 60 minutes in a quartz tube furnace at temperatures above 700 or 800°C. Incidentally, as was shown in Figure 5.10b, the 60 minute mark resides in the time interval where the 800°C annealed films became less intense than the 600°C annealed films.

5.5 Cerium Doped Silicon-Rich Silicon Nitride

After characterizing the luminescent and structural properties of the silicon-rich silicon nitride materials system, an attempt was made to sensitize Ce^{3+} ions using the silicon nanoclusters formed within in order to gauge the viability of the medium for rare earth doping applications. Cerium was chosen as a test dopant since out of the visibly luminescent lanthanides, it has a relatively large absorption cross-section which was

expected to allow for more tolerance in the silicon nanocluster bandgap energies required for sensitization.

However, as exemplified in the PL spectra of a cerium doped SRSN film that had 1% excess silicon content and 0.6 at.% cerium shown in Figure 5.15, the sample exhibited photoluminescence which was characteristic of silicon nanoclusters rather than Ce^{3+} ions. As in the undoped films, the emission peak was broad and shifted to lower energies as the annealing temperature was increased. Furthermore, the most intense emission was observed in the as-deposited and lower annealing temperature samples and the photoluminescence decayed as the annealing temperature was raised.

TEY- and TFY-XANES spectra at the Ce $M_{5,4}$-edge provided a means of analyzing the cerium incorporation at the surface and in the bulk of the films, allowing the oxidation state of the ions to be probed. As shown in Figure 5.16, the results of this analysis confirm that the cerium ions were coordinated in the desired Ce^{3+} configuration in the near-surface region as well as in the bulk of the as-deposited film and across the full annealing temperature range studied. This indicates that the reason fo the lack of cerium-related photoluminescence was not due to an unfavourable cerium oxidation state and it was either due to a lack of silicon nanoclusters with proper bandgap energies required to sensitize the cerium ions or an issue with the specific bonding of the cerium ions in the silicon nitride host matrix rendering the ions optically inactive.

At the time the study was performed, the latter explanation seemed the most likely for two main reasons. First, XEOL measurements collected simultaneously with the XANES spectra did not reveal any luminescence when excited at any soft X-ray energy, including those resonant with the Ce^{3+} ions. This was unusual based on similar work performed on silicon oxide films as will be discussed in more detail in Chapter 6. Secondly, in related work by J. Anstey [152] and R. M. Savidge [153] on cerium doped

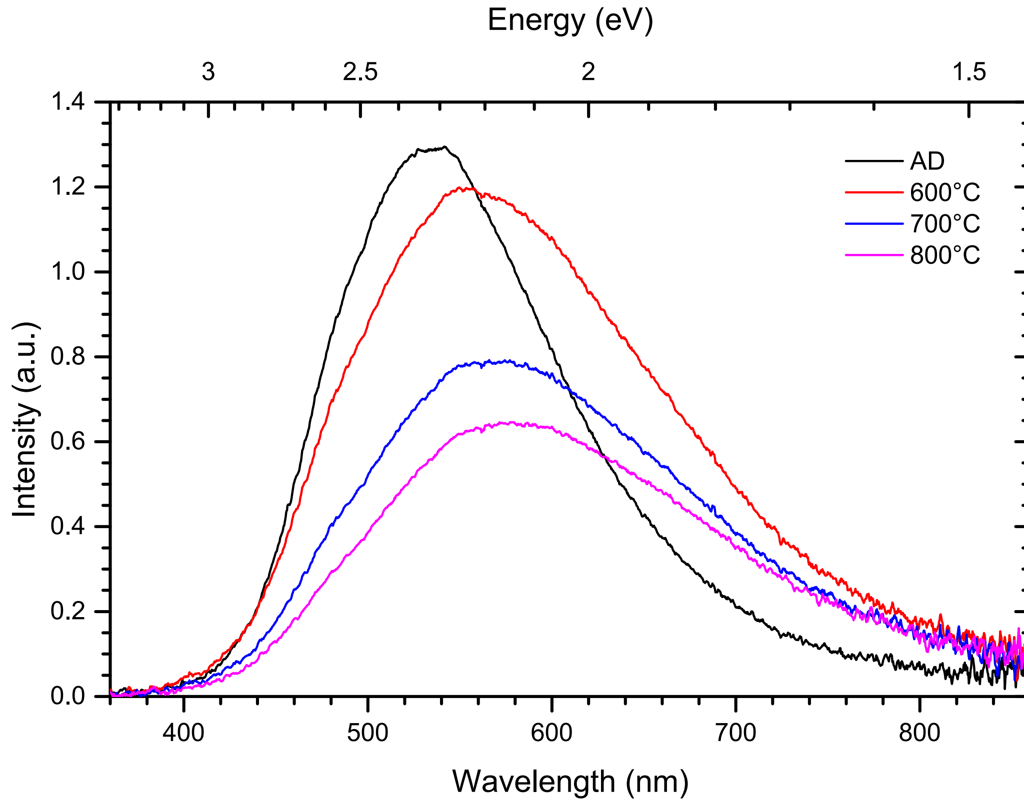

Figure 5.15: PL spectra for a cerium doped SRSN film with Si_{ex}=1% and 0.6 at.% cerium annealed for 60 minutes in a quartz tube furnace under 5% H_2 in N_2 ambient gas.

silicon nitride samples produced through ion implantation, it was found that cerium was only luminescent when incorporated in a silicon nitride host matrix if the layer contained some level of oxygen. Based on these findings, silicon-rich silicon nitride does not appear to provide a good environment for rare earth dopants in and of itself, but still holds promise in the context of silicon oxynitride films. However, several other research groups have reported the sensitization of rare earth dopants in silicon nitride [80–84]. Unless the silicon nitrides used in those studies were contaminated with oxygen, it would suggest that the issue of sensitizing the Ce^{3+} ions encountered in the SRSN films studied could potentially be addressed through optimizing the dimensions of the silicon nanoclusters, which likely need to be very small to have the appropriate bandgap energy for exciting visibly luminescent lanthanides.

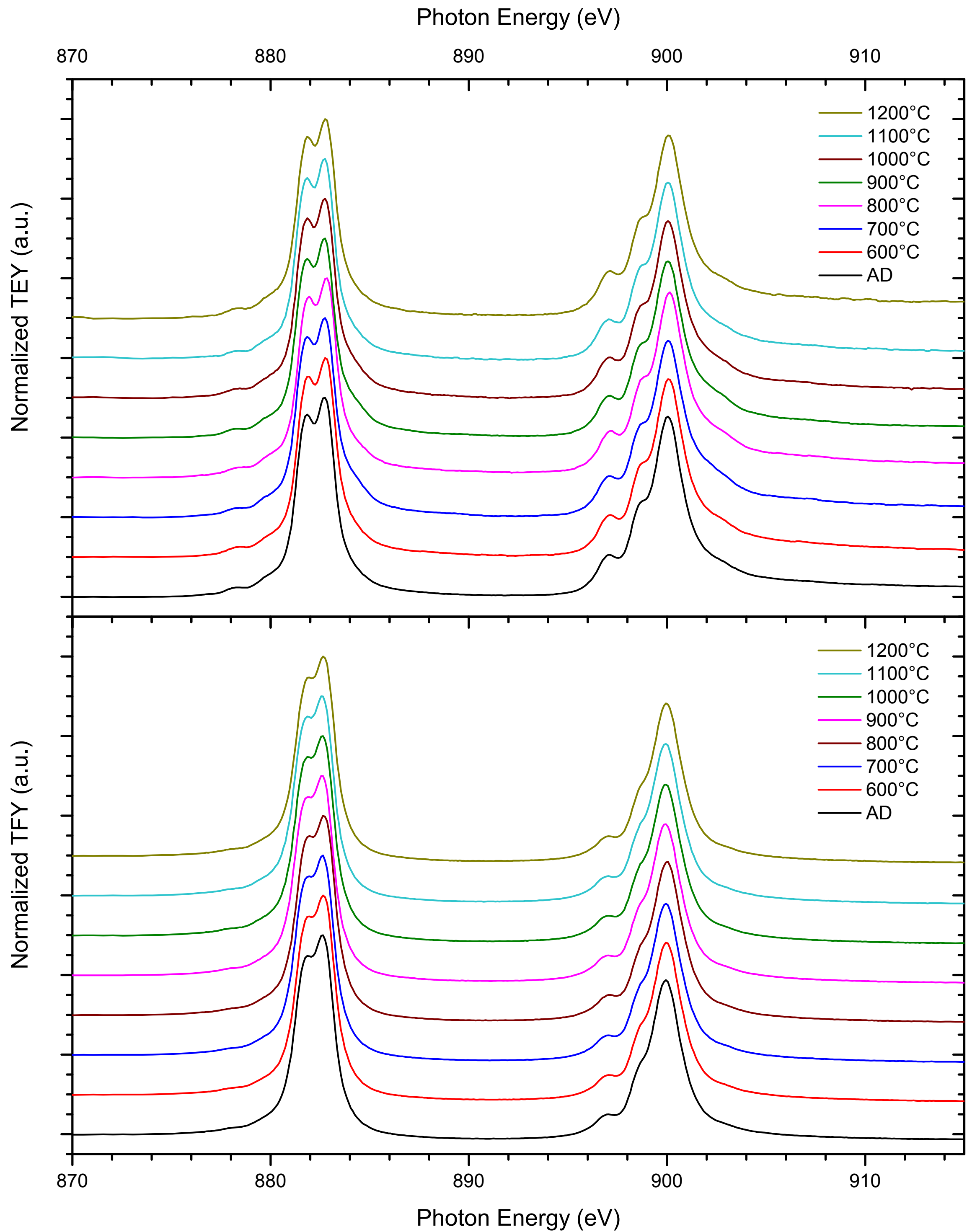

Figure 5.16: TEY- and TFY-XANES spectra at the Ce $M_{5,4}$-edge for a cerium doped SRSN film with Si_{ex}=1% and 0.6 at.% cerium annealed for 60 minutes in a quartz tube furnace under 5% H_2 in N_2 ambient gas.

Chapter 6

Study of Cerium and Terbium Doped Silicon Oxide Thin Films

The investigation of cerium and terbium doped silicon oxide films began as a follow-up to an interesting result obtained by former group member J. Li as part of her M.A.Sc. thesis project [36]. In this work, it was found that cerium disilicate nanocrystallites formed in so-called cerium doped oxygen-rich silicon oxide (ORSO) films after annealing at 1200℃, resulting in a bright blue emission which exceeded the PL intensity from Ce^{3+} ions coordinated in the silicon oxide host matrix at lower annealing temperatures. Moreover, HRTEM and XEDS analysis not only verified the presence of $Ce_2Si_2O_7$ nanocrystallites, but indicated that most if not all of the cerium in the layer had diffused into these nanostructures [37]. Having taken part in several of the experiments performed on these samples and considering that the PL from the $Ce_2Si_2O_7$ nanocrystallites likely did not originate from quantum confinement effects, I was intrigued by the possibility that this result could be expanded to convert larger portions of the cerium doped silicon oxide layer into cerium disilicate, which appeared to be a very promising photonic material for several reasons. First of all, the emission intensity from the $Ce_2Si_2O_7$ nanocrystallites was very strong, especially considering

the small size and low density of the nanostructures within the original films (*i.e.*, the layers were mostly SiO_2). Second, the $Ce_2Si_2O_7$ nanocrystallites seemed to provide a means of obtaining a high density of trivalent Ce ions in a region of film without the luminescence efficiency suffering from ion-ion interactions, which typically impose an upper limit on the optimal concentration of a rare earth dopant in silicon oxide films. Finally, as opposed to cerium ions incorporated in a silicon oxide host matrix, the bonding structure in the $Ce_2Si_2O_7$ lattice would ensure that all cerium ions in the nanocrystallites, with the possible exception of ions located at the surface, were optically active and emit at the same wavelength providing excellent colour rendition.

Revisiting this material system paid instant dividends as the initial set of films that were grown yielded exciting results that far exceeded all expectations and identified new possibilities in film structure. In fact, these initial results were so promising that what started as an interesting side project quickly became the primary focus of the remainder of my Ph.D. research. The intention was to gradually increase the cerium doping in ORSO films to determine how high of a volume fraction of cerium disilicate could be formed in the layer without reaching a solubility limit for cerium in the silicon oxide host matrix or increases in PL were mitigated by quenching due to ion-ion interactions or the cerium ions incorporating in competing phases. However, the first set of samples contained much higher cerium concentrations than anticipated and rather than forming small nanocrystallites of $Ce_2Si_2O_7$ within a silicon oxide host matrix, it was observed that more than half the layer could be converted into the cerium disilicate phase resulting in very intense PL which was over 100 times brighter than J. Li's original films. Accidental terbium contamination in these films also provided a surprising result in that despite very low concentrations of terbium being incorporated, the emission at Tb^{3+} wavelengths was even stronger than the luminescence originating from cerium disilicate.

6.1 Growth and Characterization of As-Deposited Films

Cerium and terbium co-doped silicon oxide films were initially deposited using the MAC ECR PECVD system with process gas flow rates of 1 sccm SiH_4/Ar and 19 sccm O_2/Ar, which resulted in a significant overpressure of oxygen in the chamber relative to the parameters typically used to produce SiO_2 films on this system (5 sccm SiH_4/Ar, 30 sccm O_2/Ar). The gas flow rates were chosen to provide similar growth conditions, as determined by partial pressure data, to those used by J. Li [36] to produce her so-called cerium doped oxygen-rich silicon oxide films. Additionally, it was thought that such conditions would promote the incorporation of high concentrations of cerium into the film since trivalent rare earth dopants in silicon oxide have a tendency to form bonds with oxygen atoms at octahedrally coordinated sites over silicon atoms [89], essentially allowing for the deposition of a metastable alloy of cerium oxide and silicon oxide. From this perspective, the low silane flow was also expected to keep the growth rate of silicon oxide low to enhance the cerium incorporation.

The first set of films, labelled CeORSO-01, CeORSO-02, and CeORSO-03 were grown by research associate E. Chelomentsev, who was the designated system operator at the time, using the parameters that I had specified. The deposition parameters for the samples grown using the MAC ECR PECVD system are included in Tables 6.1 and 6.2 along with their resulting compositions, thicknesses, refractive indices, and mass densities. The uncertainty in the atomic fractions for Si and O is ±1 at.% while the uncertainty is an order of magnitude lower at ±0.1 at.% for Ce and Tb since the lanthanides are much heavier elements. The pressure data is not listed for the first set of films as it, unfortunately, was not recorded (N/R). As the labelling implies, the original films were intended to be cerium doped oxygen-rich silicon oxide. However, as indicated by the compositional details, the films were in fact contaminated with low concentrations of terbium.

Table 6.1: MAC ECR PECVD system parameters and film properties

Sample Series		**CeORSO**							
Sample ID #		**01**	**02**	**03**	**23***	**24**	**25b†**	**25**	**26**
Gas Flow Rate (sccm)	SiH_4/Ar	1.0	1.0	1.0	1.0	1.0	1.0	1.0	1.0
	O_2/Ar	19.0	19.0	19.0	19.0	24.0	24.0	24.0	19.0
	RE/Ar	5.0	5.0	5.0	5.0	5.0	5.0	5.0	5.0
Gas Partial Pressure (mTorr)	SiH_4/Ar	N/R	N/R	N/R	0.10	0.09	0.09	0.09	0.10
	O_2/Ar	N/R	N/R	N/R	1.50	1.86	1.86	1.86	1.50
	RE/Ar	N/R	N/R	N/R	0.42	0.39	0.41	0.41	0.40
Chamber Pressure	Deposition (mTorr)	N/R	N/R	N/R	2.07	2.34	2.28	2.30	1.96
	Base (nTorr)	N/R	N/R	N/R	72	182	90	100	130
Temperature (°C)	Ce Cell	200	205	210	210	210	210	210	215
	Tb Cell	0	0	0	0	0	0	0	0
	RE Lines	210	210	210	220	220	220	220	220
	RE Ring	210	210	210	220	220	220	220	220
	Stage Heater	300	300	300	300	300	300	300	300
Power (W)	Discharge	500	500	500	503	502	503	503	504
	Reflected	N/R	N/R	N/R	3	2	3	3	4
Time (min.)	Deposition	60	60	60	60	60	60	60	136
Atomic Fraction (at.%)	Si	23.3	22.5	20.4	22.4	23.6	28.6	28.8	30.1
	O	67.6	66.7	67.9	66.9	68.9	65.8	67.8	67.1
	Ce	8.9	10.7	11.6	9.1	6.9	5.3	3.4	2.6
	Tb	0.2	0.2	0.1	1.5	0.6	0.3	0.1	0.1
Physical Properties	RBS Thickness (10^{15} at./cm^2)	2027	1595	1710	1790	1626	1087	1106	2556
	Opt. Thick. (Å)	2470	1910	2013	5008	2304	1597	1661	3777
	Density (g/cm^3)	3.68	3.55	3.69	1.91	3.30	2.98	2.63	2.61
	n @ 632.8 nm	1.67	1.71	1.74	1.62	1.62	1.59	1.55	1.51

* RBS analysis indicated approximately 30 at.% carbon contamination in the as-deposited CeORSO-23 film.
† Sample CeORSO-25b was grown before CeORSO-25 but with the sample stage accidentally positioned 1–2 inches below the typical height used for deposition. However, the film ended up being a high quality sample despite this peculiarity.

Table 6.2: MAC ECR PECVD system parameters and film properties (continued)

Sample Series		**CeORSO**			**CeTbORSO**			**CeSiO2**	
Sample ID #		**27**	**28**	**29**	**01**	**02**	**03**	**01**	**02**
Gas Flow Rate (sccm)	SiH_4/Ar	1.0	1.0	1.0	1.0	1.0	1.0	2.5	2.5
	O_2/Ar	20.0	20.0	20.0	19.0	19.0	19.0	12.0	15.0
	RE/Ar	5.0	10.0	10.0	5.0	5.0	5.0	4.0	5.0
Gas Partial Pressure (mTorr)	SiH_4/Ar	0.10	0.09	0.10	N/R	N/R	N/R	0.22	0.22
	O_2/Ar	1.52	1.55	1.53	N/R	N/R	N/R	1.08	1.17
	RE/Ar	0.36	0.70	0.70	N/R	N/R	N/R	0.70	0.37
Chamber Pressure	Deposition (mTorr)	1.99	2.31	2.34	2.25	2.25	2.25	1.60	1.70
	Base (nTorr)	600	400	350	3000	3000	3000	120	400
Temperature (℃)	Ce Cell	210	210	210	210	210	210	160	150
	Tb Cell	0	0	0	160	170	180	0	0
	RE Lines	220	220	220	210	210	210	200	200
	RE Ring	220	220	220	210	210	210	180	200
	Stage Heater	350	350	350	300	300	300	350	350
Power (W)	Discharge	504	504	504	508	508	508	515	509
	Reflected	4	4	4	4	4	3	15	9
Time (min.)	Deposition	60	60	90	60	60	50	60	60
Atomic Fraction (at.%)	Si	25.9	32.1	29.9	24.7	28.0	23.7	33.5	32.7
	O	65.9	66.4	66.9	67.9	64.0	67.3	66.4	67.2
	Ce	7.9	1.2	2.7	3.1	2.6	2.9	<0.1	<0.1
	Tb	0.3	0.3	0.5	4.2	5.4	6.2	<0.1	<0.1
Physical Properties	RBS Thickness (10^{15} at./cm^2)	2202	1123	1859	1266	1304	1355	2588	2787
	Opt. Thick. (Å)	3326	1585	2709	1750	1789	1825	3853	3997
	Density (g/cm^3)	3.23	2.57	2.70	3.48	3.67	3.86	2.27	2.33
	n @ 632.8 nm	1.63	1.51	1.55	1.61	1.62	1.68	1.49	1.51

Table 6.3: GIV ECR PECVD system parameters and film properties

Sample Series		**CeSiOx**							
Sample ID #		**01***	**02**	**03**	**04**	**05**	**06**	**07**	**08**
Gas Flow Rate (sccm)	SiH_4/Ar	1.0	2.0	5.0	2.5	5.0	2.5	5.0	2.5
	O_2/Ar	20.0	20.0	30.0	30.0	30.0	30.0	30.0	30.0
	Ce/Ar	5.0	5.0	5.0	5.0	5.0	5.0	5.0	10.0
Gas Partial Pressure (mTorr)	SiH_4/Ar	0.08	0.22	0.58	0.30	0.55	0.28	0.56	0.29
	O_2/Ar	2.12	2.13	3.03	3.03	2.97	3.02	3.04	3.04
	Ce/Ar	0.57	0.54	0.48	0.53	0.51	0.54	0.43	0.98
Chamber Pressure	Deposition (mTorr)	2.70	2.70	3.60	3.48	3.32	3.64	3.70	4.10
	Base (nTorr)	6000	400	200	80	200	500	400	300
Temperature (℃)	Ce Jacket	210	218	209	209	220	220	171	226
	Ce Cell	215	222	215	212	224	224	175	229
	RE Lines	250	235	235	235	235	235	250	250
	RE Showerhead	235	235	235	235	235	235	235	236
	Stage Heater	350	350	350	350	350	350	350	350
Power (W)	Discharge	501	501	501	501	501	501	501	501
	Reflected	1	1	1	1	1	1	1	1
Time (min.)	Deposition	60	60	60	60	60	120	60	120
Atomic Fraction (at.%)	Si	11.0	19.2	28.7	27.9	26.2	22.4	32.1	19.2
	O	70.8	66.0	68.4	67.7	68.8	67.4	67.5	68.9
	Ce	18.2	14.8	2.9	4.4	5.1	10.1	0.4	11.9
	Tb	<0.1	<0.1	<0.1	<0.1	<0.1	<0.1	<0.1	<0.1
Physical Properties	RBS Thickness (10^{15} at./cm^2)	2254	1370	1473	782	1597	2068	1297	2430
	Opt. Thick. (Å)	3442	1393	2189	1195	2456	3197	1961	4015
	Density (g/cm^3)	2.28	3.48	2.58	2.69	2.75	3.37	2.24	3.33
	n @ 632.8 nm	1.67	1.72	1.50	1.52	1.51	1.64	1.49	1.68

* RBS analysis indicated approximately 60 at.% carbon contamination in the as-deposited CeSiOx-01 film.

The precise origins of this contamination were never determined, but it was suspected that it must have been related to residual terbium in the chamber or, perhaps more likely, in the rare earth lines and dispersion ring, or even the cerium cell. Whatever the source, the presence of terbium combined with the oxygen-heavy growth conditions seemed to promote the incorporation of low to moderate levels of terbium as a co-dopant in all films of this variety deposited by this system. Despite numerous attempts to overcome or suppress this issue including thoroughly cleaning the chamber, coating the chamber walls with amorphous silicon prior to deposition, and even replacing the section of rare earth lines common to dopants from all three cells in the rare earth manifold, none were found to significantly reduce or prevent the incorporation of terbium in these films, although it did seem to slowly diminish with more growths after the last "intentional" terbium deposition. Since the vapour pressure produced through sublimation of the $Tb[tmhd]_3$ precursor exceeds that of $Ce[tmhd]_4$ for a given temperature [154, 155], at the high temperatures being applied, it would not take much of the contaminating precursor material for significant terbium incorporation to occur, which would explain the difficulties encountered in preventing contamination. Thankfully, rather than being detrimental, the terbium co-doping provided very interesting results in that strongly enhanced green emission corresponding to Tb^{3+} ions was observed after high temperature annealing. As a result, the original project was expanded to include the effects of terbium co-doping while also studying the formation and growth of cerium disilicate.

Samples grown with the terbium cell heated resulting in much higher terbium concentrations were labelled with the prefix "CeTbORSO" to distinguish them from the "CeORSO" samples. Likewise, two samples were given the prefix "CeSiO2" to reflect the fact that they were grown without the overpressure of oxygen in order to provide reference samples with compositions close to SiO_2. Note that the CeTbORSO

depositions were also performed by E. Chelomentsev and while chamber pressures were recorded, the partial pressures were not.

To obtain a set of cerium doped silicon oxide films without terbium co-doping, samples were later grown using the GIV ECR PECVD system, which was a recently commissioned system that had not been exposed to any terbium precursor. The films deposited by this system were all given the prefix "CeSiOx" to distinguish them from the samples produced using the MAC ECR PECVD system. Details of the deposition parameters, compositions, and physical properties for samples grown on this system are listed in Table 6.3. Notably, samples 03, 05, and 07 were grown using a standard SiO_2 recipe while the other depositions were performed with an overpressure of oxygen. Despite the move to an isolated system, even these films contained trace levels of terbium, although often at concentrations below the sensitivity limit of RBS, yet still evident in their emission spectra. The source of contamination in this case must have been from the metal organic powder that was used as a precursor, either through impurity of the purchased material or introduced through contamination when loading the cell. While the terbium emission was still visible in these spectra, the concentration was low enough that the experimental results related to cerium disilicate formation and emission could be considered to be minimally affected by the terbium ions.

The film compositions specified in Tables 6.1 to 6.3 show the relative atomic fractions of silicon, oxygen, cerium, and terbium only. There is also likely a significant concentration of hydrogen in the films due to the use of SiH_4 process gas. RBS analysis, however, is not sensitive to this element. Trace concentrations of Ar were also measured, but as a noble gas atom, it would be incorporated in the films as a trapped interstitial which should not significantly influence the host matrix bonding structure and was found to mostly out-gas upon annealing. Samples CeORSO-23 and CeSiOx-01 were unusual in that they also contained high levels of carbon originating

from the rare earth precursor, whereas carbon was not detected in any of the other films. The source of carbon in the CeSiOx-01 film was most likely a consequence of the partial pressure of silane being too low [114] and no further carbon contamination was observed after this was rectified. The presence of carbon in CeORSO-23 was more of an anomaly, but was likely related to it being the first film grown after system maintenance was performed including recharging of the cerium cell. In both cases, the carbon was found to segregate out of the silicon oxide matrix upon annealing leaving a layer of cerium and terbium co-doped SiO_x at the film surface which had luminescence properties comparable to the other films. For this reason, these samples were not excluded from the study despite the carbon irregularity in the as-deposited film. In fact, after the carbon segregated out of the silicon oxide layer upon annealing, the cerium concentration tended to be especially high since most if not all of the rare earth dopant remained in the silicon oxide matrix. The CeSiOx-01 sample provided an especially useful cerium disilicate reference sample since there was enough dopant to convert nearly the entire layer to this structure as will be discussed later.

Trends related to the cerium incorporation as a function of cell temperature are shown in Figure 6.1 for films grown by the GIV ECR PECVD system. Here, samples deposited using an overpressure of oxygen are separated from those deposited under the regular conditions used for SiO_2 films. Unlike the values listed in Table 6.3, the cerium atomic fraction in this plot is with respect to all elements in the film except for hydrogen (*i.e.*, it includes Si, O, Ce, Tb, C, and Ar values). For both sets of depositions, the cerium incorporation increases exponentially with the cerium cell temperature as indicated by the trendlines, which was expected since the vapour pressure of a β-diketonate precursor, such as $Ce[tmhd]_4$ or $Tb[tmhd]_3$, has an exponential relationship with temperature [154]. Most surprising was the fact that the CeSiOx-08 sample also fit this trend despite having been grown using a higher Ar carrier gas flow rate

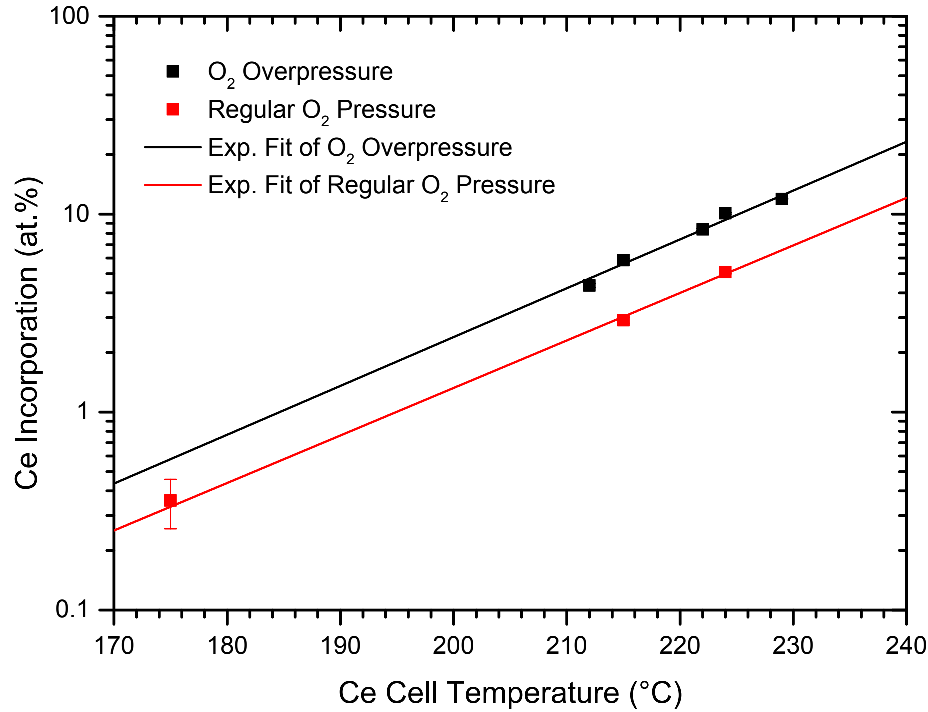

Figure 6.1: Cerium incorporation in silicon oxide films grown using the GIV ECR PECVD system with different cell temperatures.

for introducing the Ce ions into the chamber since raising this parameter typically augments the rare earth incorporation.

The use of an overpressure of oxygen can be seen to effectively double the cerium incorporation causing an upwards shift in the otherwise similar trendline and allowing for much higher doping concentrations to be achieved at reasonable cell temperatures. This is important to consider even when only moderate concentrations are desired since the temperatures of the rare earth lines and dispersion apparatus place an upper limit on the cell temperature that can be used. If the temperature of the rare earth cell exceeds the temperature of the lines or dispersion apparatus, portions of the rare earth precursor may re-solidify due to cooling before entering the deposition chamber. Heating of the lines and dispersion apparatus to high temperature is typically more difficult than heating the rare earth cell in practice and this upper limit was experimentally determined to be in the range of 210–220℃ for the MAC system and

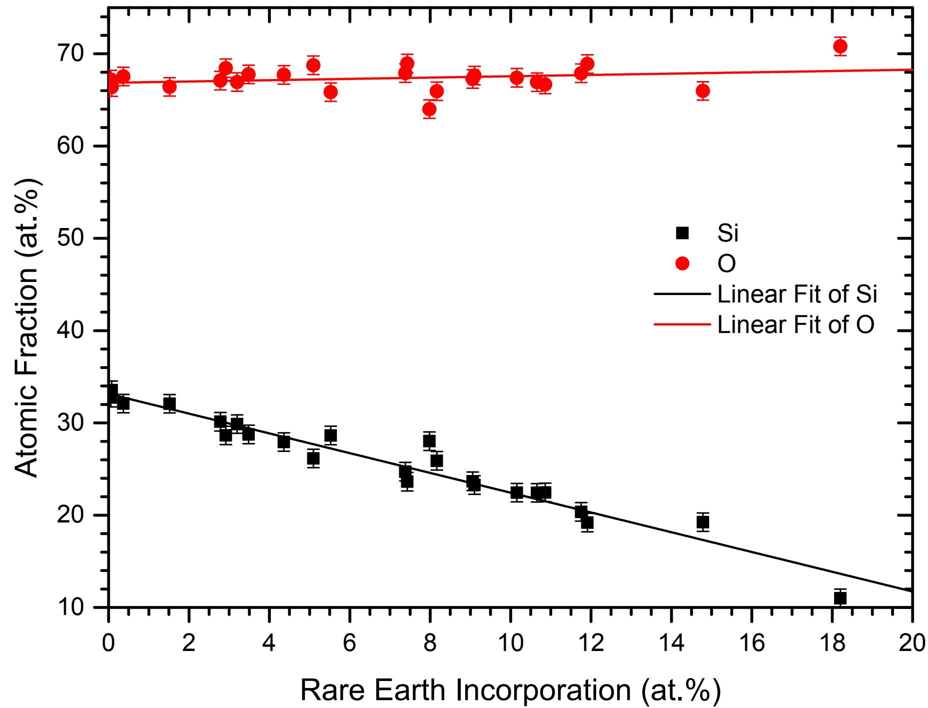

Figure 6.2: Silicon and oxygen atomic fractions as a function of rare earth incorporation in cerium and terbium co-doped silicon oxide films.

235°C for the GIV system.

The effect of using an overpressure of oxygen to increase the cerium incorporation can be better understood by comparing the relative atomic fractions of Si, O, Ce, and Tb (excluding C, Ar, and H contributions) in all of the samples grown by both systems as depicted in Figure 6.2. Here, the oxygen fraction is observed to stay approximately constant at 67% as a function of the combined Ce and Tb incorporation while a linear decrease was observed in the Si fraction. From this trend, it is evident that the rare earth ions incorporate in the silicon oxide matrix by substitutionally replacing Si atoms or, to look at it from a different perspective, the host matrix is an alloy composed of competing phases of silicon oxide, cerium oxide, and terbium oxide. By providing the overpressure of oxygen, the relative concentration of silane is decreased allowing for more rare earth ions to bond with the oxygen atoms during film growth.

The results of the VASE analysis demonstrate how the optical properties of the

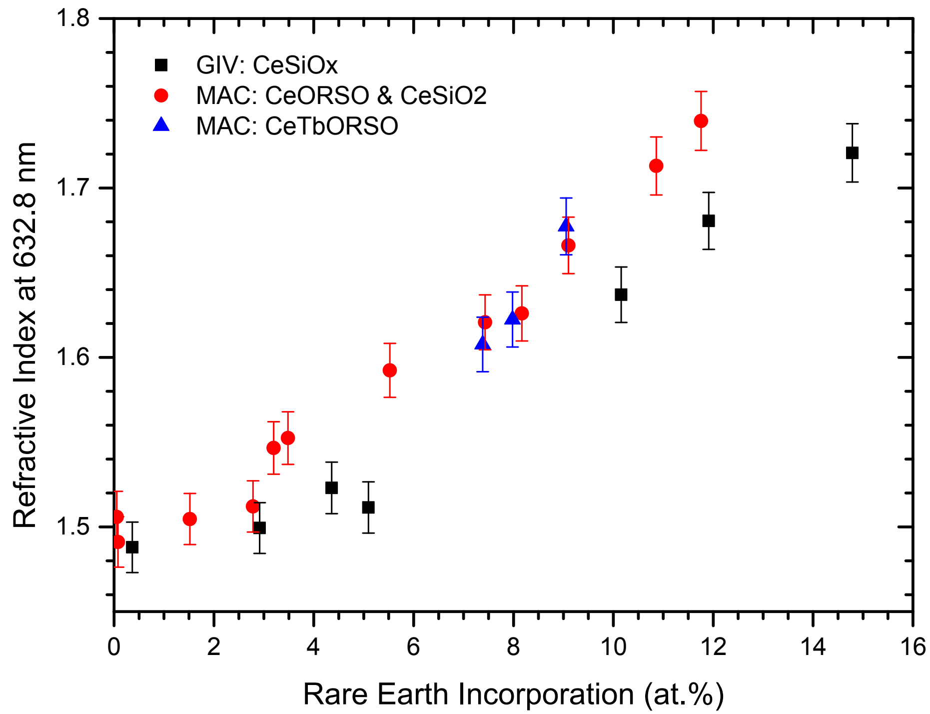

Figure 6.3: Refractive index as a function of rare earth incorporation in silicon oxide films.

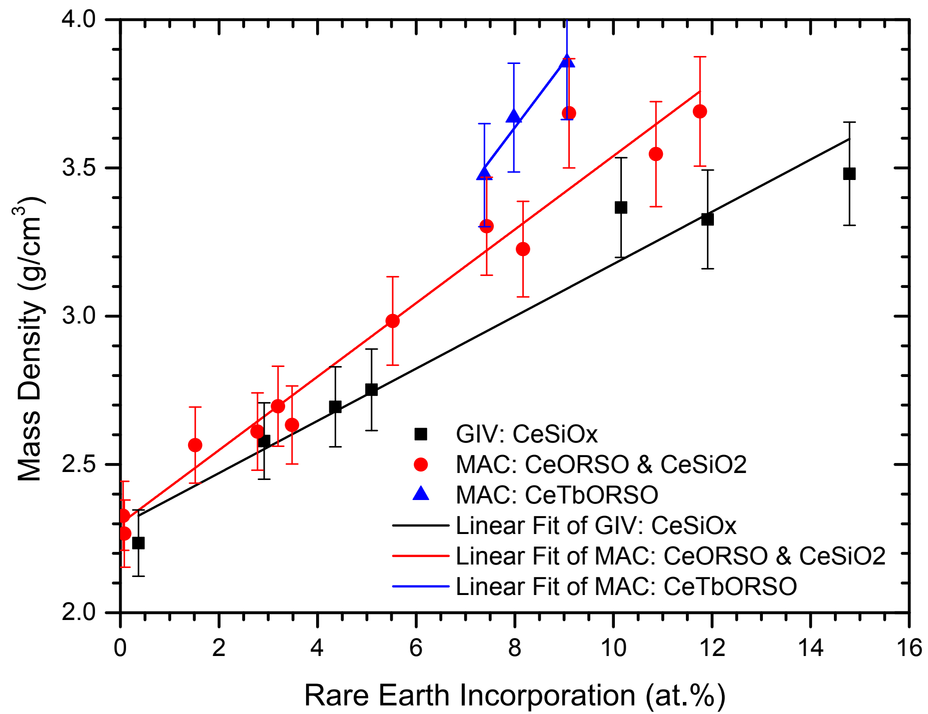

Figure 6.4: Mass density as a function of rare earth incorporation in silicon oxide films.

films were influenced by the level of rare earth doping. The refractive indices of as-deposited films grown on both deposition systems are compared in Figure 6.3. Interestingly, the refractive indices of the films grown on the MAC system tended to be higher for a given level of rare earth incorporation compared to the GIV system. This could be a result of higher hydrogen content in films produced using the GIV system or the influence of the universally higher argon and terbium concentrations in the films produced on the MAC system. However, for a given deposition system, the deposition conditions outside of the rare earth incorporation chosen (*e.g.*, oxygen overpressure) were not observed to significantly influence the refractive index. This result indicates that the refractive index would provide a convenient diagnostic for determining the approximate level of rare earth doping quickly or in the absence of RBS data, especially for doping concentrations in excess of 1 at.%. Accordingly, deposition systems configured with an *in-situ* ellipsometer could use this information to gain real time feedback on rare earth incorporation during growth.

The incorporation of cerium was also observed to significantly alter the mass density of the as-deposited films, which was calculated based on the "RBS thickness" (in units of atoms/cm^2), atomic concentrations, atomic masses, and optical thickness of the layers. Figure 6.4 shows the increasing trend for mass density with rare earth incorporation (Ce and Tb combined) in films deposited by the GIV and MAC systems. The CeSiOx-01 and CeORSO-23 samples were excluded from their respective data sets due to the influence of carbon contamination on the sample density. A baseline trend for the influence of only cerium incorporation can be established from the CeSiOx samples since they contained only trace levels of terbium. In these films, the mass density was observed to increase by over 50% from 2.2 g/cm^3 in the lightly doped films, which is consistent with the density of SiO_2 [156], to 3.5 g/cm^3 in a film containing 14.8 at.% cerium. The films grown using the MAC system followed a

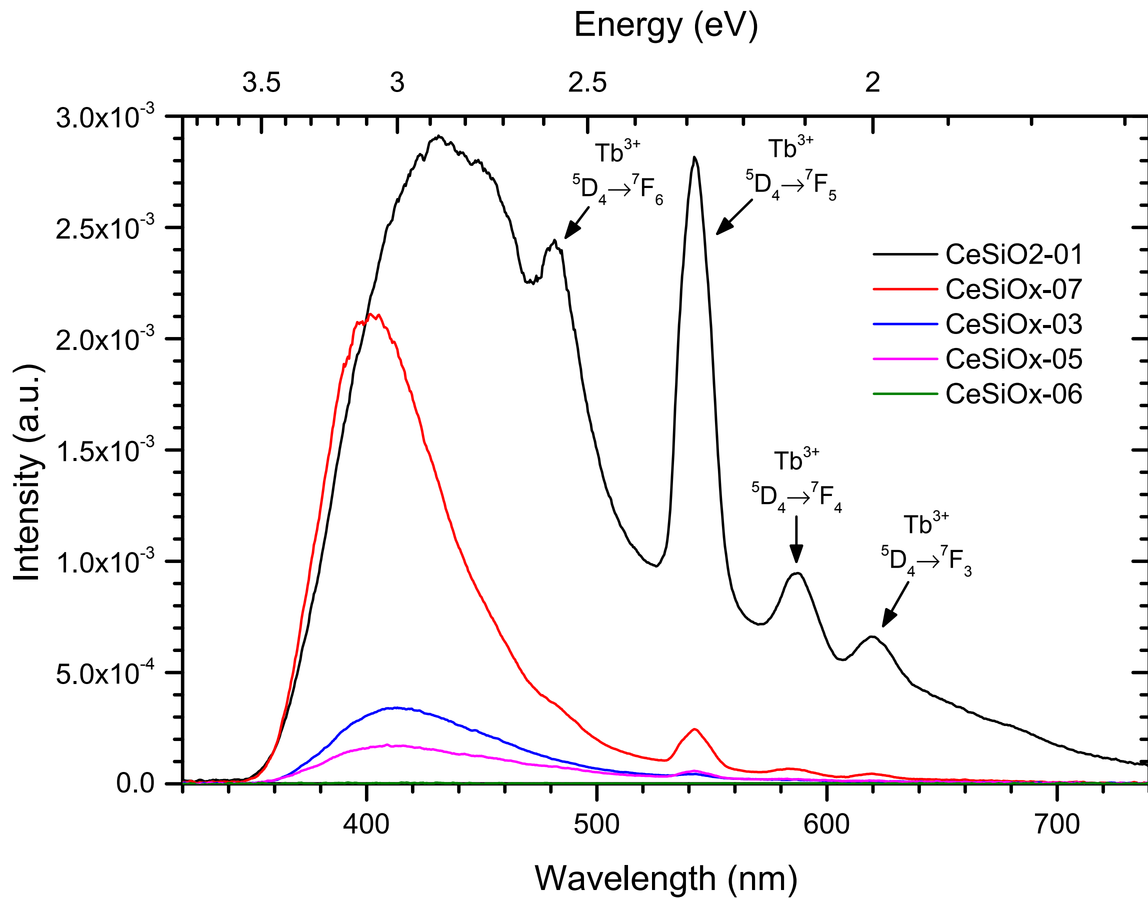

Figure 6.5: PL spectra for different compositions of as-deposited cerium doped silicon oxide films. Narrow peaks characteristic of emission lines from contaminant Tb^{3+} ions are labelled with the corresponding intra-4f transition.

similar trend in that the mass density was close to 2.2 g/cm^3 for the lightly doped samples and increased substantially at higher doping concentrations. Much like their relative refractive indices, the densities of films grown on the MAC system tended to be slightly higher than on the GIV system for a given atomic fraction of rare earth dopant. This higher density at least partially corresponds to the larger concentration of terbium, which has a larger atomic mass than cerium, within these films. For the same reason, the CeTbORSO samples were measured to have the highest mass densities for a given level of total rare earth incorporation. However, the concentration of terbium in the CeORSO and CeSiO2 samples is low enough to suggest that these films are more atomically dense in general (*i.e.*, less porous) than the films deposited using the GIV ECR PECVD system, perhaps related to differing levels of hydrogen incorporation.

The photoluminescence exhibited by the as-deposited films was found to be most intense in samples with light cerium doping and steadily became weaker as the cerium concentration was increased, as evident in the PL spectra shown in Figure 6.5. The samples included in this plot have cerium concentrations that cover a range of four orders of magnitude and it can be seen that the films containing the highest concentrations exhibit no luminescence at all. Poor luminescence was expected in AD films of any composition based on prior results for cerium doped silicon oxide and terbium doped silicon oxide films grown using this method [36]. The AD films contain many non-radiative defects and the rare earth ions would likely be coordinated in a variety of configurations, many of which could be optically inactive, especially in the highly doped films where the rare earth ions cause a larger disruption of the silicon oxide host matrix. Furthermore, in highly doped samples, the rare earth ions are located in close proximity to each other which would increase quenching effects related to ion-ion interactions. The four narrow peaks, which are most pronounced in

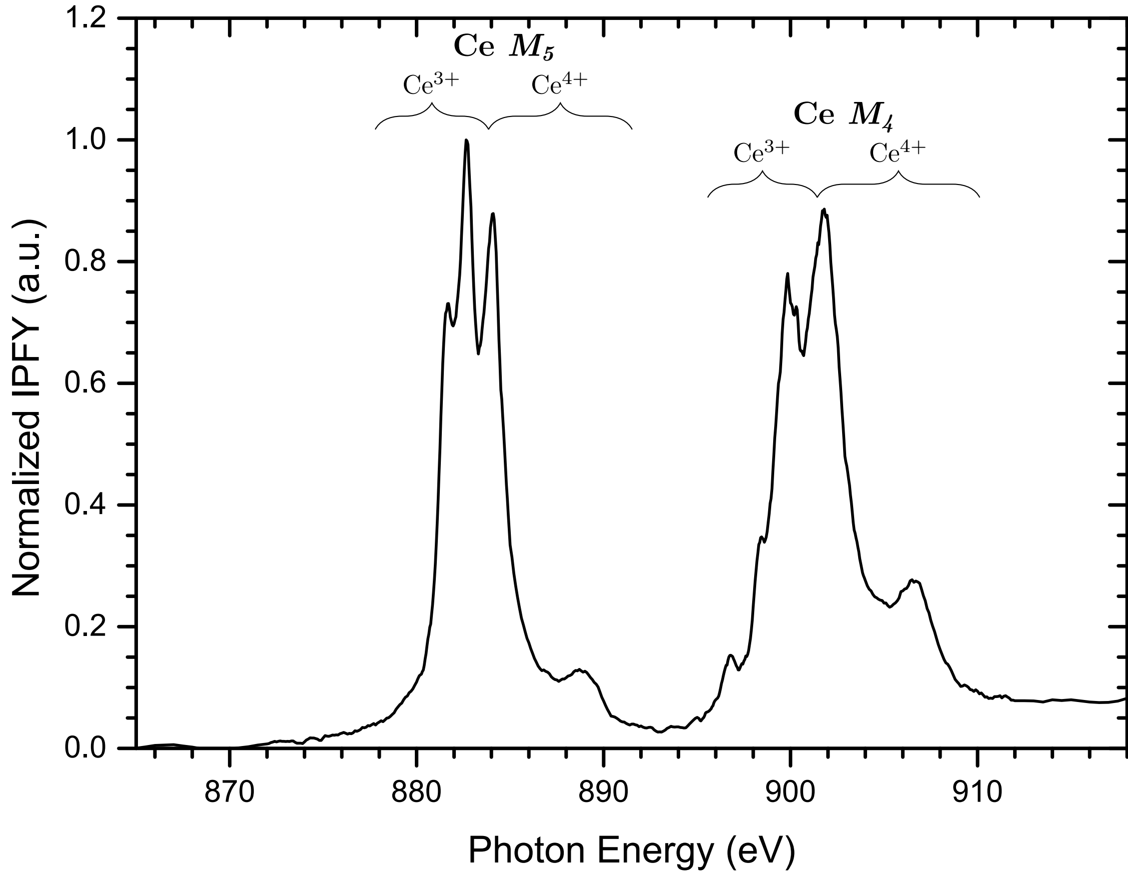

Figure 6.6: Ce $M_{5,4}$-edge IPFY-XANES spectrum for as-deposited CeORSO-01. Spectral features related to both Ce^{3+} and Ce^{4+} were observed as labelled at each absorption edge.

the CeSiO2-01 PL spectrum due to its relatively high terbium content, correspond to radiative intra-4f transitions from the $^5D_4 \rightarrow ^7F_6$, $^5D_4 \rightarrow ^7F_5$, $^5D_4 \rightarrow ^7F_4$, and $^5D_4 \rightarrow ^7F_3$ levels in Tb^{3+} ions as labelled in the plot.

Indeed, based on the Ce $M_{5,4}$ IPFY-XANES spectrum for the heavily cerium doped AD CeORSO-01 film shown in Figure 6.6, it is evident that the cerium ions are largely coordinated in the optically inactive Ce^{4+} oxidation state. While some of the cerium was also measured to be in the requisite trivalent coordination, the oxidation state alone does not determine that the ion will be optically active since other aspects of bonding and quenching mechanisms also play a vital role.

In the highest doped films, the TEM cross-section of the as-deposited layer appears

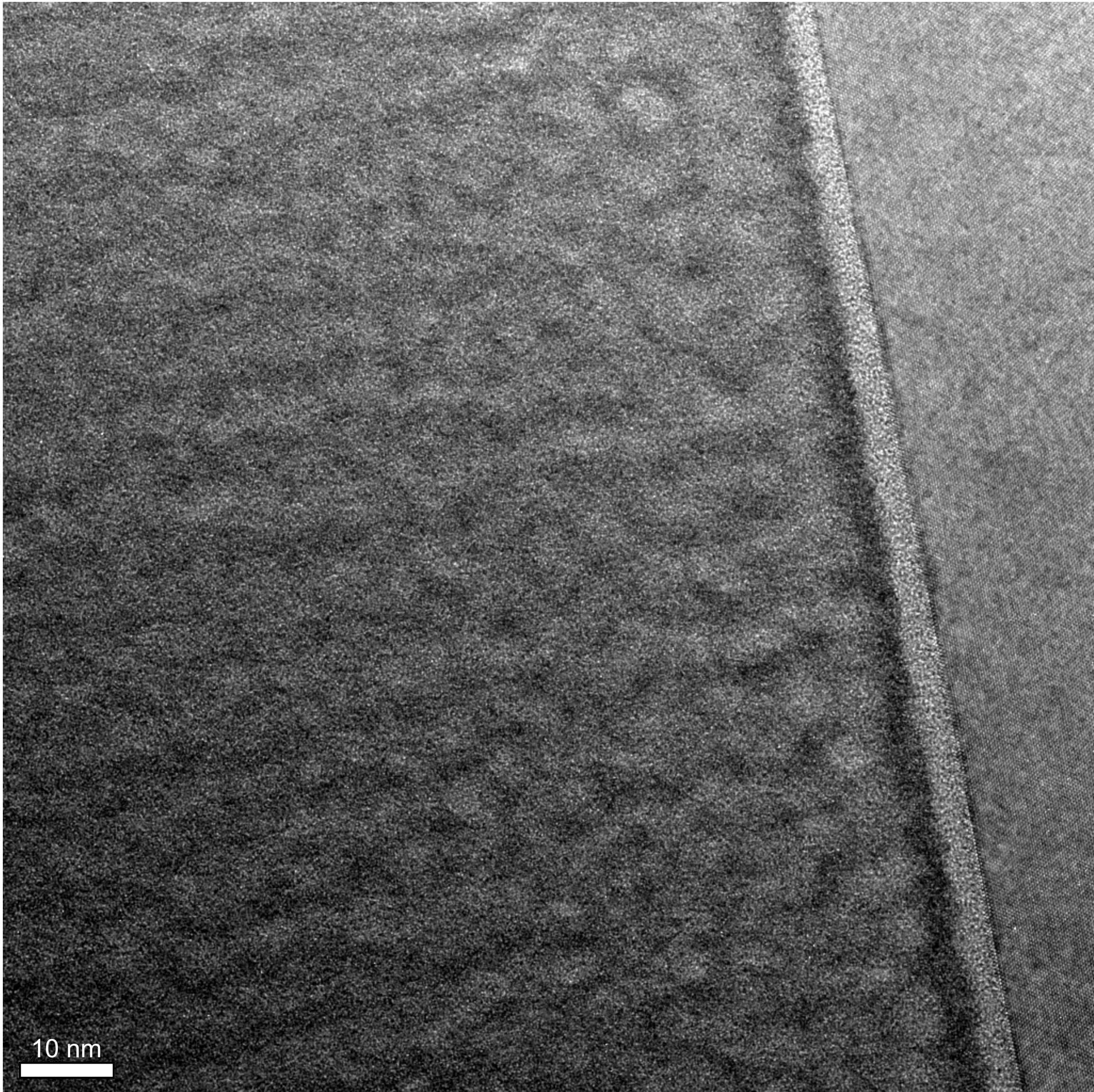

Figure 6.7: Bright-field HRTEM image of as-deposited CeORSO-03 exhibiting a non-uniform microstructure with a marbled appearance. The light and dark regions reflect a mixture of amorphous silicon oxide and cerium oxide phases, respectively.

marbled looking despite no crystalline structure being present as evidenced for the CeORSO-03 film shown in Figure 6.7. The darker regions within the film correspond to regions of higher cerium content and the marbled appearance indicates that either the cerium tends to cluster at high concentrations or it supports the concept that the layer grows as an alloy of competing phases. In either case, the non-uniform cerium distribution is consistent with the downwards trend in PL intensity in films with increasing cerium content.

6.2 Isochronal Annealing of Cerium Doped Silicon Oxide

Samples from various compositions of films grown with the MAC and the GIV ECR PECVD systems were annealed in a quartz tube furnace for 60 minutes under flowing N_2 ambient gas at temperatures ranging from 600 to 1200℃ in order to study changes in their luminescent properties, the coordination of cerium and terbium ions in the films, and the formation of nanostructures. To first characterize the effect of annealing temperature on cerium within the films, a selection of samples with minimal terbium content and covering a broad range of cerium concentrations were compared before considering the role of terbium as a co-dopant.

For films with very low cerium concentrations below 0.1 at.%, photoluminescence was measured to be brightest at the lower annealing temperatures as shown for CeSiO2-01 in Figure 6.8. The PL intensity peaked at 600℃ and gradually decreased as the temperature was raised. At the lower temperatures, the spectral distribution reflected typical Ce^{3+} emission for cerium incorporated in SiO_2 [36] with a broad peak close to 450 nm and, aside from the narrow peaks associated with Tb^{3+} luminescence, likely some emission from oxygen defect states as well. The broadening and slight blue-shifting of the broad peak as the intensity decreases at higher annealing temperatures could be attributed to the prevalence of defect related emission as luminescence from

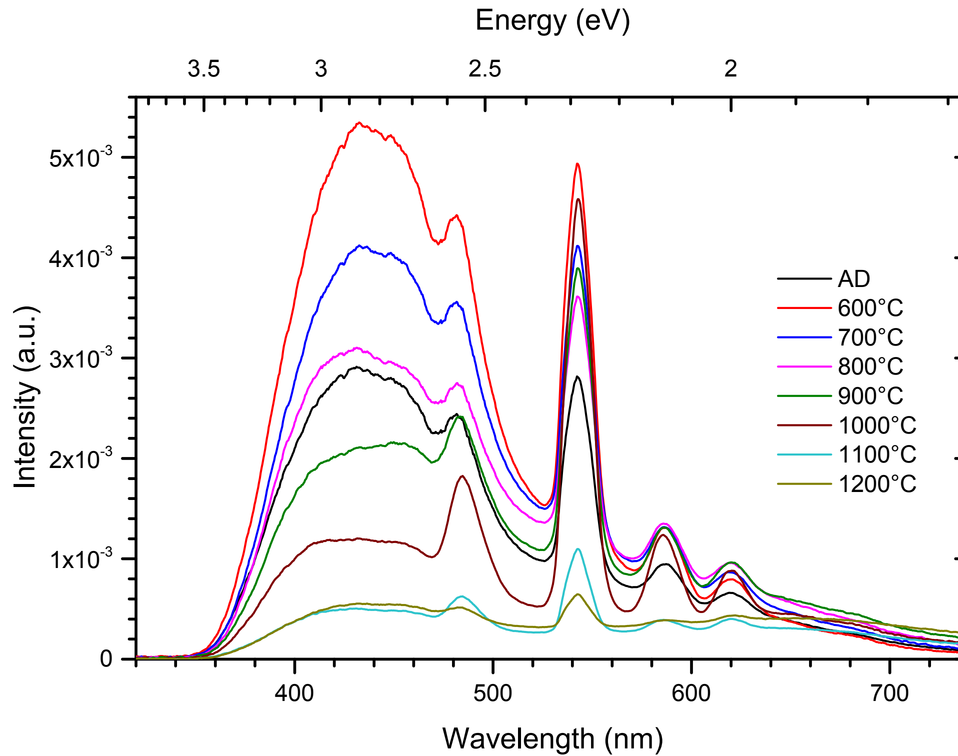

Figure 6.8: PL spectra for CeSiO2-01 annealed at different temperatures for 60 minutes.

the cerium ions declines.

The decline in cerium emission may be explained by the reduction of defect sensitizers due to annealing, cerium ions becoming coordinated in optically inactive states, or increased quenching due to ion-ion interactions as cerium diffuses within the film. To get a better idea which mechanism was responsible, the Ce $M_{5,4}$-edge TEY- and TFY-XANES spectra were compared for 600, 1000, and 1200℃ annealed films. As can be seen in Figure 6.9, the TEY spectra indicate an increase in Ce^{4+} bonding at the surface of the film at higher annealing temperatures while the TFY spectra revealed that the cerium ions remained entirely in a trivalent coordination in the bulk of the layer. While the increase in optically inactive Ce^{4+} coordinated ions at the surface would explain some of the reduction in PL intensity, the very low concentration of cerium in the film plus the fact that the ions in the bulk of the film

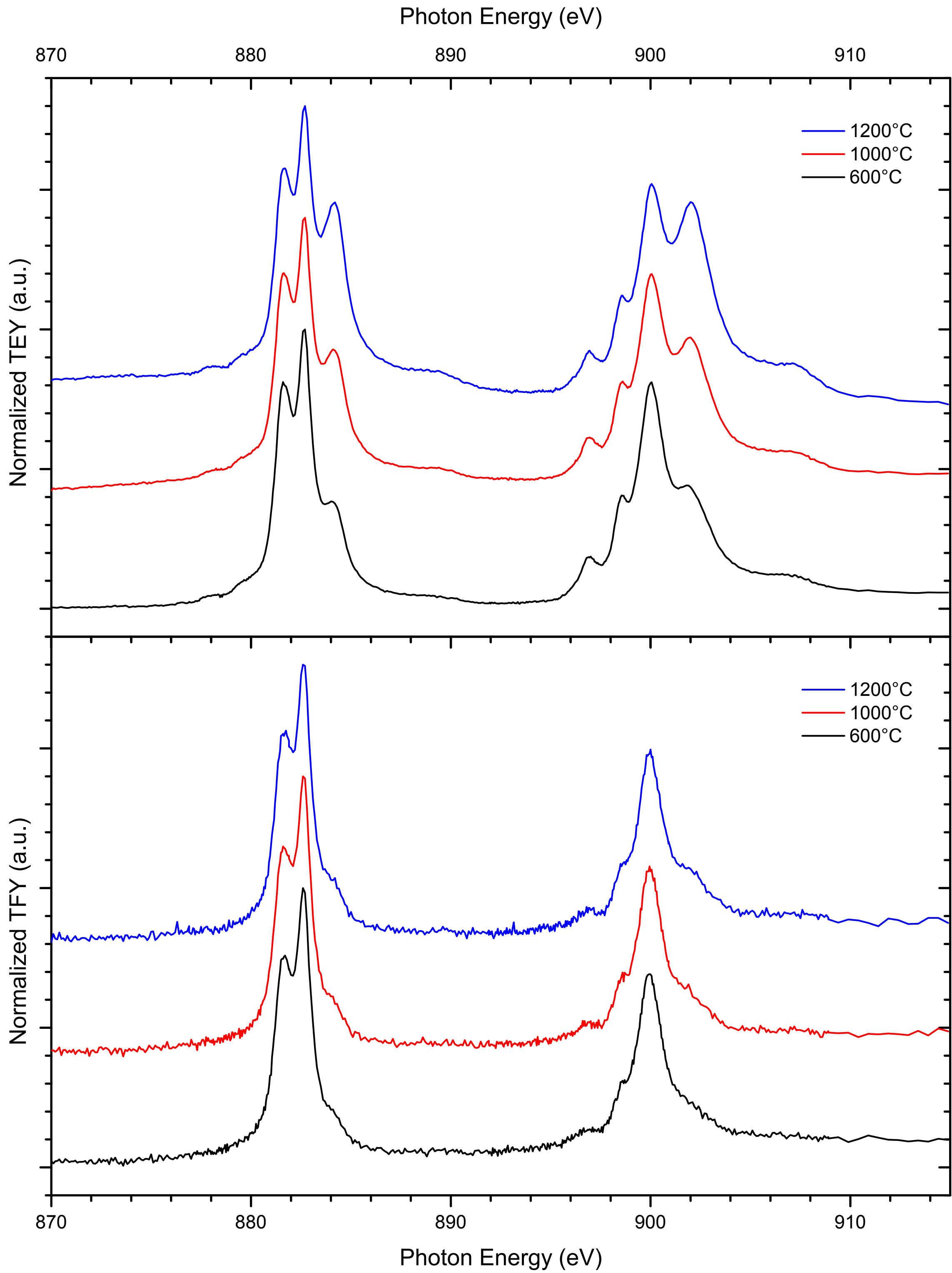

Figure 6.9: Ce $M_{5,4}$-edge TEY- and TFY-XANES spectra for CeSiO2-01 annealed at different temperatures for 60 minutes.

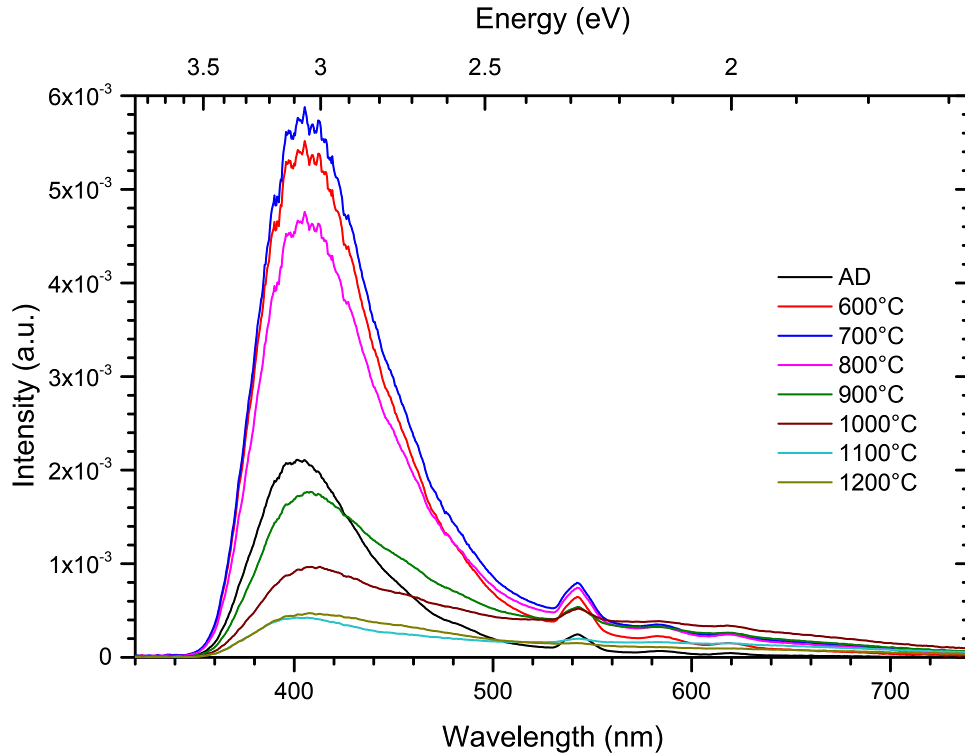

Figure 6.10: PL spectra for CeSiOx-07 annealed at different temperatures for 60 minutes.

remained in a trivalent coordination indicate that a reduction in sensitizing defects was the main reason for the decrease in cerium luminescence at higher temperatures.

The PL spectra for a lightly doped silicon oxide film with 0.4 at.% cerium (CeSiOx-07) is shown in Figure 6.10. In comparison with CeSiO2-01, which contained approximately 10 times less cerium, the most intense PL for CeSiOx-07 occurred at a slightly higher annealing temperature of 700℃. This marks the beginning of a pattern in which the annealing temperature corresponding to the brightest PL was found to increase with cerium content. Also of note was that the peak wavelength at all temperatures was shifted to just above 400 nm in this film, which is unusual for cerium incorporated in a SiO_2 host matrix. This could indicate that the coordination of cerium changes with the host matrix composition causing a shift in its emission energy or perhaps the emission observed originated from silicon oxide defects. Unfortunately,

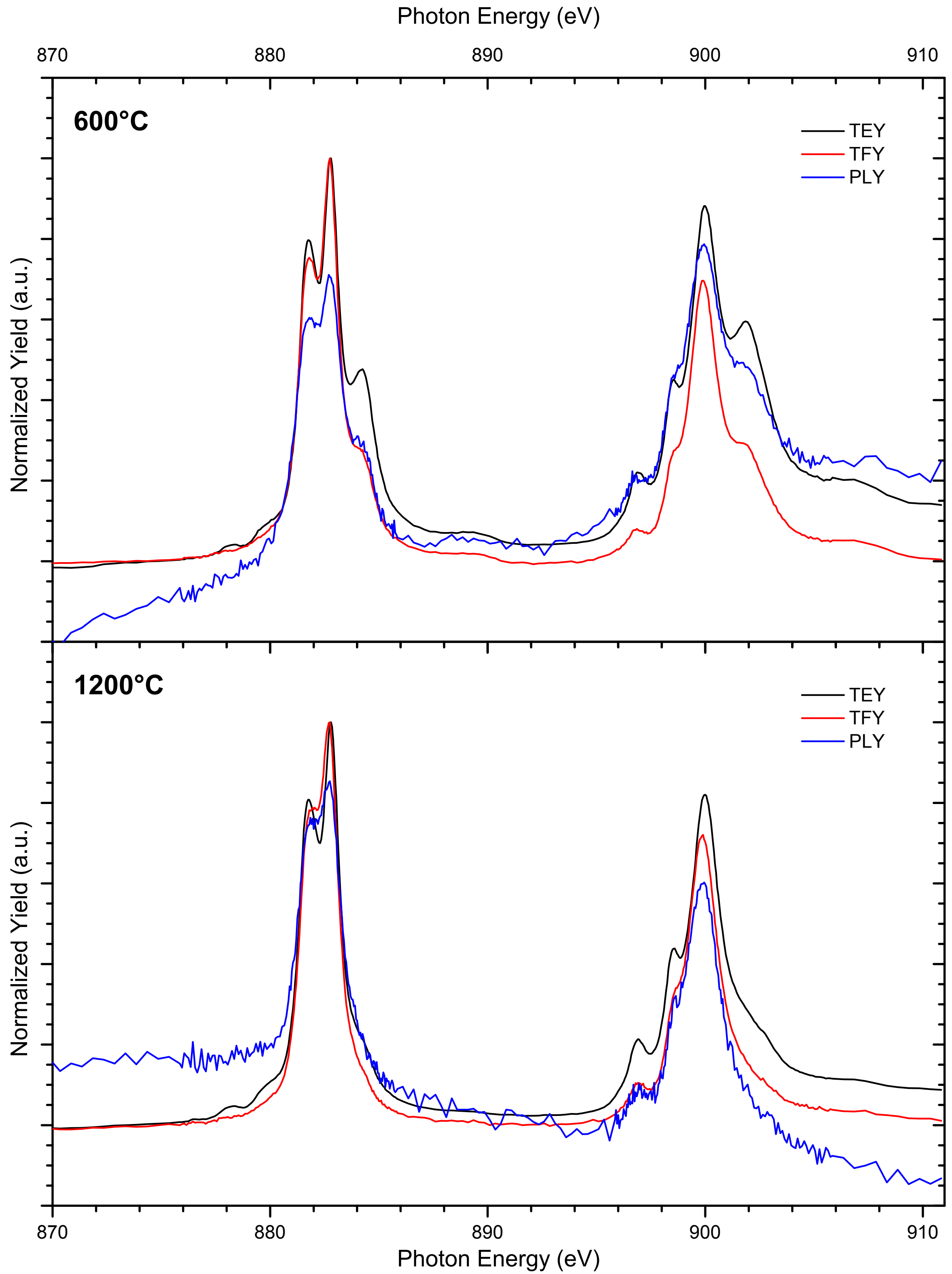

Figure 6.11: Ce $M_{5,4}$-edge TEY-, TFY-, and PLY-XANES spectra for CeSiOx-07 annealed at 600 and 1200°C for 60 minutes.

it is very difficult to distinguish between the two potential sources of emission in a substoichiometric silicon oxide film without employing advanced analysis techniques such as time-resolved photoluminescence spectroscopy. It is also worth noting that both the cerium coordination and silicon oxide defects in the films may be sensitive to the deposition conditions, in which case the blue-shifting may relate to the "Ce-SiO2" samples having been produced using the MAC ECR PECVD system while the "CeSiOx" samples were grown by the GIV ECR PECVD system. Otherwise, the PL from this sample followed a trend similar to the films with less than 0.1 at.% cerium doping with a peak in PL intensity at low temperatures followed by a gradual decline and broadening at higher temperatures.

From the TEY- and TFY-XANES spectra at the Ce $M_{5,4}$-edge shown in Figure 6.11, it is apparent that a small portion of the cerium ions in both the near-surface and bulk of the film were in a Ce^{4+} coordination state after 600℃ annealing while only trivalent ions remained after annealing at 1200℃. Curiously, the PLY-XANES spectra, also included in Figure 6.11, show that PL was excited at energies resonant with both the Ce^{3+} and Ce^{4+} ions at 600℃ rather than only the optically active trivalent ions. This may be due to the electrons excited at cerium sites migrating to nearby radiative defects before recombining, which would suggest that the PL observed in this sample was primarily related to defect emission rather than recombination in the cerium ions, although the cerium ions may still play a role in the process.

The next sample considered was a moderately doped film with 2.9 at.% cerium incorporation (CeSiOx-03). Based on its PL spectra shown in Figure 6.12, the low temperature trends remained similar to those observed for samples doped with less cerium. However, the temperature at which the PL intensity reached a maximum in the low temperature regime has now shifted up to 800℃. While there was an initial decline at 900℃, the PL intensity rose substantially as the annealing temperature was

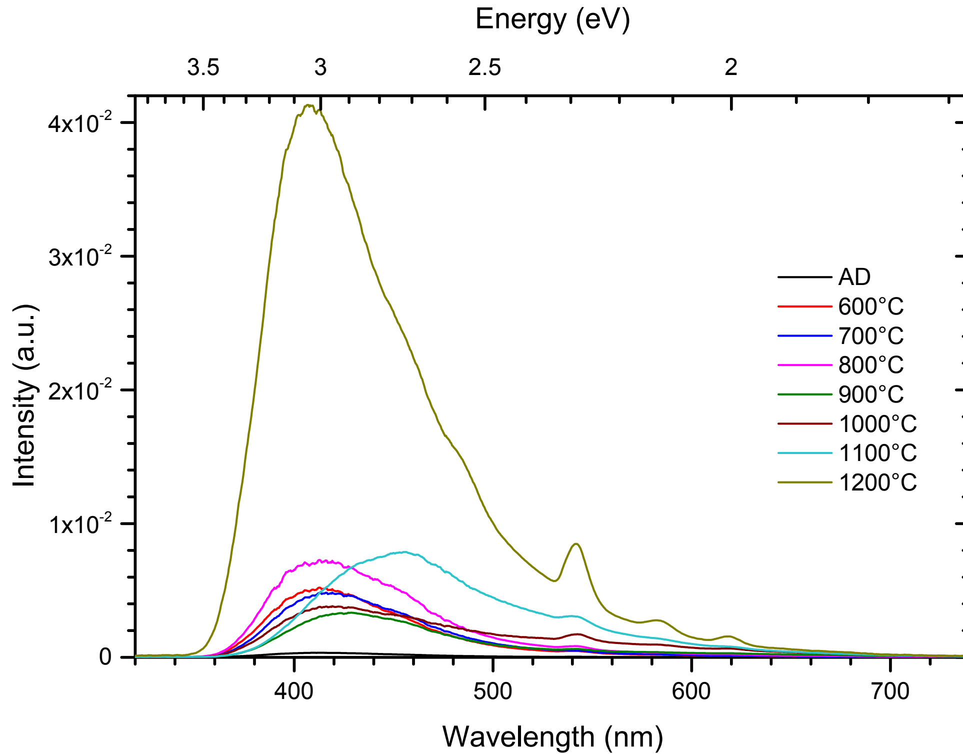

Figure 6.12: PL spectra for CeSiOx-03 annealed at different temperatures for 60 minutes.

increased further and by 1200°C, it exceeded the low temperature maximum by nearly a full order of magnitude. The resurgence of PL at high temperatures corresponds to the formation and growth of cerium disilicate ($Ce_2Si_2O_7$) nanocrystallites [35, 108, 109], the details of which are discussed later in this section.

In the photoluminescence spectra for the highly doped film with 5.2 at.% cerium content (CeSiOx-05) shown in Figure 6.13, only very weak photoluminescence is observed at temperatures below 900°C at which point cerium disilicate nanocrystallites begin to form. As the temperature was raised further, the PL intensity increased dramatically due to a corresponding increase in the density and size of the cerium disilicate nanocrystallites. The cerium emission peak was also observed to narrow, which may be due to a decrease in defect emission as the nanocrystallites gain better phase separation within the host matrix or the presence and transitions between

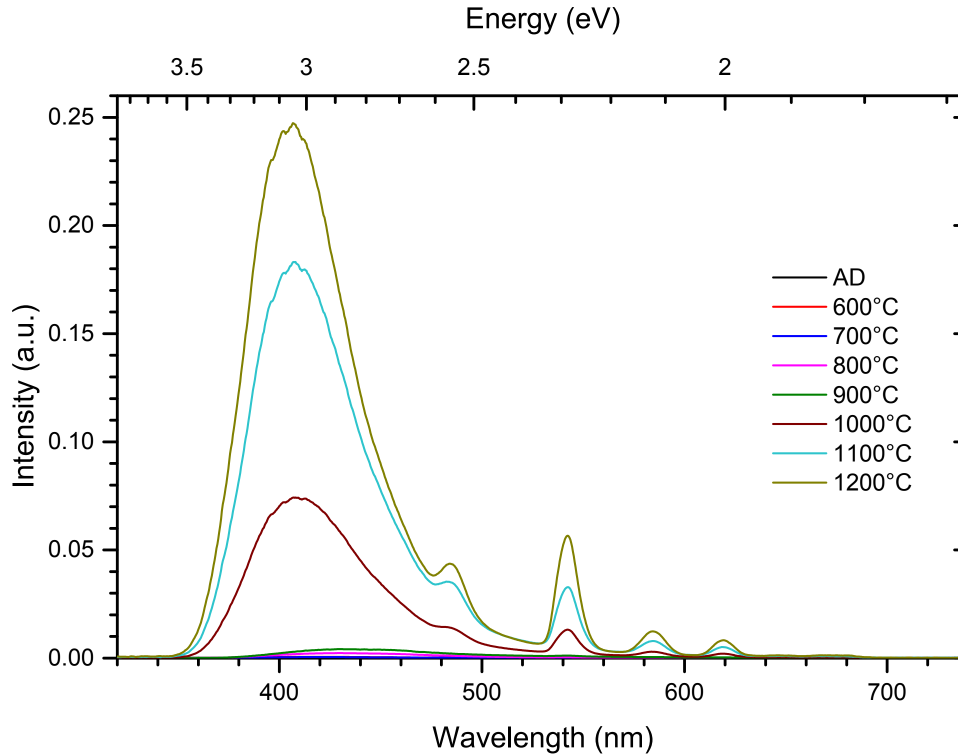

Figure 6.13: PL spectra for CeSiOx-05 annealed at different temperatures for 60 minutes.

different phases of cerium disilicate. Alternatively, the narrowing may result from the cerium ions at the surface of the nanocrystallites emitting at a slightly longer wavelength (*e.g.*, 450 nm) as a result of their bonding at the interface with the host matrix. In this case, one would expect the spectrum to narrow as the nanocrystallites become larger since there would be a lower surface to volume ratio of cerium ions.

The final film in the comparison was a very heavily doped silicon oxide film containing 18.2 at.% cerium (CeSiOx-01). The PL spectra, shown in Figure 6.14, did not exhibit any luminescence below 1000℃ at which point the emission intensity began to increase very quickly by two orders of magnitude until extremely bright emission was observed at 1200℃. Once again, the emission spectrum was observed to narrow at the higher annealing temperatures. To provide a visual example of the very high emission intensity observed from films containing cerium disilicate nanocrystallites,

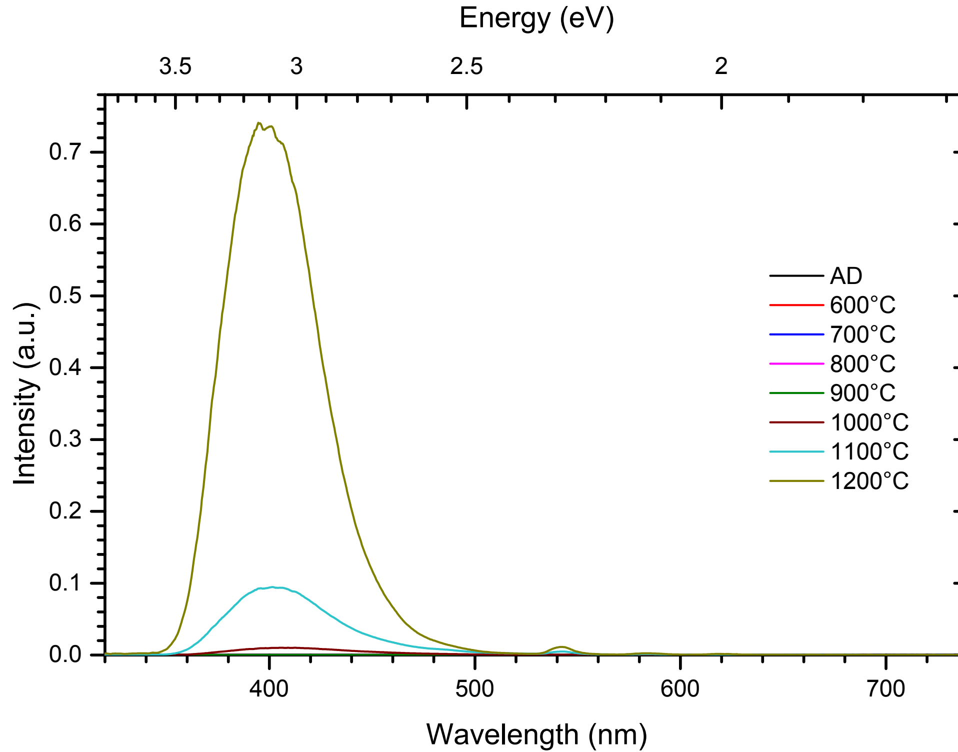

Figure 6.14: PL spectra for CeSiOx-01 annealed at different temperatures for 60 minutes.

Figure 6.15 shows a photograph, taken under normal room lighting conditions, of the PL from the heavily cerium doped sample CeORSO-03 following 1100℃ annealing for 60 minutes. Note that the large, white appearance of the emission spot is due to saturation of the digital camera's sensor since the camera did not have a fast enough shutter speed to properly capture the colour of such strong emission, although a blue tinge is visible near the edge of the spot.

To better compare the intensity of emission from each sample, the total power density (*i.e.*, integrated PL intensity) is plotted as a function of annealing temperature in Figure 6.16. Note that a semi-log scale was used since the intensities observed spanned a range of five orders of magnitude and the "annealing temperature" for the AD film was specified as the stage heater temperature of 350℃. When displayed in this manner, it becomes clear that the 900℃ annealing temperature marks the

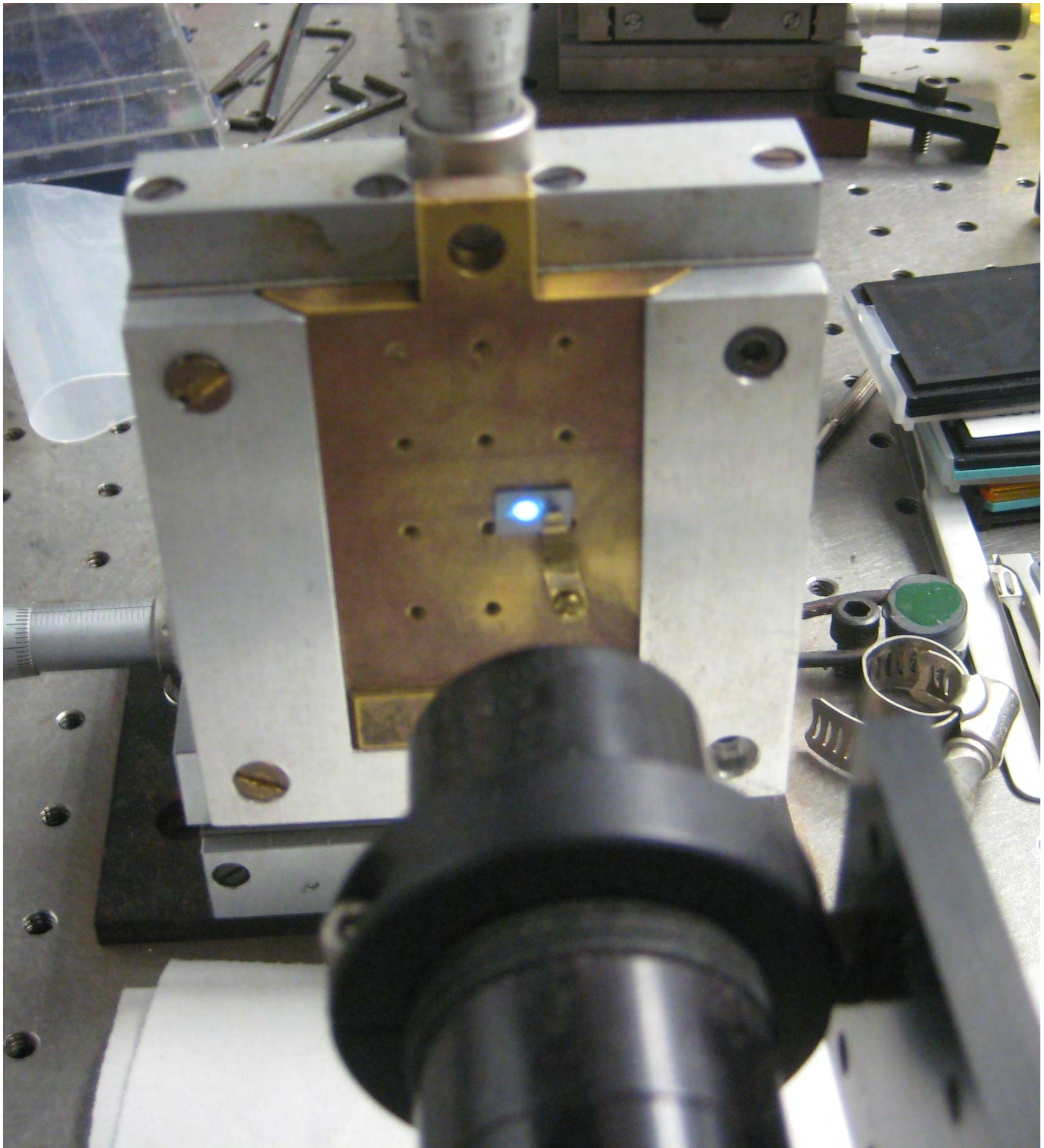

Figure 6.15: Photograph of the PL from CeORSO-03 after 1100°C annealing for 60 minutes. The image was captured under normal room lighting conditions.

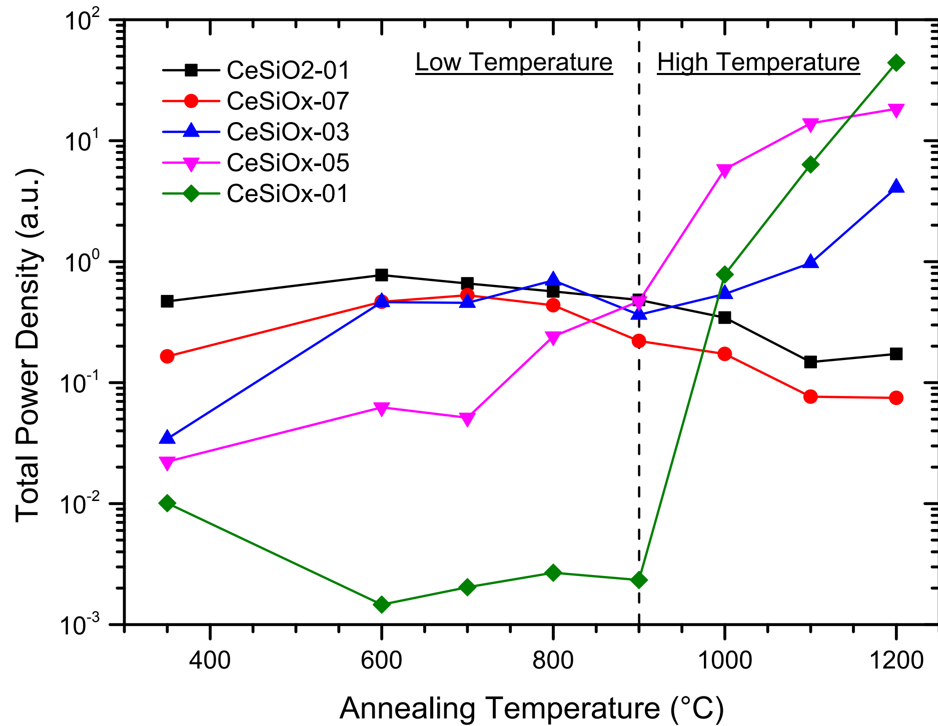

Figure 6.16: PL total power densities for several cerium doped silicon oxide films annealed at different temperatures for 60 minutes.

boundary between two stages in the thermal evolution of cerium doped silicon oxide films.

Below 900°C is a low temperature regime where the more lightly doped samples exhibit the strongest photoluminescence with the optimal annealing temperature increasing gradually from 600 to 900°C with higher cerium content. The luminescence in this region was most likely sensitized by defects in the host matrix which were removed with annealing and hence the decline in luminescence at higher temperatures. Increased cerium incorporation in the film results in a larger disruption to the silicon oxide host matrix, resulting in an increase in defect density which requires higher annealing temperatures to remove. At the same time, the cerium ions in samples with higher cerium concentration were more likely to coordinate in optically inactive configurations or suffer quenching due to ion-ion interactions resulting from their closer

proximity to other cerium ions upon deposition. Higher annealing temperatures were required to allow these ions to diffuse and coordinate in optically active configurations.

At temperatures of approximately 900℃ and higher, enough energy is available for the cerium ions to form cerium disilicate nanocrystallites. In samples with lower cerium content, the separation between cerium ions is relatively large and so it requires higher temperatures for the cerium disilicate phase to begin to form due to the larger diffusion lengths required. This is likely the reason that cerium disilicate emission was not observed from the CeSiO2-01 and CeSiOx-07 samples after a 60 minute anneal at 1200℃ whereas the PL intensity of films with higher cerium concentration began to trend upwards in the high temperature regime. However, the cerium disilicate phase would likely have begun to form for longer anneals at 1200℃. After formation, the cerium disilicate phase will continue to grow in size. Since the emission from the nanocrystallites is not based on quantum confinement effects, their PL intensity increases at a rapid rate as the nanocrystallite dimensions increase until the cerium ions that have not already been incorporated in the cerium disilicate phase become depleted. This is why the rate of increase in the total power density for CeSiOx-05 slowed down at the higher temperatures while the total power density for the CeSiOx-01 film, with more than three times the concentration of cerium, was observed to continue increasing at an exponential rate.

While the concept of cerium disilicate nanocrystallites forming within a silicon oxide host matrix was straightforward enough, many of the films studied had atomic fractions of cerium approaching the concentration of silicon in the film and it became important to consider the impact on microstructure in the higher temperature regime. Assuming 100% conversion of cerium into the cerium disilicate phase (and in the absence of terbium co-doping), the 2:11 atomic ratio of cerium to total atoms in the chemical formula $Ce_2Si_2O_7$ implies that a cerium concentration of 9.1 at.% presents a

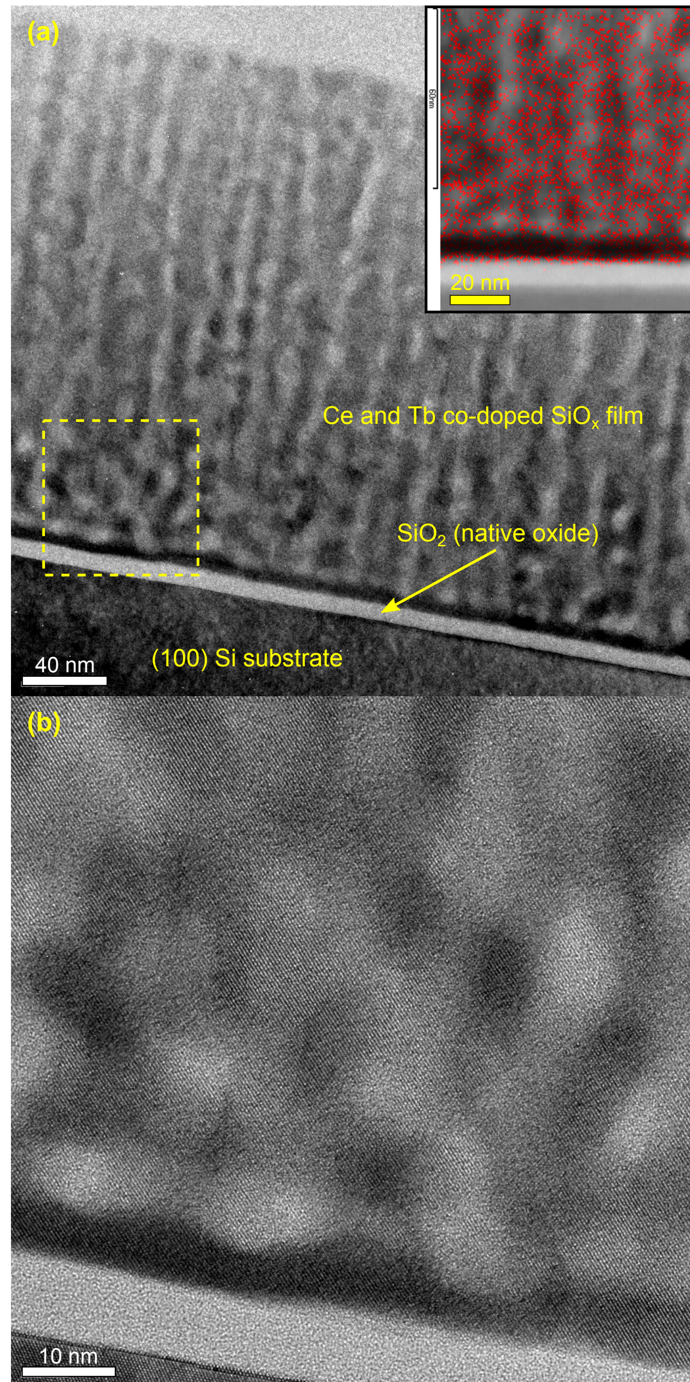

Figure 6.17: (a) Cross-sectional bright-field HRTEM image of CeORSO-01 annealed at 1000℃ for 60 minutes. The dark regions in the film correspond to cerium disilicate nanocrystallites and the lighter regions are amorphous silicon oxide. The red dots in the inset indicate the distribution of cerium in the layer as measured through XEDS analysis, which indicates that the cerium has mostly diffused into the cerium disilicate nanocrystallites. (b) A magnified view of the section of the top image marked by dashed lines shows the lattice fringes of the cerium disilicate nanocrystallites intermixed with the amorphous silicon oxide regions.

limit above which cerium disilicate becomes the dominant phase with regions of silicon dioxide intermixed as a minority phase. However, the details of this intermixing are unclear. For example, the amorphous silicon dioxide phase could make up nanoscale pockets in a reversal of the typical microstructure observed when nanostructures form within host matrix or alternatively the cerium disilicate could segregate from the silicon oxide to form separate continuous layers within the film. To gain a better understanding of the consequence of exceeding the 9.1 at.% limit, cross-sectional TEM images were taken of samples CeORSO-01 and CeORSO-03 which contained 8.9 and 11.6 at.% cerium, respectively, after high temperature annealing.

The bright-field HRTEM images for CeORSO-01 annealed at 1000℃ shown in Figure 6.17 reveal the expected microstructure for a film with less than 9.1 at.% cerium. Here, nanocrystallites of cerium disilicate, which appear darker than the silicon oxide regions in the image, were found to be distributed throughout the silicon oxide host matrix. The results of XEDS analysis, shown in the inset, indicated that the majority of cerium ions within the film had diffused to the cerium disilicate regions. In contrast, the high-angle annular dark-field (HAADF) STEM and bright-field HRTEM images for CeORSO-03 annealed at 1100℃ shown in Figure 6.18 confirm that microstructure essentially flips when the cerium concentration exceeds 9.1 at.%. Note that the light and dark regions are reversed in the HAADF STEM image compared to the bright-field HRTEM images with the bright regions representing cerium disilicate and dark regions identifying silicon oxide. The STEM image gives a view of the entire layer and shows that the cerium disilicate phase is particularly dominant in the regions near the surface of the film and the interface with the substrate. The silicon oxide is distributed in small pockets throughout the film with larger pockets approaching 50 nm in size located in the middle of the layer. This image also gives an indication of the top-down view of the film, part of which has peeled up in the background,

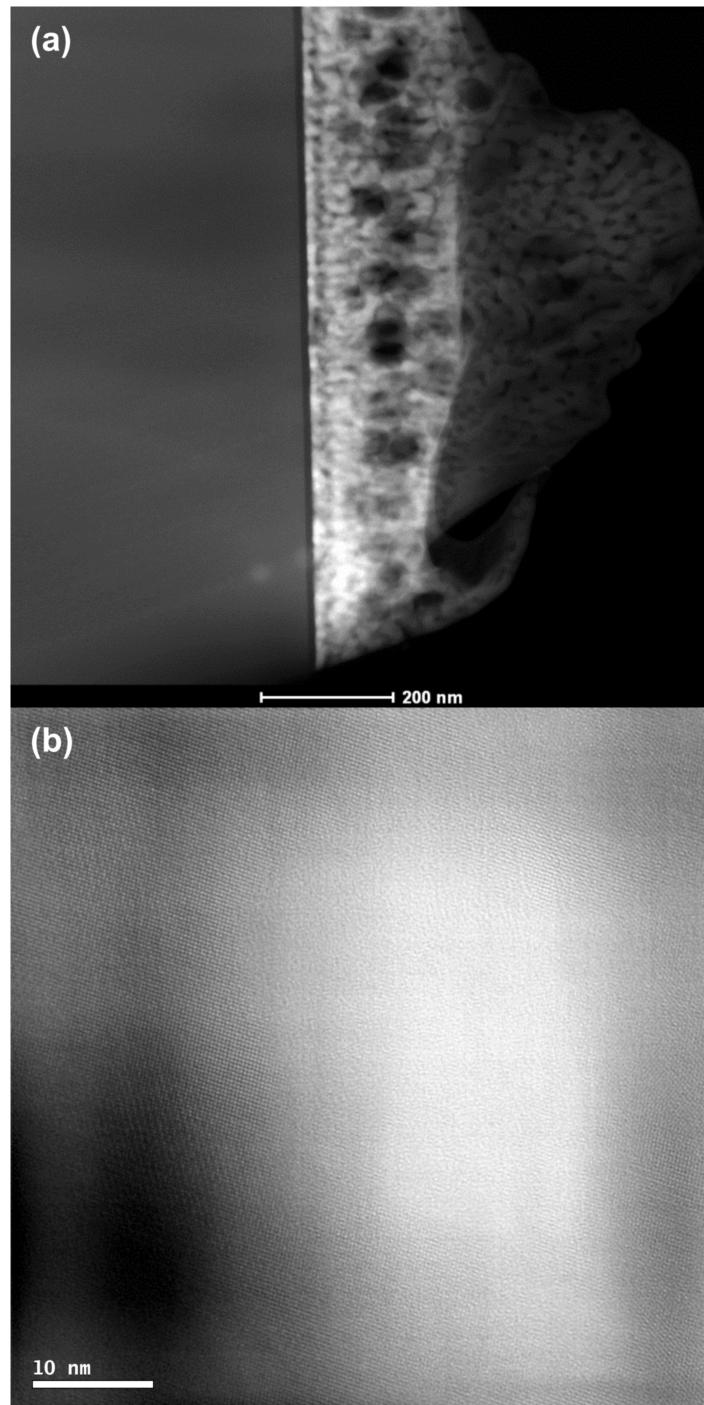

Figure 6.18: (a) Cross-sectional HAADF STEM image of CeORSO-03 annealed at 1100℃ for 60 minutes. The light and dark regions in the film are cerium disilicate nanocrystallites and amorphous silicon oxide, respectively. (b) Bright-field HRTEM image providing a magnified view of the same film, which shows a pocket of amorphous silicon oxide in the middle of the film surrounded by crystalline cerium disilicate with clearly visible lattice fringes. Note that the light and dark regions are reversed in the bright-field HRTEM image compared to the HAADF STEM image above.

revealing that the cerium disilicate is essentially a continuous structure over the lateral dimensions intermixed with small regions of silicon oxide. The HRTEM image shows the crystalline structure of the cerium disilicate phase around a 25×15 nm^2 pocket of amorphous silicon oxide located in the middle of the layer. Here, it is evident that the grain size of the nanocrystalline $Ce_2Si_2O_7$ is much larger than was observed in the CeORSO-01 film.

As opposed to merely forming nanocrystallites within a silicon oxide host matrix, for doping concentration exceeding 9.1 at.% cerium, the majority of the film was observed to convert to cerium disilicate when annealed at high temperature while the remainder formed pockets of amorphous silicon oxide within the layer. Presumably then, for a film such as CeSiOx-01 with 18.2 at.% cerium, nearly the entire layer could be converted to cerium disilicate if annealed under the conditions in which all of the cerium incorporates into the cerium disilicate phase. This is a remarkable result because it suggests that entire layers of crystalline, or at least nanocrystalline, cerium disilicate could be formed on virtually any substrate that could withstand the high temperature annealing required to initiate the crystallization. Even without forming a complete layer, the continuous nanocrystalline structure observed for the CeORSO-03 sample could enable more effective electrical excitation compared to attempting to inject charge into nanostructures embedded in an insulating host matrix like silicon oxide. The combination of strong luminescent qualities and structural versatility could make this an interesting material to consider for various device applications.

X-ray diffraction analysis was performed on the CeORSO-02 and CeORSO-03 samples annealed at 1200℃ to verify the phase of the observed nanocrystallites. The intensity vs. 2θ plot for each sample can be seen in Figure 6.19. Based on this analysis, all of the nanocrystallites present in the CeORSO-02 film were identified as G-type cerium disilicate (G-$Ce_2Si_2O_7$) [107] while 84 percent by weight (wt.%) of the

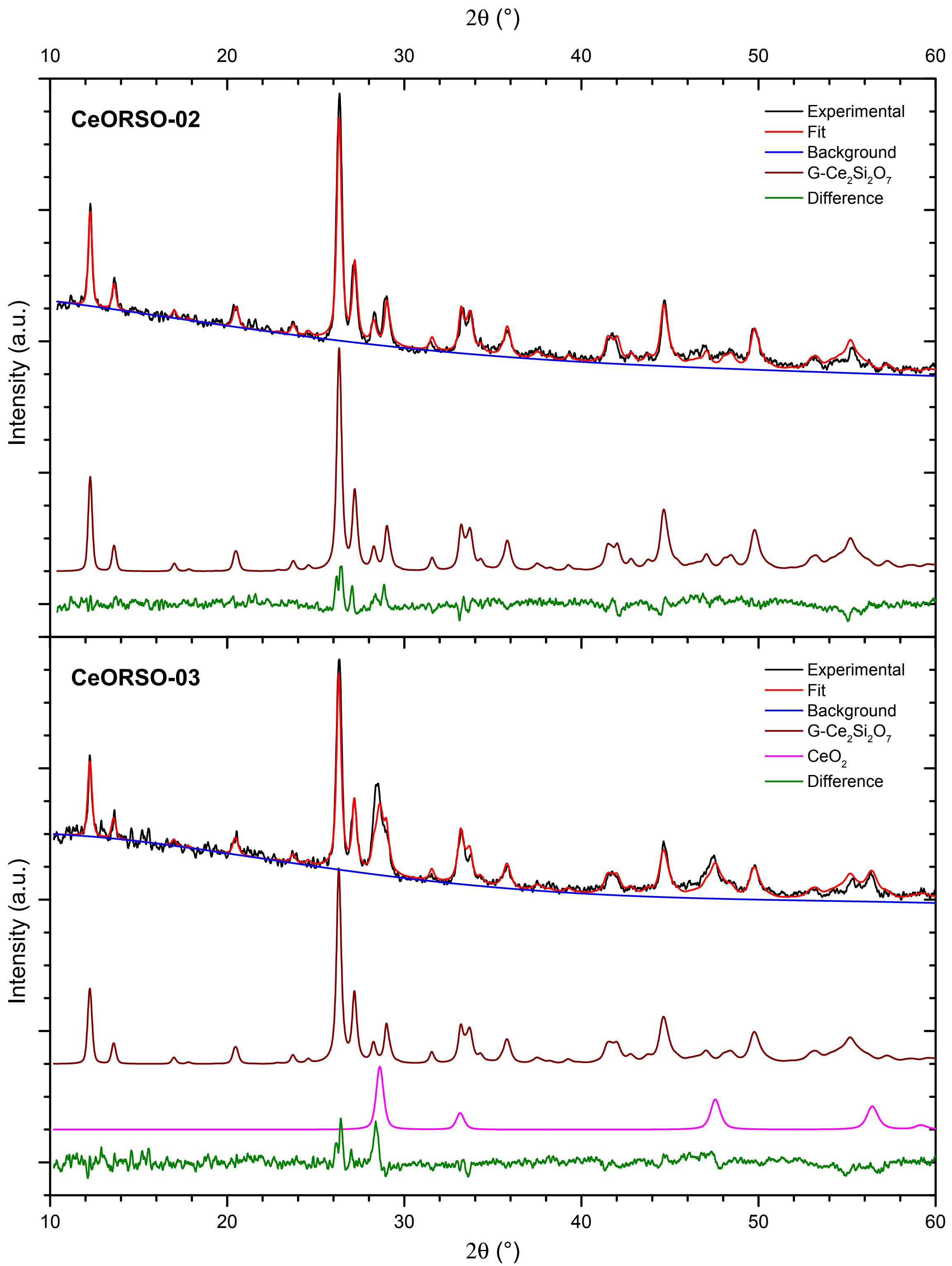

Figure 6.19: XRD spectra for CeORSO-02 and CeORSO-03 annealed at 1200°C for 60 minutes.

crystalline structure in the CeORSO-03 film was attributed to this same phase with the remaining 16 wt.% attributed to cerium dioxide (CeO_2) [157, 158]. Interestingly, neither film showed any evidence of other cerium silicate phases when annealed at this temperature.

To investigate the thermal evolution of the cerium disilicate structure in these films, XRD analysis was also performed on CeORSO-25b and CeSiOx-08 for annealing temperatures ranging from 900–1200°C. As with the CeORSO-02 and CeORSO-03 samples analyzed previously, the CeORSO-25b film was grown using the MAC ECR PECVD system and its XRD results were very similar following high temperature annealing. As shown in Figure 6.20, only a broad peak corresponding to very small CeO_2 nanocrystals was detected at 900°C. At 1000°C, small nanocrystallites of G-$Ce_2Si_2O_7$ appeared as a minor phase of 16 wt.% while the CeO_2 peaks began to narrow indicating a growth in the grain size of these nanocrystals. By 1100°C, 25 wt.% of the nanocrystallites in the film were G-$Ce_2Si_2O_7$ and further narrowing of the diffraction peaks indicated an increase in grain size for nanocrystallites of both phases. Finally, by 1200°C, 95 wt.% of the nanocrystallites in the film were converted to the G-$Ce_2Si_2O_7$ phase and the peak widths for both phases had narrowed further, indicating larger grain sizes in both phases of nanocrystallites. Overall, this analysis indicates that the amorphous cerium doped silicon oxide films grown using the MAC ECR PECVD system thermally evolve through the intial formation of CeO_2 nanocrystallites at mid-range annealing temperatures followed by a gradual transition to G-$Ce_2Si_2O_7$ nanocrystallites occurs at higher annealing temperatures. Furthermore, both types of nanocrystallites grow to larger sizes with increased annealing temperature and no other crystalline phases of cerium oxide or cerium silicate were observed.

Interestingly, the XRD results obtained for CeSiOx-08, a film grown using the GIV ECR PECVD system, demonstrate a much different thermal evolution over the

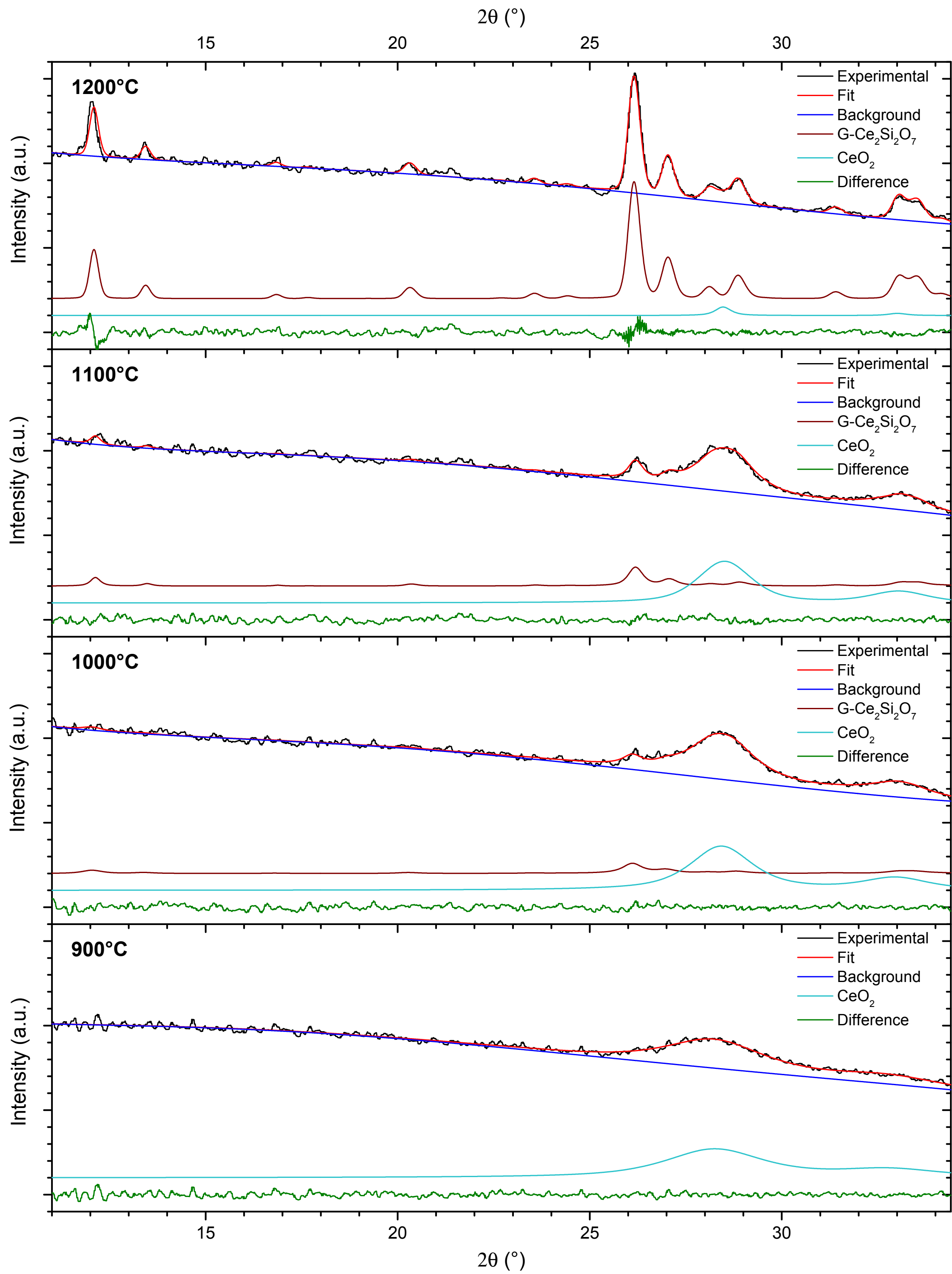

Figure 6.20: XRD spectra for CeORSO-25b annealed at 900–1200°C for 60 minutes.

900–1200°C temperature range. The results for this sample, shown in Figure 6.21, reveal that there are in fact three different phases of cerium disilicate that form within the film at various annealing temperatures but no CeO_2 nanocrystallites were detected. Nanocrystallites of $Ce_6[Si_4O_{13}][SiO_4]_2$ [110] formed at annealing temperatures as low as 900°C and remained the only crystalline phase detected in the film as the temperature was increased until 1200°C, replaced by a mixture of 13 wt.% G-$Ce_2Si_2O_7$ and 87 wt.% A-$Ce_2Si_2O_7$ [110]. There is some discrepancy between the relative peak intensities in the experimental data and the fits based on the $Ce_6[Si_4O_{13}][SiO_4]_2$ structure reported by Kępiński *et al.* [110], which is likely due to the structure being a theoretical construct rather than refined from high quality experimental data. However, the peak positions appear to be approximately the same, which indicates that the reported structure's unit cell matches that of the nanocrystallites in the film. Since the disagreement in peak intensities is minor, one can be reasonably certain that the correct phase has been identified. Unfortunately, the thin films produced in this study are not appropriate to use for the refinement of the atomic positions in the lattice necessary to improve the fit.

By contrast, the fit of the 1200°C data was very good. For this film, fluctuations were observed in the intensity of diffraction rings measured by the area detector indicating some preferred orientation in the A-$Ce_2Si_2O_7$ phase. Based on this observation, preferred orientation in the (022) and (110) directions of this phase was included in the analysis to obtain an optimal fit. While it is interesting that nanocrystallites formed within an amorphous film would have any preferred orientation rather than a random distribution, a full texture analysis would need to be performed to properly analyze the reasoning for this. Without this information, I would speculate that the preferred orientation may be related to how cerium diffuses through the sample with annealing, which appears to be towards the film/substrate interface and the film surface based

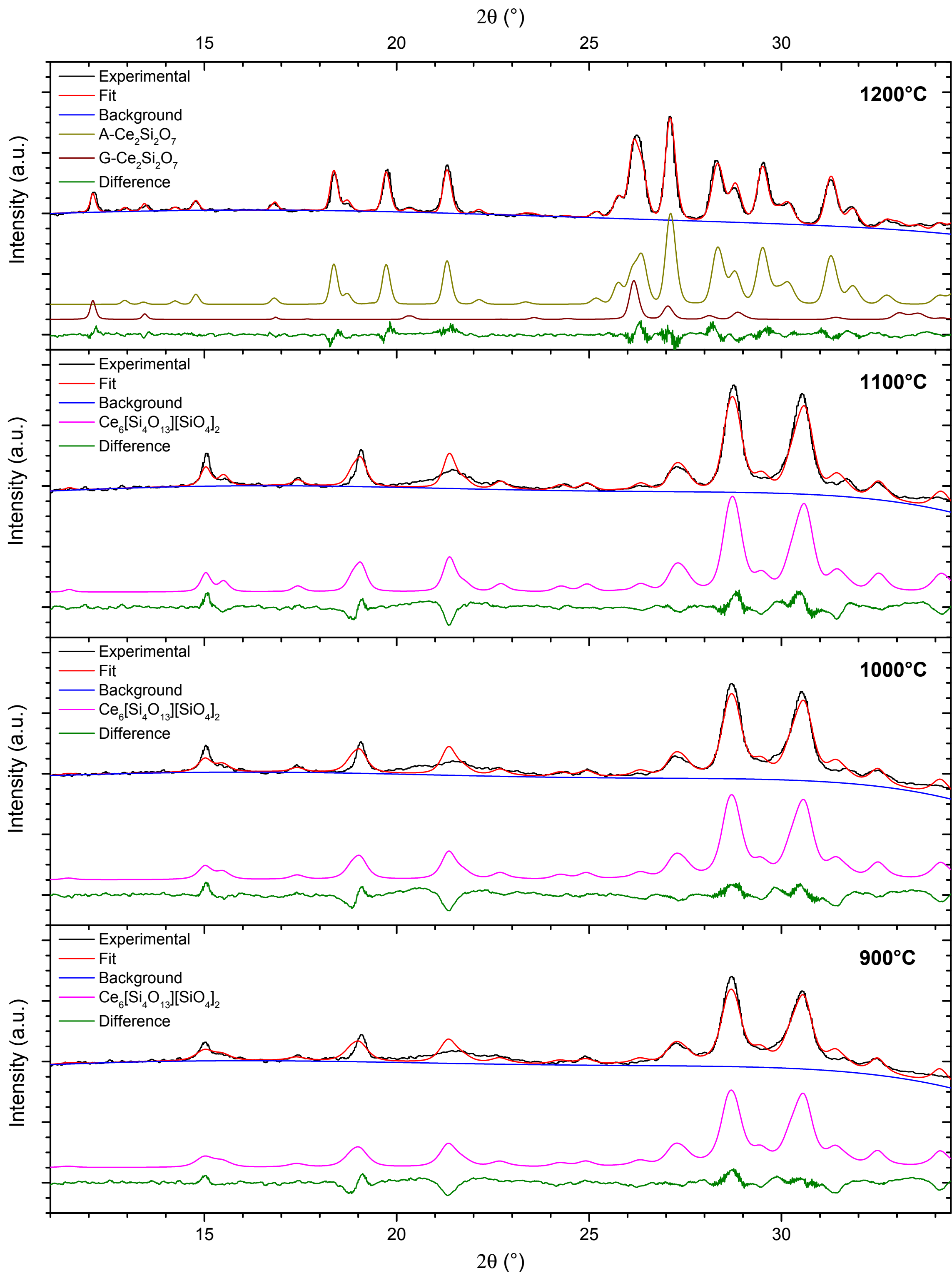

Figure 6.21: XRD spectra for CeSiOx-08 annealed at 900–1200°C for 60 minutes.

on Figures 6.17 and 6.18. Another possibility is that the preferred orientation is a result of stress in the film, which may be responsible for the columnar distribution of cerium disilicate nanocrystallites evident in Figure 6.17.

The apparent differences between the thermal evolution of cerium doped silicon oxide films grown using the MAC and GIV ECR PECVD systems are surprising, but could be reasonably explained through differences in film composition or density. As was discussed in Section 6.1, all of the samples grown using the MAC ECR PECVD system contained a small but measurable concentration of terbium which could conceivably influence the nucleation sites available in the films for nanocrystal formation, whereas none of the GIV ECR PECVD grown samples contained more than a trace concentration of terbium. The specific concentration of cerium in the film could also potentially affect the thermal evolution of the films, although this likely was not linked to the differences in phases observed since the CeORSO-03 and CeSiOx-08 samples exhibited significantly different XRD results despite having very similar atomic fractions of cerium. Alternatively, the comparison of the mass densities of the as-deposited films shown in Figure 6.4 clearly indicates that the MAC ECR PECVD grown films had consistently higher densities those grown using the GIV ECR PECVD system for a given level of rare earth incorporation. It is possible that the film density affects which phases are energetically favourable leading to the differences in formation and thermal evolution of nanocrystallites observed.

6.3 Isochronal Annealing of Cerium and Terbium Co-Doped Silicon Oxide

Having established the effect of annealing temperature on cerium within the silicon oxide matrix, the focus now shifts to the influence of terbium as a co-dopant in this materials system. Right from the initial experiments on cerium doped silicon oxide

films, it was apparent that terbium, which had been unintentionally incorporated in the initial samples, was strongly sensitized in these materials due to the very intense photoluminescence characteristic of radiative transitions from the $^5D_4 \rightarrow ^7F_6$, $^5D_4 \rightarrow ^7F_5$, $^5D_4 \rightarrow ^7F_4$, and $^5D_4 \rightarrow ^7F_3$ levels in Tb^{3+} ions that was observed. The terbium luminescence was orders of magnitude more intense than what had previously been observed in silicon-rich silicon oxide or silicon dioxide films [36] despite only low concentrations of terbium being present in the films. However, the question remained as to what was acting as a sensitizer in the material and how it was interacting with the terbium ions. To study this phenomenon, the properties of films with different ratios of cerium to terbium atoms were compared after annealing in a quartz tube furnace under flowing N_2 gas for 60 minutes at temperatures ranging from 600 to 1200°C.

The first film considered was CeSiO2-01 as the lightest cerium doped sample and consequently the closest in composition to silicon dioxide. The PL spectra for this sample can be found by referring back to Figure 6.8 including labels designating the intra-4f transition responsible for each of the Tb^{3+} luminescence peaks. In order to compare changes in the luminescence from cerium and terbium in these films, the height of the broad peak at short wavelengths corresponding to Ce^{3+} emission was plotted along with the height of the largest Tb^{3+} peak, which was consistently the $^5D_4 \rightarrow ^7F_5$ transition in all samples, as well as the ratio of these spectral components in Figure 6.22. Note that the peak heights were used to represent the emission intensity from cerium and terbium components rather than integrating the appropriate regions of each spectrum since this approach avoided the influence of overlapping spectral components and it proved quite difficult to fit the spectra in a consistent and reliable manner. To reduce the impact of the cerium background upon which the terbium emission lines were superimposed, the terbium peak height was taken as the difference

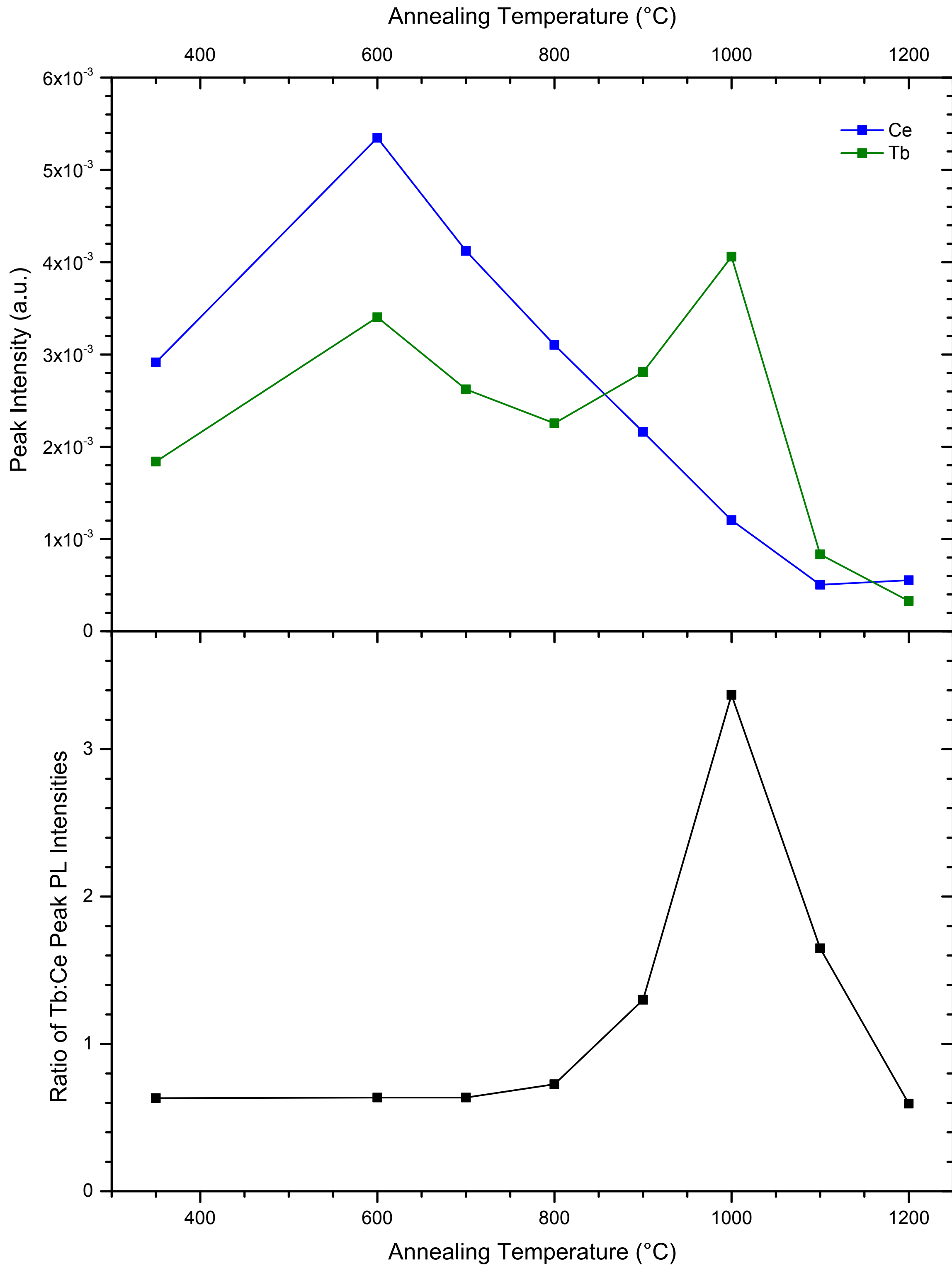

Figure 6.22: Comparison of peak PL intensities of cerium and terbium ions for CeSiO2-01 annealed at different temperatures for 60 minutes.

between the top and the base. A comparison of the peak heights, while not an accurate representation of the relative emission intensity of cerium and terbium, provided a convenient and consistent measure of the general trends in luminescenece from each component since their spectral shapes were found to remain fairly uniform for a given film over the different annealing conditions studied.

In Figure 6.22, it can be observed that the individual trends for emission from cerium and terbium ions were similar with both spectral components peaking in intensity at a low or mid-range annealing temperature before gradually decaying at higher temperatures. For the cerium component, the peak intensity occurred after 600℃ annealing while the brightest terbium emission was observed at 1000℃. Reaching a peak in PL intensity at a low- to mid-range temperature is typical for silicon dioxide films individually doped with cerium or terbium [36], although it was unusual that the terbium emission peaked at two separate temperatures. Furthermore, the change in terbium luminescence for temperatures up to 800℃ matched very closely the trend for luminescence from the Ce^{3+} ions. This low temperature correlation in the PL trends of the cerium and terbium spectral components raised the possibility that the terbium could be sensitized by the cerium ions as had been reported in a study by O. M. Ntwaeaborwa *et al.* [31]. However, the flat line in the ratio of the Tb:Ce peaks across this temperature range suggests that this probably wasn't the case since an energy transfer from cerium to terbium ions would be expected to increase this ratio. An increase in this ratio was observed at 1000℃, but from the previous analysis of this sample, the cerium coordination seemed to remain constant over the annealing temperature range and the higher temperature terbium peak was most likely due to a separate defect sensitizer which only excited the terbium ions.

The lack of cerium sensitization of terbium ions in this film was further evidenced by XANES and XEOL analysis at the O K-, Ce $M_{5,4}$-, and Si K-edges as shown in

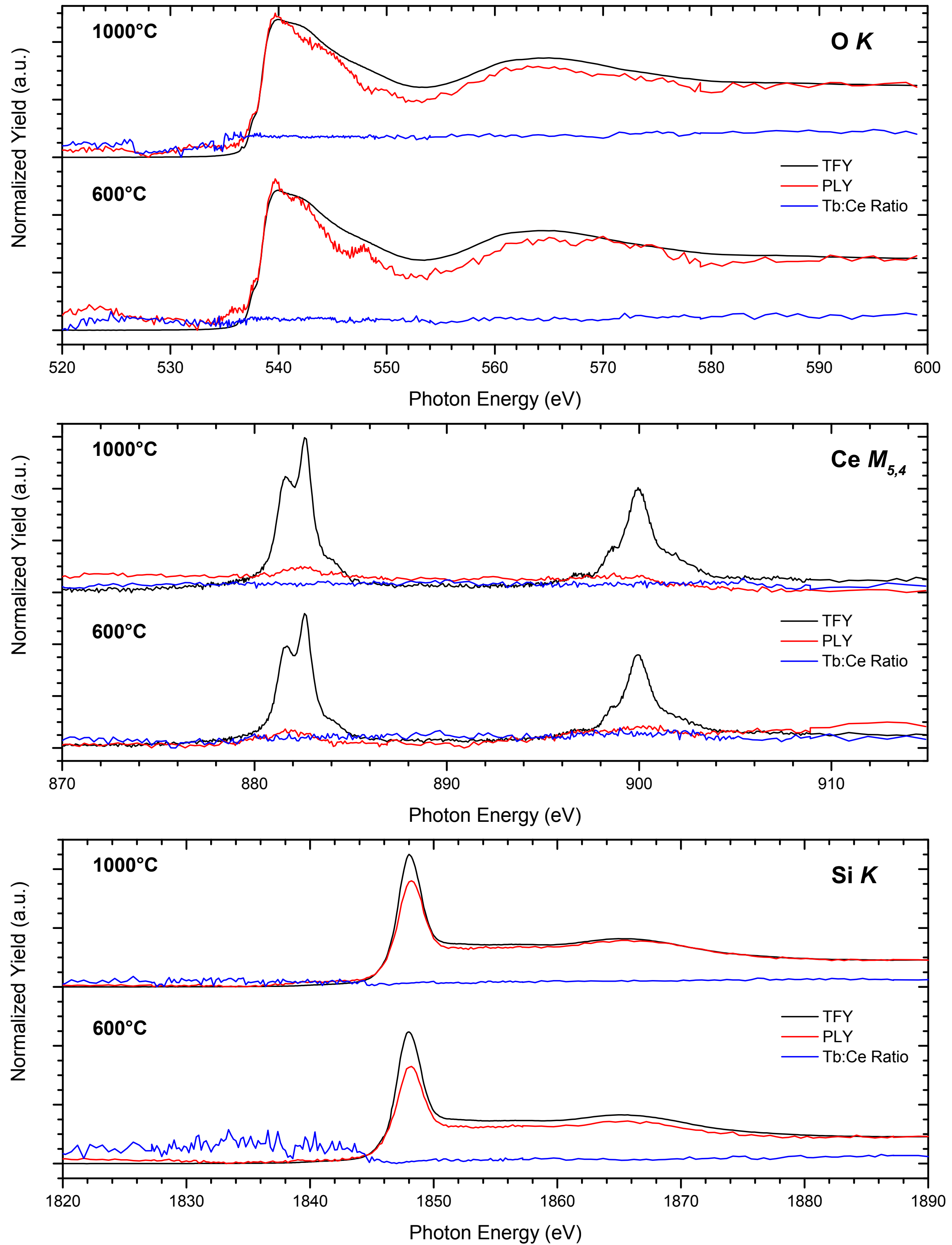

Figure 6.23: Comparison of XANES and XEOL spectra for 600 and 1000℃ annealed CeSiO2-01 at the O K, Ce $M_{5,4}$, and Si K absorption edges.

Figure 6.23. Here, the XANES spectra were compared with the normalized PLY and the ratio of peak intensities measured from terbium and cerium components in the XEOL spectra in order to probe site which may be sensitizing the rare earth ions. The PLY was consistent with features related to silicon oxide at the O and Si K-edges and there was a very weak increase in emission with features related to Ce^{3+} ions at the Ce $M_{5,4}$-edge for both the 600 and 1000°C annealed films. However, no significant fluctuation was observed in the Tb:Ce emission ratio spectra at any absorption edge for either film, which suggested that both types of rare earth ions were being excited through defects in the silicon oxide host matrix.

At the opposite end of the spectrum, CeSiOx-05 was a sample with a high concentration of cerium and only trace levels of terbium in which cerium disilicate nanocrystallites formed after high temperature annealing. The PL spectra for this film can be found by referring to Figure 6.13 and the trends in the cerium and terbium peaks are shown in Figure 6.24. The photoluminescence from both the cerium and terbium components of the photoluminescence were observed to increase in tandem as the annealing temperature was increased beyond 900°C consistent with the formation and growth of the cerium disilicate phase. This behaviour was atypical for terbium luminescence in a silicon oxide matrix, which usually decreases as the annealing temperature approaches 1200°C. Furthermore, the intensity of the Tb^{3+} emission in this film was also much stronger than would be observed in terbium doped silicon oxide with the same terbium concentration. These peculiarities combined with the increased ratio of terbium to cerium related emission over this temperature range indicated a strong possibility that the terbium was being sensitized by the cerium disilicate nanocrystallites in the film. Normally, one might expect the cerium peak to be suppressed if it was responsible for sensitizing the terbium, but in this case the cerium concentration far exceeds that of terbium and so it would not be significantly

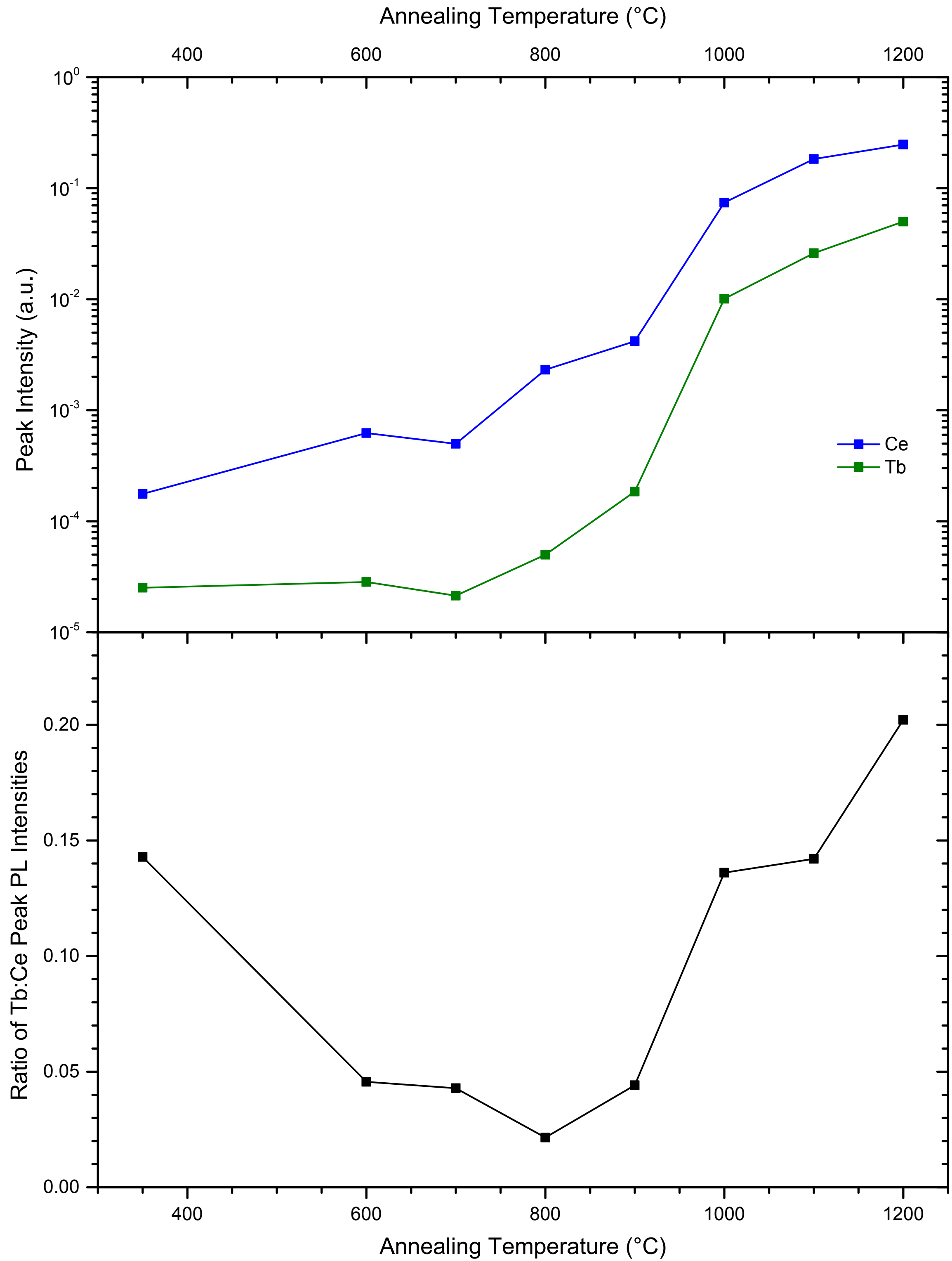

Figure 6.24: Comparison of peak PL intensities of cerium and terbium ions for CeSiOx-05 annealed at different temperatures for 60 minutes.

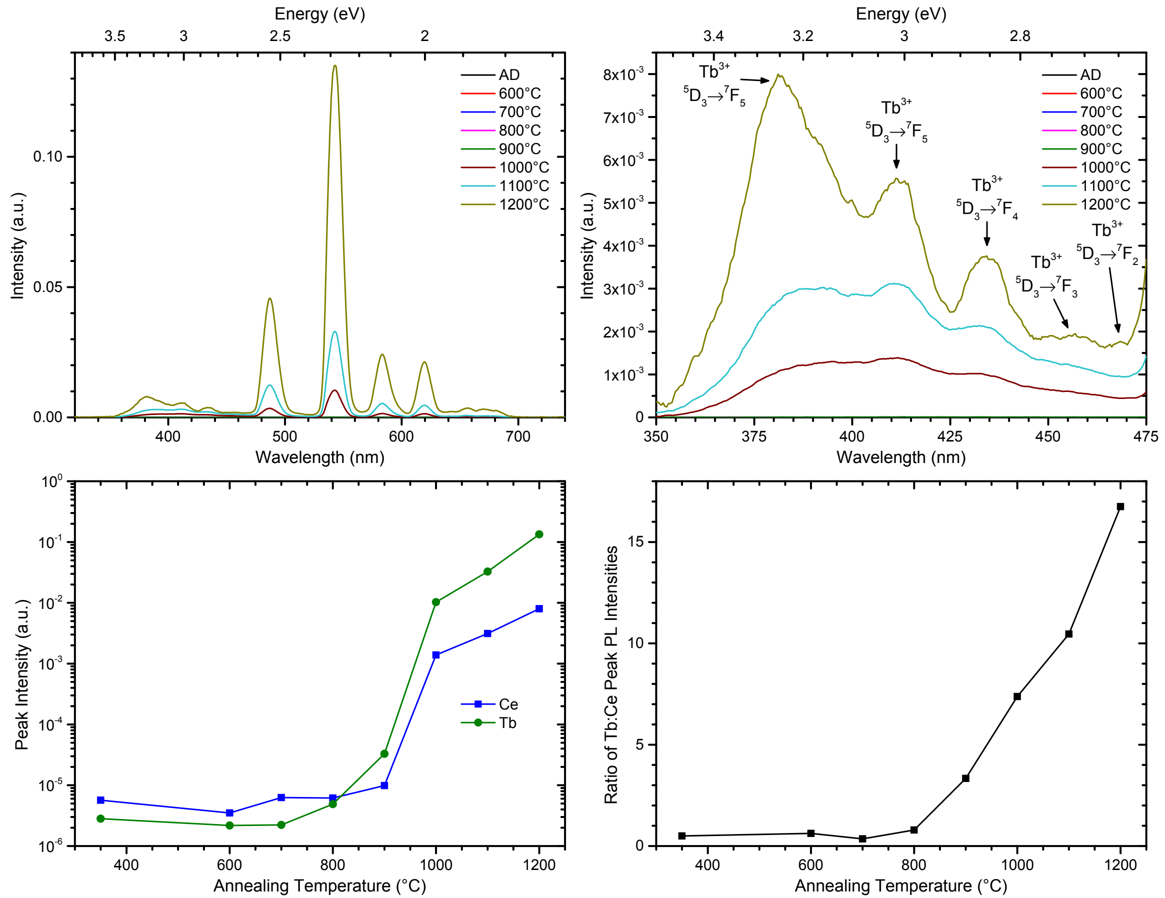

Figure 6.25: Comparison of the PL spectra and peak intensities of cerium and terbium ions for CeORSO-25b annealed at different temperatures for 60 minutes. The top right plot shows a magnified view of the region of the PL spectra corresponding to cerium emission where several weak Tb^{3+} emission lines were observed in addition to the typical, much stronger emission lines at longer wavelengths.

affected.

The next sample considered was CeORSO-25b, a film with a similar atomic fraction of cerium to CeSiOx-05 and a terbium concentration very close to that of CeSiO2-01. The isochronal PL spectra are displayed in Figure 6.25 along with plots of the emission associated with cerium and terbium at each annealing temperature. In this sample, the peak luminescence intensity for both cerium and terbium increased at an exponential rate above 900℃ and, much like in CeSiOx-05, the ratio of terbium to cerium emission also steadily increased in this high temperature regime. However, in this case, the

terbium emission was much stronger than the cerium emission, which appeared to be substantially suppressed compared to the CeSiOx-05 sample, allowing for additional weaker Tb^{3+} emission lines to be observed including the labelled $^5D_3\rightarrow^7F_6$, $^5D_3\rightarrow^7F_5$, $^5D_3\rightarrow^7F_4$, $^5D_3\rightarrow^7F_3$, and $^5D_3\rightarrow^7F_2$ transitions. In fact, the terbium peak was measured to be approximately 33 times higher than the strongest terbium peak in CeSiO2-01. Also, the XRD spectra discussed previously for this sample shown in Figure 6.20 show that the exponential increase in cerium and terbium emission at temperatures above 900°C coincides with the formation and growth of G-$Ce_2Si_2O_7$ nanocrystallites. Together, these results provided a strong indication that the cerium disilicate phase was indeed acting as a sensitizer for the Tb^{3+} ions, most likely through the excitation of ground state electrons into the $^5D_3$, $^5L_{10}$, or $^5D_2$ levels. According to Figure 2.7, the energy required to excite into the $^5D_3$ level is 3.26 eV which is approximately equivalent to the energy of the cerium disilicate photoluminescence peak following 1200°C annealing where terbium sensitization was strongest.

To support this hypothesis, XANES and XEOL analyses were conducted at the O K and Ce $M_{5,4}$ absorption edges to compare the site specific PL behaviour for the cerium and terbium components of the emission spectrum in cerium disilicate containing films with trace and light terbium doping. For this analysis, CeSiOx-08 was used rather than CeSiOx-05 as the sample with trace levels of terbium co-dopant since it contained a higher volume fraction of cerium disilicate – mostly A-$Ce_2Si_2O_7$ with a minor amount of G-$Ce_2Si_2O_7$ according to the XRD spectra shown in Figure 6.21) – within it giving it a more pronounced feature in the O K-edge spectrum. CeORSO-25b was chosen as the lightly co-doped film and both samples were annealed at 1200°C for 60 minutes. The resulting X-ray absorption and photoluminescence yield spectra are plotted in Figure 6.26 along with the ratio of terbium to cerium related photoluminescence. At the O K-edge, the TFY spectra for both samples exhibited absorption features

related to cerium disilicate and silicon oxide which correspond to the low energy shoulder at 537 eV and the main peak at 540.6 eV, respectively. The larger cerium disilicate feature in the CeSiOx-08 sample reflects its higher cerium content and the significant fraction of the layer that has converted to this phase. In both samples, the photoluminescence was more strongly resonant with the cerium disilicate feature than silicon oxide, although strong emission was stimulated through both sites. In the film with trace terbium co-doping, the Tb:Ce emission ratio was observed to decrease when excited through cerium disilicate sites. That is not to say the terbium emission decreased, but rather the component of the XEOL spectrum corresponding to cerium luminescence increased by a relatively greater amount, likely indicating that a saturation of the Tb^{3+} excited states was reached. However, in the CeORSO-25b film, which contained a higher terbium concentration and a smaller volume fraction of cerium disilicate, there was a well-defined peak in the otherwise constant Tb:Ce emission ratio corresponding to excitation through cerium disilicate specific sites. A similar set of results was obtained at the Ce $M_{5,4}$-edge with an increase in the Tb:Ce emission ratio observed when exciting through Ce^{3+} sites in CeORSO-25b while the CeSiOx-08 exhibited an inverted relationship which could be attributed to saturation. Note that the strange shape of the PLY, particularly for the CeSiOx-08 sample, was caused by a soft X-ray absorption saturation artifact resulting from having high concentrations of cerium inside a light host matrix as was discussed previously in Section 4.5. Combined, these results confirmed that cerium disilicate does indeed sensitize Tb^{3+} ions in cerium and terbium co-doped silicon oxide films.

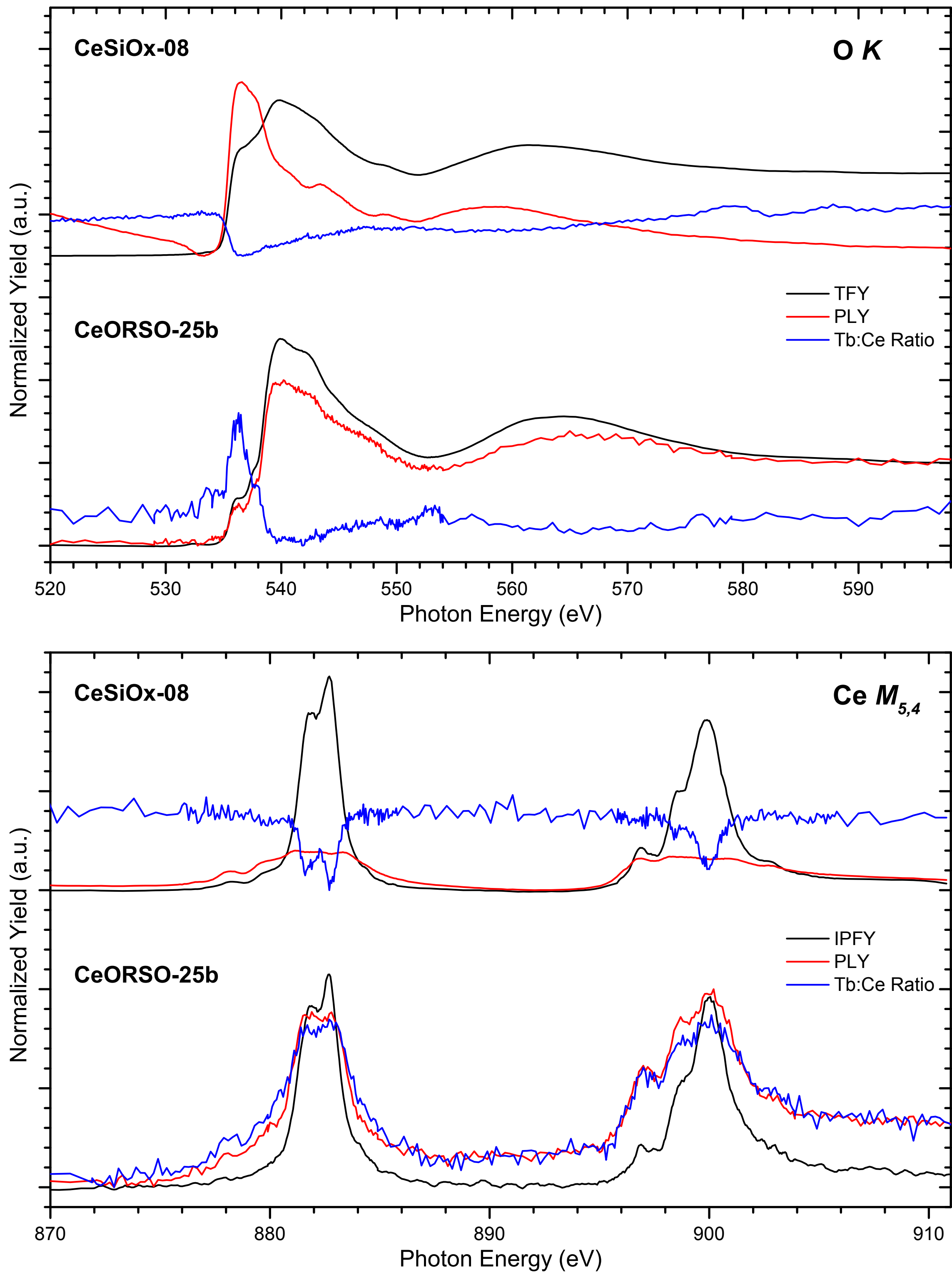

Figure 6.26: Comparison of XANES and XEOL spectra for 1200°C annealed CeSiOx-08 and CeORSO-25b at the O K and Ce $M_{5,4}$ absorption edges.

6.4 Isothermal Annealing of Cerium and Terbium Co-Doped Silicon Oxide

To further investigate the interaction between cerium disilicate nanocrystallites and terbium ions, a series of isothermal anneals were performed on films with different cerium and terbium concentrations at 1200℃ in a quartz tube furnace under flowing N_2 gas for times ranging from as short as five minutes to nine hours in duration. As was observed in the silicon-rich silicon nitride materials system, even minor changes in temperature were found to significantly alter the luminescence and structural properties of the cerium and terbium co-doped silicon oxide films. Isothermal annealing allowed for changes in the films to be studied in finer detail and, since annealing at temperatures above 1200℃ tends to cause problems regarding film integrity, allowed for an extended range of annealing conditions over which the growth of the cerium disilicate nanocrystallites could be studied compared to the 60 minute isochronal anneals.

In high cerium content films with trace levels of terbium co-dopant, large changes were observed in luminescence originating from both the Ce^{3+} and Tb^{3+} ions over the initial 30 minutes of annealing as evidenced by the PL spectra for CeSiOx-08 shown in Figure 6.27. Here, it can be observed that within in the first 30 minutes of annealing the cerium peak narrows, increases in amplitude, and becomes more symmetrical as its long wavelength tail disappears. XRD analysis was performed on the samples annealed for 7.5, 15, 60, and 240 minutes to help identify structural changes in the film. Fits of the intensity vs. 2θ spectra plotted in Figure 6.28 indicate that $Ce_6[Si_4O_{13}][SiO_4]_2$ nanocrystallites form within the first several minutes of annealing and remain the only crystalline phase present up to the 15 minute mark. However, this phase completely disappeared within 60 minutes of annealing, replaced by A-$Ce_2Si_2O_7$ nanocrystallites which remained the only phase present through 240 minutes

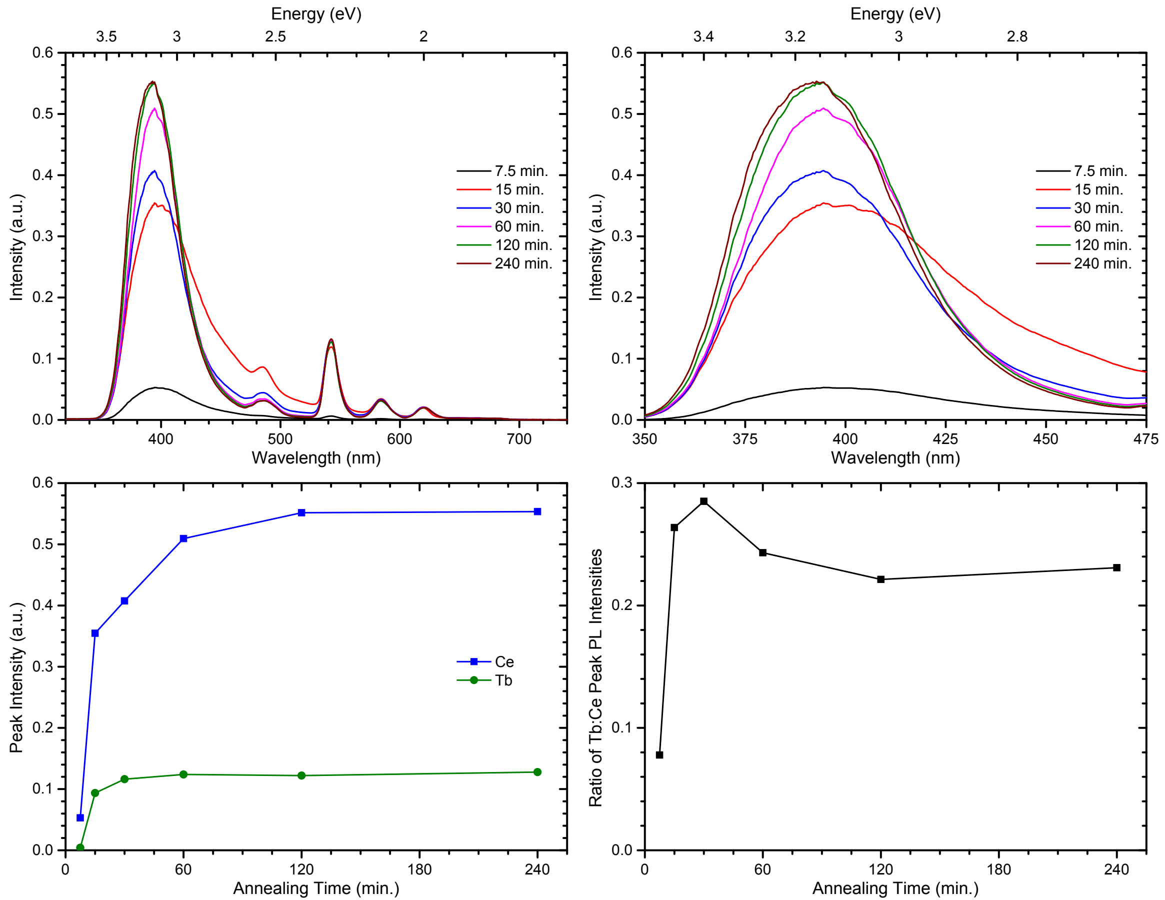

Figure 6.27: Comparison of the PL spectra and peak intensities of cerium and terbium ions for CeSiOx-08 annealed for different times at 1200°C. The top right plot shows a magnified view of the region of the PL spectra corresponding to cerium emission.

of annealing. Similar to the XRD analysis of the isochronally annealed CeSiOx-08 sample, the A-$Ce_2Si_2O_7$ phase exhibited preferred orientation in the (022) and (110) directions and this characteristic became more pronounced with longer annealing time.

Based on the PL and XRD results for this particular film, the increase in emission intensity after longer annealing times can be attributed to more of the cerium in the layer being converted into a cerium disilicate phase and the change in the PL spectral shape can be attributed to the conversion of $Ce_6[Si_4O_{13}][SiO_4]_2$ nanocrystallites into the A-$Ce_2Si_2O_7$ phase and possibly a reduction in radiative defects as the annealing time was increased. The A-$Ce_2Si_2O_7$ phase appeared to stabilize after 120 minutes of

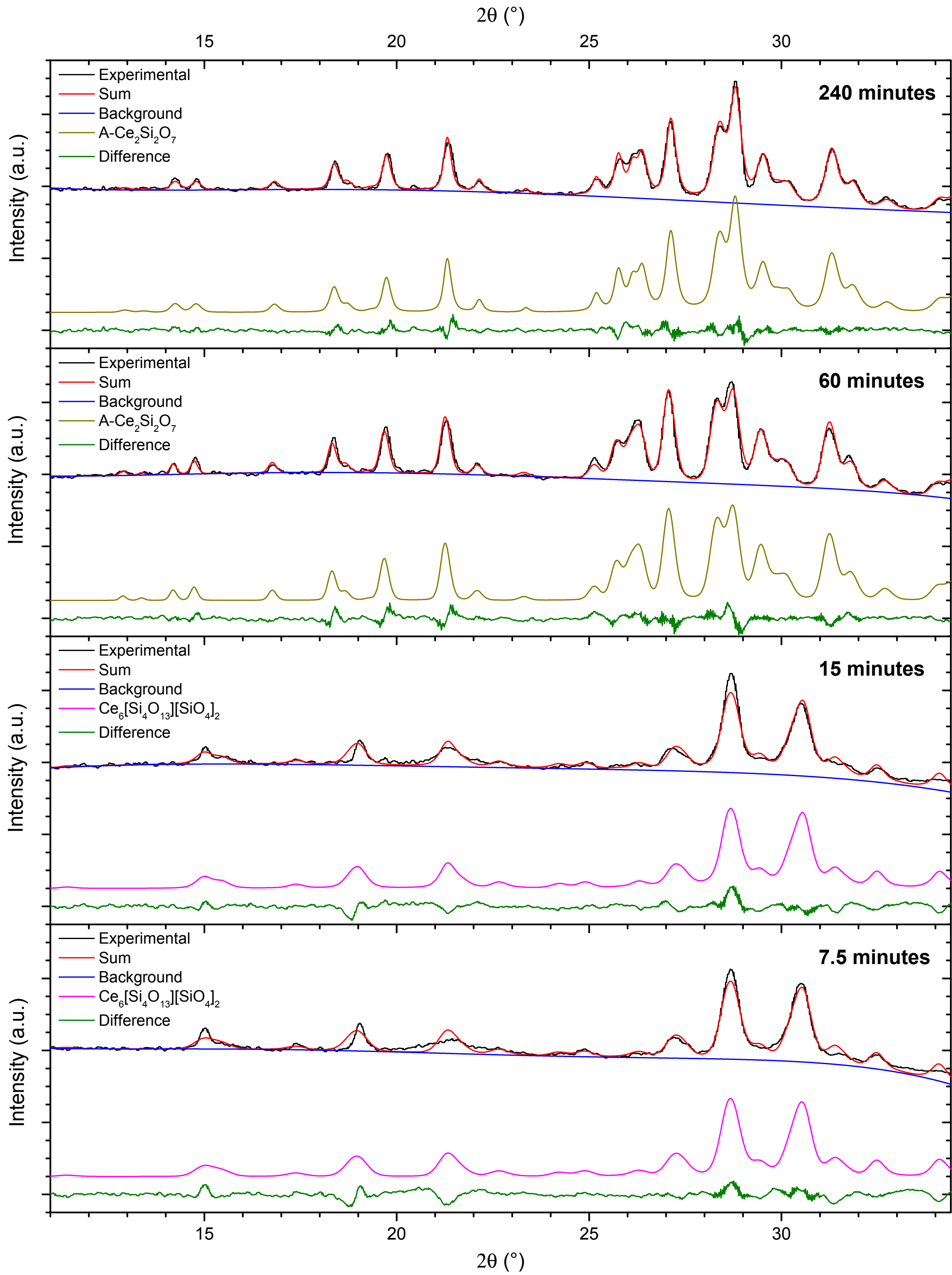

Figure 6.28: XRD spectra for CeSiOx-08 annealed at 1200°C for 7.5–240 minutes.

annealing. The minimal changes in the cerium luminescence observed beyond this time likely resulted from the reduction of defects and increases in the preferred orientation within the nanocrystallites as the average grain size continued to grow and grain boundaries became less prevalent. Due to the very low concentration of terbium in the film, Tb^{3+} essentially plateaued after 30 minutes of annealing when enough cerium disilicate was formed to saturate the excited states of the Tb^{3+} ions as discussed in Section 6.3. As a result, the ratio of Tb^{3+} to Ce^{3+} related emission increased rapidly in the early stages of annealing as cerium disilicate began to form and peaked at the 30 minute mark when the terbium saturation condition was met. Since further growth of cerium disilicate did not contribute to increased terbium excitation, the ratio decreased as the annealing time was extended further. It is possible that certain phases of cerium disilicate may sensitize the Tb^{3+} ions more effectively than others. However, if the specific phase was a factor, it was not clearly evident based on the analysis of this film since samples containing only $Ce_6[Si_4O_{13}][SiO_4]_2$ or A-$Ce_2Si_2O_7$ nanocrystallites were both found to exhibit similar terbium-related emission and any difference was likely minor compared to the aforementioned influences of cerium disilicate growth and terbium saturation.

In comparison, for films with a slightly more balanced ratio of cerium and terbium doping, the Tb^{3+} luminescence was not found to reach a similar plateau as exemplified by the PL spectra and peak intensity trends for CeORSO-25b shown in Figure 6.29. Here, both the Ce^{3+} and Tb^{3+} emission components were observed to follow a trend corresponding to the growth of the cerium disilicate phase similar to the changes in the cerium peak of the CeSiOx-08 film. The most significant changes in the emission peaks as well as the ratio of terbium to cerium emission occurred during the first several minutes of annealing as the cerium disilicate nanocrystallites, most likely the G-$Ce_2Si_2O_7$ phase as observed in the isochronal study of this sample (refer to

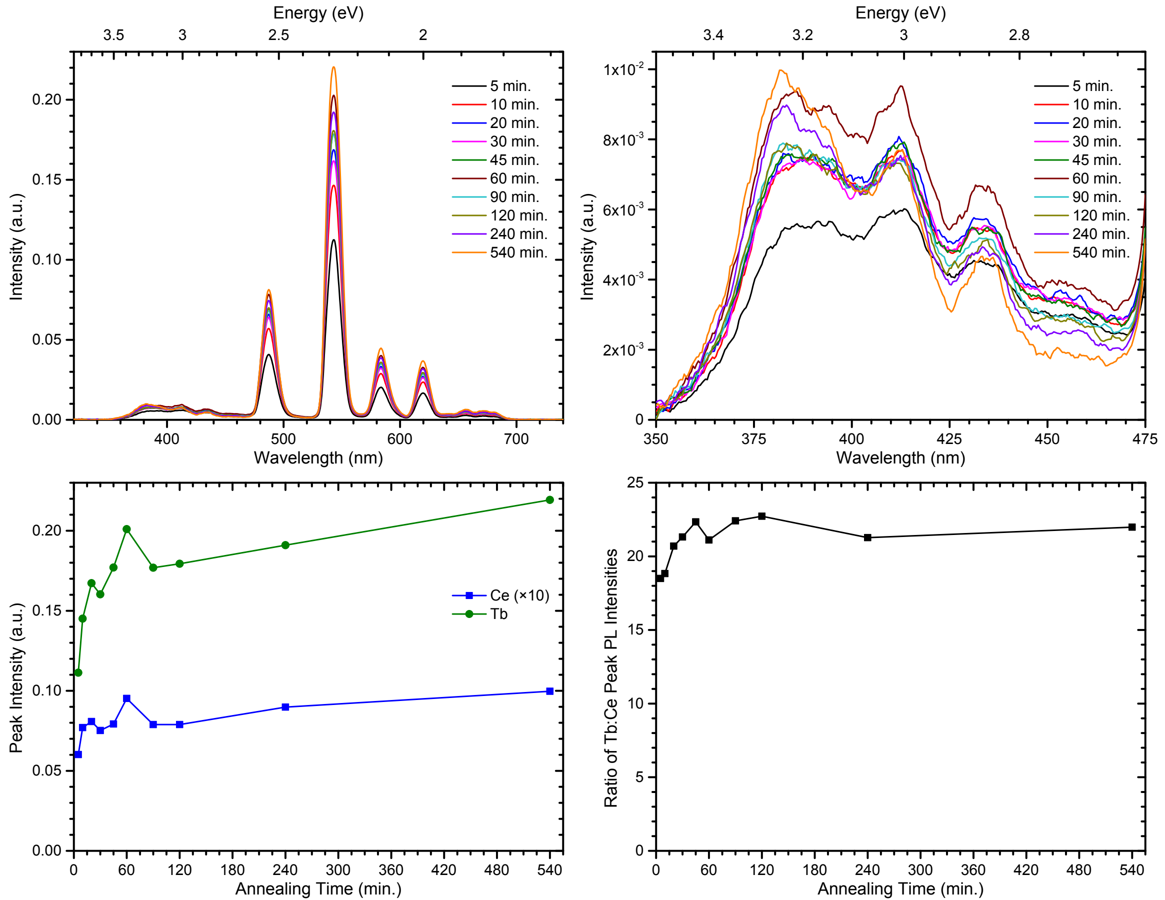

Figure 6.29: Comparison of the PL spectra and peak intensities of cerium and terbium ions for CeORSO-25b annealed for different times at 1200°C. The top right plot shows a magnified view of the region of the PL spectra corresponding to cerium emission where several weak Tb^{3+} emission lines were observed in addition to the typical, much stronger emission lines at longer wavelengths.

Figure 6.20), initially began to form and grow. However, it should be noted that the changes in the cerium peak were much smaller in magnitude than for terbium due to suppression related to the role of cerium disilicate as a sensitizer, so a 10 times multiplier was used in the plot comparing these trends as specified in the legend. On an absolute scale, the cerium emission peak went relatively unchanged over the range of annealing times studied. This was because the higher terbium concentration in the film allowed for nearly all of the energy absorbed by cerium disilicate to be transferred to the terbium ions and since this excitation channel did not reach saturation levels, the cerium peak remained suppressed. Close inspection of the PL spectra revealed

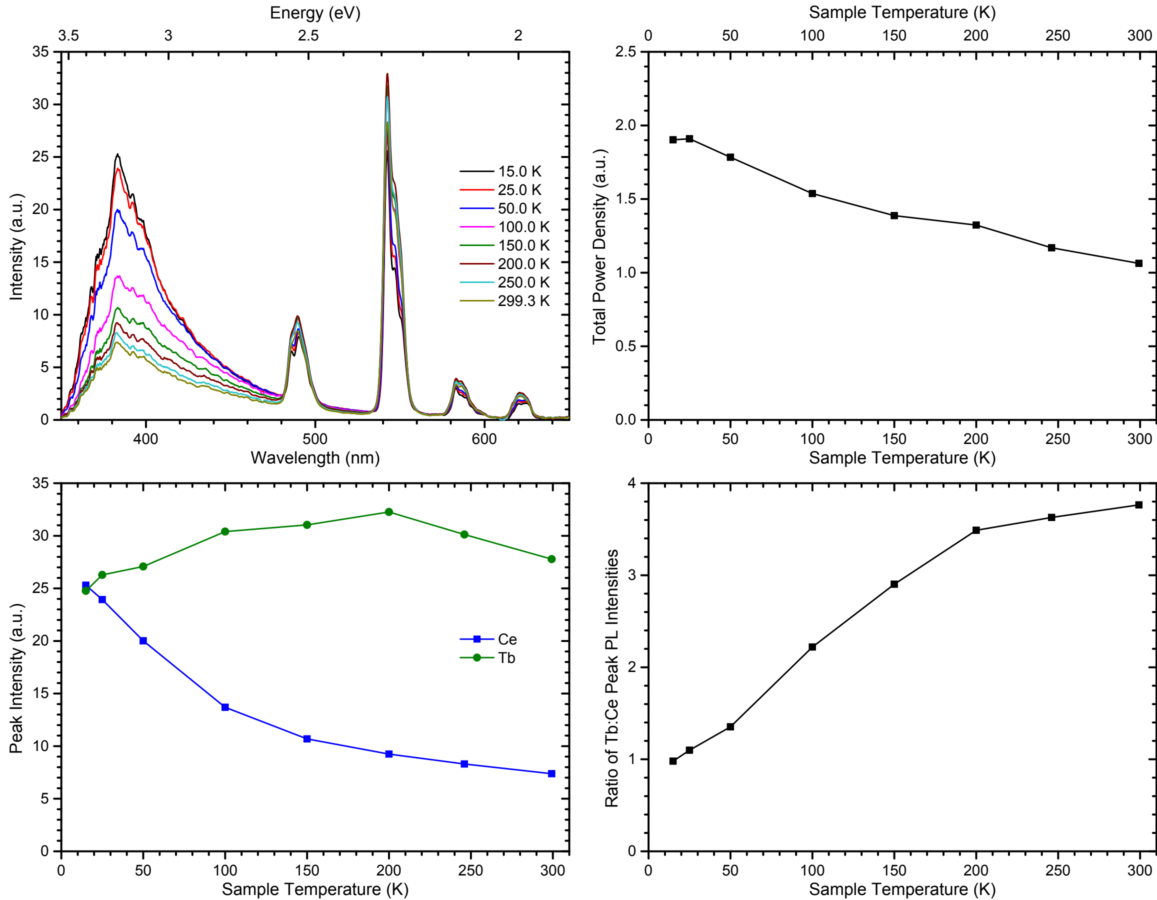

Figure 6.30: Comparison of the low temperature PL spectra, total power density, and peak intensities of cerium and terbium ions at different sample temperatures for CeORSO-03 annealed at 1200°C for 60 minutes.

that in addition to the small increases in intensity, a gradual narrowing of the cerium peak occurred as the annealing time was increased much like what was observed in the CeSiOx-08 isothermal PL spectra as the cerium disilicate phase continued to grow.

To further explore the sensitization of terbium by cerium disilicate, low temperature photoluminescence spectroscopy was performed on sample CeORSO-03 annealed at 1200°C for 60 minutes. The sample was cooled from room temperature (299.3 K) down to 15 K and PL spectra were measured at several temperatures during cooling as shown in Figure 6.30 along with plots of the trends in the cerium and terbium emission peaks as well as the total power density. For this analysis, the Ocean Optics

S2000 CCD spectrometer was used in place of the USB2000+ since it provided better resolution of the terbium peaks, albeit at the cost of worse performance at wavelengths below 400 nm which is the reason for the distorted shape of the cerium disilicate peak. Upon cooling, there was an initial increase in the emission from both the cerium and terbium components down to approximately 200 K, which was likely due to a reduction in non-radiative recombination, and the Tb^{3+} emission linewidths narrowed. As the sample was cooled further, the Tb^{3+} emission lines became weaker and narrower while the intensity of the $Ce_2Si_2O_7$ peak increased at a greater rate causing a large decline in the ratio of Tb^{3+} to $Ce_2Si_2O_7$ peak intensities. These trends continued all the way down to 15 K. Overall, the total power density of the photoluminescence was measured to increase at a fairly steady rate throughout the entire cooling process.

The observed behaviour suggests that the sensitization of Tb^{3+} ions by cerium disilicate occurs through a non-resonant energy transfer process. This could mean that the process relies on thermal broadening to bridge an offset between the participating cerium disilicate and the Tb^{3+} energy levels or possibly involves charge transfer through nearby defect states. In either case, the Tb^{3+} luminescence would be expected to weaken at lower temperatures due to the decreased phonon cut-off energy in the system and the increase in cerium disilicate emission could be attributed to a combination of reduced sensitization of the terbium ions and further quenching of non-radiative recombination at lower temperatures.

As a measure of the applicability of cerium and terbium co-doped silicon oxide films to display or solid state lighting applications, the PL spectra from six films with different ratios of cerium and terbium co-dopants annealed at 1200℃ for 60 minutes were used to calculate their chromaticity coordinates based on the CIE 1931 standard [121]. The PL spectrum of each sample is shown in Figure 6.31 underneath a colour patch representing its simulated emission colour based on this standard and

the coordinates for the samples were plotted on the chromaticity diagram shown in Figure 6.32. Here, it can be clearly seen that by varying the level of Tb co-doping, the emission colour can be tuned over a large range extending from violet or deep blue, associated with cerium disilicate, to the green colour that is characteristic of luminescence from Tb^{3+} ions.

In the context of display or solid state lighting applications, the large range of colours accessible by this material could make it a convenient platform on which to base devices. If combined with an appropriate red emitter, a large area of colour space would be accessible including the entire Planckian locus, which is the line that represents the chromaticity for different temperatures of blackbody radiation. This capability is especially important in solid state lighting where light sources are often targeted to have chromaticities at specific points along this curve.

Finally, to provide a visual comparison of the luminescence exhibited by the cerium and terbium doped silicon oxide and silicon-rich silicon nitride films studied in this research, Figure 6.33 shows photographs of the brightest PL from four different types of samples captured under normal room lighting conditions. In the top two images, the very strong blue emission from cerium disilicate nanocrystallites formed in CeSiOx-08 annealed at 1200℃ for 240 minutes is contrasted by similarly intense green emission from Tb^{3+} ions sensitized by cerium disilicate in CeORSO-25b annealed at 1200℃ for 480 minutes. The bottom two images show the relatively weak blue PL from Ce^{3+} ions incorporated in the silicon oxide host matrix in CeSiOx-07 and orange luminescence from amorphous Si-ncs formed in a 3% excess silicon content SRSN film grown by PECVD, both films annealed at 700℃ for 60 minutes under flowing N_2 ambient gas. Similar to Figure 6.15, the highly intense emission from the CeSiOx-08 and CeORSO-25b films caused the centre of the PL spot to appear white in the photographs due to saturation of the digital camera's CCD sensor.

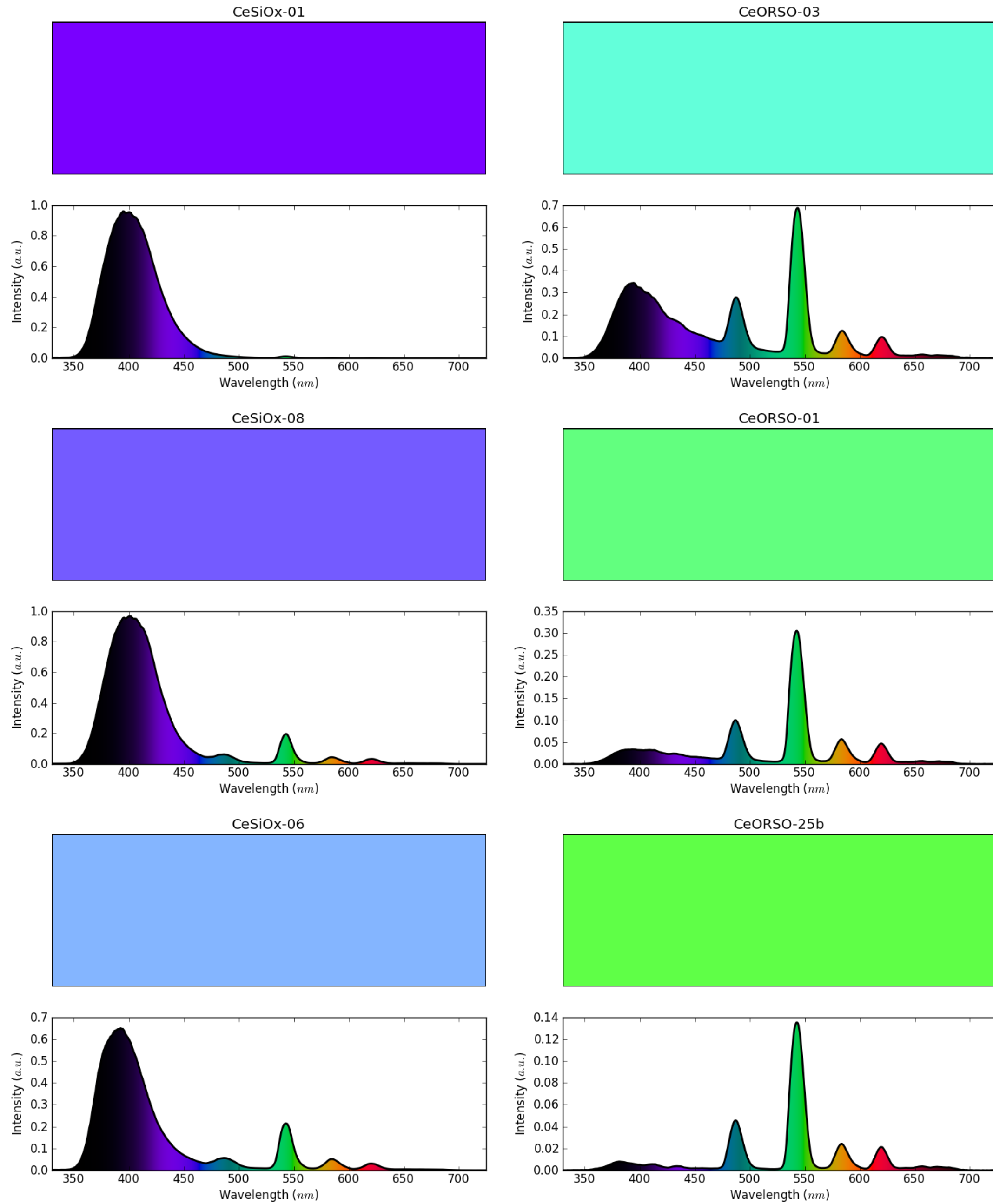

Figure 6.31: Comparison of PL spectra for films containing different ratios of cerium and terbium co-dopants annealed at 1200°C for 60 minutes. By varying the ratio of Tb^{3+} to $Ce_2Si_2O_7$ luminescence in the films, the chromaticity of the total emission spectrum can be controlled from violet-blue to green. The colours underneath the spectral curves represent the chromaticity of emission from each specific wavelength and the colour patch above each spectrum represents the chromaticity for the entire spectrum based on the CIE 1931 standard [121].

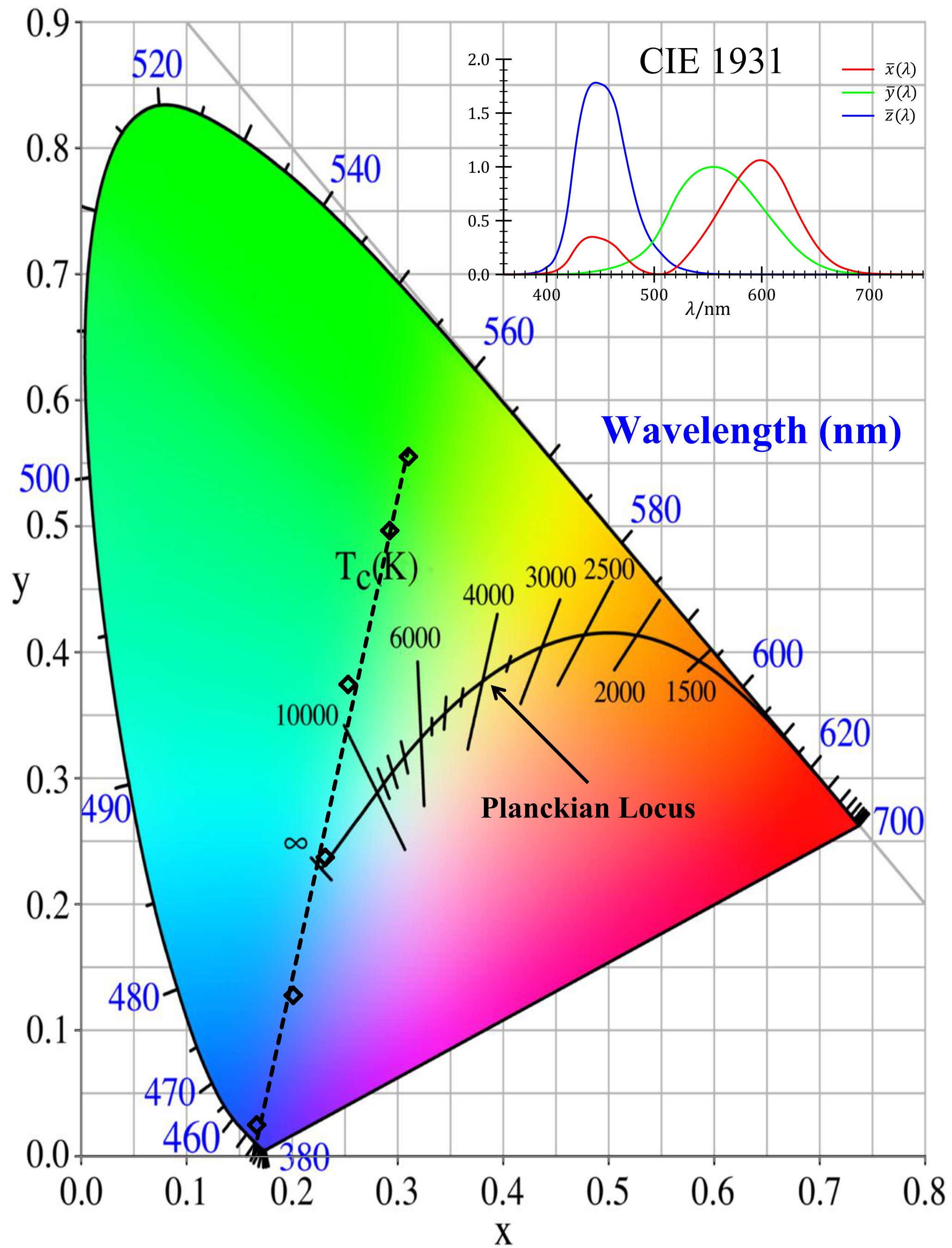

Figure 6.32: CIE 1931 chromaticity diagram depicting the emission colour for films containing different ratios of cerium and terbium co-dopants annealed at 1200°C for 60 minutes. The dashed line represents the linear best fit of the colour space coordinates of each sample and the Planckian Locus indicates the chromaticity of blackbody radiation of various temperatures. The CIE standard observer colour matching functions [121] upon which the chromaticity calculations were based are shown in the inset.

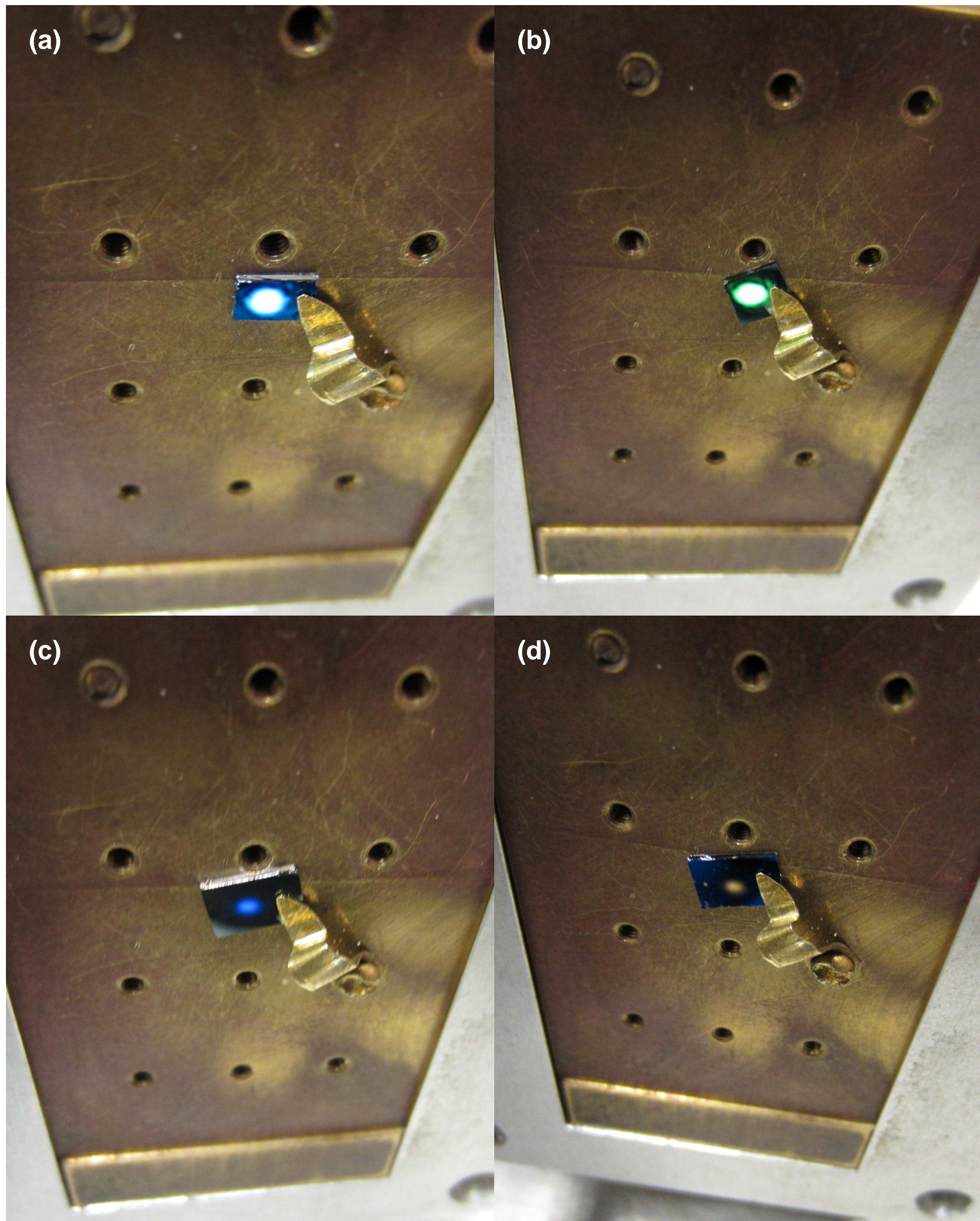

Figure 6.33: Photographic comparison of PL from (a) $Ce_2Si_2O_7$ nanocrystallites formed in CeSiOx-08 annealed at 1200℃ for 240 minutes, (b) Tb^{3+} ions sensitized by $Ce_2Si_2O_7$ in CeORSO-25b annealed at 1200℃ for 480 minutes, (c) Ce^{3+} ions incorporated in the silicon oxide host matrix in CeSiOx-07 annealed at 700℃ for 60 minutes, and (d) amorphous Si-ncs formed in a SRSN film with moderate excess silicon content (Si_{ex}=2%) annealed at 700℃ for 60 minutes.

Chapter 7

Conclusions

Through experiment, it has been demonstrated that bright luminescence can be attained from Si-ncs formed in SRSN thin films deposited by radio frequency PECVD, ICP CVD, and ECR PECVD using different combinations of source gases. Each system produced films with highly tuneable luminescence through adjustment of the process gas flow rates. Post-deposition annealing only had a minor impact on the peak PL energy, but the annealing temperature and ambient gas strongly affected the PL intensity. For 60 minute anneals in a quartz tube furnace, the best results were achieved at low temperatures under flowing 5% H_2 in N_2 gas. Hydrogen appeared to play an important role in enhancing luminescence from SRSN films. Much of this may be attributed to hydrogen passivation of dangling bonds at the Si-nc surfaces, but XANES spectra at the Si K- and $L_{3,2}$-edge also indicated that hydrogen incorporated within the AD film may increase the number of nucleation sites for Si-nc formation. In addition, the XANES spectra provided evidence of composition-dependent phase separation and structural re-ordering of both the Si-ncs and the nitride host matrix upon annealing. Unfortunately, self-absorption or photon scattering from void formation in the film obscures the Si–Si and Si–N resonance peaks at the Si $L_{3,2}$-edge, and a full account of this effect has yet to be realized. This obstacle must be addressed before realistic

information about the Si-nc and nitride host matrix structures could be derived from such spectra.

Expanding upon the results obtained from the isochronal annealing experiments, an extended series of isothermal anneals of SRSN films was performed at 600 and 800°C using a rapid thermal processor. Based on these experiments, it has been shown that the luminescent and structural properties were in accordance with those expected from theory if emission occurs through quantum confinement effects. The PL peak steadily shifted to lower energy as the annealing time was increased at both temperatures correspondingly with increasing diameter of Si-ncs. Further, the peak shifting occurred more slowly as it became lower in energy, which could be expected since a greater number of additional Si atoms must be added to further increase the Si-nc diameter and make the nanoclusters grow larger in size. Remarkably, the Si-ncs appeared to form and grow very rapidly, with large, abrupt shifts in peak PL intensities of 0.45 and 0.57 eV relative to the AD film after only 2 s of annealing at 600 and 800°C, respectively. The apparent fast growth was indicative of a fast transient diffusion mechanism for excess silicon within SRSN films. It was also interesting to note that the total power density showed an increasing trend with longer annealing times over the time period studied for the lower temperature anneals. However, the total power density during the higher temperature anneals peaked after 6–30 s of annealing before steadily decaying with longer times. The decay in total power density observed in the higher temperature data was attributed to the Si-ncs undergoing Ostwald ripening and restructuring in the silicon nitride host matrix. XANES spectra at the Si K- and $L_{3,2}$-edges, which revealed a steady increase in the Si–Si bonding resonance in the 600°C films following an abrupt increase after 2 s of annealing, support the proposed growth model. These spectra also exhibited large changes in the Si–N resonance as the films were annealed. At 800°C, a much larger increase in the Si–Si resonance

was observed after 2 s of annealing, but this peak did not grow noticeably larger as the annealing time was further increased, which supports the suggestion of Ostwald ripening. There was also a large change in the Si–N resonance between 10 and 60 s of annealing, which suggested that the decay in luminescence intensity observed at longer annealing times could be related to restructuring of the silicon nitride matrix.

Preliminary work on cerium doped SRSN films was inconclusive as to the viability of the silicon-rich silicon nitride host matrix for rare earth sensitization. Despite the cerium ions coordinating in the requisite Ce^{3+} oxidation state, cerium-related luminescence was not observed in any of the samples tested. It remains unclear if the lack of Ce^{3+} emission was due to inadequate dimensions of the silicon nanocluster sensitizers or a limitation imposed by the silicon nitride host matrix.

In addition to the studies of SRSN films, an investigation of the cerium and terbium co-doped silicon oxide materials system was conducted. The films characterized in this research were deposited using two different ECR PECVD systems with *in-situ* rare earth doping. Films were grown using deposition parameters typical for SiO_2 as well as with a significant overpressure of oxygen. It was found that under both conditions, the rare earth ions substitutionally replaced silicon in the film and that the films grown under oxygen-heavy conditions had more than double the rare earth incorporation for a given rare earth cell temperature, allowing for very high cerium doping concentrations in excess of 10 at.% to be achieved. The photoluminescence in as-deposited films was most intense in the lightly doped films and extemely weak in the most highly doped films due to strong quenching related to ion-ion interactions and a significant portion of cerium atoms being coordinated in the optically inactive Ce^{4+} coordination. The substitutional replacement of silicon with the rare earth dopants combined with the significant degree of Ce^{4+} bonding and HRTEM images showing a marbled microstructure suggested that the film growth occurred as an alloy

of competing silicon oxide and cerium oxide phases.

Isochronal annealing studies on cerium doped silicon oxide films revealed trends in the luminescent and structural properties of the films corresponding to two distinct temperature ranges: the low temperature regime for annealing below 900℃ and the high temperature regime from 900–1200℃. The PL of the most lightly doped films, with up to 0.4 at.% cerium, was found to be most intense in the low temperature regime where Ce^{3+} ions were sensitized by defects in the silicon oxide host matrix. By contrast, the heavily doped films had very weak PL in the low temperature regime where the cerium ions were found to largely coordinate in optically inactive Ce^{4+} states and were more prone to quenching from ion-ion interactions due to their high concentration. However, the films doped with more than 0.4 at.% cerium exhibited a strong increase in PL at temperatures above 900℃ which coincided with the formation and growth of cerium disilicate nanocrystallites. The luminescence from these nanocrystallites was violet or blue in colour, having a peak wavelength between 380–405 nm, and exceeded the most intense PL observed in the low temperature regime by up to two orders of magnitude.

TEM and XEDS analysis indicated that after high temperature annealing, large volume fractions of the heavily cerium doped silicon oxide films were converted into $Ce_2Si_2O_7$ nanocrystallites with most of the cerium ions incorporating in these nanostructures. In silicon oxide films doped with up to 8.9 at.% cerium, $Ce_2Si_2O_7$ remained the minority phase and the film microstructure consisted of $Ce_2Si_2O_7$ nanocrystallites dispersed throughout the amorphous silicon oxide host matrix. However, it was found that in films doped with higher concentrations of cerium, such as one film which contained 11.6 at.% cerium, the microstructure of the film was reversed and the cerium disilicate phase formed a continuous structure with regions of amorphous silicon oxide distributed in small pockets throughout the layer. This result indicated that it may be

possible to form an entire layer of cerium disilicate by annealing a cerium doped silicon oxide film with the appropriate composition. XRD analysis revealed that films grown using the two different ECR PECVD systems thermally evolved through a different progression of phases. Upon annealing, the films grown using the MAC ECR PECVD system were found to form CeO_2 nanocrystals at 900°C before converting to G-$Ce_2Si_2O_7$ at higher temperatures while films deposited by the GIV ECR PECVD system were found to form $Ce_6[Si_4O_{13}][SiO_4]_2$ nanocrystallites at 900°C, which were then converted into A-$Ce_2Si_2O_7$ by 1200°C with perhaps an intermediary G-$Ce_2Si_2O_7$ phase. The reason for the differences in thermal evolution between samples produced by each system was unclear, but may be related to the higher mass density or influence of low levels of terbium co-dopant in the MAC ECR PECVD grown films.

Cerium and terbium co-doped silicon oxide films were also studied through the isochronal annealing of samples with varying composition. Narrow peaks characteristic of the $^5D_4 \rightarrow ^7F_6$, $^5D_4 \rightarrow ^7F_5$, $^5D_4 \rightarrow ^7F_4$, and $^5D_4 \rightarrow ^7F_3$ intra-4f transitions in Tb^{3+} ions were observed in the PL spectra of all of the samples tested along with the emission from Ce^{3+} ions and cerium disilicate nanocrystallites described previously. In the as-deposited films and those annealed in the low temperature regime, the Tb^{3+} ions were sensitized by defects in the silicon oxide host matrix and possibly through energy transfer from Ce^{3+} ions as well, which had been reported in previous studies. However, the results of the PL, XANES, and XEOL analysis did not support this energy transfer mechanism as the sensitization pathway in the films tested. In samples containing cerium disilicate nanocrystallites, the Tb^{3+} emission was found to be especially strong, up to two orders of magnitude more intense than the brightest emission observed in the low temperature regime. Trends in PL and XRD spectra confirmed a strong correlation between the enhanced Tb^{3+} emission and the formation and growth of the cerium disilicate nanocrystallites in the films. In addition to the $^5D_4 \rightarrow ^7F_{3\text{–}6}$

emission lines of Tb^{3+} ions observed in all films, samples containing cerium disilicate nanocrystallites and more than trace levels of terbium co-dopant exhibited weak emission lines corresponding to the $^5D_3 \rightarrow ^7F_6$, $^5D_3 \rightarrow ^7F_5$, $^5D_3 \rightarrow ^7F_4$, $^5D_3 \rightarrow ^7F_3$, and $^5D_3 \rightarrow ^7F_2$ transitions in Tb^{3+} ions. XANES and XEOL analysis were applied to probe the site specific luminescence in films with different levels of terbium co-doping. This analysis revealed that not only was the Tb^{3+} luminescence enhanced when excited through energies resonant with cerium disilicate compared to other energies including the silicon oxide host matrix, but the ratio of terbium to cerium related luminescence was also higher as long as the films contained sufficient level of terbium co-doping. These results confirmed that the Tb^{3+} ions were being sensitized through an energy transfer process from the cerium disilicate nanocrystallites and this was likely occurring through the excitation of ground state electrons into the $^5D_3$, $^5L_{10}$, or $^5D_2$ levels of the Tb^{3+} ions.

Isothermal annealing experiments at 1200°C on cerium and terbium co-doped silicon oxide films provided more detailed information on the formation of cerium disilicate nanocrystallites and their interaction with Tb^{3+} ions. In this work, XRD analysis of a GIV ECR PECVD grown film indicated that $Ce_6[Si_4O_{13}][SiO_4]_2$ nanocrystallites formed within the first minutes of annealing and remained the only crystalline phase present through at least 15 minutes. By the 60 minute mark, only A-$Ce_2Si_2O_7$ nanocrystallites were found in the film and this phase exhibited preferred orientation which became more pronounced as the annealing time increased further. The structural changes were linked with blue-shifting and narrowing of the cerium disilicate peak in the PL spectra, but it was unclear if the sensitization of Tb^{3+} ions was affected by the specific phase of cerium disilicate in the film. Low temperature PL analysis of a sample containing G-$Ce_2Si_2O_7$ nanocrystallites cooled to temperatures ranging from 15–300 K indicated that the nature of the energy transfer process through which

cerium disilicate nanocrystallites sensitize Tb^{3+} ions was likely non-resonant, either relying on thermal broadening or perhaps charge transfer through nearby defect states to bridge a small energy offset between the donor and acceptor energy levels. Finally, the chromaticities of films containing different relative concentrations of cerium and terbium and annealed at 1200°C for 60 minutes were compared to determine how well the emission colour could be tuned by controlling the ratio of cerium disilicate to Tb^{3+} emission. It was found that the photoluminescence from the films had chromaticities that formed a linear path through colour space, extending from violet through various shades of blue and into the green chromaticities characteristic of Tb^{3+} emission. If combined with an appropriate red colour component, a large portion of colour space including the entire Planckian locus could be accessed making it favourable for display and solid state lighting applications.

Chapter 8

Future Work

The results presented in this thesis indicate that silicon-rich silicon nitride and cerium and terbium co-doped silicon oxide films are both promising candidate materials for silicon-based visible luminescenct devices. Using this research as a foundation, there is significant opportunity to further explore both material systems.

Relative to the extensive research that has been conducted on the silicon-rich silicon oxide material system, the study of silicon-rich silicon nitride is still in its infancy. An in-depth study focused on modeling the complex growth behaviour of silicon nanoclusters, including the fast initial growth and eventual Ostwald ripening processes discussed in Sections 5.3 and 5.4, would be valuable for better understanding the properties of these materials as well as optimizing the deposition and processing conditions. Additionally, it has yet to be determined why in certain cases, the silicon nanoclusters formed in silicon-rich silicon nitride films have amorphous rather than crystalline structure regardless of the annealing conditions while other films produced with the same technique but with a different deposition system only contain crystalline silicon nanoclusters. It would also be interesting to study the role of hydrogen, which has already been observed to play an important role in the luminescence of silicon nanoclusters, in the nucleation and growth of silicon nanoclusters.

To date, very little work has been reported in literature on rare earth doped SRSN, especially regarding the sensitization of rare earth ions that emit in the visible spectrum. The preliminary experiments conducted for cerium doped SRSN discussed in Section 5.5 warrant a full follow-up study to determine the precise reason that Ce^{3+} luminescence was not observed despite the cerium ions having the appropriate oxidation state. Photoluminescence excitation (PLE) spectroscopy, in which PL spectra are measured as a function of excitation energy, could be used to monitor the bandgap energies of the silicon nanoclusters formed in the films and may also provide a means of resonantly exciting the Ce^{3+} ions to verify that they are coordinated in an optically active state. With this information, the film composition and annealing conditions can be refined to obtain silicon nanoclusters that have bandgap energies resonant with the excitation energy of the Ce^{3+} ions. If successful, further studies can be conducted to measure the quantum efficiency of the films, optimize parameters such as doping concentrations, and model the sensitizing behaviour. If the cerium ions prove to be optically inactive in the silicon-rich silicon nitride host matrix despite being coordinated in the trivalent oxidation state, various compositions of silicon-rich silicon oxynitride or carbonitride films could be tested as alternative host matrix materials which may be more favourable for cerium luminescence. The sensitization of other visibly emitting rare earth dopants such as terbium, europium, or praseodymium could also be studied using a similar combination of XANES and PLE spectroscopy to develop green and red emitters to accompany the blue emitting cerium doped materials.

The study of cerium and terbium co-doped silicon oxide films containing cerium disilicate nanocrystallites presented in this thesis is the initial research conducted on this material and the intriguing results open many avenues for further study of this relatively unknown material system. Even basic material properties such as

the band structure of the different cerium disilicate phases remains unknown and would provide valuable insight on the experimental results that have been obtained thus far. Currently, photoluminescence excitation, time-resolved photoluminescence spectroscopy, and quantum efficiency studies are being conducted on these materials to more closely examine the sensitization of the terbium ions. The materials are also currently being investigated for use as a downshifting layer in solar cells due to their transparency at near-infrared and visible wavelengths, strong absorption of ultraviolet light by the cerium disilicate nanocrystallites, and efficient energy transfer to the Tb^{3+} ions which emit at wavelengths favourable for many solar cell materials.

Another interesting application to explore is the development of a three or four level laser system based on the cerium disilicate to Tb^{3+} energy transfer process. For a four level laser, the $^5D_4$ level of the Tb^{3+} ions could be the upper laser level, the $^7F_5$ level (or one of the other $^7F_{0–6}$ levels) of the Tb^{3+} ions could serve as the lower laser level, and the cerium disilicate conduction and valence bands could act as the pump band and ground state, respectively. The much shorter lifetime of electrons in the conduction band of cerium disilicate (approximately on the order of nanoseconds) compared to the very long lifetime of electrons in the $^5D_4$ level (on the order of milliseconds) along with the fast non-radiative energy transfer process from the cerium disilicate to the Tb^{3+} ions is ideal for achieving population inversion at the upper laser level. Also, since the film can be patterned using the same methods as silicon oxide, such as photolithography, it would be reasonably straightforward to design the laser cavity (e.g., a ridge waveguide laser) and implement the design on a chip.

It would also be interesting to investigate the sensitization of other co-dopants in cerium doped silicon oxide films containing cerium disilicate nanocrystallites as a substitute or supplement for terbium, particularly a red emitting rare earth ion such as europium or praseodymium. Given how effective cerium disilicate has been found

to sensitize terbium, it may be possible to also efficiently sensitize other rare earth ions through a similar energy transfer process or alternatively use the Tb^{3+} ions as an intermediary to transfer energy to a different type of rare earth ion. Developing a red emitter of similar intensity to the blue and green luminescence obtained in the cerium and terbium co-doped silicon oxide films would allow for the chromaticity of a light emitting device based on this material system to be controlled over a large area of colour space including chromaticities consistent with the Planckian locus, which is favourable for display and solid state lighting applications.

Finally, for either of the silicon-rich silicon nitride or cerium and terbium co-doped silicon oxide materials to be useful in most practical applications, it is necessary to develop efficient electroluminescent devices. This may prove to be quite challenging due to the insulating nature of these materials and difficulty of charge injection into the nanostructures. However, films containing cerium disilicate have an inherent advantage in that luminescence from this phase is not reliant on quantum confinement effects and so the structural dimensions of cerium disilicate are not restricted to the nanoscale. This allows for large, continuous networks of nanocrystallites or even entire layers of cerium disilicate to be formed without limiting their radiative efficiency. For these materials, it would then be theoretically possible to directly contact the cerium disilicate phase to inject charge carriers and take advantage of a continuous structure for conduction rather than relying on the more complicated and generally inefficient methods, such as quantum tunneling or hot carrier injection, that have typically been employed to obtain electroluminescence from silicon nanoclusters.

References

[1] G. E. Moore, "Cramming more components onto integrated circuits," *Electronics*, vol. 38, no. 8, pp. 114–117, 1965.

[2] R. R. Schaller, "Moore's law: past, present and future," *IEEE Spectrum*, vol. 34, pp. 52–59, June 1997.

[3] G. E. Moore, "Progress in digital integrated electronics," *Technical Digest, International Electron Devices Meeting*, vol. 21, pp. 11–13, Sept. 1975.

[4] S. E. Thompson and S. Parthasarathy, "Moore's law: the future of Si microelectronics," *Materials Today*, vol. 9, pp. 20–25, June 2006.

[5] S. J. Wind, D. J. Frank, and H.-S. Wong, "Scaling silicon MOS devices to their limits," *Microelectronic Engineering*, vol. 32, pp. 271–282, Sept. 1996.

[6] Y. Taur, D. A. Buchanan, W. Chen, D. J. Frank, K. E. Ismail, S.-H. Lo, G. A. Sai-Halasz, R. G. Viswanathan, H.-J. C. Wann, S. J. Wind, and H.-S. Wong, "CMOS scaling into the nanometer regime," *Proceedings of the IEEE*, vol. 85, pp. 486–504, Apr. 1997.

[7] L. B. Kish, "End of Moore's law: thermal (noise) death of integration in micro and nano electronics," *Physics Letters A*, vol. 305, pp. 144–149, Dec. 2002.

[8] B. Jalali and S. Fathpour, "Silicon photonics," *Journal of Lightwave Technology*, vol. 24, pp. 4600–4615, Dec. 2006.

[9] S. Ossicini, L. Pavesi, and F. Priolo, *Light Emitting Silicon for Microphotonics*, vol. 194 of *Springer Tracts in Modern Physics*. Berlin, Germany: Springer Berlin Heidelberg, 2003.

[10] A. Liu, R. Jones, L. Liao, D. Samara-Rubio, D. Rubin, O. Cohen, R. Nicolaescu, and M. Paniccia, "A high-speed silicon optical modulator based on a metal-oxide-semiconductor capacitor," *Nature*, vol. 427, pp. 615–618, Feb. 2004.

[11] L. Brus, "Electronic wave functions in semiconductor clusters: experiment and theory," *The Journal of Physical Chemistry*, vol. 90, pp. 2555–2560, June 1986.

[12] C. Kittel, *Introduction to Solid State Physics*. New York, New York: John Wiley & Sons, Inc., 8th ed., 2004.

[13] L. T. Canham, "Silicon quantum wire array fabrication by electrochemical and chemical dissolution of wafers," *Applied Physics Letters*, vol. 57, no. 10, p. 1046, 1990.

[14] D. J. Lockwood, "Progress in light emission from silicon nanostructures," in *Spectroscopy of Emerging Materials* (E. C. Faulques, D. L. Perry, and A. V. Yeremenko, eds.), vol. 165 of *NATO Science Series II: Mathematics, Physics and Chemistry*, ch. 8, pp. 97–114, Dordrecht, Netherlands: Kluwer Academic Publishers, 2005.

[15] Y. Kanemitsu, "Efficient light emission from crystalline and amorphous silicon nanostructures," vol. 100, pp. 209–217, 2002.

[16] D. Kovalev, H. Heckler, M. Ben-Chorin, G. Polisski, M. Schwartzkopff, and F. Koch, "Breakdown of the k-conservation rule in Si nanocrystals," *Physical Review Letters*, vol. 81, pp. 2803–2806, Sept. 1998.

[17] M. J. Chen, J. L. Yen, J. Y. Li, J. F. Chang, S. C. Tsai, and C. S. Tsai, "Stimulated emission in a nanostructured silicon pn junction diode using current injection," *Applied Physics Letters*, vol. 84, no. 12, p. 2163, 2004.

[18] N. Daldosso, M. Luppi, S. Ossicini, E. Degoli, R. Magri, G. Dalba, P. Fornasini, R. Grisenti, F. Rocca, L. Pavesi, S. Boninelli, F. Priolo, C. Spinella, and F. Iacona, "Role of the interface region on the optoelectronic properties of silicon nanocrystals embedded in SiO_2," *Physical Review B*, vol. 68, pp. 1–8, Aug. 2003.

[19] L. Khriachtchev, M. Räsänen, S. Novikov, and J. Sinkkonen, "Optical gain in Si/SiO_2 lattice: Experimental evidence with nanosecond pulses," *Applied Physics Letters*, vol. 79, no. 9, p. 1249, 2001.

[20] K. S. Min, K. V. Shcheglov, C. M. Yang, H. A. Atwater, M. L. Brongersma, and A. Polman, "Defect-related versus excitonic visible light emission from ion beam synthesized Si nanocrystals in SiO_2," *Applied Physics Letters*, vol. 69, no. 14, p. 2033, 1996.

[21] L. Pavesi, L. Dal Negro, C. Mazzoleni, G. Franzò, and F. Priolo, "Optical gain in silicon nanocrystals," *Nature*, vol. 408, pp. 440–444, Nov. 2000.

[22] L. Pavesi and D. J. Lockwood, eds., *Silicon Photonics*, vol. 94 of *Topics in Applied Physics*. Berlin, Germany: Springer Berlin Heidelberg, 2004.

[23] G. Y. Sung, N.-M. Park, J.-H. Shin, K.-H. Kim, T.-Y. Kim, K. S. Cho, and C. Huh, "Physics and device structures of highly efficient silicon quantum dots based silicon nitride light-emitting diodes," *IEEE Journal of Selected Topics in Quantum Electronics*, vol. 12, pp. 1545–1555, Nov. 2006.

[24] M. V. Wolkin, J. Jorne, P. M. Fauchet, G. Allan, and C. Delerue, "Electronic states and luminescence in porous silicon quantum dots: the role of oxygen," *Physical Review Letters*, vol. 82, pp. 197–200, Jan. 1999.

[25] L. Dal Negro, J. H. Yi, V. Nguyen, Y. Yi, J. Michel, and L. C. Kimerling, "Spectrally enhanced light emission from aperiodic photonic structures," *Applied Physics Letters*, vol. 86, no. 26, p. 261905, 2005.

[26] N.-M. Park, C.-J. Choi, T.-Y. Seong, and S.-J. Park, "Quantum confinement in amorphous silicon quantum dots embedded in silicon nitride," *Physical Review Letters*, vol. 86, pp. 1355–1357, Feb. 2001.

[27] D. Comedi, O. H. Y. Zalloum, J. Wojcik, and P. Mascher, "Light emission from hydrogenated and unhydrogenated Si-nanocrystal/Si dioxide composites based on PECVD-grown Si-rich Si oxide films," *IEEE Journal of Selected Topics in Quantum Electronics*, vol. 12, pp. 1561–1569, Nov. 2006.

[28] F. Delachat, M. Carrada, G. Ferblantier, J.-J. Grob, and A. Slaoui, "Properties of silicon nanoparticles embedded in SiN_x deposited by microwave-PECVD," *Nanotechnology*, vol. 20, p. 415608, Oct. 2009.

[29] A.-S. Keita, A. En Naciri, F. Delachat, M. Carrada, G. Ferblantier, and A. Slaoui, "Spectroscopic ellipsometry investigation of the optical properties of nanostructured Si/SiN_x films," *Journal of Applied Physics*, vol. 107, no. 9, p. 093516, 2010.

[30] B. Rezgui, A. Sibai, T. Nychyporuk, M. Lemiti, G. Bremond, D. Maestre, and O. Palais, "Effect of total pressure on the formation and size evolution of silicon quantum dots in silicon nitride films," *Applied Physics Letters*, vol. 96, no. 18, p. 183105, 2010.

[31] O. M. Ntwaeaborwa, H. C. Swart, R. E. Kroon, P. H. Holloway, and J. R. Botha, "Enhanced luminescence and degradation of SiO_2:Ce,Tb powder phosphors prepared by a sol-gel process," *Journal of Physics and Chemistry of Solids*, vol. 67, pp. 1749–1753, Aug. 2006.

[32] O. M. Ntwaeaborwa, H. C. Swart, R. E. Kroon, J. R. Botha, and P. H. Holloway, "Cathodoluminescence degradation of SiO_2:Ce,Tb powder phosphors prepared by a sol-gel process," *Journal of Vacuum Science & Technology A: Vacuum, Surfaces, and Films*, vol. 25, no. 4, pp. 1152–1155, 2007.

[33] O. M. Ntwaeaborwa, M. S. Dhlamini, R. A. Harris, J. R. Botha, U. Buttner, and H. C. Swart, "Characterization of sol-gel SiO_2:Ce,Tb powder and pulsed laser deposited thin film phosphors," *Physica Status Solidi (C)*, vol. 5, pp. 602–605, Feb. 2008.

[34] Z. Liu, N. Dai, H. Luan, Y. Sheng, J. Peng, Z. Jiang, H. Li, L. Yang, and J. Li, "Enhanced green luminescence in Ce-Tb-Ca codoped sintered porous glass," *Optics Express*, vol. 18, pp. 21138–21146, Sept. 2010.

[35] J. Li, O. H. Y. Zalloum, T. Roschuk, C. L. Heng, J. Wojcik, and P. Mascher, "Light Emission from Rare-Earth Doped Silicon Nanostructures," *Advances in Optical Technologies*, vol. 2008, pp. 1–10, 2008.

[36] J. Li, "Light emission from rare earth-doped silicon oxide thin films deposited by ECR-PECVD," Master's thesis, McMaster University, 2008.

[37] J. Li, O. Zalloum, T. Roschuk, C. Heng, J. Wojcik, and P. Mascher, "The formation of light emitting cerium silicates in cerium-doped silicon oxides," *Applied Physics Letters*, vol. 94, no. 1, p. 011112, 2009.

[38] T. Roschuk, P. R. J. Wilson, J. Li, O. H. Y. Zalloum, J. Wojcik, and P. Mascher, "Structure and luminescence of rare earth-doped silicon oxides studied through their X-ray absorption near edge structure and X-ray excited optical luminescence," *Physica Status Solidi (B)*, vol. 247, pp. 248–253, Feb. 2010.

[39] G. H. Dieke, *Spectra and Energy Levels of Rare Earth Ions in Crystals.* New York, New York: John Wiley & Sons, Inc., 1968.

[40] G. Ertl and J. Küppers, *Low Energy Electrons and Surface Chemistry, Monographs in Modern Chemistry, Vol. 4*. Weinheim, Germany: Verlag Chemie, 1974.

[41] P. R. J. Wilson, T. Roschuk, K. Dunn, E. N. Normand, E. Chelomentsev, O. H. Y. Zalloum, J. Wojcik, and P. Mascher, "Effect of thermal treatment on the growth, structure and luminescence of nitride-passivated silicon nanoclusters," *Nanoscale Research Letters*, vol. 6, p. 168, Jan. 2011.

[42] T. Roschuk, P. R. J. Wilson, J. Li, J. Wojcik, and P. Mascher, "X-ray spectroscopy studies of luminescent Si-based materials," in *5th IEEE International Conference on Group IV Photonics*, pp. 288–290, IEEE, 2008.

[43] P. R. J. Wilson, T. Roschuk, O. Zalloum, J. Wojcik, and P. Mascher, "The effects of deposition and processing parameters on the electronic structure and photoluminescence from nitride-passivated silicon nanoclusters," *ECS Transactions*, vol. 16, no. 21, pp. 33–41, 2009.

[44] P. R. J. Wilson, T. Roschuk, K. Dunn, E. Normand, E. Chelomentsev, J. Wojcik, and P. Mascher, "Effect of annealing time on the growth, structure, and luminescence of nitride-passivated silicon nanoclusters," *ECS Transactions*, vol. 28, no. 3, pp. 51–59, 2010.

[45] T. Roschuk, P. R. J. Wilson, O. H. Y. Zalloum, J. Wojcik, J. Li, and P. Mascher, "Silicon nanocluster-based materials studies on the SGM and PGM beamlines," *CLS Activity Report*, vol. 2007, pp. 53–54, 2008.

[46] T. Roschuk, P. R. J. Wilson, J. Li, J. Wojcik, and P. Mascher, "Luminescent rare earth doped Si-based materials," *CLS Activity Report*, vol. 2008, pp. 70–71, 2009.

[47] T. Roschuk, P. R. J. Wilson, J. Wojcik, and P. Mascher, "Luminescent silicon-based materials – Si $L_{3,2}$-edge studies," *CLS Activity Report*, vol. 2008, pp. 72–73, 2009.

[48] P. R. J. Wilson, T. Roschuk, K. Dunn, E. Normand, E. Chelomentsev, J. Wojcik, and P. Mascher, "Isothermal investigation of luminescent nitride-passivated silicon nanoclusters," *CLS Activity Report*, vol. 2009, pp. 99–100, 2010.

[49] P. R. J. Wilson, Z. Khatami, R. Dabkowski, K. Dunn, E. Chelomentsev, J. Wojcik, and P. Mascher, "XANES and XEOL investigation of cerium and terbium co-doped silicon oxide films," *ECS Transactions*, vol. 45, pp. 43–48, Apr. 2012.

[50] P. Wilson, "Sensitization of terbium by cerium disilicate ($Ce_2Si_2O_7$) formed in silicon oxide films for tuneable blue/green emission." US Provisional Patent Application, October 2012. US 61/713,784.

[51] P. Wilson, "Sensitization of rare earth ions by cerium disilicate." US Provisional Patent Application, May 2013. US 61/829,457.

[52] P. Wilson, J. Li, and P. Mascher, "Formation of complete or partial layers of rare earth silicates through deposition." US Provisional Patent Application, May 2013. US 61/821,350.

[53] P. R. J. Wilson, T. Roschuk, K. Dunn, M. Betti, J. Wojcik, and P. Mascher, "The influence of structural ordering on luminescence from nitride- and oxynitride-passivated silicon nanoclusters," *ECS Transactions*, vol. 19, no. 8, pp. 19–28, 2009.

[54] R. Dabkowski, P. Wilson, J. Wojcik, and P. Mascher, "Technical review of a new ECR-PECVD reactor and characterization of un-doped and Ce-doped silicon oxynitride thin films," in *Society of Vacuum Coaters 54th Annual Technical Conference Proceedings*, pp. 283–289, 2011.

[55] V. Donzella, P. R. J. Wilson, K. A. Dunn, J. Wojcik, and P. Mascher, "Optical and physical characterization of SRSO and SRSN gradient thin films," *Journal of Materials Science and Engineering A: Structural Materials: Properties, Microstructure and Processing*, vol. 1, no. 2, pp. 152–160, 2011.

[56] T. Roschuk, P. R. J. Wilson, J. Li, K. A. Dunn, J. Wojcik, I. F. Crowe, R. M. Gwilliam, M. P. Halsall, A. P. Knights, and P. Mascher, "Structure and luminescence of rare earth-doped silicon oxides studied through XANES and XEOL," *ECS Transactions*, vol. 25, no. 9, pp. 213–222, 2009.

[57] A. Podhorodecki, G. Zatryb, J. Misiewicz, J. Wojcik, P. R. J. Wilson, and P. Mascher, "Green light emission from terbium doped silicon rich silicon oxide films obtained by plasma enhanced chemical vapor deposition," *Nanotechnology*, vol. 23, p. 475707, Nov. 2012.

[58] K. Dunn, E. Chelomentsev, R. Dabkowski, P. Wilson, T. Roschuk, and J. Wojcik, "Calibration and comparison of SiC_xN_y thin films deposited by ICP-CVD," in *Society of Vacuum Coaters 53rd Annual Technical Conference Proceedings*, 2010.

[59] K. Dunn, E. Chelomentsev, P. Wilson, T. Roschuk, J. Wojcik, and P. Mascher, "Luminescent SiC_xN_y thin films deposited by ICP-CVD," in *Society of Vacuum Coaters 53rd Annual Technical Conference Proceedings*, 2010.

[60] Z. Khatami, P. R. J. Wilson, K. Dunn, J. Wojcik, and P. Mascher, "The influence of carbon on the structure and photoluminescence of amorphous silicon carbonitride thin films," *ECS Transactions*, vol. 45, pp. 153–160, Apr. 2012.

[61] J. M. Chelikowsky and M. L. Cohen, "Nonlocal pseudopotential calculations for the electronic structure of eleven diamond and zinc-blende semiconductors," *Physical Review B*, vol. 14, pp. 556–582, July 1976.

[62] J. Schmidt, M. Kerr, and P. P. Altermatt, "Coulomb-enhanced Auger recombination in crystalline silicon at intermediate and high injection densities," *Journal of Applied Physics*, vol. 88, no. 3, p. 1494, 2000.

[63] J. Haynes and W. Westphal, "Radiation resulting from recombination of holes and electrons in silicon," *Physical Review*, vol. 101, pp. 1676–1678, Mar. 1956.

[64] J. Haynes, "Experimental proof of the existence of a new electronic complex in silicon," *Physical Review Letters*, vol. 4, pp. 361–363, Apr. 1960.

[65] J. R. Haynes, "Experimental observation of the excitonic molecule," *Physical Review Letters*, vol. 17, pp. 860–862, Oct. 1966.

[66] P. Dean, J. Haynes, and W. Flood, "New radiative recombination processes involving neutral donors and acceptors in silicon and germanium," *Physical Review*, vol. 161, pp. 711–729, Sept. 1967.

[67] C. E. Jones, "Temperature, stress, and annealing effects on the luminescence from electron-irradiated silicon," *Journal of Applied Physics*, vol. 44, no. 12, p. 5402, 1973.

[68] A. D. Yoffe, "Low-dimensional systems: quantum size effects and electronic properties of semiconductor microcrystallites (zero-dimensional systems) and some quasi-two-dimensional systems," *Advances in Physics*, vol. 42, pp. 173–262, Apr. 1993.

[69] A. D. Yoffe, "Semiconductor quantum dots and related systems: electronic, optical, luminescence and related properties of low dimensional systems," *Advances in Physics*, vol. 50, pp. 1–208, Jan. 2001.

[70] J. D. Plummer, M. Deal, and P. D. Griffin, *Silicon VLSI Technology: Fundamentals, Practice, and Modeling.* Upper Saddle River, New Jersey: Prentice Hall, 2000.

[71] H. Takagi, H. Ogawa, Y. Yamazaki, A. Ishizaki, and T. Nakagiri, "Quantum size effects on photoluminescence in ultrafine Si particles," *Applied Physics Letters*, vol. 56, no. 24, p. 2379, 1990.

[72] D. Xie, M. P. Wang, and W. H. Qi, "A simplified model to calculate the surface-to-volume atomic ratio dependent cohesive energy of nanocrystals," *Journal of Physics: Condensed Matter*, vol. 16, pp. L401–L405, Sept. 2004.

[73] T. R. Roschuk, *A study of luminescent Si-based materials through X-ray spectroscopies.* PhD thesis, McMaster University, 2009.

[74] S. V. Deshpande, E. Gulari, S. W. Brown, and S. C. Rand, "Optical properties of silicon nitride films deposited by hot filament chemical vapor deposition," *Journal of Applied Physics*, vol. 77, no. 12, p. 6534, 1995.

[75] T.-Y. Kim, N.-M. Park, K.-H. Kim, G. Y. Sung, Y.-W. Ok, T.-Y. Seong, and C.-J. Choi, "Quantum confinement effect of silicon nanocrystals in situ grown in silicon nitride films," *Applied Physics Letters*, vol. 85, no. 22, p. 5355, 2004.

[76] M. Molinari, H. Rinnert, and M. Vergnat, "Evolution with the annealing treatments of the photoluminescence mechanisms in a-SiN_x:H alloys prepared by reactive evaporation," *Journal of Applied Physics*, vol. 101, no. 12, p. 123532, 2007.

[77] V. A. Gritsenko, K. S. Zhuravlev, A. D. Milov, H. Wong, R. W. M. Kwok, and J. B. Xu, "Silicon dots/clusters in silicon nitride: photoluminescence and electron spin resonance," *Thin Solid Films*, vol. 353, pp. 20–24, Sept. 1999.

[78] K. S. Cho, N.-M. Park, T.-Y. Kim, K.-H. Kim, G. Y. Sung, and J. H. Shin, "High efficiency visible electroluminescence from silicon nanocrystals embedded in silicon nitride using a transparent doping layer," *Applied Physics Letters*, vol. 86, no. 7, p. 071909, 2005.

[79] J. Warga, R. Li, S. N. Basu, and L. Dal Negro, "Electroluminescence from silicon-rich nitride/silicon superlattice structures," *Applied Physics Letters*, vol. 93, no. 15, p. 151116, 2008.

[80] L. Dal Negro, R. Li, J. Warga, and S. N. Basu, "Silicon nanocrystals in silicon nitride structures: towards efficient light emission under optical and electrical pumping," in *5th IEEE International Conference on Group IV Photonics*, vol. 1, pp. 35–37, IEEE, 2008.

[81] Z. Yuan, D. Li, M. Wang, P. Chen, D. Gong, L. Wang, and D. Yang, "Photoluminescence of Tb^{3+} doped SiN_x films grown by plasma-enhanced chemical vapor deposition," *Journal of Applied Physics*, vol. 100, no. 8, p. 083106, 2006.

[82] R. Li, J. R. Schneck, J. Warga, L. D. Ziegler, and L. Dal Negro, "Carrier dynamics and erbium sensitization in silicon-rich nitride nanocrystals," *Applied Physics Letters*, vol. 93, no. 9, p. 091119, 2008.

[83] S. Yerci, R. Li, S. O. Kucheyev, T. van Buuren, S. N. Basu, and L. Dal Negro, "Energy transfer and 1.54 μm emission in amorphous silicon nitride films," *Applied Physics Letters*, vol. 95, no. 3, p. 031107, 2009.

[84] S. Yerci, R. Li, and L. Dal Negro, "Electroluminescence from Er-doped Si-rich silicon nitride light emitting diodes," *Applied Physics Letters*, vol. 97, no. 8, p. 081109, 2010.

[85] L. Dal Negro, M. Cazzanelli, L. Pavesi, S. Ossicini, D. Pacifici, G. Franzò, F. Priolo, and F. Iacona, "Dynamics of stimulated emission in silicon nanocrystals," *Applied Physics Letters*, vol. 82, no. 26, p. 4636, 2003.

[86] L. Dal Negro, M. Cazzanelli, N. Daldosso, Z. Gaburro, L. Pavesi, F. Priolo, D. Pacifici, G. Franzò, and F. Iacona, "Stimulated emission in plasma-enhanced chemical vapour deposited silicon nanocrystals," *Physica E: Low-dimensional Systems and Nanostructures*, vol. 16, pp. 297–308, Mar. 2003.

[87] P. M. Fauchet, J. Ruan, H. Chen, L. Pavesi, L. Dal Negro, M. Cazzaneli, R. G. Elliman, N. Smith, M. Samoc, and B. Luther-Davies, "Optical gain in different silicon nanocrystal systems," *Optical Materials*, vol. 27, pp. 745–749, Feb. 2005.

[88] H. Chen, J. H. Shin, P. M. Fauchet, J.-Y. Sung, J.-H. Shin, and G. Y. Sung, "Ultrafast photoluminescence dynamics of nitride-passivated silicon nanocrystals using the variable stripe length technique," *Applied Physics Letters*, vol. 91, no. 17, p. 173121, 2007.

[89] A. J. Kenyon, "Recent developments in rare-earth doped materials for optoelectronics," *Progress in Quantum Electronics*, vol. 26, no. 4-5, pp. 225–284, 2002.

[90] B. R. Judd, "Optical absorption intensities of rare-earth ions," *Physical Review*, vol. 127, pp. 750–761, Aug. 1962.

[91] G. S. Ofelt, "Intensities of crystal spectra of rare-earth ions," *The Journal of Chemical Physics*, vol. 37, no. 3, p. 511, 1962.

[92] L. Smentek, "Theoretical description of the spectroscopic properties of rare earth ions in crystals," *Physics Reports*, vol. 297, pp. 155–237, Apr. 1998.

[93] L. Smentek, "Judd-Ofelt theory: past, present and future," *Molecular Physics*, vol. 101, pp. 893–897, Apr. 2003.

[94] B. G. Wybourne, "The fascination of the rare earths–then, now and in the future," *Journal of Alloys and Compounds*, vol. 380, pp. 96–100, Oct. 2004.

[95] B. M. Walsh, "Judd-Ofelt theory: principles and practices," in *Advances in Spectroscopy for Lasers and Sensing* (B. Bartolo and O. Forte, eds.), ch. 21, pp. 403–433, Dordrecht, Netherlands: Kluwer Academic Publishers, 2006.

[96] W. J. Miniscalco, "Erbium-doped glasses for fiber amplifiers at 1500 nm," *Journal of Lightwave Technology*, vol. 9, no. 2, pp. 234–250, 1991.

[97] D. L. Dexter, "A theory of sensitized luminescence in solids," *The Journal of Chemical Physics*, vol. 21, no. 5, p. 836, 1953.

[98] T. Förster, "Zwischenmolekulare energiewanderung und fluoreszenz," *Annalen der Physik*, vol. 437, no. 1-2, pp. 55–75, 1948.

[99] P. G. Kik, M. L. Brongersma, and A. Polman, "Strong exciton-erbium coupling in Si nanocrystal-doped SiO_2," *Applied Physics Letters*, vol. 76, no. 17, p. 2325, 2000.

[100] D. E. Blakie, "Coupled luminescence centres in erbium-doped silicon rich silicon oxide thin films deposited by ECR-PECVD," Master's thesis, McMaster University, 2006.

[101] A. Polman and F. C. J. M. van Veggel, "Broadband sensitizers for erbium-doped planar optical amplifiers: review," *Journal of the Optical Society of America B*, vol. 21, no. 5, p. 871, 2004.

[102] T. Jüstel, H. Nikol, and C. Ronda, "New developments in the field of luminescent materials for lighting and displays," *Angewandte Chemie International Edition*, vol. 37, pp. 3084–3103, Dec. 1998.

[103] C. M. Wong, S. R. Rotman, and C. Warde, "Optical studies of cerium doped yttrium aluminum garnet single crystals," *Applied Physics Letters*, vol. 44, no. 11, p. 1038, 1984.

[104] R.-J. Xie and N. Hirosaki, "Silicon-based oxynitride and nitride phosphors for white LEDs—A review," *Science and Technology of Advanced Materials*, vol. 8, pp. 588–600, Oct. 2007.

[105] H. van Hal and H. Hintzen, "Compound formation in the Ce_2O_3-SiO_2 system," *Journal of Alloys and Compounds*, vol. 179, pp. 77–85, Feb. 1992.

[106] A. C. Tas and M. Akinc, "Phase relations in the system Ce_2O_3-$Ce_2Si_2O_7$ in the temperature range 1150° to 1970℃ in reducing and inert atmospheres," *Journal of the American Ceramic Society*, vol. 77, pp. 2953–2960, Nov. 1994.

[107] A. C. Tas and M. Akinc, "Crystal structures of the high-temperature forms of $Ln_2Si_2O_7$ (Ln = La, Ce, Pr, Nd, Sm) revisited," *Journal of the American Ceramic Society*, vol. 77, pp. 2968–2970, Nov. 1994.

[108] W. C. Choi, H. N. Lee, E. K. Kim, Y. Kim, C.-Y. Park, H. S. Kim, and J. Y. Lee, "Violet/blue light-emitting cerium silicates," *Applied Physics Letters*, vol. 75, no. 16, p. 2389, 1999.

[109] L. Kępiński, D. Hreniak, and W. Stręk, "Microstructure and luminescence properties of nanocrystalline cerium silicates," *Journal of Alloys and Compounds*, vol. 341, pp. 203–207, July 2002.

[110] L. Kępiński, M. Wołcyrz, and M. Marchewka, "Structure evolution of nanocrystalline CeO_2 supported on silica: effect of temperature and atmosphere," *Journal of Solid State Chemistry*, vol. 168, pp. 110–118, Oct. 2002.

[111] E. L. Belokoneva, T. L. Petrova, M. A. Simonov, and V. A. Belov, "Crystal structure of synthetic TR analogs of apatite $Dy_{4.67}[GeO_4]_3O$ and $Ce_{4.67}[SiO_4]_3O$," *Kristallografiya*, vol. 17, no. 3, pp. 490–493, 1972.

[112] J. M. S. Skakle, C. L. Dickson, and F. P. Glasser, "The crystal structures of $CeSiO_4$ and $Ca_2Ce_8(SiO_4)_6O_2$," *Powder Diffraction*, vol. 15, pp. 234–238, Jan. 2000.

[113] H. Zhang, "Study of optimal deposition conditions for an inductively coupled plasma chemical vapour deposition (ICP-CVD) system," Master's thesis, McMaster University, 2005.

[114] R. P. Dabkowski, "Installation of a New Electron Cyclotron Plasma Enhanced Chemical Vapour Deposition (ECR- PECVD) Reactor and a Preliminary Study of Thin Film Depositions," Master's thesis, McMaster University, 2012.

[115] K. Dunn, "Luminescent SiCxNy thin films deposited by ICP-CVD," Master's thesis, McMaster University, 2011.

[116] M. Mayer, *SIMNRA user's guide, report IPP 9/113.* Garching, Germany: Max-Planck-Institut für Plasmaphysik, 1997.

[117] W.-K. Chu, J. W. M. Mayer, and M.-A. Nicolet, *Backscattering Spectrometry.* New York, New York: Academic Press, Inc., 1978.

[118] J. R. Tesmer and M. Nastasi, *Handbook of Modern Ion Beam Materials Analysis.* Pittsburgh, Pennsylvania: Materials Research Society, 1995.

[119] J. Hale and B. Johs, *CompleteEASE™ Data Analysis Manual*. Lincoln, Nebraska: J. A. Woollam Co., Inc., 2011.

[120] O. H. Y. Zalloum, M. Flynn, T. Roschuk, J. Wojcik, E. Irving, and P. Mascher, "Laser photoluminescence spectrometer based on charge-coupled device detection for silicon-based photonics," *Review of Scientific Instruments*, vol. 77, no. 2, p. 023907, 2006.

[121] T. Smith and J. Guild, "The C.I.E. colorimetric standards and their use," *Transactions of the Optical Society*, vol. 33, no. 3, p. 73, 1931.

[122] M. Kness, "ColorPy - A Python package for handling physical descriptions of color and light spectra." `http://markkness.net/colorpy/ColorPy.html`, 2008.

[123] T. Regier, J. Krochak, T. K. Sham, Y. F. Hu, J. Thompson, and R. I. R. Blyth, "Performance and capabilities of the Canadian Dragon: the SGM beamline at the Canadian Light Source," *Nuclear Instruments and Methods in Physics Research Section A: Accelerators, Spectrometers, Detectors and Associated Equipment*, vol. 582, pp. 93–95, Nov. 2007.

[124] Y. F. Hu, L. Zuin, G. Wright, R. Igarashi, M. McKibben, T. Wilson, S. Y. Chen, T. Johnson, D. Maxwell, B. W. Yates, T. K. Sham, and R. Reininger, "Commissioning and performance of the variable line spacing plane grating monochromator beamline at the Canadian Light Source," *Review of Scientific Instruments*, vol. 78, p. 083109, Aug. 2007.

[125] M. Kasrai, W. N. Lennard, R. W. Brunner, G. M. Bancroft, J. A. Bardwell, and K. H. Tan, "Sampling depth of total electron and fluorescence measurements in Si L- and K-edge absorption spectroscopy," *Applied Surface Science*, vol. 99, pp. 303–312, Aug. 1996.

[126] S. Eisebitt, T. Böske, J.-E. Rubensson, and W. Eberhardt, "Determination of absorption coefficients for concentrated samples by fluorescence detection," *Physical Review B*, vol. 47, pp. 14103–14109, June 1993.

[127] J. G. Chen, "NEXAFS investigations of transition metal oxides, nitrides, carbides, sulfides and other interstitial compounds," *Surface Science Reports*, vol. 30, pp. 1–152, Jan. 1997.

[128] J. Stöhr, *NEXAFS Spectroscopy.* Berlin, Germany: Springer-Verlag, 1992.

[129] D. M. Pease, D. L. Brewe, Z. Tan, J. I. Budnick, and C. C. Law, "Accurate X-ray absorption spectra obtained from concentrated bulk samples by fluorescence detection," *Physics Letters A*, vol. 138, pp. 230–234, June 1989.

[130] G. D. Meitzner and D. A. Fischer, "Distortions of fluorescence yield X-ray absorption spectra due to sample thickness," *Microchemical Journal*, vol. 71, pp. 281–286, Apr. 2002.

[131] E. Curis, J. Osán, G. Falkenberg, S. Bénazeth, and S. Török, "Simulating systematic errors in X-ray absorption spectroscopy experiments: sample and beam effects," *Spectrochimica Acta Part B: Atomic Spectroscopy*, vol. 60, pp. 841–849, July 2005.

[132] D. Alders, T. Hibma, G. A. Sawatzky, K. C. Cheung, G. E. van Dorssen, M. D. Roper, H. A. Padmore, G. van der Laan, J. Vogel, and M. Sacchi, "Grazing incidence reflectivity and total electron yield effects in soft x-ray absorption spectroscopy," *Journal of Applied Physics*, vol. 82, no. 6, p. 3120, 1997.

[133] B. Gilbert, R. Andres, P. Perfetti, G. Margaritondo, G. Rempfer, and G. De Stasio, "Charging phenomena in PEEM imaging and spectroscopy," *Ultramicroscopy*, vol. 83, pp. 129–139, May 2000.

[134] T. Tanaka, K. K. Bando, N. Matsubayashi, M. Imamura, and H. Shimada, "Measurement of X-ray absorption spectra (XAS) of insulators by the partial electron yield method using an electron flood gun," *Journal of Electron Spectroscopy and Related Phenomena*, vol. 114-116, pp. 1077–1081, Mar. 2001.

[135] D. Vlachos, A. J. Craven, and D. W. McComb, "Specimen charging in X-ray absorption spectroscopy: correction of total electron yield data from stabilized zirconia in the energy range 250-915 eV," *Journal of Synchrotron Radiation*, vol. 12, pp. 224–33, Mar. 2005.

[136] G. Meitzner, "Experimental aspects of X-ray absorption spectroscopy," *Catalysis Today*, vol. 39, pp. 281–291, Mar. 1998.

[137] E. A. Stern and K. Kim, "Thickness effect on the extended-x-ray-absorption-fine-structure amplitude," *Physical Review B*, vol. 23, pp. 3781–3787, Apr. 1981.

[138] R. Carboni, S. Giovannini, G. Antonioli, and F. Boscherini, "Self-absorption correction strategy for fluorescence yield soft X-ray near edge spectra," *Physica Scripta*, vol. 2005, no. T115, p. 986, 2005.

[139] D. Haskel, "FLUO: Correcting XANES for self-absorption in fluorescence measurements." `http://www.aps.anl.gov/~haskel/fluo.html`, 1999.

[140] A. J. Achkar, T. Z. Regier, H. Wadati, and Y. J. Kim, "Bulk sensitive x-ray absorption spectroscopy free of self-absorption effects," *Physical Review B*, vol. 83, pp. 2–5, Feb. 2011.

[141] J. Kawai and H. Takahashi, "Si X-ray absorption near edge structure (XANES) of Si, SiC, SiO_2, and Si_3N_4 measured by an electron probe X-ray microanalyzer (EPMA)," *Spectrochimica Acta Part B: Atomic Spectroscopy*, vol. 54, pp. 231–234, Jan. 1999.

[142] A. Savitzky and M. J. E. Golay, "Smoothing and differentiation of data by simplified least squares procedures," *Analytical Chemistry*, vol. 36, pp. 1627–1639, July 1964.

[143] Bruker AXS, *General Area Detector Diffraction System (GADDS) User Manual*. Madison, Wisconsin: Bruker AXS, Inc., 1999.

[144] Bruker AXS, *Topas 4.2 User Manual*. Karlsruhe, Germany: Bruker AXS GmbH, 2009.

[145] N. Daldosso, G. Das, S. Larcheri, G. Mariotto, G. Dalba, L. Pavesi, A. Irrera, F. Priolo, F. Iacona, and F. Rocca, "Silicon nanocrystal formation in annealed silicon-rich silicon oxide films prepared by plasma enhanced chemical vapor deposition," *Journal of Applied Physics*, vol. 101, no. 11, p. 113510, 2007.

[146] I. Coulthard and T. K. Sham, "Luminescence from porous silicon: an optical X-ray absorption fine structures study at the Si $L_{3,2}$-edge," *Solid State Communications*, vol. 110, pp. 203–208, Mar. 1999.

[147] C. M. Hessel, E. J. Henderson, J. A. Kelly, R. G. Cavell, T.-K. Sham, and J. G. C. Veinot, "Origin of luminescence from silicon nanocrystals: a near edge X-ray absorption fine structure (NEXAFS) and X-ray excited optical luminescence (XEOL) study of oxide-embedded and free-standing systems," *Journal of Physical Chemistry C*, vol. 112, pp. 14247–14254, Sept. 2008.

[148] Y. F. Hu, K. H. Tan, P. S. Kim, P. Zhang, S. J. Naftel, T. K. Sham, I. Coulthard, and B. W. Yates, "Soft X-ray excited optical luminescence: some recent applications," *Review of Scientific Instruments*, vol. 73, no. 3, p. 1379, 2002.

[149] R. Sammynaiken, S. J. Naftel, T. K. Sham, K. W. Cheah, B. Averboukh, R. Huber, Y. R. Shen, G. G. Qin, Z. C. Ma, and W. H. Zong, "Structure and

electronic properties of SiO_2/Si multilayer superlattices: Si K edge and $L_{3,2}$ edge X-ray absorption fine structure study," *Journal of Applied Physics*, vol. 92, no. 6, p. 3000, 2002.

[150] T. K. Sham, D. T. Jiang, I. Coulthard, J. W. Lorimer, X. H. Feng, K. H. Tan, S. P. Frigo, R. A. Rosenberg, D. C. Houghton, and B. Bryskiewicz, "Origin of luminescence from porous silicon deduced by synchrotron-light-induced optical luminescence," *Nature*, vol. 363, pp. 331–334, May 1993.

[151] T. K. Sham, S. J. Naftel, and I. Coulthard, *Chemical Applications of Synchrotron Radiation*. River Edge, New Jersey: World Scientific, 2002.

[152] J. Anstey, "A study of the light emission from SiNx films," Master's thesis, McMaster University, 2011.

[153] R. M. Savidge, "Down-shifting of light by ion implanted samples for photovoltaic applications," Master's thesis, McMaster University, 2012.

[154] R. C. Mehrotra, R. Bohra, and D. P. Gaur, *Metal β-Diketonates and Allied Derivatives*. New York, New York: Academic Press, Inc., 1978.

[155] Strem Chemical, Inc., "Metal TMHD Compounds." `http://www.strem.com/resource/18/175/metal_tmhd_compounds/`, 2013.

[156] W. M. Haynes, ed., *CRC Handbook of Chemistry and Physics*. Boca Raton, Florida: CRC Press/Taylor and Francis, 93rd ed., 2013.

[157] M. Yashima and T. Takizawa, "Atomic displacement parameters of ceria doped with rare-earth oxide $Ce_{0.8}R_{0.2}O_{1.9}$ (R = La, Nd, Sm, Gd, Y, and Yb) and correlation with oxide-ion conductivity," *The Journal of Physical Chemistry C*, vol. 114, pp. 2385–2392, Feb. 2010.

[158] M. Yashima and T. Takizawa, "Atomic displacement parameters of ceria doped with rare-earth oxide $Ce_{0.8}R_{0.2}O_{1.9}$ (R = La, Nd, Sm, Gd, Y, and Yb) and correlation with oxide-ion conductivity," *The Journal of Physical Chemistry C*, vol. 114, pp. 10670–10670, June 2010.